

BUCKLING AND DAMAGE RESISTANCE OF TRANSVERSELY-
LOADED COMPOSITE SHELLS

by

Brian L. Wardle

B. S., Aerospace Engineering
The Pennsylvania State University (1992)

S. M., Aeronautics and Astronautics
Massachusetts Institute of Technology (1995)

Submitted to the Department of Aeronautics and Astronautics in Partial
Fulfillment of the Requirements for the Degree of

Doctor of Philosophy
in Aeronautics and Astronautics

at the

Massachusetts Institute of Technology
June 1998

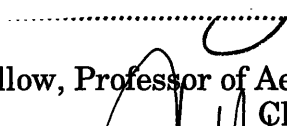
© 1998 Massachusetts Institute of Technology
All rights reserved

Signature of Author




.....
Department of Aeronautics and Astronautics
April 28, 1998

Certified by



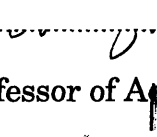
.....
Paul A. Lagace
MacVicar Faculty Fellow, Professor of Aeronautics and Astronautics
Chairman, Thesis Committee

Certified by



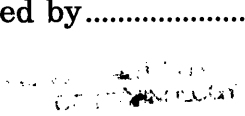
.....
John W. Hutchinson
Gordon McKay Professor of Applied Mechanics, Harvard University
Thesis Committee

Certified by



.....
S. Mark Spearing
Boeing Assistant Professor of Aeronautics and Astronautics
Thesis Committee

Accepted by



.....
Jaime Peraire
Associate Professor of Aeronautics and Astronautics
Chairman, Department Graduate Committee

JUL 08 1998

LIBRARIES

BUCKLING AND DAMAGE RESISTANCE OF TRANSVERSELY- LOADED COMPOSITE SHELLS

by

Brian L. Wardle

Submitted to the Department of Aeronautics and Astronautics
on April 28, 1998 in Painful Fulfillment of the
Requirements for the Degree of Doctor of Philosophy in
Aeronautics and Astronautics

ABSTRACT

Experimental and numerical work was conducted to better understand composite shell response to transverse loadings which simulate damage-causing impact events. The quasi-static, centered, transverse loading response of laminated graphite/epoxy shells in a $[\pm 45_n/0_n]_s$ layup having geometric characteristics of a commercial fuselage are studied. The singly-curved composite shell structures are hinged along the straight circumferential edges and either free or simply supported along the curved axial edges. Key components of the shell response are response instabilities due to limit-point and/or bifurcation buckling. Experimentally, deflection-controlled shell response is characterized via load-deflection data, deformation-shape evolutions, and the resulting damage state. Finite element models are used to study the kinematically nonlinear shell response, including bifurcation, limit-points, and postbuckling. A novel technique is developed for evaluating bifurcation from nonlinear prebuckling states utilizing asymmetric spatial discretization to introduce numerical perturbations. Advantages of the asymmetric meshing technique (AMT) over traditional techniques include efficiency, robustness, ease of application, and solution of the actual (not modified) problems. The AMT is validated by comparison to traditional numerical analysis of a benchmark problem and verified by comparison to experimental data. Applying the technique, bifurcation in a benchmark shell-buckling problem is correctly identified. Excellent agreement between the numerical and experimental results are obtained for a number of composite shells although predictive capability decreases for stiffer (thicker) specimens which is attributed to compliance of the test fixture. Restraining the axial edge (simple support) has the effect of creating a more complex response which involves unstable bifurcation, limit-point buckling, and dynamic collapse. Such shells were noted to bifurcate into asymmetric deformation modes but were undamaged during testing. Shells in this study which were damaged were not observed to bifurcate. Thus, a direct link between bifurcation and atypical damage could not be established although the mechanism (bifurcation) was identified. Recommendations for further work in these related areas are provided and include extensions of the AMT to other shell geometries and structural problems.

Thesis Supervisor: Paul A. Lagace

Title: MacVicar Faculty Fellow, Professor of Aeronautics and Astronautics

Acknowledgment

Many thanks to Paul for his efforts throughout this work. Thanks also to John Hutchinson and Mark Spearing for their comments and guidance. Thanks also to the other Profs. in TELAC and especially to Deb-ster and Ping for their help whenever needed. Thanks to John Kane for helping out in the lab. Of course, my UROPs did the real work: thanks to Doug MacIvor for helping get things started and Kim Murdoch who was there through experiments and STAGS til the bitter(?) end. Huge thanks and a shout out to Allen Waters down at Langley - Folks, that man knows his finite elements. Special thanks to my family and Gram for support over the years. Most of all, thanks to Cecelia for support and understanding - it meant a lot.

I used up all the good quotes in my Master's thesis. Speaking of which, the length of this thesis is 0.49 Wardles - I win.

Foreword

This work was performed in the Technology Laboratory for Advanced Composites (TELAC) in the Department of Aeronautics and Astronautics at the Massachusetts Institute of Technology. This work was sponsored by NASA Langley Research Center under NASA Grant NAG-1-991.

Table of Contents

List of Figures	7
List of Tables.....	15
Nomenclature	16
1 INTRODUCTION	17
2 BACKGROUND	22
2.1 Damage Resistance.....	22
2.1.1 Plates.....	23
2.1.2 Shells.....	25
2.2 Elastic Stability.....	27
2.2.1 Definitions	28
2.2.2 Shell Buckling.....	32
2.2.3 Finite Element Modeling	33
3 APPROACH	39
3.1 General Overview	39
3.2 Numerical (Finite Element) Modeling	45
3.3 Experiments	48
4 FINITE ELEMENT MODELING.....	51
4.1 Modeling Overview	51
4.2 Asymmetric Meshing Technique for Bifurcation.....	54
4.3 Benchmark Shell Buckling Problem.....	58
4.3.1 Comparison to Previous Work (Limit-point Buckling)	58
4.3.2 Bifurcation Buckling.....	61
4.3.3 Mesh Refinement and Convergence.....	73
4.4 Analysis of Previous Experimental Work	75
4.4.1 Description of Experiments.....	77
4.4.2 Load-deflection and Mode-shape Comparisons.....	78
4.4.3 Modeling Assumptions and Experimental Realities.....	93
4.5 Summary	98

5	EXPERIMENTS	100
5.1	Manufacturing Procedures.....	100
5.1.1	Graphite/Epoxy Prepreg Layup	100
5.1.2	Curing	101
5.1.3	Final Specimen Preparation	107
5.2	Curvature and Thickness Mapping.....	108
5.3	Test Fixture (Boundary Conditions).....	113
5.4	Testing Procedures.....	119
5.4.1	Specimen Set-up in Fixture.....	122
5.4.2	Quasi-static Testing and Mode-shape Measurement.....	124
5.5	Damage Evaluation.....	128
6	RESULTS.....	133
6.1	Experimental Observations.....	133
6.1.1	Loading Response.....	133
6.1.2	Mode-shape Evolutions.....	143
6.1.3	Damage Development.....	166
6.2	Numerical Analysis	171
6.2.1	Loading Response.....	171
6.2.2	Mode-shape Evolutions.....	193
7	DISCUSSION.....	207
7.1	Experimental and Numerical Comparisons	207
7.2	Boundary Conditions	228
7.2.1	Modeling Assumption at Circumferential (Hinged) Edge.....	228
7.2.2	Effect of Axial Edge Restraint.....	233
7.3	Damage Resistance.....	245
7.4	Asymmetric Meshing Technique (AMT).....	246
8	CONCLUSIONS AND RECOMMENDATIONS.....	249
8.1	Conclusions.....	249
8.2	Recommendations.....	251
	References	254
	Appendix A MANUFACTURING DATA.....	265
	Appendix B NUMERICAL COMPARISON TO PREVIOUS EXPERIMENTAL LOAD-DEFLECTION DATA.....	267

List of Figures

Figure 2.1	Illustration of typical shell instability [19].	26
Figure 2.2	Load-deflection curves showing limit-point and bifurcation buckling behavior (as in [43]).	29
Figure 3.1	Illustration of generic composite shell specimen.	41
Figure 3.2	Illustration of restrained shell with local coordinate system used to describe boundary condition at shell axial edge.	44
Figure 4.1	Illustration of a 10 x 10 mesh and curvilinear shell coordinate system. (The x and y (curvilinear) vectors are in the plane of the shell while z is everywhere perpendicular to the shell surface.)	53
Figure 4.2	Illustration of an asymmetrically meshed shell discretized into two shell units in the circumferential (y) direction.	57
Figure 4.3	Configuration for benchmark shell problem.	59
Figure 4.4	Numerical analysis and previously reported results [61, 71] for load-deflection response of benchmark shell problem.	60
Figure 4.5	Central spanwise deformation modes for benchmark problem at different values of center deflection, w_c , using STAGS with a symmetric (10x10) mesh.	62
Figure 4.6	Load versus center and edge deflections for benchmark problem using STAGS with a symmetric (10x10) mesh.	63
Figure 4.7	Load-deflection response for benchmark problem using STAGS with a symmetric (10x10) mesh incorporating scaled eigenmode imperfections into the initial geometry.	65
Figure 4.8	Central spanwise plot of the linear bifurcation mode for benchmark shell problem.	66
Figure 4.9	Load-deflection response for benchmark problem using STAGS with a symmetric (10x10) mesh incorporating scaled eigenmode deformations (equivalence transform) near the bifurcation point.	67
Figure 4.10	Central spanwise deformation modes for benchmark problem at different values of center deflection, w_c , using STAGS with a symmetric (10x10) mesh and the equivalence transform method (2.0% thickness).	69

Figure 4.11	Load-deflection response for benchmark problem using STAGS with symmetric (10x10) and asymmetric (10x6 / 10x5) meshes.	70
Figure 4.12	Central spanwise deformation modes for benchmark problem at different values of center deflection, w_c , using STAGS with an asymmetric (10x6 / 10x5) mesh.	71
Figure 4.13	Load versus center and edge deflections for benchmark problem using STAGS with an asymmetric (10x6 / 10x5) mesh.	72
Figure 4.14	Numerical analysis of load-deflection response for benchmark shell problem using various asymmetric meshes.	74
Figure 4.15	Load-deflection response for benchmark problem using STAGS with asymmetric (20x12 / 20x9) and (20x12 / 20x5) meshes.	76
Figure 4.16	Central load-deflection results from numerical analyses and experiment [21] for the transverse buckling response of composite shell specimen $R_6S_3T_1$.	80
Figure 4.17	Central load-deflection results from numerical analyses and experiment [21] for the transverse buckling response of composite shell specimen $R_{12}S_3T_1$.	81
Figure 4.18	Numerical analysis results of central spanwise deformation modes for specimen $R_6S_3T_1$ at different values of normalized center deflection.	82
Figure 4.19	Measured [21] central spanwise deformation modes for specimen $R_6S_3T_1$ at different values of normalized center deflection.	83
Figure 4.20	Numerical analysis results of central spanwise deformation modes for specimen $R_{12}S_3T_1$ at different values of normalized center deflection.	84
Figure 4.21	Measured [21] central spanwise deformation modes for specimen $R_{12}S_3T_1$ at different values of normalized center deflection.	85
Figure 4.22	Numerical analysis results of central axial deformation modes for specimen $R_6S_3T_1$ at different values of normalized center deflection.	87
Figure 4.23	Measured [21] central axial deformation modes for specimen $R_6S_3T_1$ at different values of normalized center deflection.	88

Figure 4.24	Numerical analysis results of central axial deformation modes for specimen $R_{12}S_3T_1$ at different values of normalized center deflection.	89
Figure 4.25	Measured [21] central axial deformation modes for specimen $R_{12}S_3T_1$ at different values of normalized center deflection.	90
Figure 4.26	Numerical analysis results of central spanwise deformation modes for specimen $R_6S_3T_1$ at different values of normalized center deflection, w_c/T_1 , near the bifurcation point.	91
Figure 4.27	Numerical analysis results of edge spanwise deformation modes for specimen $R_6S_3T_1$ at different values of normalized center deflection, w_c/T_1 , near the bifurcation point.	92
Figure 4.28	Load versus center and edge deflections from numerical analysis of specimen $R_{12}S_3T_1$.	94
Figure 4.29	Central load-deflection results from numerical analyses and experiment [21] for the transverse buckling response of composite shell specimen $R_{12}S_3T_2$.	96
Figure 5.1	Illustration of cylindrical mold.	102
Figure 5.2	Cure assembly.	105
Figure 5.3	Nominal temperature, pressure, and vacuum profiles for cure cycle.	106
Figure 5.4	Locations used for mapping shell thickness.	109
Figure 5.5	Illustration of overhead view of curvature measuring setup.	110
Figure 5.6	Measurements and associated locations used in radii and twist calculations.	111
Figure 5.7	Side-view illustration of original test fixture.	115
Figure 5.8	Illustration of rod/cushion assembly.	116
Figure 5.9	Illustration of laser operation and grooved insert in the rod-cushion assembly.	117
Figure 5.10	Illustration of test fixture modification used to restrain axial shell edges.	118
Figure 5.11	Three-view schematic (to scale) of lower support for axial shell edge. (Note: all dimensions in inches)	120
Figure 5.12	Three-view schematic (to scale) of upper support for axial shell edge. (Note: all dimensions in inches)	121
Figure 5.13	Illustration of test fixture and shell mounted in testing machine.	125
Figure 5.14	Deflection-measurement assembly.	127

Figure 5.15	Sample planar x-ray picture showing damaged region.	130
Figure 5.16	Examples of visible damage in cross-sections of a T_2 shell: (top) entire specimen thickness, and (bottom) magnified view of lower right corner.	132
Figure 6.1	Experimental load-deflection response for specimen $R_{12}S_3T_1-1$.	135
Figure 6.2	Experimental load-deflection response for specimen $R_{12}S_3T_1-2$.	136
Figure 6.3	Experimental load-deflection response for specimen $R_{12}S_3T_2-1$.	139
Figure 6.4	Experimental load-deflection response for specimen $R_{12}S_3T_2-2$.	140
Figure 6.5	Experimental load-deflection response for specimen $R_{12}S_3T_3-1$.	141
Figure 6.6	Experimental load-deflection response for specimen $R_{12}S_3T_3-2$.	142
Figure 6.7	Experimental load-deflection responses for specimens of different thicknesses.	144
Figure 6.8	Measured central spanwise deformation modes for specimen $R_{12}S_3T_1-1$ at different values of center deflection.	146
Figure 6.9	Measured left spanwise deformation modes for specimen $R_{12}S_3T_1-1$ at different values of center deflection.	147
Figure 6.10	Measured right spanwise deformation modes for specimen $R_{12}S_3T_1-1$ at different values of center deflection.	148
Figure 6.11	Measured central spanwise deformation modes for specimen $R_{12}S_3T_1-2$ at different values of center deflection.	149
Figure 6.12	Measured left spanwise deformation modes for specimen $R_{12}S_3T_1-2$ at different values of center deflection.	150
Figure 6.13	Measured right spanwise deformation modes for specimen $R_{12}S_3T_1-2$ at different values of center deflection.	151
Figure 6.14	Measured central spanwise deformation modes for specimen $R_{12}S_3T_2-1$ at different values of center deflection.	153
Figure 6.15	Measured left spanwise deformation modes for specimen $R_{12}S_3T_2-1$ at different values of center deflection.	154
Figure 6.16	Measured right spanwise deformation modes for specimen $R_{12}S_3T_2-1$ at different values of center deflection.	155
Figure 6.17	Measured central spanwise deformation modes for specimen $R_{12}S_3T_3-1$ at different values of center deflection.	156

Figure 6.18	Measured left spanwise deformation modes for specimen $R_{12}S_3T_3-1$ at different values of center deflection.	157
Figure 6.19	Measured right spanwise deformation modes for specimen $R_{12}S_3T_3-1$ at different values of center deflection.	158
Figure 6.20	Measured central spanwise deformation modes for specimen $R_{12}S_3T_2-2$ at different values of center deflection.	159
Figure 6.21	Measured left spanwise deformation modes for specimen $R_{12}S_3T_2-2$ at different values of center deflection.	160
Figure 6.22	Measured right spanwise deformation modes for specimen $R_{12}S_3T_2-2$ at different values of center deflection.	161
Figure 6.23	Measured central spanwise deformation modes for specimen $R_{12}S_3T_3-2$ at different values of center deflection.	162
Figure 6.24	Measured left spanwise deformation modes for specimen $R_{12}S_3T_3-2$ at different values of center deflection.	163
Figure 6.25	Measured right spanwise deformation modes for specimen $R_{12}S_3T_3-2$ at different values of center deflection.	164
Figure 6.26	X-ray photographs of specimen type $R_{12}S_3T_2$ loaded to: (top) 1096 N ($w_c = 16.0$ mm), and (bottom) 1737 N ($w_c = 19.1$ mm).	168
Figure 6.27	X-ray photographs of specimen type $R_{12}S_3T_3$ loaded to: (top) 1987 N ($w_c = 15.0$ mm), and (bottom) 2746 N ($w_c = 16.6$ mm).	169
Figure 6.28	Load-deflection results from numerical analyses for specimen $R_{12}S_3T_1-1$ using symmetric meshes.	173
Figure 6.29	Load-deflection results from numerical analyses for specimen $R_{12}S_3T_1-1$ using symmetric and asymmetric meshes.	175
Figure 6.30	Load-deflection results from numerical analyses for specimen $R_{12}S_3T_1-1$ using various asymmetric meshes.	177
Figure 6.31	Central spanwise bifurcation mode evaluated at 126 N for specimen $R_{12}S_3T_1-1$ using a symmetric (20x20) mesh.	179
Figure 6.32	Load-deflection results from numerical analyses of specimen $R_{12}S_3T_1-1$ using a 20x20 symmetric mesh incorporating scaled eigenmode deformations (equivalence transform) near the bifurcation point.	180
Figure 6.33	Load-deflection results from numerical analyses of specimen $R_{12}S_3T_1-1$ using a 20x20 symmetric mesh and a 20x20 symmetric mesh with a 0.5% t imperfection based on the eigenmode in Figure 6.31.	182

Figure 6.34	Load-deflection results from numerical analyses of specimen $R_{12}S_3T_{1-1}$ using a 20x20 symmetric mesh with 50% and 100% t imperfections based on the eigenmode in Figure 6.31.	183
Figure 6.35	Load-deflection results from numerical analyses for specimens $R_{12}S_3T_{1-1}$ and $R_{12}S_3T_{1-2}$ using an asymmetric (20x12 / 20x5) mesh.	185
Figure 6.36	Load-deflection results from numerical analyses for specimen $R_{12}S_3T_{2-1}$ using symmetric and asymmetric meshes.	186
Figure 6.37	Load-deflection results from numerical analyses for specimens $R_{12}S_3T_{2-1}$ and $R_{12}S_3T_{2-2}$ using an asymmetric (20x12 / 20x7) mesh.	187
Figure 6.38	Load-deflection results from numerical analyses for specimen $R_{12}S_3T_{3-1}$ using symmetric and asymmetric meshes.	189
Figure 6.39	Blow-up of Figure 6.38 in area of bifurcation: load-deflection results from numerical analyses for specimen $R_{12}S_3T_{3-1}$ using symmetric and asymmetric meshes.	190
Figure 6.40	Load-deflection results from numerical analyses for specimens $R_{12}S_3T_{3-1}$ and $R_{12}S_3T_{3-2}$ using an asymmetric (20x12 / 20x7) mesh.	191
Figure 6.41	Load-deflection results from numerical analyses for specimens $R_{12}S_3T_{1-1}$, $R_{12}S_3T_{2-1}$, and $R_{12}S_3T_{3-1}$ using asymmetric meshes.	192
Figure 6.42	Numerical analysis results of central spanwise deformation modes for specimen $R_{12}S_3T_{1-2}$ at different values of center deflection.	195
Figure 6.43	Numerical analysis results of left spanwise deformation modes for specimen $R_{12}S_3T_{1-2}$ at different values of center deflection.	196
Figure 6.44	Numerical analysis results of right spanwise deformation modes for specimen $R_{12}S_3T_{1-2}$ at different values of center deflection.	197
Figure 6.45	Numerical analysis results of central spanwise deformation modes for specimen $R_{12}S_3T_{2-2}$ at different values of center deflection.	199
Figure 6.46	Numerical analysis results of left spanwise deformation modes for specimen $R_{12}S_3T_{2-2}$ at different values of center deflection.	200

Figure 6.47	Numerical analysis results of right spanwise deformation modes for specimen $R_{12}S_3T_{2-2}$ at different values of center deflection.	201
Figure 6.48	Numerical analysis results of central spanwise deformation modes for specimen $R_{12}S_3T_{3-2}$ at different values of center deflection.	203
Figure 6.49	Numerical analysis results of left spanwise deformation modes for specimen $R_{12}S_3T_{3-2}$ at different values of center deflection.	204
Figure 6.50	Numerical analysis results of right spanwise deformation modes for specimen $R_{12}S_3T_{3-2}$ at different values of center deflection.	205
Figure 7.1	Illustration of deflection-controlled "snap" utilizing load-deflection results from numerical analyses for specimen $R_{12}S_3T_{1-1}$ (see Figure 6.29).	209
Figure 7.2	Numerical and experimental load-deflection results for specimen $R_{12}S_3T_{1-1}$.	210
Figure 7.3	Numerical and experimental load-deflection results for specimen $R_{12}S_3T_{2-1}$.	211
Figure 7.4	Numerical and experimental load-deflection results for specimen $R_{12}S_3T_{3-1}$.	212
Figure 7.5	Measured central spanwise deformation modes for specimen $R_{12}S_3T_{1-2}$ at different values of center deflection.	216
Figure 7.6	Numerical analysis results of central spanwise deformation modes for specimen $R_{12}S_3T_{1-2}$ at different values of center deflection.	217
Figure 7.7	Measured left spanwise deformation modes for specimen $R_{12}S_3T_{1-2}$ at different values of center deflection.	218
Figure 7.8	Numerical analysis results of left spanwise deformation modes for specimen $R_{12}S_3T_{1-2}$ at different values of center deflection.	219
Figure 7.9	Measured right spanwise deformation modes for specimen $R_{12}S_3T_{1-2}$ at different values of center deflection.	220
Figure 7.10	Numerical analysis results of right spanwise deformation modes for specimen $R_{12}S_3T_{1-2}$ at different values of center deflection.	221
Figure 7.11	Measured central spanwise deformation modes for specimen $R_{12}S_3T_{2-2}$ at different values of center deflection.	223

Figure 7.12	Numerical analysis results of central spanwise deformation modes for specimen $R_{12}S_3T_2-2$ at different values of center deflection.	224
Figure 7.13	Measured central spanwise deformation modes for specimen $R_{12}S_3T_3-2$ at different values of center deflection.	225
Figure 7.14	Numerical analysis results of central spanwise deformation modes for specimen $R_{12}S_3T_3-2$ at different values of center deflection.	226
Figure 7.15	Numerical load-deflection results for specimen $R_{12}S_3T_1-1$ utilizing different assumptions on the u-component of displacement at the circumferential boundary condition (hinged).	230
Figure 7.16	Numerical load-deflection results for specimen $R_{12}S_3T_2-1$ utilizing different assumptions on the u-component of displacement at the circumferential boundary condition (hinged).	231
Figure 7.17	Numerical load-deflection results for specimen $R_{12}S_3T_3-1$ utilizing different assumptions on the u-component of displacement at the circumferential boundary condition (hinged).	232
Figure 7.18	Experimental load-deflection response of composite shell $R_{12}S_3T_1$ with axial edges restrained and free [21].	235
Figure 7.19	Numerical load-deflection results for composite shell $R_{12}S_3T_1$ with axial edges restrained and free.	236
Figure 7.20	Experimental load-deflection response of composite shell $R_{12}S_3T_2$ with axial edges restrained and free [21].	238
Figure 7.21	Numerical load-deflection results for composite shell $R_{12}S_3T_2$ with axial edges restrained and free.	239
Figure 7.22	Experimental load-deflection response of composite shell $R_{12}S_3T_3$ with axial edges restrained and free [21].	240
Figure 7.23	Numerical load-deflection results for composite shell $R_{12}S_3T_3$ with axial edges restrained and free.	241
Figure 7.24	Experimental central spanwise deformation modes for specimen $R_{12}S_3T_1$ at different values of center deflection with axial edges free [21].	243
Figures B.1- B.18	Loading response comparison from numerical analysis and experimental data [21] for composite shells.	269- 286

List of Tables

Table 4.1	AS4/3501-6 Ply Data	77
Table 5.1	Results of Thickness and Curvature Mapping	113
Table 6.1	Peak Load and Associated Center Deflection	167
Table A.1	Radius and Thickness Data	266
Table B.1	Measured Values of Radius Used in Numerical Analysis	268

Nomenclature

E	Young's modulus
G	shear modulus
n	structural scaling parameter
R	shell radius
R_n	scaled shell radius
R_x	rotation about x -direction
R_y	rotation about y -direction
R_z	rotation about z -direction
S_n	scaled shell span
t	shell thickness
T_n	scaled shell thickness
u	displacement component in x -direction
v	displacement component in y -direction
w	displacement component in z -direction
w_c	w displacement at shell center
x	axial direction
X_1	base for generic scaled structural variable
X_n	generic scaled structural variable
y	curvilinear circumferential direction
z	transverse direction
β	axial twist
γ	spanwise twist
ν	Poisson's ratio
θ	ply angle

CHAPTER 1

INTRODUCTION

Laminated composite materials continue to see increased use in structural applications. Performance advantages over traditional metallic structures abound: high specific stiffness and strength, mechanical tailoring capabilities, and excellent fatigue characteristics are some of the attributes that make structures built from laminated composites attractive to designers. This is especially true in the aerospace community where composites are seen to provide increased performance for both military and commercial structures.

In the aircraft industry, composites initially replaced secondary structures that were typically made from aluminum, *e.g.*, [1, 2]. Damage considerations in the design of secondary structures are typically not critical. However, composites have seen increased application in design of primary aerospace structures where damage is a critical design issue. Primary composite structures in the V-22 Osprey, single-stage to orbit (SSTO) reusable launch vehicles, and the space shuttle are just some examples [3, 4]. Composites are also being used in large commercial aircraft designs. The Beechcraft Starship was the first all-composite aircraft certified by the FAA and, even more recently, composites have seen application in primary structures such as the empennage of the Boeing 777. The use of composites in primary aerospace structures necessitates a more detailed understanding of damage and failure mechanisms of these materials [5].

Laminated composite structures are prone to damage from transverse

loading events, such as impact, due to their relatively low through-thickness strength. Impact damage is manifested in various modes, such as delamination, fiber breakage, and matrix cracking, thus making damage quantification and detection difficult. Damage from impact events is known to cause significant degradation in the operational performance of composite structures. Impacted composite structures can have a reduction in static strength in excess of 50% [6-8]. Thus, impact damage, and the resulting performance degradation, become significant concerns when composites are to be used in primary load-bearing structures such as an aircraft fuselage or wing.

This need to understand damage and failure of aircraft structures is formalized in safety regulations written and enforced by aircraft governing agencies [9-11]. Safety and reliability of the structural design must be demonstrated. This daunting task is accomplished through a damage tolerance design philosophy. Damage tolerance is a measure of the ability of a material/structure to "perform" (given particular requirements) with damage present [12]. Safety regulations are written with this philosophy in mind. In order to design damage tolerant structures, engineers must first understand and characterize the damage types likely to occur during the life of a composite structure. Damage states are characterized in a damage resistance study which measures the damage incurred by a material/structure due to a particular event [12].

One aspect of the damage tolerance requirement is that structures must tolerate damage until such damage can be reasonably detected. Inspectibility and inspection intervals thus become key in assessing damage tolerance because the largest critical damage (including mode) which cannot be observed must be 'tolerated' between inspection intervals. With this in mind,

impact damage in composites is typically separated into two categories: barely visible impact damage (BVID) which describes the threshold of visually inspectible damage, and visible impact damage (VID) which is damage that typically would be found during an inspection. BVID usually results from a "low-velocity" [13], non-ballistic impact. For a typical composite aerospace structure such as a fuselage, impact damage (including BVID) can result from bird-strike, runway kickup, tool drop, and accidental contact with ground-service vehicles. A key observation from past work is that impacted composite structures, particularly 'thin' structures, can be damaged internally with little or no visible surface damage (*e.g.*, [14, 15]). In aircraft design with composites, damage tolerance issues (impact damage) can become a limiting design consideration.

Due to the importance of damage to design with composites, impact damage resistance and tolerance have been investigated extensively in recent years for composite plates and cylinders (tubes) [7, 14, 16]. However, relatively few studies have focused on composite shell structures, primarily due to additional complexities in testing and analyzing these structures relative to plates. Unfortunately, most aircraft structures are more accurately characterized as shells, *e.g.*, wing and fuselage sections. Preliminary studies that have focused on composite shell sections indicate that structural and damage response of shells can be quite different than those in plates. Experimental damage modes have been shown to be different through-thickness (*e.g.*, [17]) as have the in-plane distribution and extent of damage (delamination and matrix cracking) [18]. The key difference between plate and shell behavior is the presence of an instability in the shell response [19-21]. Shells, unlike plates, can experience either bifurcation or limit-point buckling during transverse loading. Thus, there is a substantial need to characterize

the loading and damage response of composite shell structures, particularly instability behavior.

The objective of this work is to better understand composite shell response to transverse loadings which may damage the structure. This objective is accomplished with a combined experimental and numerical approach. The experimental program builds on previous experimental work and gives insight into the response of shell structures with boundary conditions (supported on all four sides) representative of a fuselage structure. Numerical modeling is performed to further the understanding of the elastic buckling of these shell structures, particularly differences caused by limit-point and bifurcation buckling. The numerical models are compared to previous numerical and experimental results, as well as new experimental data from this work. In this way, experimentation and numerical modeling is used synergistically to provide better understanding of the shell response, particularly damage resistance.

The work is organized in this document as follows. Relevant previous work relating to damage resistance and elastic stability, particularly for shells, is reviewed in chapter 2. This is followed, in chapter 3, by problem definition and the combined experimental/numerical approach used in this work. In chapter 4, numerical (finite element) modeling is discussed, particularly in regard to evaluating shell instabilities. A new method for evaluating bifurcation using finite elements is detailed. Also included in chapter 4 are solutions of a benchmark shell buckling problem and comparison of theory with previous experimental work. Experimental procedures are outlined in chapter 5. In chapter 6, results of the experimental program and numerical modeling are presented. This is followed by a discussion of these results in chapter 7. Finally, in chapter 8, conclusions are drawn based on the results of the

investigation and recommendations are made for future research.

CHAPTER 2

BACKGROUND

Significant strength and performance losses due to damage provide the impetus for studying the damage resistance and damage tolerance of composite structures. As discussed in chapter 1, damage resistance studies facilitate damage tolerant design by identifying the damage that must be tolerated. Damage tolerance of composite plate and shell structures has been reviewed previously, *e.g.*, [18], and is not treated in this chapter because the current work focuses solely on damage resistance. A review of past work on the damage resistance of composite plates and shells is given in section 2.1 to identify key issues and provide a basis for subsequent discussion. Stability, particularly for composite shells, is then discussed in section 2.2 because buckling is known to be a key component in the type of shell response considered in this work, *e.g.*, [21]. Section 2.2 also includes a discussion of numerical modeling (finite element) issues related to the prediction of shell response, particularly instabilities. This review of past modeling efforts provides the necessary background for discussion of present modeling efforts in subsequent chapters.

2.1 Damage Resistance

In this section, a review of previous work on the response and damage resistance of composite structures is presented. Damage resistance is a measure of the damage incurred by a material/structure due to a particular

event [12]. The current understanding of damage issues (resistance and tolerance) for composite structures is based primarily on experience with plate structures. Therefore, to study shells, it is instructive to consider past work with plates. In this section, key conclusions based on plate experience are first discussed as a prelude to the discussion of shells. A more detailed treatment of composite plate and shell damage resistance can be found in reference [18].

2.1.1 Plates

Reviews of the extensive literature on the impact damage to composite structures show that nearly all the past work concerns composite plates [7, 14, 16]. One of the key results of that work, as mentioned previously, is that composites can be damaged without visible signs of the damage, *i.e.*, the damage is nondetectable. Damage is often incurred due to out-of-plane, or transverse, impacts due to the relatively low through-thickness strength of composites. Furthermore, this nondetectable damage can significantly degrade structural performance. This, coupled with the probability of such loadings during service, has prompted many investigations into the damage resistance of composites. As noted previously, these damage resistance studies have been dominated by investigations of plate configurations. This is due, in large part, to the relative simplicity of this structural element.

A second key finding, relevant to this work, is that many impact events which cause barely visible impact damage (BVID) are quasi-static in nature. This means that the static response of the structure adequately represents the impact event, including damage resistance. The impact and quasi-static equivalence has been found independently by a number of researchers, *e.g.*, [13, 22-27], and is based on peak force from the two test conditions being equal. This finding is important with regard to testing composite structures because

impact events of this type, which are difficult to perform and calibrate, can be approximated with readily available, easy to use quasi-static tests. Additionally, the impact response of these cases can be studied via static analyses rather than more involved and time-consuming dynamic analyses. Thus, for composite plates, many impact events are found to be quasi-static in nature and peak force is noted to be an excellent impact damage resistance metric.

Along with the general findings regarding BVID and impact/quasi-static equivalence, the response (impact and quasi-static) and damage resistance of composite plates has been shown to be a function of many parameters. These specific parameters include material, stacking sequence, specimen geometry, boundary conditions, and indenter/impactor geometry [16]. Damage resistance is therefore a combination of both local and global (structural) effects [28]. The most common approach to the local problem is to model behavior at the loading site with a Hertzian-type nonlinear contact law [12]. The contact law is static in nature but has been widely applied to impact events as well as to structures that are not isotropic [25, 29]. In these cases, the form of the contact law is fit to indentation data from tests on composite plates. Beyond effects due to stresses induced at boundaries, damage in composite plates begins local to the contact region and grows outward. Contact laws ignore all the composite damage modes including fiber breaks, fiber splits, delamination, matrix cracking, and crazing. To predict plate response, the contact law is typically combined with a structural model, *e.g.*, [12, 30, 31]. Thus, experience with composite plates clearly shows that damage forms at the loading site due to both local contact effects and structural response.

2.1.2 Shells

In contrast to composite plates, investigations of the damage resistance of composite shells are sparse and largely inconclusive. Reviews focusing on the extant literature on composite shell damage resistance have appeared previously [18, 21] and key points relating to the current work are discussed here. Recent experimental studies into the damage resistance and response of transversely-loaded composite shells indicate that, as with plates, an impact regime exists where a quasi-static representation is adequate [18, 19]. The regime encompasses a wide range of structural configurations including shells representative of actual aircraft structures. As with composite plates, damage to impacted composite shells can be in the barely-visible regime (BVID) [17, 19, 20, 31]. Some comparative studies, *e.g.*, [32], have found that composite plate and shell damage resistance are similar while others have noted distinct differences in damage mode/extent and/or structural response [17, 19-21, 31-35]. The ambiguity is likely due to the range of structural and material parameters considered in the studies. Despite this ambiguity, observed differences in plate and shell impact damage resistance imply that the current understanding of composite damage resistance, based on experience with plates, may be inadequate to address damage tolerance concerns for general composite structures.

Given that damage resistance is a structural phenomenon, and that plates and shells differ only in radius/radii (structural parameter), it follows that shell damage resistance could well differ from that of plates. Transversely loaded convex shells, in contrast to plates, can experience a response instability (buckling) [34-37]. A typical instability response for a transverse, center-loaded composite shell is presented in Figure 2.1 to illustrate this behavior [19]. Deflection is nondimensionalized with respect to shell thickness

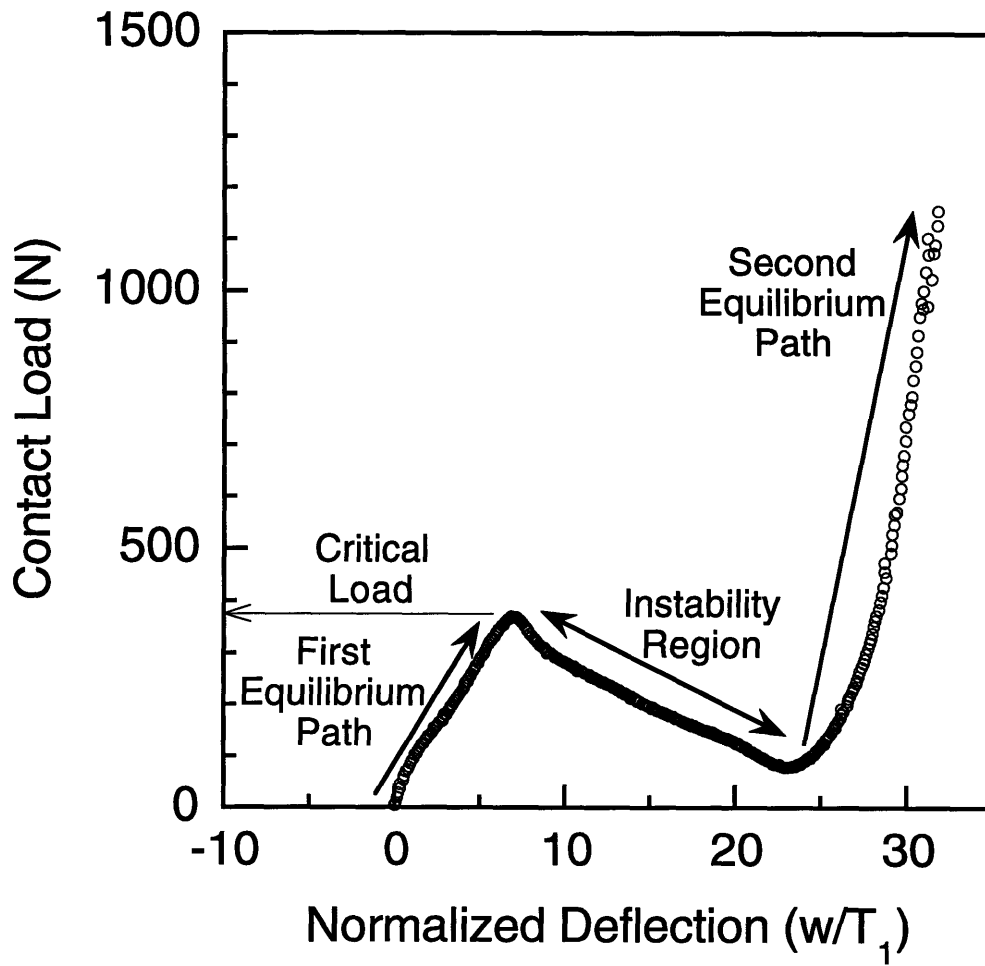


Figure 2.1 Illustration of typical shell instability [19].

to illustrate the large-deflection, nonlinear behavior of the response. Convex shells with an instability were found to have improved damage resistance compared with plates [19], and it was proposed that the instability provides a mechanism, not available for plates, to dissipate impact energy. Damage resulting from impact not only depends on the magnitude of the peak force, but also upon which equilibrium path the peak force occurs. Furthermore, asymmetric and atypical damage distributions and extents for shells (as compared to plates) were observed and attributed to asymmetric deformation modes due to buckling. Thus, shell instability (buckling) is linked to response and damage resistance differences between plates and shells.

Instabilities are key to understanding the response of composite shells to damaging transverse loads. Noted differences in response, damage mode, and damage extent have all been attributed to shell instabilities (buckling). Asymmetric and atypical damage distributions have been observed [19, 38] and asymmetric deformation modes due to buckling identified [21]. Due to asymmetric deformations, the maximum curvature change along the shell surface does not occur at the loading site. This implies that the maximum bending stress will occur away from the loading site. Thus, damage may form away from the loading site. This has not been observed in previous work with composite plates. These various damage issues related to shell stability necessitate detailed consideration of buckling to gain a better understanding of composite shell damage resistance. Thus, buckling, particularly finite element modeling of shell buckling, is discussed in detail in section 2.2.

2.2 Elastic Stability

Stability of structural systems has received considerable attention over the years due to its importance in structural failures. In section 2.2.1, a brief

introduction is presented to introduce terminology and provide background for the discussion of shell buckling in section 2.2.2. These two sections are built upon in the last section to provide a discussion of finite element modeling of shell buckling.

2.2.1 Definitions

The mathematical definition of stability, credited to Poincaré (see [39]), serves as the basis for use of the term in structural stability. In the original definition, singular behavior at a critical point is termed either a limit or bifurcation point, with the term buckling associated only with the latter. In structural stability problems, however, the two types of instability are *both* referred to as buckling – bifurcation buckling and limit-point buckling (also referred to as nonlinear collapse, see [40]). Thus, in modern structural usage, stability and buckling are used interchangeably and it is understood that buckling occurs either at a limit or bifurcation point. The two types of structural buckling are distinguished by considering the pre- and post-buckling deformation states. Bifurcation buckling involves switching to a different deformation state (eigenmode) at the bifurcation point, whereas in limit-point buckling, the mode of deformation does not change. The change in deformation state is often called "switching" or "branching" and can be calculated for linear systems using a simple eigenanalysis. Switching to a new deformation state via bifurcation occurs whenever the new state is associated with lower strain energy than the state on the primary path [40-42].

The distinction between the two types of buckling is often illustrated using a load-deflection plot for a generic structure and loading as in Figure 2.2 where deflection is in the same direction as the load. Alternatively, load can be plotted versus the amplitude of the bifurcation mode to highlight the mode

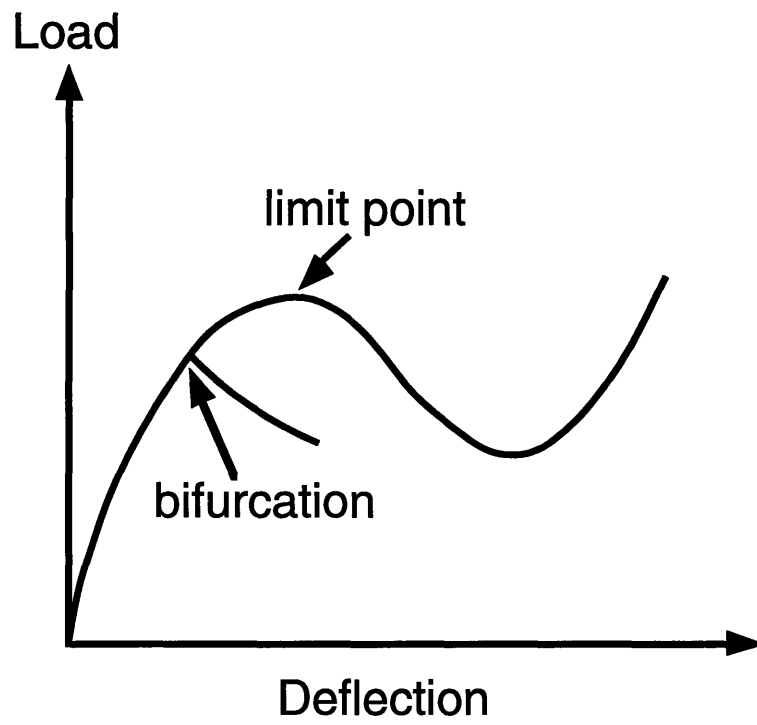


Figure 2.2 Load-deflection curves showing limit-point and bifurcation buckling behavior (as in [43]).

switch. However, plots such as Figure 2.2 are utilized when limit-point and bifurcation buckling are both possible. The path corresponding to the prebuckling behavior, and also associated with the limit point, is called the primary path. On this path, prebuckling deformations grow nonlinearly until the tangent stiffness equals zero at the limit point. If a bifurcation point associated with lower energy occurs before the limit point, the structure will take the path (termed the secondary path) associated with the bifurcation point. A characteristic of a bifurcation point is that the tangent stiffness is discontinuous (representing the "switch" between the primary and secondary paths), whereas it is continuous at a limit point. A negative slope for the secondary path is shown in Figure 2.2 which is common for structures which undergo bifurcation buckling. However, the secondary path at a bifurcation point may have positive slope, *e.g.*, pressure-loaded spherical caps have a 30% reduction in tangent stiffness (slope) at the bifurcation point [44].

Although not meaningful from a practical standpoint, mention should be made of non-simple bifurcation [45, 46]. In non-simple bifurcation, multiple bifurcation modes exist at (or very near) a given critical load as opposed to only one mode in simple bifurcation. Non-simple bifurcation, also called compound buckling [45, 47], is often encountered in *analysis* of axially compressed cylinders where many eigenmodes are associated with (nearly) the same critical load. In reality, as opposed to idealized models, imperfections and nonlinear postbuckling interact such that these multiple bifurcation paths are rarely encountered.

When considering postbuckling of structural systems, the method of load introduction must always be specified because different response paths can result [19, 35]. Structures can be tested either in load- or deflection-control, also referred to as "dead loading" and loading in a "hard device",

respectively [48]. A load-controlled response will progress along the first equilibrium path (see Figure 2.1) until a critical load is reached where the response transitions dynamically (at a constant force) to the second equilibrium path. The dynamic transition is termed "snapping" and the response a "snap-through" instability. This is in contrast to a deflection-controlled test, such as the data in Figure 2.1, where the entire instability region can be characterized and no "snapping" occurs. A detailed treatment of stability and transitions between equilibrium paths, based on thermodynamic equilibrium considerations, can be found in reference [48].

The influence of geometric imperfections (imperfection sensitivity) on the buckling response of structures is known to be extremely important in many cases. The effect of imperfections has recently seen a resurgence of interest in both experimental characterization of such imperfections, and the inclusion of imperfections in numerical models [49-51]. Imperfections have many effects on the resulting response, including reduction of the critical buckling load, changing the mode of buckling, or even elimination of buckling from the response entirely. A key conclusion regarding imperfections, attributed to Koiter (see [45]), is that the greatest reduction in buckling load is *not* due to an imperfection which has the form of the first buckling mode. This non-intuitive finding will be discussed in the context of numerical modeling in section 2.2.3 and chapter 4. Imperfection sensitivity for the type of shells considered in this work is also discussed in the next section.

With the aforementioned definitions of stability for generic structures, attention in the next section is restricted to elastic stability of transversely-loaded shells. Inelastic considerations, such as plasticity and damage, represent second order effects which are outside the scope of the current work. It will be shown in the following sections and in chapter 4 that elastic buckling

for composite shells considered in this work represents a significant challenge in itself.

2.2.2 Shell Buckling

The bulk of previous work on stability has focused on structural elements (such as bars and columns) under purely compressive loading. The stability of thin shell structures, of interest in this work, is far more complicated than those of bars [45]. Paraphrasing [43], a property of the thinness of a shell is that it has significant membrane stiffness relative to bending stiffness. A shell can absorb membrane strain energy through small deformations whereas much larger bending deformations are required to absorb an equivalent energy in bending. If the shell is loaded so that significant compressive membrane strain energy is built up, this energy may be exchanged to bending strain energy through the process of buckling. This *qualitative* definition of shell buckling aids in understanding buckling of the transversely-loaded thin shells considered in this work. Kinematics due to the shell radius give rise to geometric coupling between in- and out-of- plane displacements. Due to this coupling, compressive membrane stresses develop under transverse loading. Buckling then occurs when it is energetically favorable to exchange compressive membrane strain energy for bending strain energy.

The current work is concerned with the response of thin composite shells to centered, transverse loading. The two-dimensional response of these structures, particularly when buckling occurs, involves large deflections and rotations (and thus highly nonlinear kinematics). Due to these response characteristics, the problem has been analyzed exclusively by the finite element method. Finite element modeling of shell buckling is discussed in

section 2.2.3. While quantitative evaluation of shell buckling requires the use of finite elements, it is qualitatively similar to simple arch behavior/buckling. Simple, shallow arch response to pressure or center point-loads has been analyzed for many years using a variety of assumptions and modeling techniques, *e.g.*, [41, 42, 52-54]. The behavior of such arches depends on many factors including geometry, loading, and material properties. Both limit-point and bifurcation buckling can occur in the arch response, as well as an entirely stable behavior. These distinctions have been useful in the study of composite arches [55] and also in categorizing the experimental response of the composite shells [56] considered in chapter 4. In the measured response of the composite shells, as with arches, bifurcation involves a primary deformation mode/path symmetric to the loading (arch/shell center) which transitions to an asymmetric, or inextensional [41, 42] mode. Thus, composite shells of interest in this work have a stable response (inflection point) or buckle at either a bifurcation (asymmetric mode) or limit point (symmetric mode).

While distinctions based on arch response allow a qualitative interpretation of two-dimensional composite shell response, a quantitative description is complicated by many factors. These include laminate couplings, specifics of the boundary conditions and mechanisms of load introduction, large-rotation kinematics, and two-dimensional behavior (axial variation). These and other issues make a quantitative description of the shell response difficult. Prediction of composite shell response, particularly with the finite element method, are discussed in the following section.

2.2.3 Finite Element Modeling

Prediction of the structural response of transversely loaded composite shells requires significant analytical/computational effort due to nonlinear

geometric/kinematic couplings, large rotations, and buckling. One approach to modeling the shell behavior utilizes an assumed-modes approach which has been found useful in predicting arch and shell response [35-37, 54, 55, 57]. A *priori* knowledge of the correct displacement modes (*e.g.*, asymmetric modes for shell bifurcation) is useful but not necessary in an assumed-modes approach provided a sufficient number of terms are included in the displacement function. With the assumed-modes approach, only a few idealized boundary conditions can be solved, which severely limits the technique. In contrast, the finite element method provides the ability to efficiently consider various boundary conditions/loadings for shells where nonlinear kinematics are required. Thus, the finite element method is by far the most popular analysis tool for analyzing these problems.

Nonlinear (kinematic) shell formulations, corotational procedures [58], and their accompanying solvers, are commonly applied to the solution of shell stability problems with finite element methods. Within these formulations, path-parameter methods, *e.g.*, [59], allow limit points to be easily traversed and postbuckling to be assessed. These techniques are ideal for calculating limit-point behavior because the response involves the nonlinear growth of a prebuckling deformation state. However, bifurcation and the associated postbuckling pose significant difficulties in the numerical formulation and practical solution of the problem. In a discretized numerical representation of the structure, as in a finite element model, branching to the new bifurcation state must be induced because the secondary deformation state, and the associated path, do not exist in the model. Path-parameter methods for evaluating limit points will typically miss or "step over" bifurcation points [46, 60]. The finite element routines increment past a bifurcation point and evaluate the primary path, masking the bifurcation point. Thus, if a

bifurcation point exists, the calculated response will be in error (overprediction of critical load) because the bifurcation path represents a lower energy state. For example, the limit-point response of a benchmark large-deflection, large-rotation shell buckling problem was originally solved without considering bifurcation [61] and the limit-point response (symmetric deformations) was generated rather than the lower-energy bifurcation solution (asymmetric deformations).

Overlooking bifurcation in these types of shell buckling problems is pandemic in the literature. For example, all reported finite element analyses of shell buckling problems of the type considered herein find only the limit-point response. These analyses effectively ignore bifurcation because of the imposition of quarter models due to assumed symmetries, *e.g.*, [32, 34, 62-72]. Many of these analyses consider the benchmark problem mentioned previously and others consider composite shell response directly relevant to this work. Proper analysis of these shells requires consideration of bifurcation. To evaluate the bifurcation response, a full model, *i.e.*, with no assumed symmetries, is needed because the secondary path is typically associated with asymmetric deformation modes.

To evaluate bifurcation with finite element techniques, the bifurcation point must first be identified before a switch is made to the secondary solution path. Finding bifurcation points on nonlinear primary solution paths, while not automatic, can be accomplished through careful monitoring of characteristics of the primary solution path. In particular, a change in sign of the determinant of the stiffness (or, more correctly, the tangent stiffness) matrix indicates that a bifurcation point has been passed [46, 73]. In practice, two converged solution points (converged tangent stiffness matrices) from the primary path "cradle" the bifurcation point [46]. Cradling involves determining successively

smaller load/deflection ranges within which the bifurcation point lies. At the first point, the stiffness matrix will have a positive determinant, and at the second point the matrix will have a negative determinant. A bifurcation point exists between two such points. Subsequent evaluations of solutions within this range allow the bifurcation point to be cradled over successively smaller ranges until it is sufficiently determined. "Sufficiently determined" is a subjective decision of the analyst. While this method provides a way to determine bifurcation points, they can be overlooked in practice, *e.g.*, in the benchmark problem of section 4.3.

Branches from the nonlinear primary path can only be calculated in an improvised manner [60] which requires insight and additional effort on the part of the analyst. Thus, after identifying the bifurcation point, myriad issues related to switching/branching to the secondary equilibrium path remain. Various techniques exist for inducing bifurcation in finite element analyses. These all include modifying the structure so that structural response is biased toward the bifurcation mode, and thus the secondary path. After switching to the secondary path has occurred, postbuckling is easily evaluated using the nonlinear techniques discussed earlier. Asymmetric boundary conditions and eccentric loadings (*e.g.*, [74, 75]) are sometimes utilized to bias the model. By far the most common technique utilizes biases based on eigenmodes of the structure, *e.g.*, [46, 60, 73, 76]. In this technique, bifurcation is identified using a standard eigenvalue analysis of the structure which also yields the eigenmode(s). The number and amplitude of eigenmodes must be selected (subjectively) by the analyst when performing a branch switch. Typically, and for simplicity, only the first eigenmode is used.

One method for branch switching introduces geometric imperfections into the structure which have the form of the calculated eigenmode(s). If the

imperfection amplitude is large enough, bifurcation will be induced because the shell geometry is biased towards this deformation mode. In trying different amplitudes, the goal is to obtain an imperfection that is large enough to induce bifurcation, but small enough that the modified problem (due to imperfections) still represents the original problem. As with cradling the bifurcation point, this is an iterative process of trial and error. Finally, there is the choice of where on the primary path to evaluate and introduce the eigenmodes. Introduction and evaluation near the bifurcation point, rather than in the initial configuration, is desired to minimize the effect of the imperfections on the prebuckling response. While many analyses introduce the geometric imperfection into the initial model of the structure, differences have been noted when the imperfection is introduced near the bifurcation point [69].

A more sophisticated method involves introducing the eigenmode(s) as a solution to the incremental shell deformation. The eigenmodes are determined at the first of the two points which ultimately cradle the bifurcation point. After the mode(s) and amplitude(s) are selected by the analyst, they are placed in the model and the energy of the system is minimized with respect to load. Thus, the first of the cradling points becomes the bifurcation point and, given that the deformation state has been predetermined, the next "solution" is found by finding the load which minimizes the energy of the system. While bifurcation can be induced close to the true bifurcation point, the subjective choices of eigenmode number and amplitude remain, as well as the trial-and-error method of scaling the eigenmode(s) to obtain a converged solution.

While the finite element technique provides a robust method for considering various boundary conditions and structural configurations, care must be taken when utilizing this method for stability problems. Bifurcation for the type of shell structures considered in this work, while clearly an

important aspect of the response, is typically ignored in the literature. In either case, using scaled eigenmodes to induce bifurcation requires subjective decisions by the analyst. The analyst must have some insight into what is required of the bias (eigenmode number and amplitude) and interactively adjust the finite element code [60].

Damage resistance studies of composite shells rely on accurate prediction of the structural response. Bifurcation must therefore be considered. Finite element models must be able to properly capture such bifurcation if predictive capabilities for damage resistance are to be attained.

CHAPTER 3

APPROACH

The objective of the current work is to better understand composite shell response to transverse loadings which may damage the structure. To accomplish this objective, a combined experimental and numerical approach is used to study the response of composite shell structures to transverse loading. The assessment of response differences due to either limit-point or bifurcation buckling is of particular importance in this study since buckling has been shown to be a key mechanism in the impact of shells, including damage resistance. Both experimentation and numerical modeling provide insight into these processes and their effect on damage resistance of composite shell structures.

The general approach taken in this research, including specimen geometry and boundary conditions, is explained in section 3.1. In section 3.2, numerical modeling efforts are discussed, particularly the evaluation of buckling behavior in the nonlinear response of shells. The experimental component of this work is described in section 3.3.

3.1 General Overview

Experiments, combined with numerical modeling (finite element analysis), are used to gain a better understanding of the response of laminated composite shell structures to transverse loadings which may cause damage. Previous experimental work has established the importance of buckling

instabilities in the response of such composite shells, including effects on damage resistance [18, 19, 21]. Therefore, a significant challenge, both experimentally and numerically, is to evaluate shell buckling and how this behavior might affect damage formation. Thus, before embarking on further experimentation, numerical modeling was used to assess and predict shell response. Elastic models, which do not consider the formation of damage during loading, are used to analyze the previous experimental work which was largely free of damage formation. Prediction of the nonlinear, large-deflection, large-rotation response, including buckling, represents the state-of-the-art in numerical (finite element) modeling. Traditional methods for evaluating shell buckling are utilized as well as a novel technique which is detailed in chapter 4. A benchmark large-deflection shell buckling problem and previous experimental data are used to verify and validate the numerical models.

Insights from the initial elastic modeling and previous experimental work are used to design the experimental portion of this work. In particular, boundary conditions and damage formation were identified as key areas for further exploration. With regard to boundary conditions, the free axial edges (see Figure 3.1) are the primary difference between the previous experimental boundary conditions and a fuselage section. An aerospace structure such as a wing or fuselage would be supported on all four sides. The test fixture from the previous work is therefore modified to restrain the shells along the axial edges while maintaining the hinged condition along the circumferential edges. Load-deflection and mode-shape data from testing are used to characterize the shell response with the new boundary conditions. Damage resistance for these more realistically restrained shells is characterized to assess whether asymmetric (atypical) damage forms at the loading site or whether damage forms away from the loading site, as well as when (with respect to loading) damage occurs.

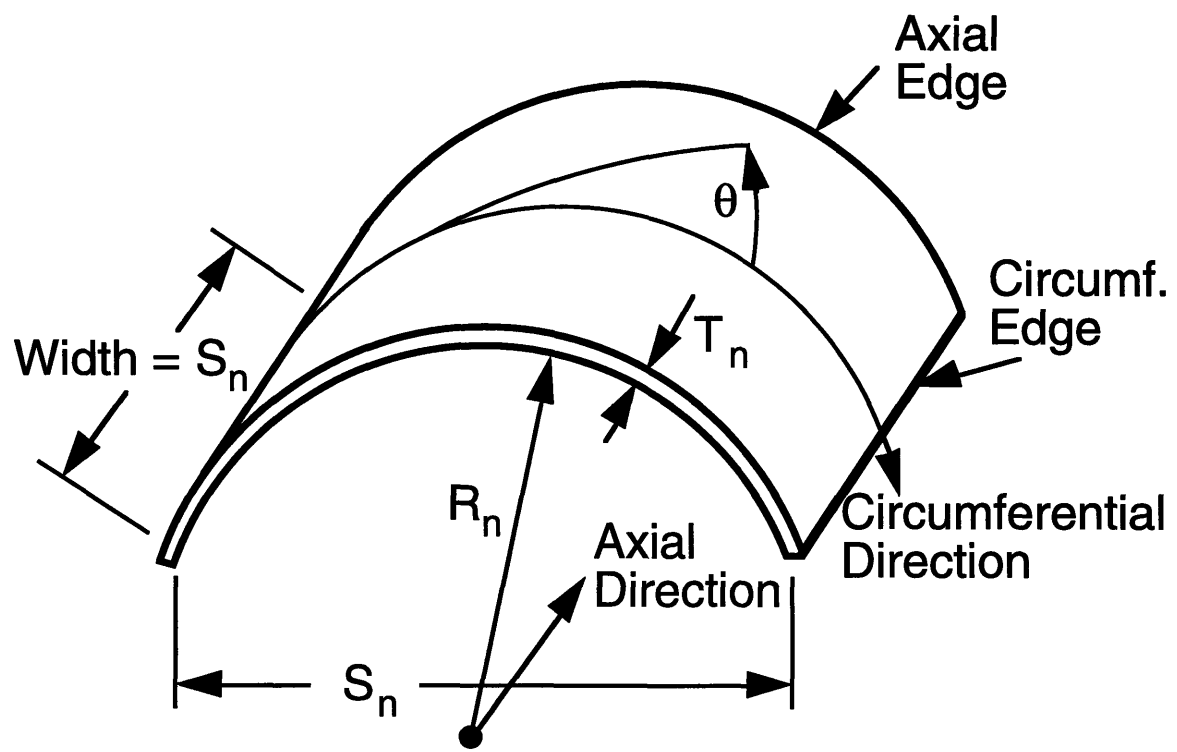


Figure 3.1 Illustration of generic composite shell specimen.

Previous experimental results, as well as the numerical modeling, indicate that this may occur due to the asymmetric deformation modes inherent in bifurcation. Shell damage, which is atypical compared to plates in both extent and distribution, is of significant interest because tolerance requirements, based on known plate behavior, may not adequately address this damage. Finally, numerical models are developed for comparison to the new experimental data. Effects of the structural response, particularly buckling, on damage formation are considered by evaluating stress states from the numerical models on a ply-by-ply basis.

Due to complexities in the loading and the existence of discontinuities, it is difficult, if not impossible, to study damage issues by direct analysis of a specific full-scale aerospace component such as a fuselage or wing. Therefore, it is desirable to obtain a more general understanding of damage issues via a much 'simpler' structural element. The general understanding can then be applied to specific cases as appropriate. This simpler structure needs a "proper" resemblance to the actual structure in that it should have the same geometrical characteristics and loading conditions. With this in mind, a curved section of a fuselage is envisioned for analysis. This structural element is a singly curved cylindrical composite shell with rectangular planform which has previously been investigated in experimental impact and quasi-static tests [18, 21]. The static idealization is justified due to the equivalence of impact and quasi-static responses previously demonstrated for these structures and impact regimes of interest [38] (see chapter 2). Thus, the transverse static loading of this structural element is studied in an effort to understand the shell response, particularly buckling and damage resistance.

The composite shells studied are made from Hercules AS4/3501-6 graphite/epoxy prepreg tape in a $[\pm 45_n/0_n]_s$ layup. This layup and material

system have been used previously in both damage resistance [19-21, 38] and tolerance studies [77]. Thus, results from this work can be directly compared to the previous work, the only difference being in the axial boundary condition. The scaling parameter, n , takes on the values 1, 2, and 3 to give three different laminate thicknesses. Individual plies have a thickness of 0.134 mm and are grouped in this fashion to create effective plies. The orientation of ply angle, θ , with respect to the specimen axes and structural parameters are identified in Figure 3.1. Using effective plies as the basis for scaling, the structural variables are represented as:

$$X_n = n(X_1) \quad (3.1)$$

where X represents a structural parameter (radius, span, or thickness). Base values, X_1 , for each of the parameters are: $R_1 = 152$ mm (6"), $S_1 = 102$ mm (4"), and $T_1 = 0.804$ mm (6 plies). It should be noted that S_3 (305 mm) and T_2 (1.608 mm) approximately correspond to values for stringer spacing (span) and thickness for a typical commercial aircraft and that R_6 (0.914 m) and R_{12} (1.829 m) correspond to general aviation and commercial aircraft fuselage radii, respectively [78]. Specifics of the structural parameters studied are given in sections 3.2 and 3.3.

All shells considered in this work are centrally loaded as indicated in Figure 3.2. Specifics of the load introduction are detailed in chapters 4 and 5 for the numerical modeling and experimental portion of the work, respectively. Two different sets of boundary conditions are considered – one set from previous experimental work [21] and a second set which is more representative of a typical aerospace structure (supported on all four edges). In the previous work, pinned/no in-plane sliding (hinged) boundary conditions were used along the circumferential edges while the axial edges were traction free. The hinged

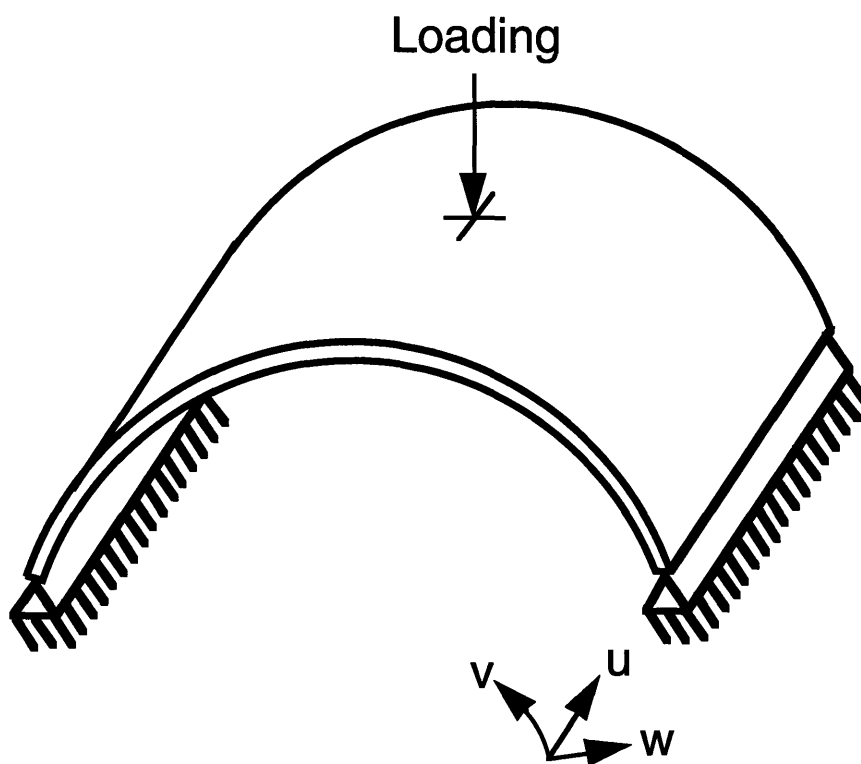


Figure 3.2 Illustration of restrained shell with local coordinate system used to describe boundary condition at shell axial edge.

condition along the circumferential edge and a local right-handed, orthogonal, curvilinear coordinate system is illustrated in Figure 3.2 to help clarify the idealized boundary conditions. The v - and w - displacement components are restrained (fixed) along the circumferential edge while rotation is allowed (free) about the x -axis (u -displacement component). The u -displacement is not restrained during testing, but the shell edge will experience some frictional restraint during loading. The importance of this boundary condition is addressed in chapter 4.

A second set of boundary conditions are used in the experimental component of this work. The curved axial edges are restrained in addition to the hinged condition on the circumferential edges from the previous work. In the case of a fuselage, the shell structure would be supported on the circumferential edges by stringers and on the axial edges by stringers or frames. The out-of-plane component of displacement (w) is restrained along the axial edges which gives a simple-support condition. The true boundary condition of a fuselage lies somewhere between simply supported and fully clamped. Thus, the experimental simple-support boundary condition is a reasonable idealization of the actual boundary condition.

3.2 Numerical (Finite Element) Modeling

Modeling of the shell structures considered necessarily incorporates both limit-point and bifurcation buckling. The nonlinear response of these composite shells to static transverse loading is investigated numerically using the finite element method. The finite element code STAGS (SStructural Analysis of General Shells), available at the Structural Materials Branch of NASA Langley Research Center, is used to analyze the nonlinear response of shell structures in this work [73]. The specimens analyzed are thin, monolithic

composite laminates which are relevant as wing or fuselage structures and correspond to composite shells which have either previously been tested [21] or which are tested in this work. Analysis of thick laminates, *i.e.*, including transverse shear in the analysis, is beyond the scope of this work.

The STAGS finite element routine utilizes von Kármán nonlinear kinematics [73] and shell elements. This formulation allows for large rotations and small strains but ignores transverse shear deformation. This is appropriate in the analysis of thin shells [79]. STAGS uses a corotational procedure [72] with the Riks arc-length method [59] to calculate large deformation nonlinear behavior of structures. To assess limit-point versus bifurcation buckling (including asymmetric deformation modes), eigenvalue analyses can be conducted near limit points to determine whether the solution path bifurcates rather than approaches a limit point. This is traditionally accomplished manually by terminating the nonlinear analysis near an expected bifurcation point and performing a linear bifurcation analysis. The eigenmode(s) from the bifurcation analysis is(are) then arbitrarily scaled and superposed on the shell structure to form an imperfect shell. The nonlinear analysis is then restarted (with the imperfections) to determine if the solution follows a new, and oftentimes asymmetric, bifurcation path. Alternatively, a novel approach to inducing bifurcation is introduced in this work utilizing asymmetric meshing of the shell in the circumferential direction. Advantages of this new technique and comparison to traditional techniques, such as using scaled eigenmodes, are discussed in detail in chapter 4.

Elastic analyses of a benchmark large-deflection shell problem from the literature as well as previous experimental results from quasi-static testing of composite shells [21] is undertaken. Damage is not considered in these initial calculations as the numerical comparisons simply serve to validate the models

and investigate the new technique for bifurcation. The benchmark problem [61] has the same idealized boundary conditions as the first set of experimental results (see Figure 3.2). Load-deflection curves and mode-shape evolutions for a variety of composite shells, previously unavailable in the literature, are used to assess the accuracy and limitations of the numerical modeling techniques. Eighteen different shell configurations were tested in stroke control in that previous work [21]. In addition to the three thicknesses described in section 3.1, two radii and three different span values were considered (see equation 3.1): n takes on the values 6 and 12 for radius and 1, 2, and 3 for span. A comparison of the average response characteristics (force-deflection data) between the finite element results and experiments is detailed in chapter 4. Deflection-mode data at different deflections (stroke values) give additional insight into the shell response and are also compared with those predicted from the analysis. These comparisons are used to give credence to the finite element analyses and the new technique for evaluating bifurcation.

Shells from the experimental portion of this work (section 3.3) are also analyzed using the finite element technique. Load-deflection data and mode-shape evolutions are compared to determine whether the models capture the data. Of particular importance for these cases is the presence of bifurcation versus limit-point buckling. It is unknown whether bifurcation into asymmetric modes will occur and whether those modes will affect damage formation. However, it is particularly important to assess whether the models capture the mode-shape behavior observed in the experiments because these cases closely represent real aerospace structures. If the response for these cases can be captured, stresses can then be evaluated to correlate with damage data. With regard to any type of damage prediction, it is important to note that the uncertain understanding of damage modes and adequate failure

criteria for composites limit even the most complex analyses. A large number of different (but similar) criteria, all involving engineering approximations, are available in the open literature for analyzing composites, *e.g.*, [80, 81]. However, calculation of the structural response is the primary goal of this research. Thus, any observed shell damage which is atypical of well-known plate damage can be considered by evaluating ply stresses that result from the calculated structural response, and comparing those distributions and magnitudes with available damage data. Progressive or multi-mode damage modeling will not be considered as it is beyond the scope of this work.

3.3 Experiments

In the experimental portion of this work, the response of composite shells with boundary conditions representative of a real structure are considered. A fuselage or wing structure is supported on all four edges and therefore an axial restraint is added to the boundary conditions (hinged on the circumferential edge) considered previously. A knife-edge restraint is added to the axial edges which acts to restrain the out-of-plane motion of the axial edges. These knife-edge restraints are added to the circumferential hinge constraints of the test fixture used previously [18, 21]. The addition of the axial restraint to the shell edges is the only difference between the new experimental work and the previous experiments discussed in section 3.2. Utilizing the new boundary conditions, two specific goals are accomplished through the experimental program: characterization of the loading response including mode-shape evolutions, and evaluation of damage resistance. Damage, particularly comparison between shells with symmetric and asymmetric deformation modes, is explored for insight into damage processes/mechanisms. Destructive damage evaluation (sectioning) is also

used to investigate damage formation away from the loading site.

The composite shells are centrally loaded in stroke control using the same 12.7 mm (0.5") diameter hemispherical steel tup used previously. Although eighteen shells were tested previously, a smaller test matrix is used in this work because the curved knife edges which restrain the axial edges do not allow radius or span adjustment. Therefore, only thickness can be varied giving three specimen types – T_1 , T_2 , and T_3 . Radius and span are set equal to 1829 mm (72") and 305 mm (12"), respectively, because these values are closest to a typical commercial fuselage. Six total specimens are loaded in two rounds of testing. All testing procedures are detailed in chapter 5.

In the first round of tests, the load-deflection response for each of the shell types with the new boundary conditions is characterized. These tests are conducted in stroke control until either buckling or gross damage is observed. The test fixture can not restrain the shells on the circumferential edge after the instability region (second equilibrium path in Figure 2.1), and gross damage is undesirable because of inspectibility issues related to Barely Visible Damage (BVD). Shell response on the second equilibrium path is associated with symmetric deformations and tensile membrane stresses, much like the response of plates. As differences in plate and shell response are of interest in this work, it is not essential that this response regime (second equilibrium path) be characterized. Thus, loading is terminated so that the shells remain in the test fixture or so they are not severely damaged. After testing, the shells are evaluated for damage using x-radiography and sectioning. X-radiography characterizes damage at the loading site while sectioning allows damage formation away from the loading site to be investigated.

The primary goal of the second round of testing is to obtain mode-shape evolutions for each of the specimens. The load-deflection response from the

first round of testing is used to determine stroke intervals at which to take mode-shape data in the second round of testing. A sufficient number (typically 6 or 7) of evenly spaced mode-shapes are desired for each specimen to provide insight into the buckling process. Additional mode shape locations may be considered if interesting points are identified on the initial load-deflection curves. Mode shapes are taken at these predetermined intervals at three equally-spaced axial locations on the shell surface. This provides a detailed characterization of the deformation of the shell surface. Load-deflection data is also acquired during the second round of testing to determine the repeatability of the tests and, thus, the effectiveness of the boundary conditions (test fixture). These tests are terminated at a mode-shape location (stroke) before reaching the peak load from the first round of tests. Damage is known to scale with peak load for composite plates [13, 23, 26], and preliminary work indicates a similar relationship for shell structures in most cases [38]. Thus, if different peak loads are reached in each round of testing, the process of damage formation can be interrogated.

CHAPTER 4

FINITE ELEMENT MODELING

Modeling procedures for predicting the response of shell structures are discussed in this chapter. The specific finite element method utilized is first discussed, particularly issues related to calculation of buckling. A novel technique for exploring bifurcation within nonlinear finite element formulations is developed and discussed. The utility of this method is illustrated *vis-a-vis* a benchmark shell buckling problem from the literature, and the models using this technique are validated by comparison to composite shell buckling data.

4.1 Modeling Overview

The STAGS (S_Tructural Analysis of General Shells) finite element code available at the Structural Materials Branch of NASA Langley Research Center [73] was used to analyze the elastic response of transversely (center) loaded shells. This code is used extensively to analyze the nonlinear response of (composite) shell structures. The 410 shell element available in STAGS was utilized for its applicability to the thin shell structures in this work [79]. This "workhorse" element in the STAGS code employs the nonlinear Kirchhoff-Love shell hypothesis which ignores transverse shear. However, it is known to be extremely accurate for modeling thin shell structures. It is a displacement-based four-node quadrilateral C^1 shell element having a cubic (translations and rotations) bending field and a linear/cubic (in-plane translation/transverse rotations) membrane field. The 410 element has three translational and three

rotational degrees of freedom per node and also includes drilling rotational stiffness. The true Newton capability is utilized to iteratively solve the resulting nonlinear equations. Arbitrarily large rotations, but small strains, are modeled using the standard nonlinear corotational procedure [72] in STAGS and limit points are easily traversed using the Riks arc-length procedure [59].

The right-handed curvilinear coordinate system used in this work is shown for a generic shell in Figure 4.1. In Figure 4.1, a 10 by 10 mesh of 100 elements is used to discretize the shell along the axial (x) and circumferential (y , curvilinear) directions, respectively. This mesh has previously been shown to give a converged limit-point solution (using STAGS) to the benchmark problem analyzed in section 4.3 [72]. The mesh shown in Figure 4.1 utilizes one *shell unit* in STAGS. A *shell unit* is one of several substructures within STAGS which can be conveniently (and independently) discretized and then connected/joined with other substructures (beam, plate, shell, or parts thereof) or individual elements.

Boundary conditions are the same for all shells analyzed in this section. Shells are free of traction on the axial edges and hinged on the circumferential edges. The circumferential edge (hinged) constraint is represented in the model by setting all nodal displacements (u , v , w) and rotations (Ry , Rz) equal to zero except the x -axis rotation (Rx) where zero moment is enforced. The shells are point-loaded at the center of the shell surface in all cases. The point-load assumption and variations in boundary conditions are discussed in subsequent sections. Quarter-symmetry is not assumed because a full model of the shell is required to investigate bifurcation as noted in chapter 2. Shell discretization is further discussed in the next section because asymmetric discretization/meshing is utilized to investigate bifurcation.

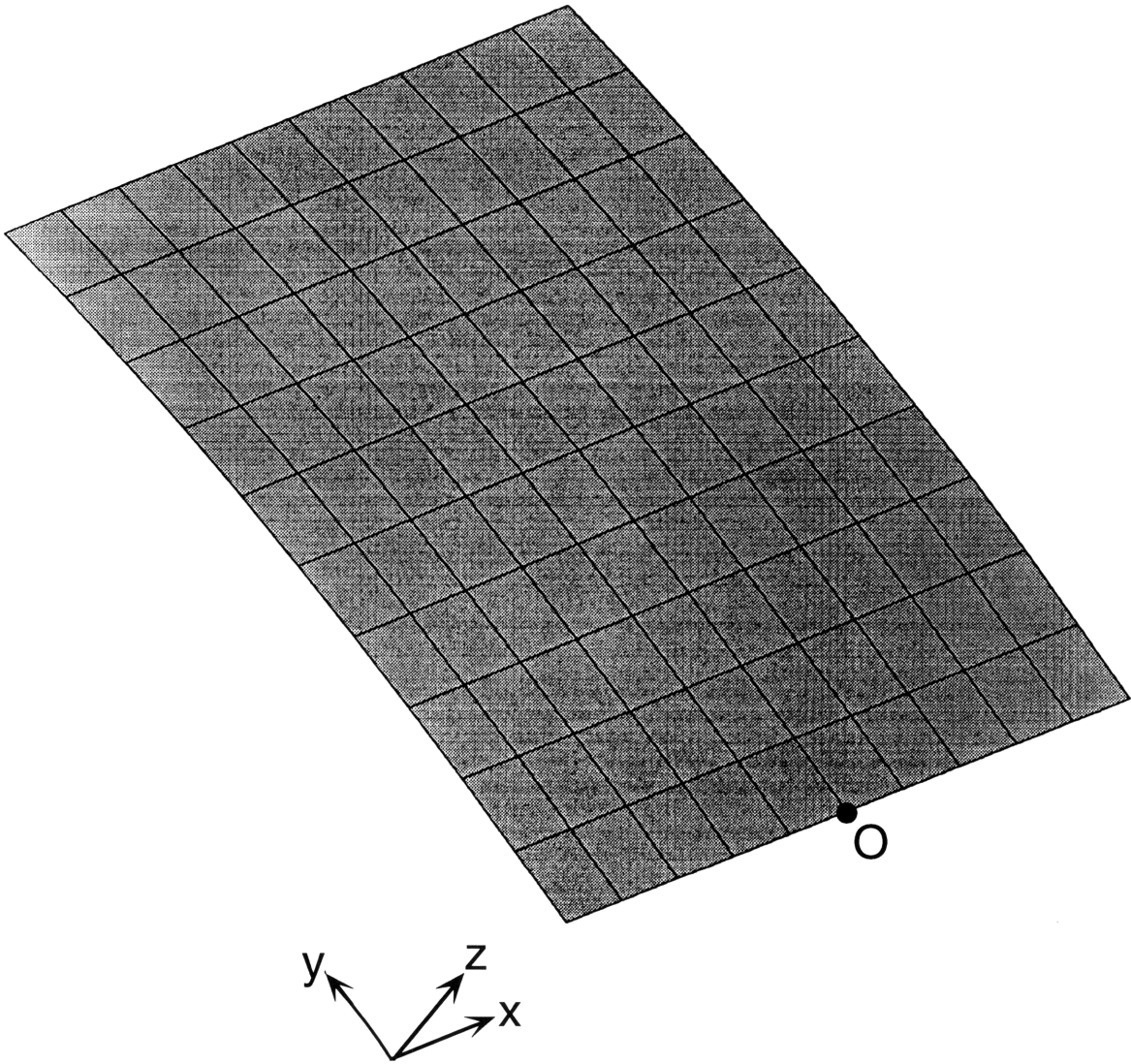


Figure 4.1 Illustration of a 10 x 10 mesh and curvilinear shell coordinate system. (The x and y (curvilinear) vectors are in the plane of the shell while z is everywhere perpendicular to the shell surface.)

As discussed in section 2.2.3, bifurcation from a nonlinear prebuckling state is significantly more challenging within finite element formulations than evaluating limit points. Path-parameter methods, such as the arc-length method utilized in STAGS, can easily evaluate limit points but can step over, or miss, bifurcation points during a nonlinear analysis [46, 60]. Issues arise in both evaluating whether a bifurcation point exists, and also in switching/branching to the secondary (bifurcation) path. A change in sign of the determinant of the stiffness (or, more correctly, the tangent stiffness) matrix is monitored within STAGS to indicate whether a bifurcation point has been passed [46, 73]. Successive analyses cradle the indicated bifurcation point and allow it to be sufficiently determined. Cradling of the bifurcation point is the preferred technique to find bifurcation points within the STAGS code [73]. Two standard techniques to switch/branch to the secondary path within STAGS are explored *vis-a-vis* a benchmark problem in section 4.3. Both techniques utilize eigenmodes of the bifurcation point. Eigenmode(s) are either introduced as geometric imperfections in the structural model, or are imposed as a solution near the bifurcation point. The latter method is called the "equivalence transform" technique within STAGS and is preferred as the more robust method for calculating bifurcation paths. However, as discussed in section 2.2.3, both methods require significant and subjective interaction on the part of the analyst to be successful. An alternative technique for assessing bifurcation is explored in section 4.2 to address these issues.

4.2 Asymmetric Meshing Technique for Bifurcation

The novel approach used in this work for inducing bifurcation arises from considering the effect imperfections have on the numerical representation of the structure in the finite element model. Traditional techniques for inducing

bifurcation introduce biases or imperfections into the numerical model of the structure by introducing a geometric imperfection in the structural model or by assuming a form of the solution. These biases or imperfections act as perturbations on the nonlinear stiffness (tangent stiffness) matrix or loading vector of the numerical model. The perturbations due to the fictitious imperfection allow a transition to the secondary bifurcation path because it is the preferred lowest energy state. The novel technique developed in this work introduces perturbations into the model by meshing the structure asymmetrically. The resulting perturbation in the nonlinear mathematical model acts to induce bifurcation in the same way mathematically as geometric imperfections. Geometric imperfections create a "built-in" asymmetry in the nonlinear stiffness matrix by altering, or perturbing, the problem geometry. The asymmetric meshing technique (AMT) also creates an asymmetric nonlinear stiffness matrix for the shell structure. However, the root of the perturbations in the AMT is the asymmetric spatial variation in discretization. Asymmetry using the AMT is thus "built-in" to the numerical model without altering/perturbing the actual problem (geometry or loading).

The AMT provides a simple method for perturbing the numerical model of the actual structure without modifying the original problem. This is in contrast to traditional techniques which modify the original problem either by imposing structural imperfections or solutions based on the buckling response. Traditional techniques also require prior knowledge of the structural response, particularly the bifurcation mode(s). In the AMT, the solution to the bifurcation response simply relies on numerical perturbations and is not based on *a priori* assumptions/knowledge. The actual problem, not a modified one, is solved using the AMT which allows the true bifurcation point to be directly determined and traversed. The tangent stiffness matrix does not need to be

monitored nor is the analyst required to initiate a branch switch. The AMT thus does not require prior knowledge of the structural response and avoids subjective choices by the analyst such as the number and amplitude of eigenmodes to use in a branch switch.

To induce bifurcation with the AMT, the shell is meshed asymmetrically in the circumferential (y) direction. An asymmetric mesh of this sort can be obtained in a variety of ways and different meshes are discussed in the context of the benchmark shell problem in section 4.3. The asymmetric mesh in Figure 4.2 is the most prevalent mesh used throughout this work and compares very closely with the 100 element symmetric mesh in Figure 4.1. The asymmetric mesh in Figure 4.2 is comprised of two shell units, rather than one shell unit in the symmetric case (see Figure 4.1). The first shell unit covers 60% of the shell in the circumferential (y) direction, while the second shell unit covers the remaining 40%. The first shell unit is meshed identically to the symmetric case in Figure 4.1 with 6 elements along the curved surface. The second shell unit contains five, rather than four, elements in the circumferential direction. This creates an asymmetric mesh with 11 elements (total) in the circumferential direction and 110 elements to represent the entire shell. Various asymmetric discretization schemes are compared in section 4.3 *vis-a-vis* the benchmark problem. The 60% / 40% distribution of Figure 4.2 was chosen for two reasons. One, the asymmetry can be easily varied by simply changing the mesh refinement in the second (40%) part of the shell. This does not require changing the loading definition which is on the first shell unit. Two, mesh refinement at the loading point was anticipated (but never required) which is more easily accomplished within one shell unit, rather than across two which would be the case for a 50% / 50% distribution.

Discretization in this work is described by giving the number of elements

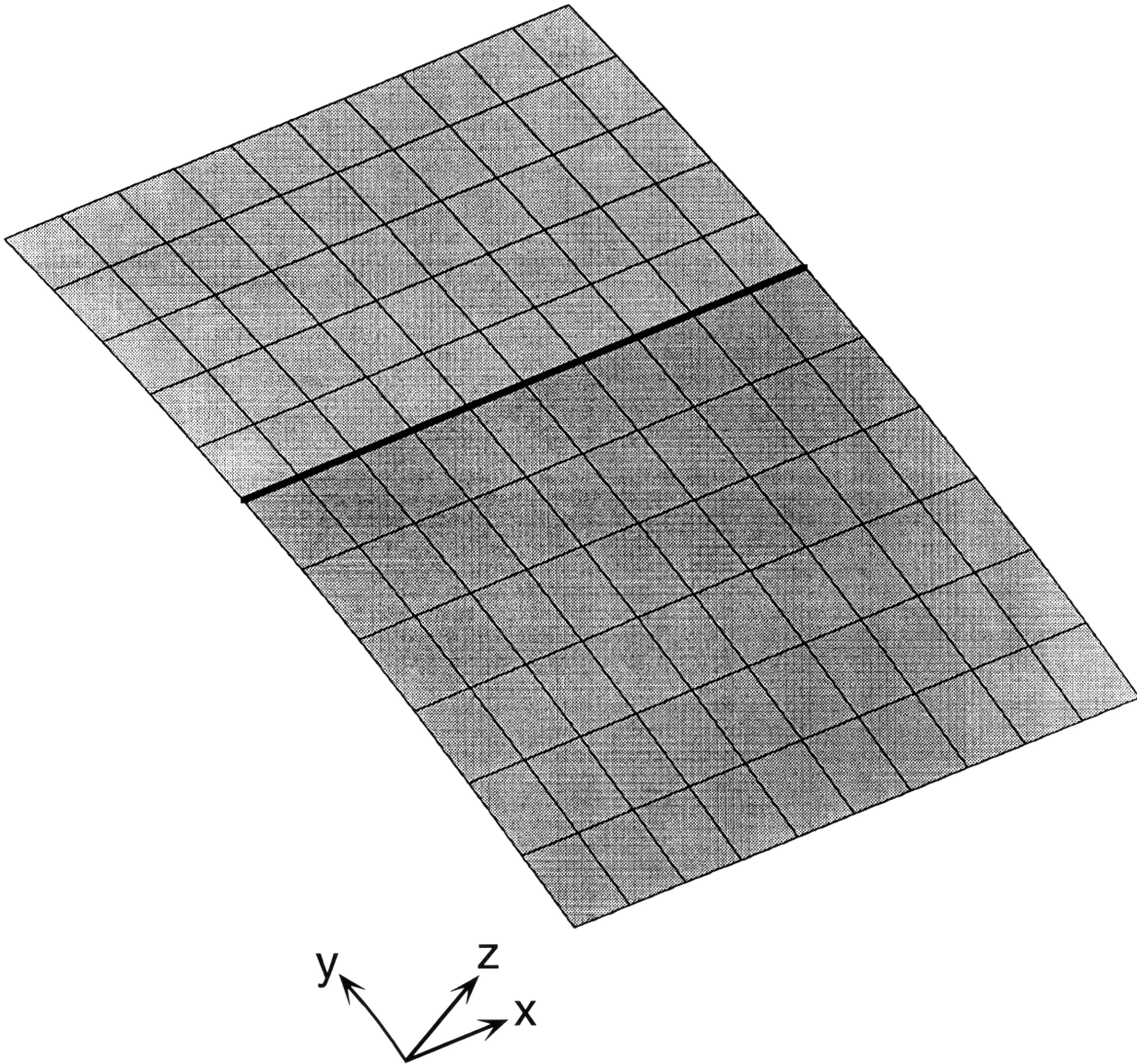


Figure 4.2 Illustration of an asymmetrically meshed shell discretized into two shell units in the circumferential (y) direction.

in the axial (x) and circumferential (y) directions for the first (60% of surface) and second (40% of surface) shell units, respectively. The asymmetric mesh of 110 elements in Figure 4.2 is denoted by a $10 \times 6 / 10 \times 5$ mesh while the symmetric mesh in Figure 4.1 is denoted as a 10×10 mesh (one shell unit). It is important to note that element compatibility is the same as compatibility between shell units. Thus, a $10 \times 6 / 10 \times 4$ mesh of 100 elements is identical to a 10×10 mesh.

4.3 Benchmark Shell Buckling Problem

Characteristics of the type of shell buckling considered in this work are illustrated through a benchmark isotropic shell buckling problem, apparently solved originally by Sabir and Lock [61]. The benchmark is used in the literature to evaluate large-rotation, large-deflection finite element models. The utility and performance characteristics of the asymmetric meshing technique, relative to other traditional methods, are identified through the benchmark problem.

4.3.1 Comparison to Previous Work (Limit-point Buckling)

The configuration of the benchmark isotropic shell problem is given in Figure 4.3. The singly-curved shell has a radius of 2.54 m (100"), a thickness of 6.35 mm (1/4"), and a width and span both of 508 mm (20"). The shell material has a Young's modulus, E , of 3.10275 GPa and a Poisson's ratio, ν , of 0.3. The square-planform shell is point-loaded at the center and has boundary conditions of hinged on the circumferential edges and free on the axial edges. Both load and deflection are taken as positive in the $-z$ shell coordinate direction (see Figure 4.1). Results of the original analysis [61] and a more recent analysis from the literature [71] are compared with a STAGS solution

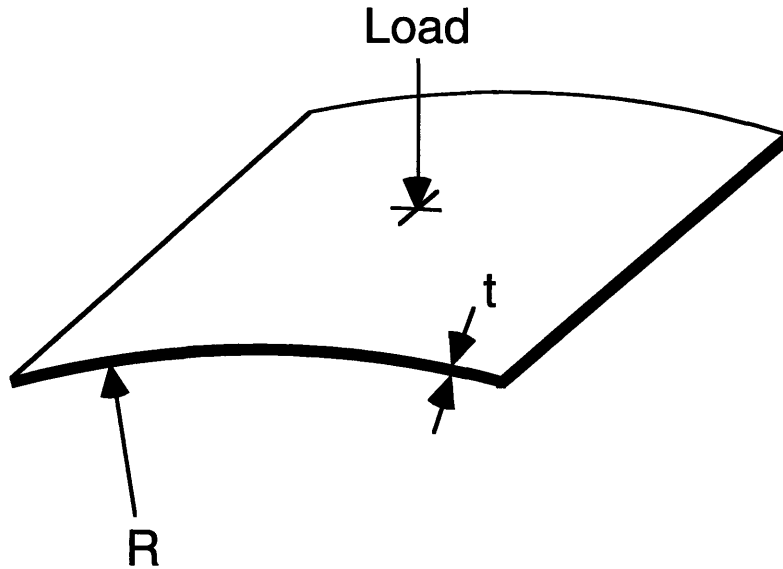


Figure 4.3 Configuration for benchmark shell problem.

using a 10 x 10 mesh in Figure 4.4. The somewhat coarse 10 x 10 mesh represents a converged solution checked against a finer 20 x 20 element mesh and repeats the limit-point response found in the literature. The shell response is noted to experience negative loads in the postbuckling region to maintain equilibrium. In a deflection- (stroke-) controlled experiment, the ability to apply both positive and negative load would be necessary to measure the benchmark response in Figure 4.4. The STAGS solution for the benchmark is also the same as that reported in reference [72] using STAGS and quarter-symmetry. All solutions found in the literature for this problem match those given in Figure 4.4.

The shell response shown in Figure 4.4, using the symmetric mesh, represents a limit-point solution where the shell buckles into a mode corresponding to the prebuckling deformations. The mode is symmetric with respect to the loading along the circumferential shell direction as illustrated in

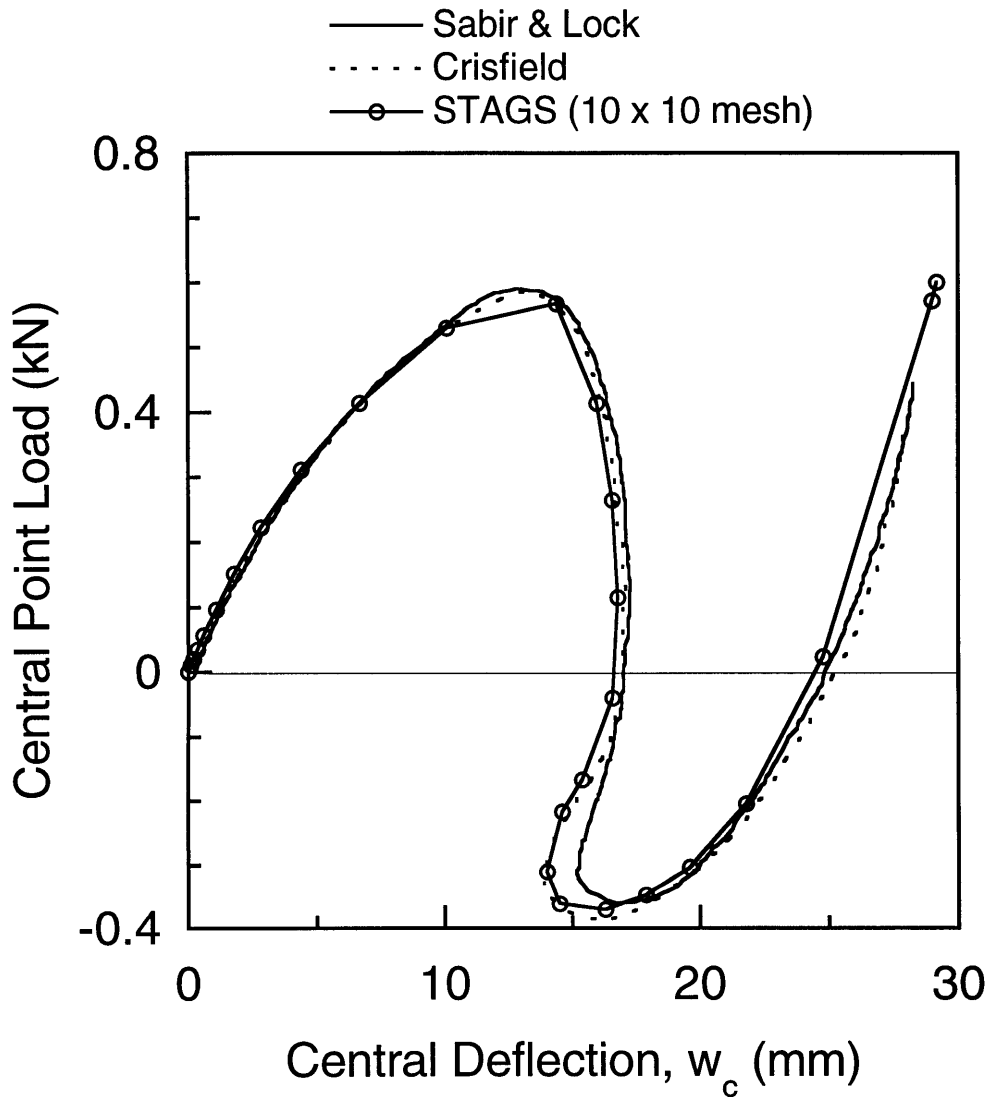


Figure 4.4 Numerical analysis and previously reported results [61, 71] for load-deflection response of benchmark shell problem.

the mode-shape evolution in Figure 4.5. Mode shapes of the shell mid-surface are provided at discrete values of center displacement (w_c) to reference the load-deflection response in Figure 4.4. The mode shapes in Figure 4.5, and throughout this work, are provided in a global Cartesian frame (different than the curvilinear frame in Figures 4.1 and 4.2) to best visualize the shape of the shell during buckling. The Cartesian frame is coincident with the curvilinear shell frame at the center of the shell, with the origin at the midpoint of the axial (hinged) boundary condition (point O in Figure 4.1). The modes in Figure 4.5 are along the center of the shell, and the initial shell geometry is given by the case of w_c equal to 0.0 mm.

Both the load and deflection are noted to decrease after the critical (limit) point in Figure 4.4. This behavior is termed "snapback" and has been rationalized by considering the variation in behavior in the axial direction, *i.e.*, the behavior at the shell center as in Figure 4.5 versus that at the free axial edges. The center of the shell buckles before the edges of the shell due to the loading at the center. After the edges buckle, they snap-through to a fully inverted configuration whereas the center of the shell is restrained by the loading (negative in this region of the response). This can be seen in the load versus center and edge deflection plots in Figure 4.6. The snapback behavior is attributed to the edge response first lagging, then leading, the response at the center of the shell. Both free edges follow the edge response in Figure 4.6, because the response of this isotropic shell is symmetric in the axial direction with respect to the shell center.

4.3.2 Bifurcation Buckling

All solutions in the literature for the benchmark problem evaluate the limit-point response using quarter-symmetries, effectively ignoring bifurcation.

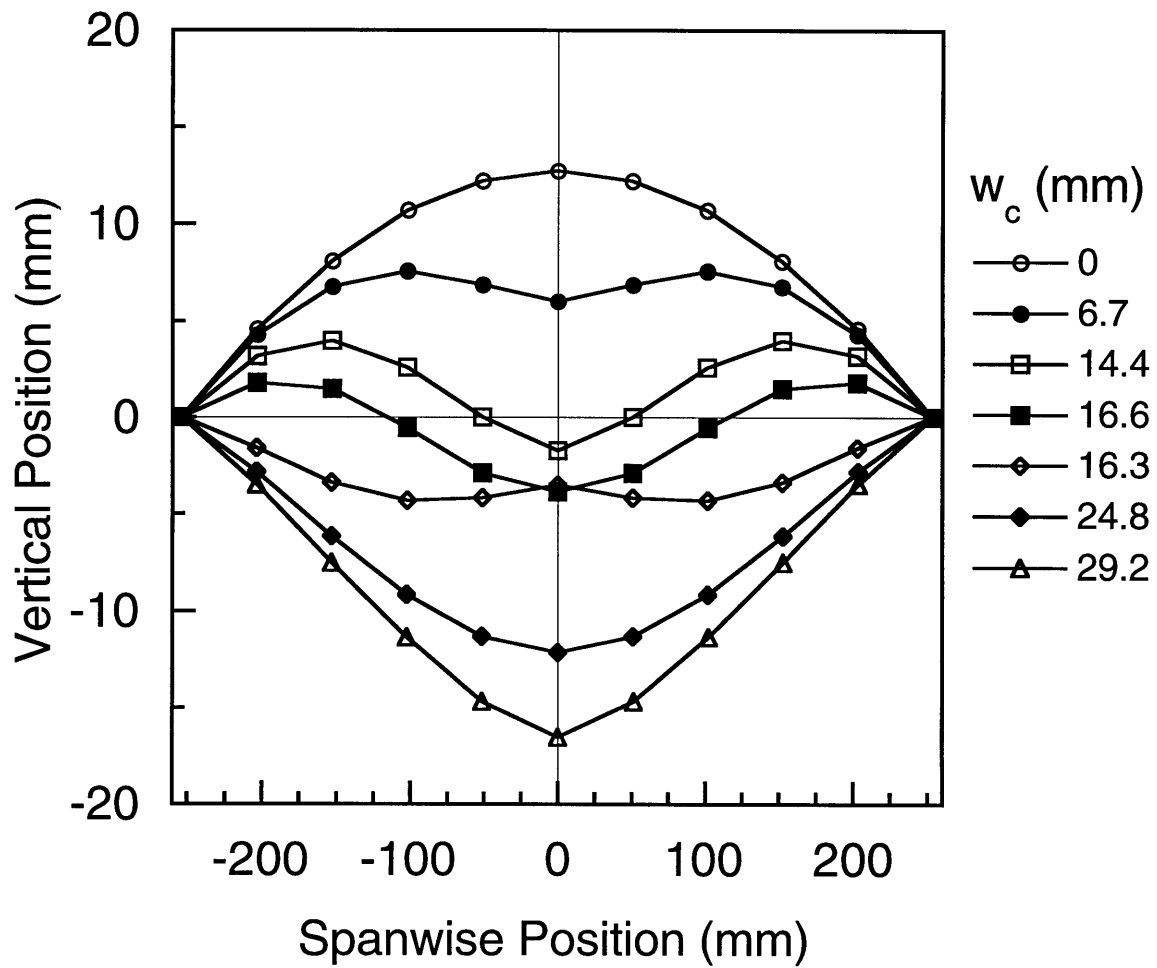


Figure 4.5 Central spanwise deformation modes for benchmark problem at different values of center deflection, w_c , using STAGS with a symmetric (10x10) mesh.

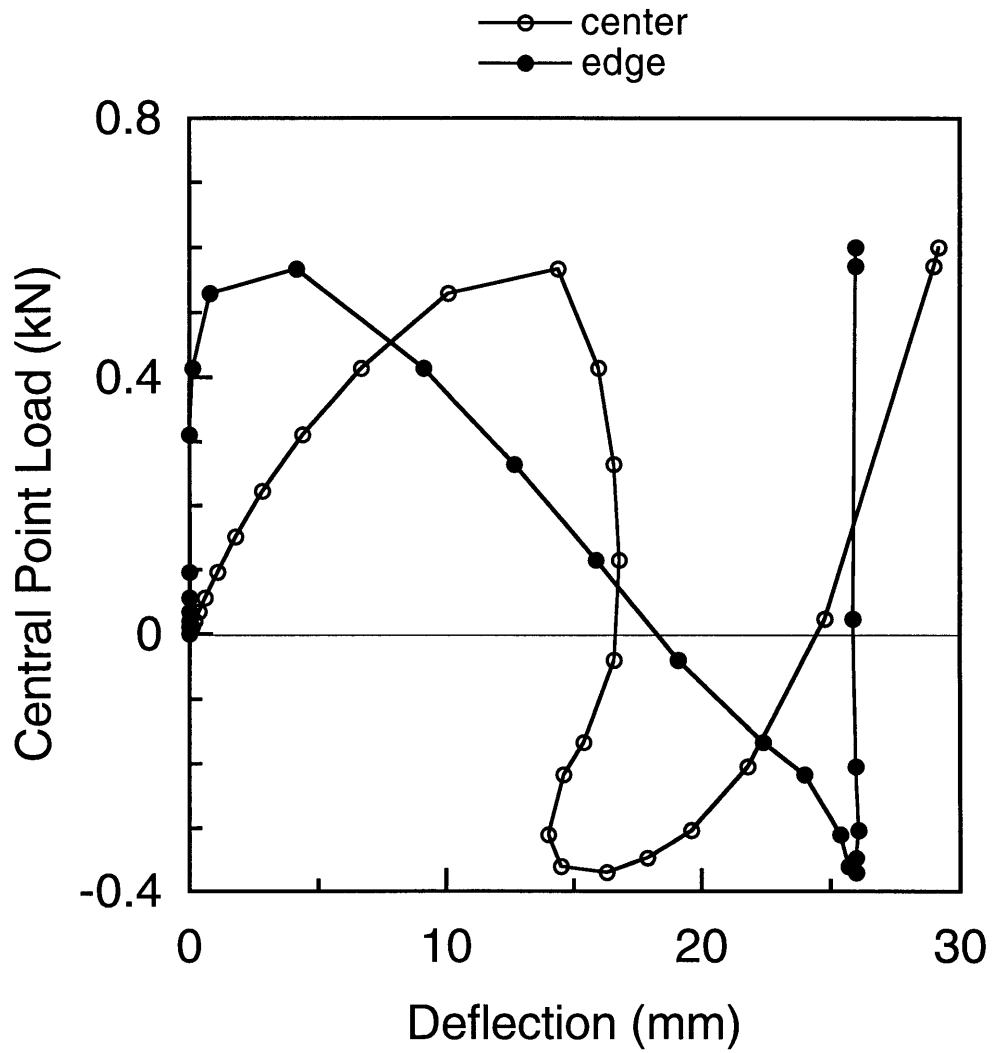


Figure 4.6 Load versus center and edge deflections for benchmark problem using STAGS with a symmetric (10x10) mesh.

To consider bifurcation, two traditional techniques are utilized to evaluate the benchmark response for comparison to the AMT. As noted in chapter 2, bifurcation can be identified in a nonlinear finite element analysis by monitoring the determinant of the tangent stiffness matrix. Taking this approach, bifurcation is indicated in the benchmark problem (10x10 mesh) between 410 N and 530 N. The first technique to evaluate bifurcation uses geometric imperfections in the problem geometry. An imperfection in the form of the first linear eigenmode is used to modify the initial shell geometry. This results in an asymmetric nonlinear shell stiffness matrix which triggers the bifurcation response shown in Figure 4.7. The largest translational component of the eigenmode is scaled as a percentage of the shell thickness to give the three different responses. A plot of this eigenmode in Figure 4.8 reveals that it is dominated by an asymmetric mode in the circumferential direction, in contrast to the symmetric prebuckling deformation in Figure 4.5. The smallest imperfection amplitude (0.1 %) is not large enough to cause the shell to bifurcate and the limit-point response is computed. This can be seen by comparing the response in Figure 4.7 to that of Figure 4.4. Larger values of imperfection (1.0% and 10%) induce bifurcation at different values of critical load, 509 N and 441 N, respectively, with different postbuckling characteristics. Varying the imperfection amplitude gives a range of responses and buckling loads. In practice, the response is computed at various values of imperfection amplitude until the smallest one which causes bifurcation is identified.

A second, and more sophisticated technique for evaluating bifurcation is the equivalence transform technique. This branching procedure, discussed in section 4.1, was used to calculate the bifurcation response and the results are shown in Figure 4.9. Bifurcation is induced at 509 N because the previous

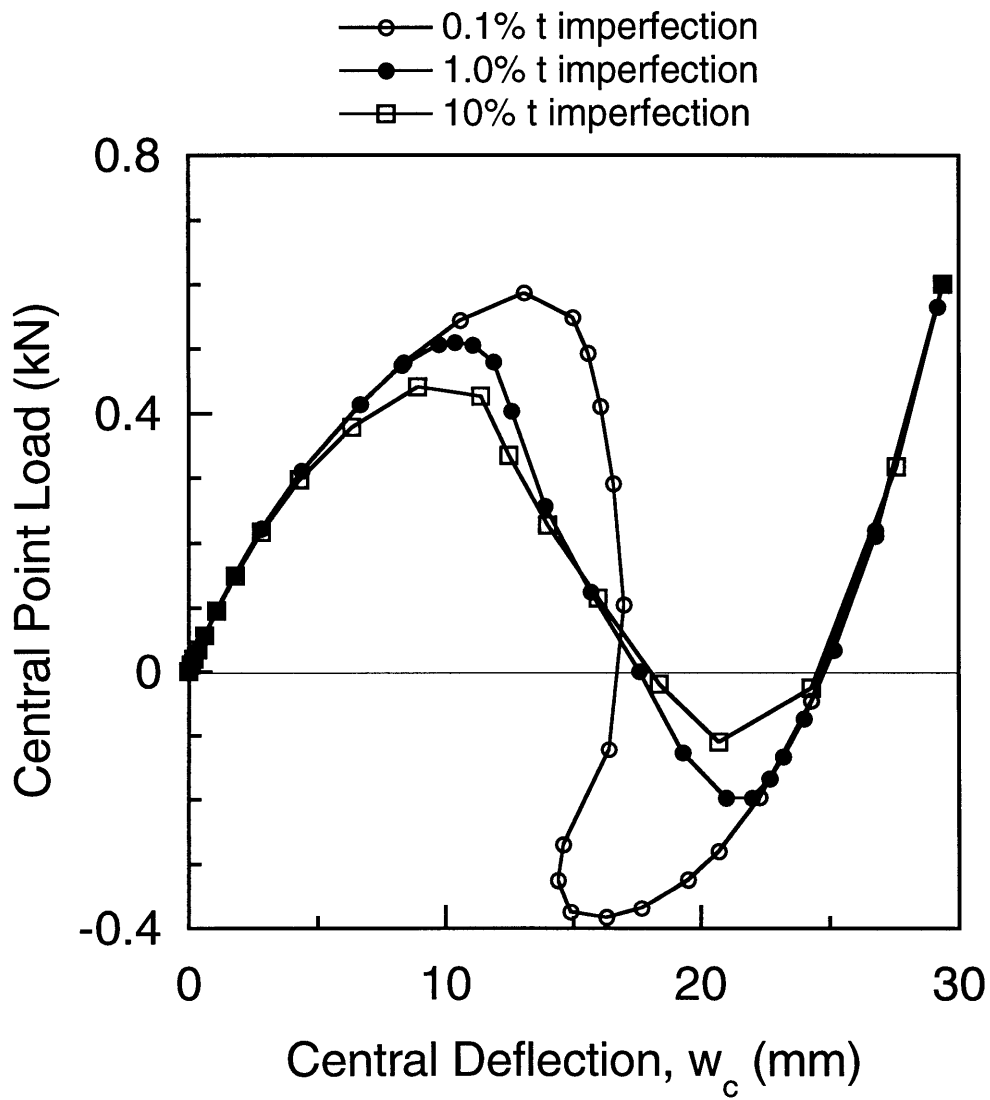


Figure 4.7 Load-deflection response for benchmark problem using STAGS with a symmetric (10x10) mesh incorporating scaled eigenmode imperfections into the initial geometry.

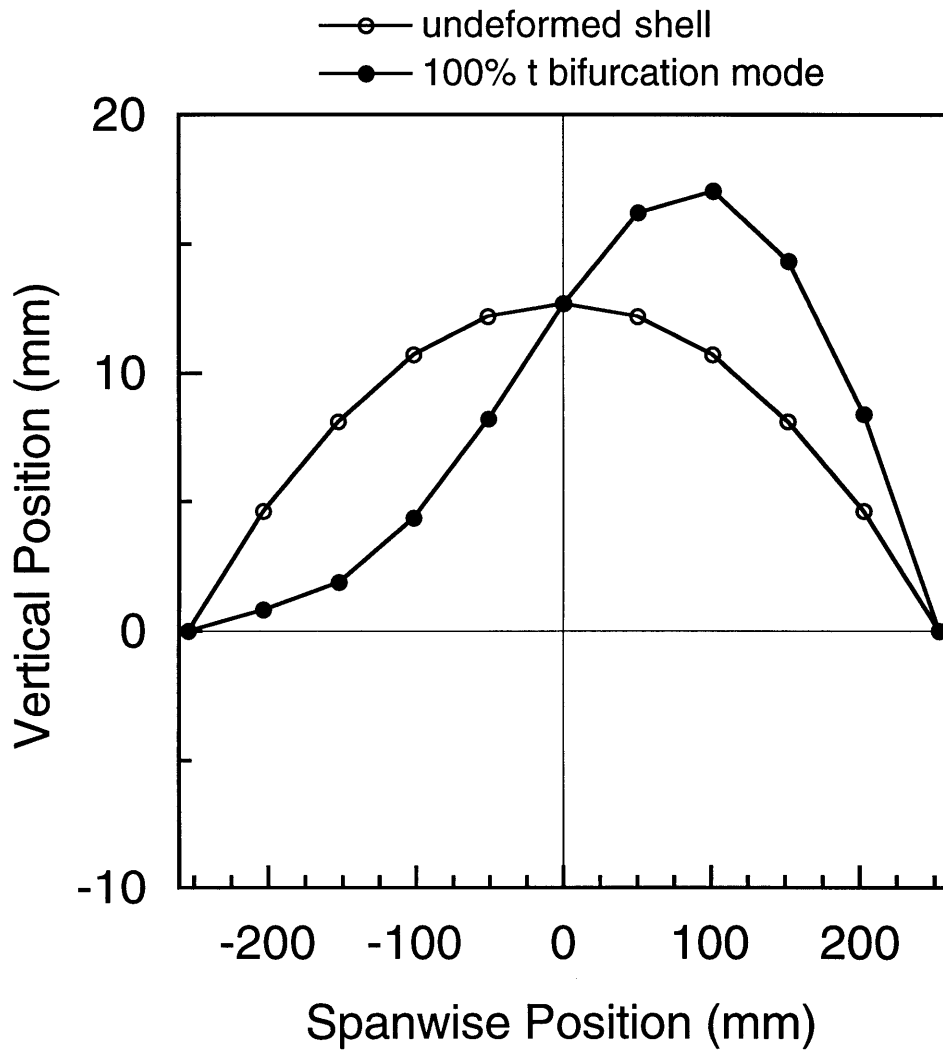


Figure 4.8 Central spanwise plot of the linear bifurcation mode for benchmark shell problem.

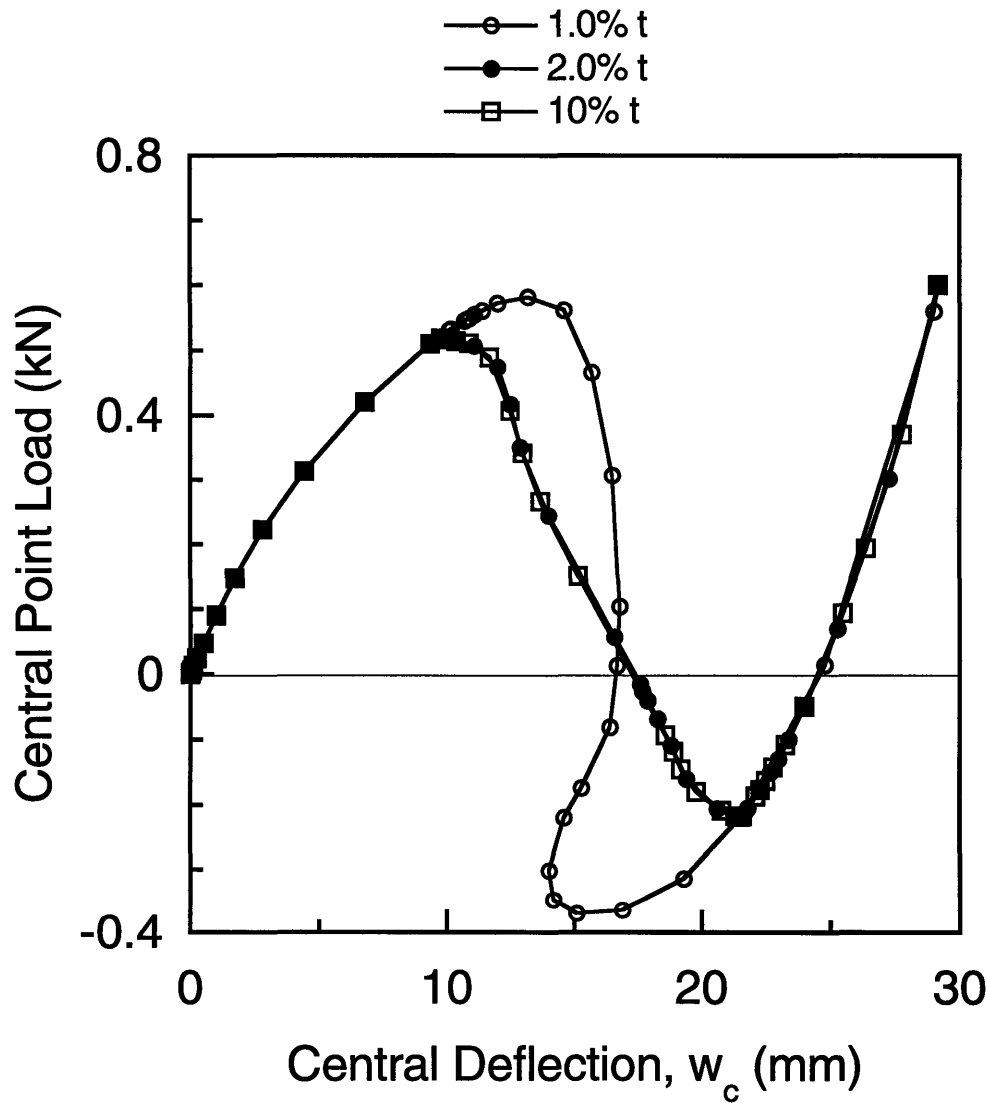


Figure 4.9 Load-deflection response for benchmark problem using STAGS with a symmetric (10x10) mesh incorporating scaled eigenmode deformations (equivalence transform) near the bifurcation point.

analyses using the symmetric mesh and geometric imperfections indicate a bifurcation point between loads of 509 N and 530 N. The first eigenmode is taken from the tangent stiffness matrix as evaluated at 509 N and then used to initiate the branch switch. Again, a small (1.0% thickness) imperfection amplitude misses the bifurcation point entirely, while larger values induce bifurcation much like the response found in Figure 4.7. An eigenmode amplitude of 2.0% (relative to specimen thickness) is used to calculate deformation-shape evolutions for the benchmark problem in Figure 4.10. In contrast to the symmetric modes in Figure 4.5, the bifurcation response in Figure 4.10 is dominated by an asymmetric mode in the postbuckling regime until the response rejoins the limit-point solution on the second equilibrium path. It is clear from Figures 4.7 through 4.10 that bifurcation into an asymmetric mode occurs in this benchmark problem, and that the limit-point solutions previously presented miss the asymmetric behavior and overestimate the buckling load by approximately 12%.

Bifurcation can also be investigated using the asymmetric meshing technique described in section 4.2. Bifurcation in the benchmark is investigated using a 10x6 / 10x5 mesh (see Figure 4.2) and the results are compared to the limit-point response in Figure 4.11. The bifurcation response previously identified is found directly, including the bifurcation point and postbuckling response, using the asymmetric meshing technique. The buckling load for the asymmetric mesh (510 N) corresponds with that found with the equivalence transform technique in Figure 4.9. Asymmetric mode shapes in the postbuckling region for the asymmetric mesh are given in Figure 4.12 for comparison to those in Figure 4.10 and excellent agreement is noted. The behavior of the edge and center of the shell in Figure 4.13 are noted to have similar characteristics as those for the limit-point solution given in Figure 4.6

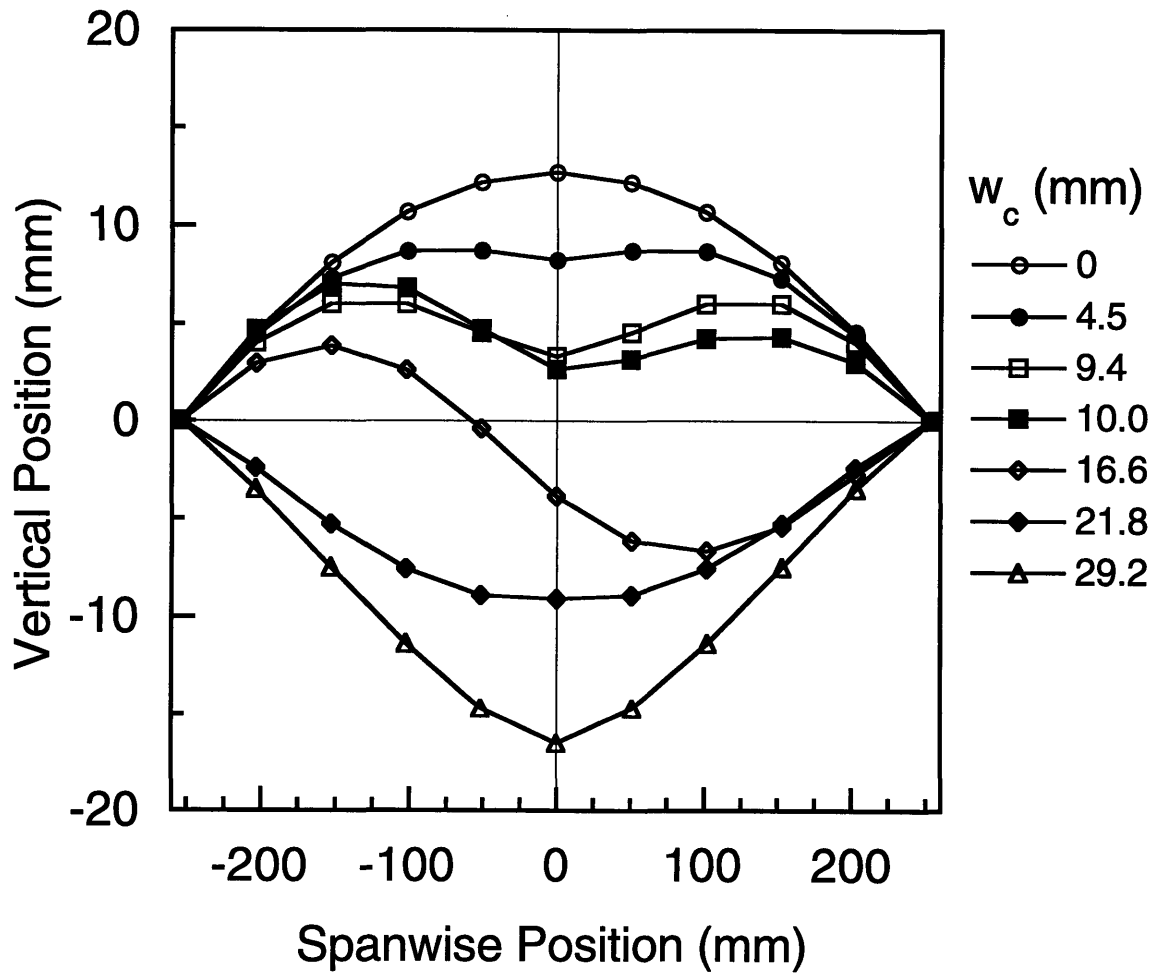


Figure 4.10 Central spanwise deformation modes for benchmark problem at different values of center deflection, w_c , using STAGS with a symmetric (10x10) mesh and the equivalence transform method (2.0% thickness).

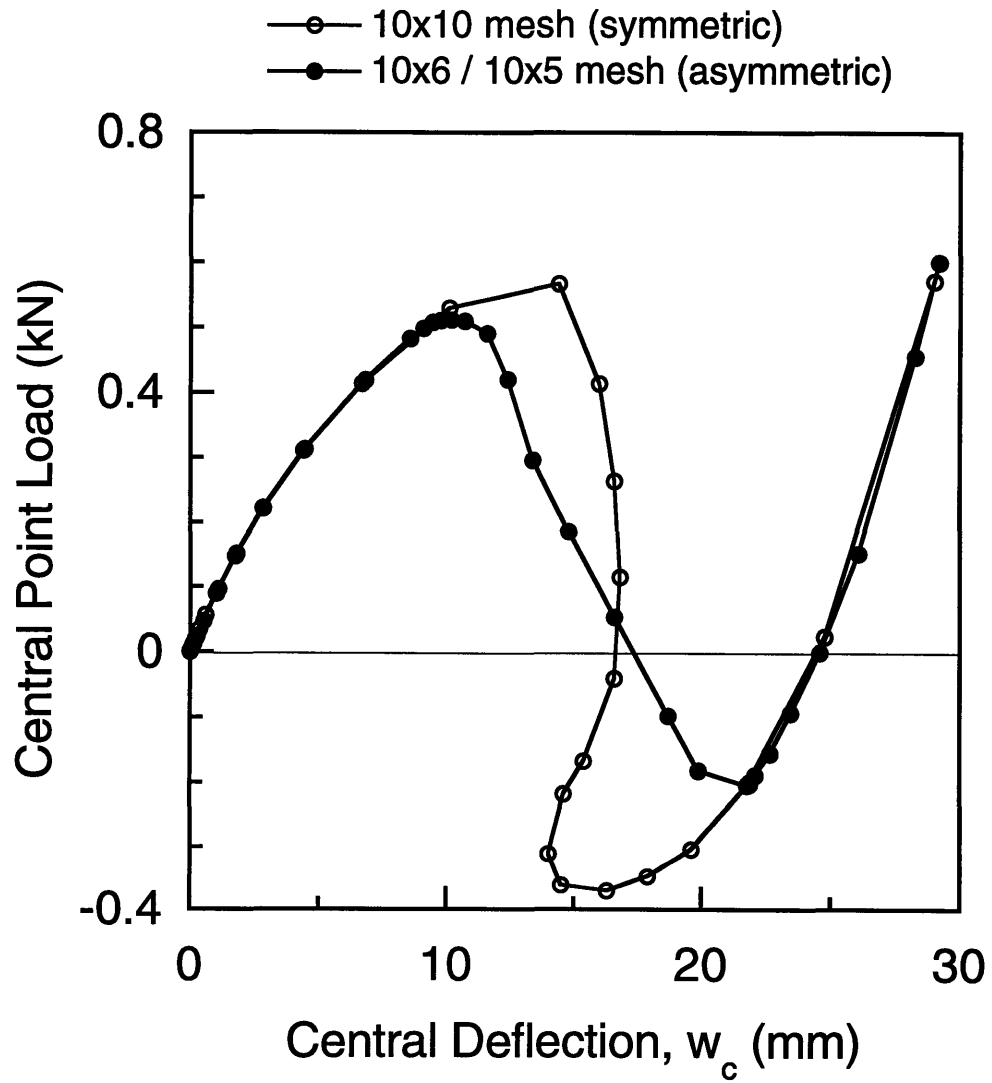


Figure 4.11 Load-deflection response for benchmark problem using STAGS with symmetric (10x10) and asymmetric (10x6 / 10x5) meshes.

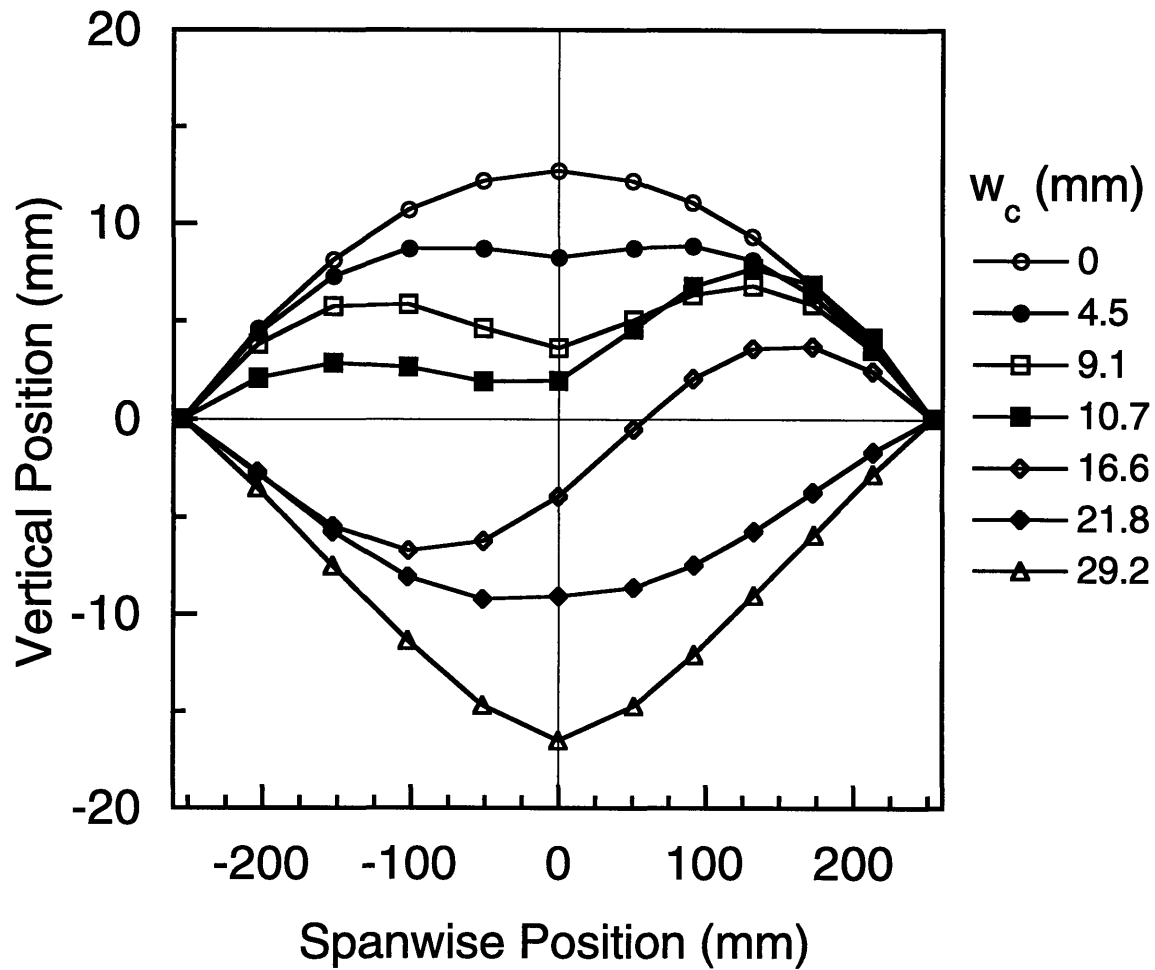


Figure 4.12 Central spanwise deformation modes for benchmark problem at different values of center deflection, w_c , using STAGS with an asymmetric (10x6 / 10x5) mesh.

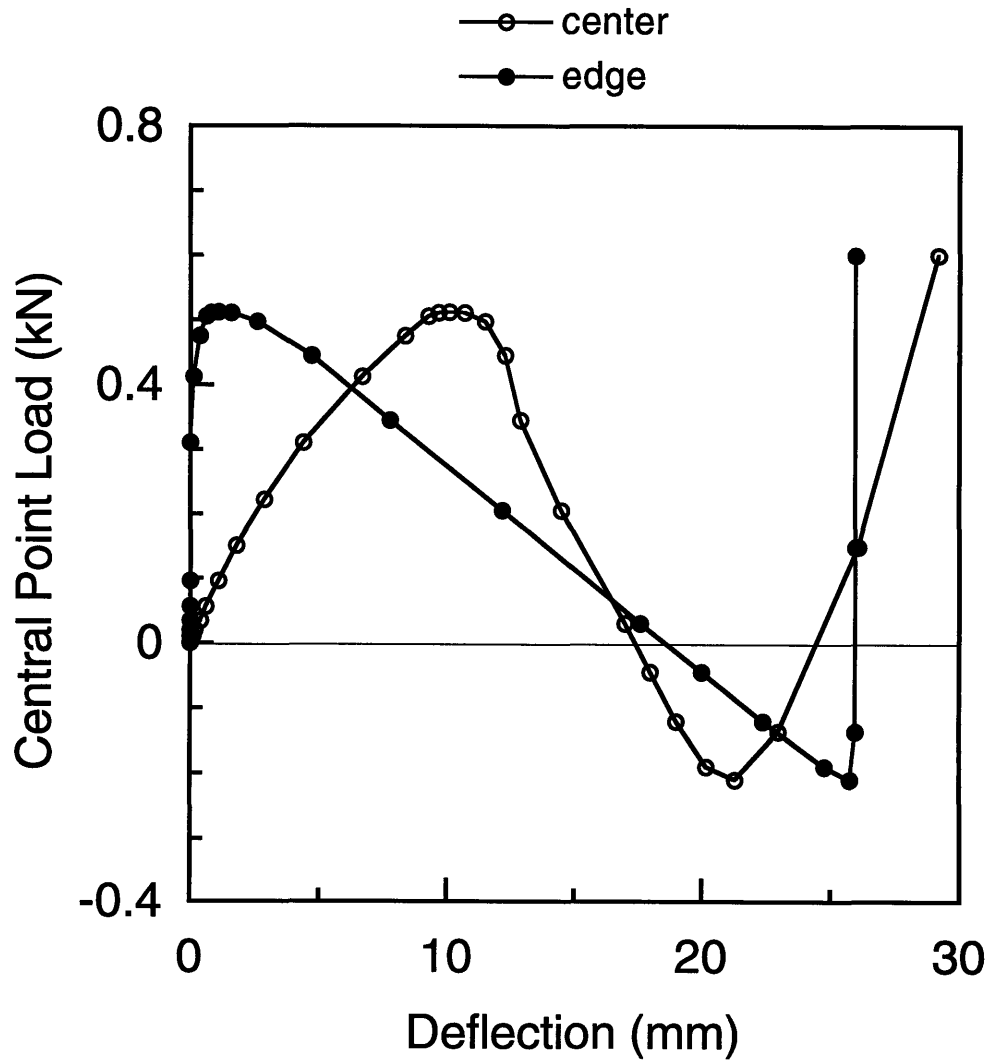


Figure 4.13 Load versus center and edge deflections for benchmark problem using STAGS with an asymmetric (10x6 / 10x5) mesh.

except that snapback is not evident at the center of the shell. The center of the shell (where loading is applied) first leads the edge response, then lags it through the latter part of the postbuckling region before it again leads on the second equilibrium path. Thus, although snapback is not a feature of the bifurcation response, the behavior of the shell does vary in the axial direction, *i.e.*, the shell does not deform as an arch.

4.3.3 Mesh Refinement and Convergence

In the previous examples involving the benchmark problem, the shell was discretized using a 10x6 / 10x5 mesh. The question arises as to how changing the asymmetric mesh will affect the response, aside from the usual convergence issues associated with mesh refinement. Many analyses of the benchmark were conducted using different asymmetric meshes. Of these, three solutions are presented in an exploded view in Figure 4.14 to show the excellent agreement among the various meshes. In the cases shown in Figure 4.14, and in all other cases where bifurcation is induced, different asymmetric meshes give the same response including buckling modes. From these studies it can be concluded that if the perturbation exists, the model will evaluate the same (lowest-energy) bifurcation response. Thus, the form of the asymmetric mesh is found to be irrelevant when bifurcation is induced. This leads to the question as to whether bifurcation is always induced.

It is a common feature of finite element analyses that successive mesh refinement should converge to an exact solution in the limit of infinitely many elements. However, further refinement of the asymmetric meshes discussed does not lead to a convergence to the bifurcation path. Rather, subsequent refinement of the mesh moves the solution from the (correct) bifurcation path to the primary path. This is illustrated by the solutions to the benchmark

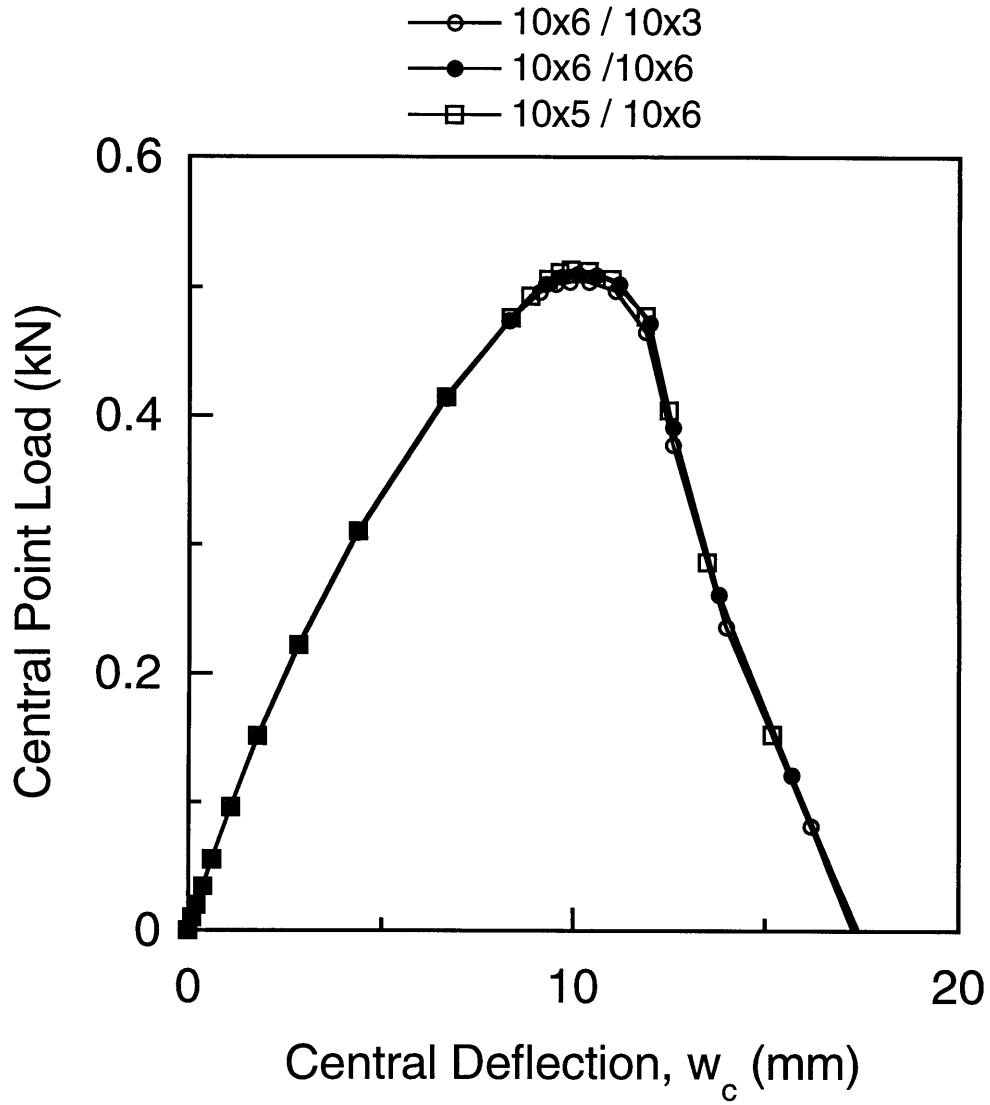


Figure 4.14 Numerical analysis of load-deflection response for benchmark shell problem using various asymmetric meshes.

problem given in Figure 4.15 using two different refined asymmetric meshes. The more refined mesh, 20x12 / 20x9, does not induce bifurcation but rather shows the limit-point response. A less refined, but more asymmetric mesh (20x12 / 20x5), finds the correct bifurcation response. This indicates that, if the perturbation (asymmetry) is not strong enough, the limit-point response will be found. This is due to numerical roundoff in the finite element model and is a manifestation of the same effect which causes small eigenmode amplitudes to miss bifurcation. Thus, as with the equivalence transform technique, either the limit-point or bifurcation response will be evaluated using the AMT depending on the strength of the induced perturbation. During the analysis of bifurcation using asymmetric meshing, it is clear when bifurcation is induced - a path different (and of lower energy) than the primary path results. In the analyses of shells in this chapter, a 10x6 / 10x5 mesh is found to provide converged bifurcation solutions. However, other shell geometries/materials are likely to have different convergence behavior and may require more refined meshes than the 10x6 / 10x5 mesh used for the shells in this chapter.

4.4 Analysis of Previous Experimental Work

Previous finite element analyses have been hampered by a lack of experimental data by which to validate the analyses. The studies rely on comparison to other analyses for verification, *e.g.*, [82] and the benchmark problem discussed in section 4.3. Recent experimental data allows the unique opportunity to validate the current analysis technique by comparison to large-deflection, large-rotation, composite shell data [18, 21]. Load-deflection and mode-shape evolutions are available for these tests and are used for comparison to results from the STAGS finite element models utilizing the

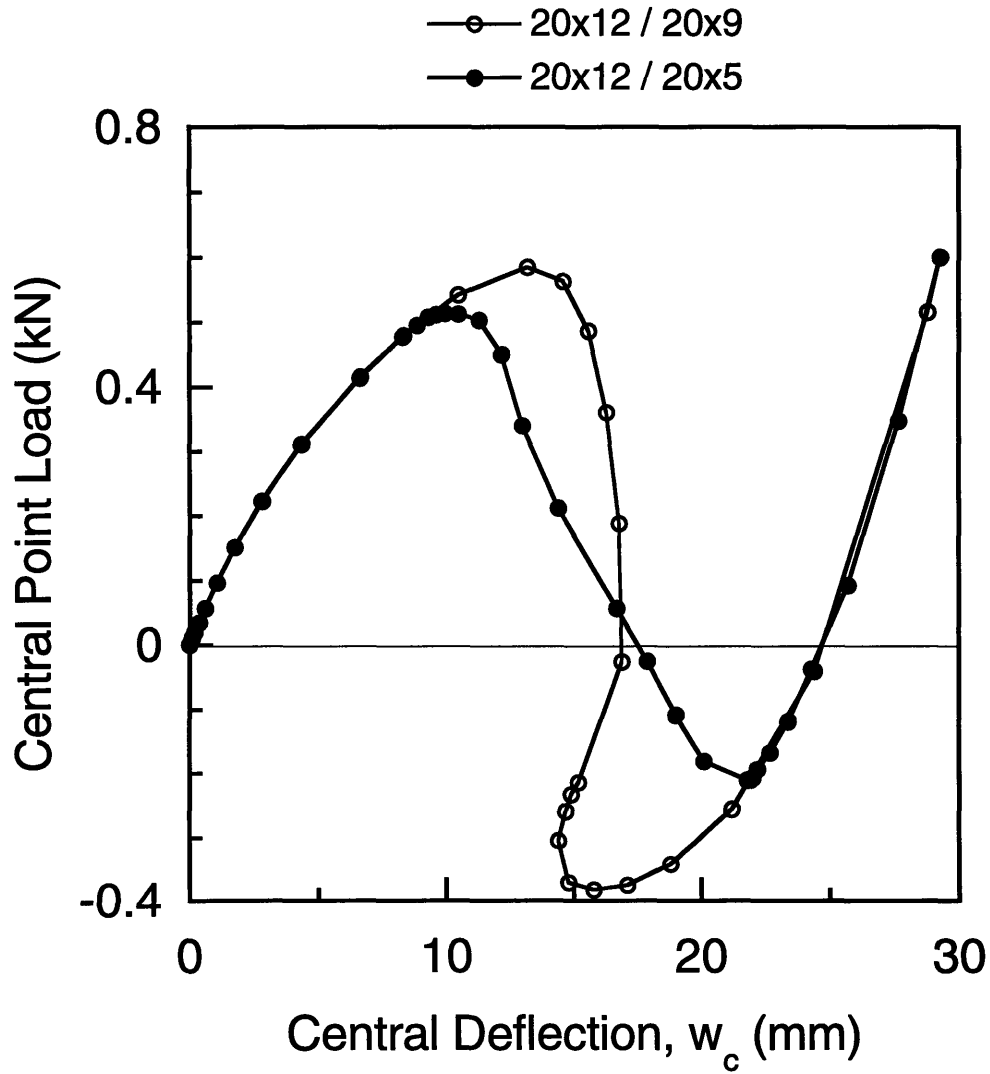


Figure 4.15 Load-deflection response for benchmark problem using STAGS with asymmetric (20x12 / 20x9) and (20x12 / 20x5) meshes.

AMT.

4.4.1 Description of Experiments

Full details of the experiments analyzed in this section can be found in References [21, 56]. These shells share many characteristics of the composite shells considered in the experimental portion of the current work (see section 3.3). The composite shells were manufactured from Hercules AS4/3501-6 graphite/epoxy prepreg tape in a $[\pm 45_n/0_n]_s$ layup where n takes on the values 1, 2, and 3. Ply material properties for this material system are given in Table 4.1. Effective laminate properties are computed within STAGS based on these ply properties. Structural parameters and the orientation of ply angle, θ , are as shown previously in Figure 3.1. Note that the 0° ply direction is along the curvilinear y -axis (circumferential direction) of the shell. While only thickness (t) is varied in the current experimental work, radius, span, and thickness were varied in the experiments analyzed in this section. Specimens are designated as in chapter 3 (equation 3.1) with subscripts indicating scale factors of the base values. This gives eighteen specimens with different structural parameters: $R_6, R_{12}, S_1, S_2, S_3, T_1, T_2, T_3$. Experimental values of radius are

Table 4.1 AS4/3501-6 Ply Data

E_{11}	142 GPa
E_{22}	9.81 GPa
G_{12}	6.00 GPa
ν_{12}	0.3
ply thickness	0.134 mm

given in Appendix B and are used in the analysis while nominal laminate properties, including thickness, are used. Due to the test fixture design, nominal and experimental values for span are identical.

The experimental boundary conditions are idealized as hinged on the circumferential edges and free on the axial edges which are the same as for the benchmark problem. The loading is idealized as point loading in the center of the shell as for the benchmark problem. This differs from the experiments where a 12.7 mm (1/2") diameter hemispherical steel indenter was used to load the center of the shell. The analysis uses the path-parameter (Riks arc-length) method to increment the loading. This also differs from the experiments wherein the load was introduced under displacement (stroke) control. An important consequence of this is that, in the experiments, negative load can not be applied to the shell center such that contact is lost at a zero-load crossing after bifurcation. Thus, experimental data is available for postbuckling only until zero load is reached. In the analysis, the asymmetric discretization scheme (60%/40%) utilized in the benchmark problem is again used here. All results represent converged solutions attained through mesh refinement studies. Those studies show that a 10x6 / 10x5 mesh is adequate to capture the entire response including bifurcation and postbuckling. Numerical and experimental load-deflection comparisons for all specimens tested in the previous work are presented in Appendix B. Loading and boundary condition idealizations are discussed in the context of the results in the next section.

4.4.2 Load-deflection and Mode-shape Comparisons

As discussed previously, both load-deflection and mode-shape data are available for comparison to the finite element results. As in the benchmark problem, both deflection and load are considered positive in the direction of load

application ($-z$ in the coordinate system from Figure 4.1). Numerical comparisons to measured load-deflection and mode-shape evolutions for specimens $R_6S_3T_1$ and $R_{12}S_3T_1$ are presented in Figures 4.16 to 4.25. To analyze these specimens, a more refined asymmetric mesh of $30 \times 12 / 30 \times 9$ was utilized. This mesh provides the same response as a $10 \times 6 / 10 \times 5$ mesh but generates smoother (more datapoints) deflection mode shapes in both the axial and circumferential directions for comparison to the experimental data. Although this mesh missed the bifurcation path in the benchmark problem, it is successful in capturing bifurcation for these composite cases. This is most likely due to the difference in material and geometric properties. In the results presented, displacement is nondimensionalized with respect to specimen thickness ($T_1 = 0.804$ mm) to emphasize the large-deflection nature of the shell behavior. Both limit-point (symmetric mesh) and bifurcation (asymmetric mesh) solutions are provided in all cases.

Bifurcation is clearly the critical consideration in the buckling response of the shells as shown in Figures 4.16 and 4.17. Bifurcation from the nonlinear (and symmetric) primary equilibrium path occurs at 67% of the limit-point buckling load for both these shells. The entire postbuckling regime shown is dominated by the deformation mode associated with the bifurcation. Excellent agreement is obtained between the load-deflection bifurcation solutions and the experimental data in Figures 4.16 and 4.17.

Comparison of central mode-shape evolutions for these two specimens in Figures 4.18 to 4.21 provide further evidence that the analysis captures the experimental behavior. Mode shapes corresponding to the concave side of the shell are presented at discrete values of nondimensionalized center displacements (w_c/T_n) to reference the load-deflection plots in Figures 4.16 and 4.17. For specimen $R_6S_3T_1$, symmetric mode shapes are evident for

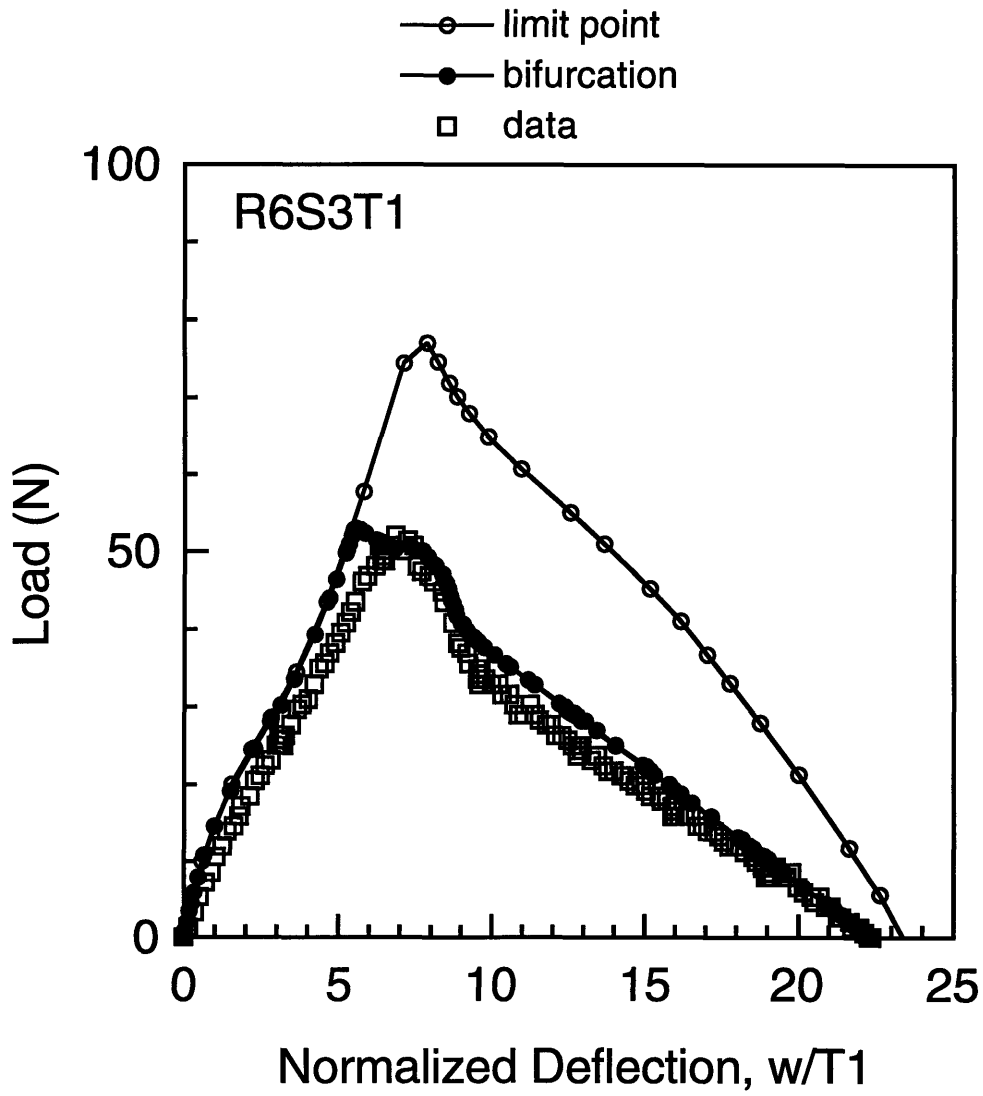


Figure 4.16 Central load-deflection results from numerical analyses and experiment [21] for the transverse buckling response of composite shell specimen $R_6S_3T_1$.

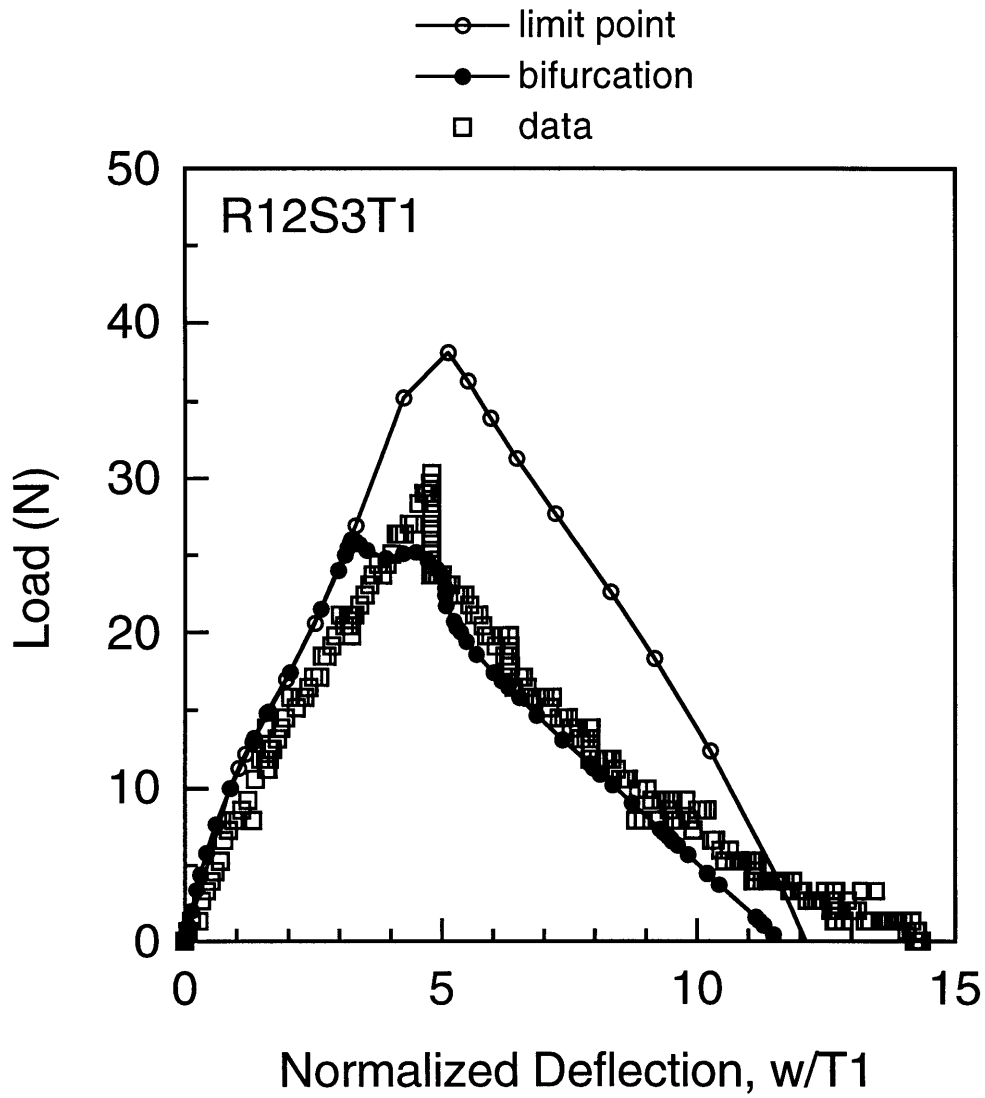


Figure 4.17 Central load-deflection results from numerical analyses and experiment [21] for the transverse buckling response of composite shell specimen $R_{12}S_3T_1$.

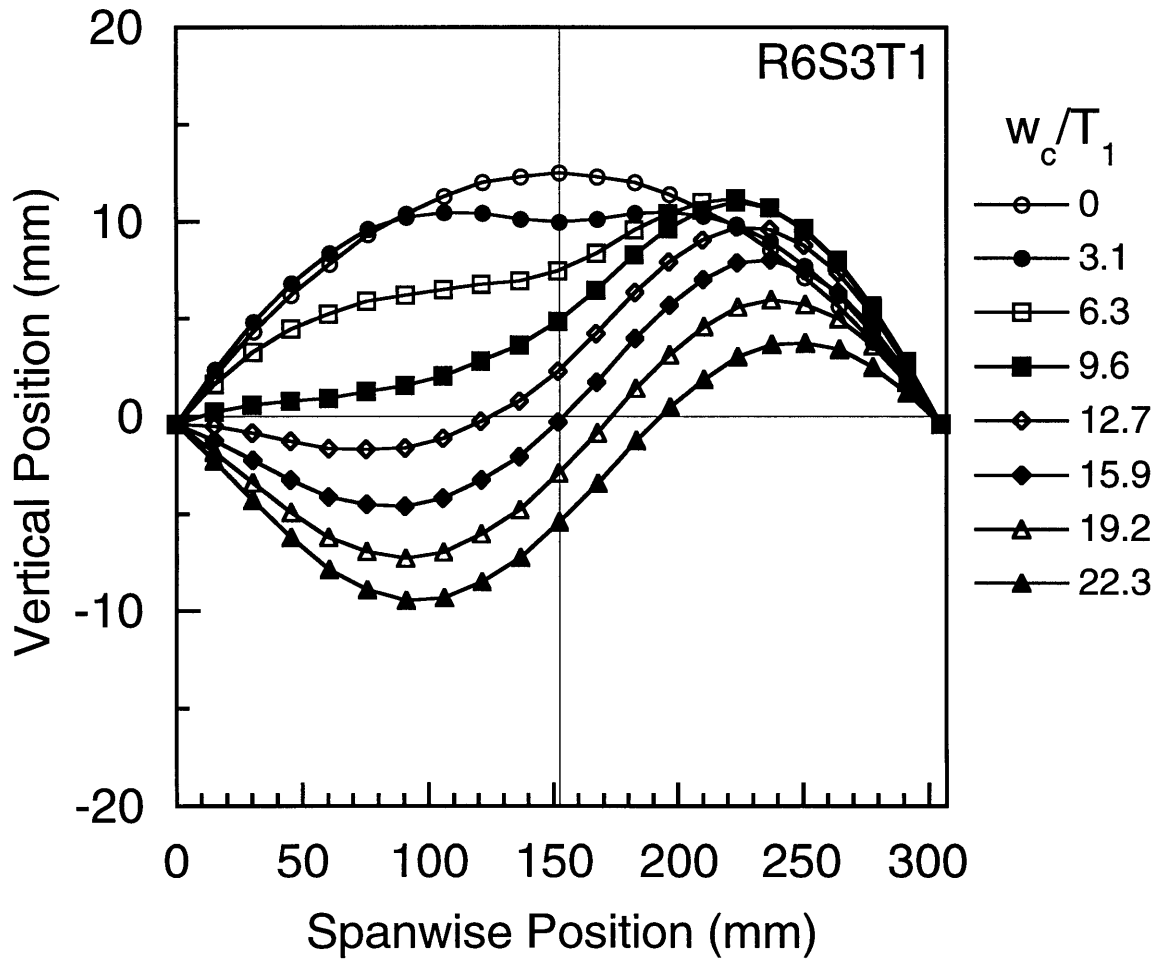


Figure 4.18 Numerical analysis results of central spanwise deformation modes for specimen $R_6S_3T_1$ at different values of normalized center deflection.

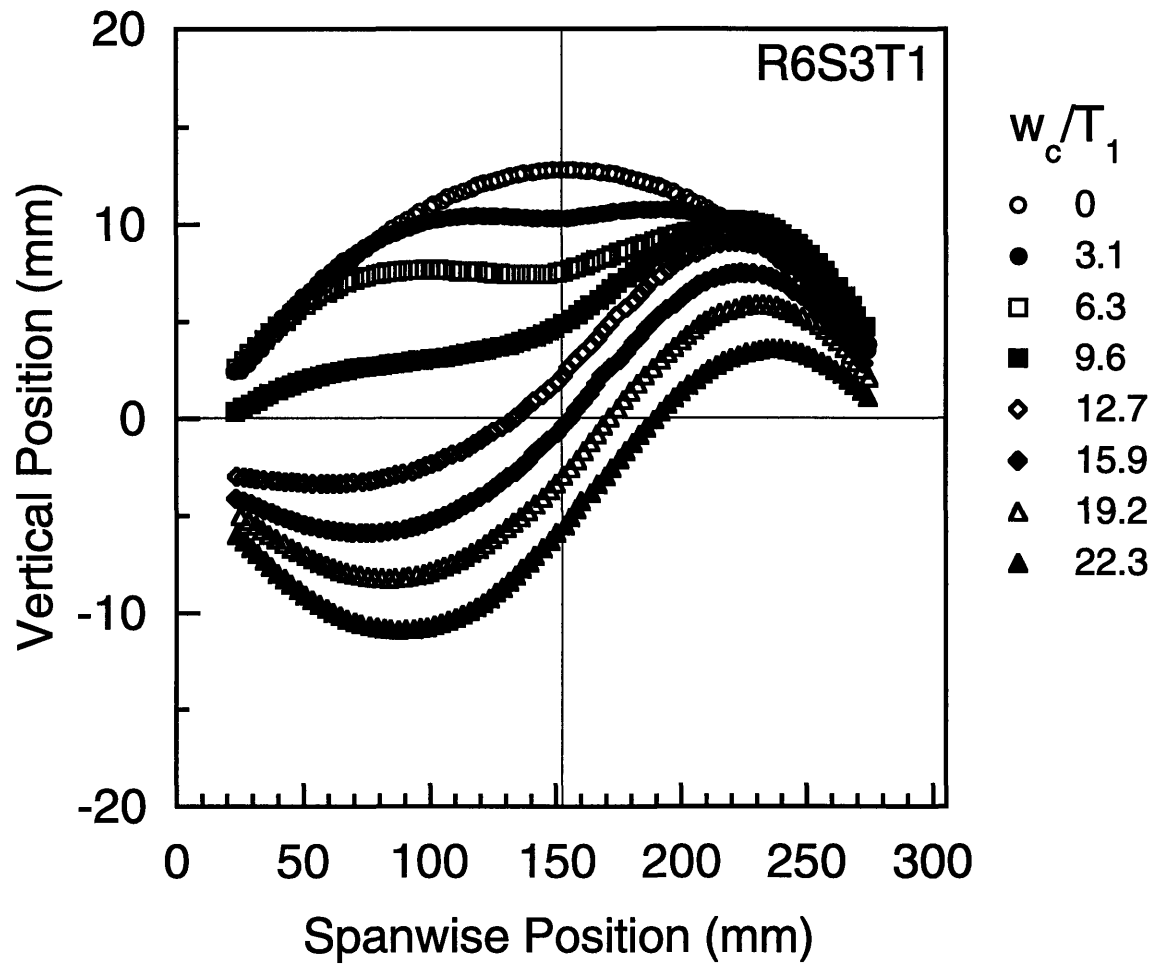


Figure 4.19 Measured [21] central spanwise deformation modes for specimen $R_6S_3T_1$ at different values of normalized center deflection.

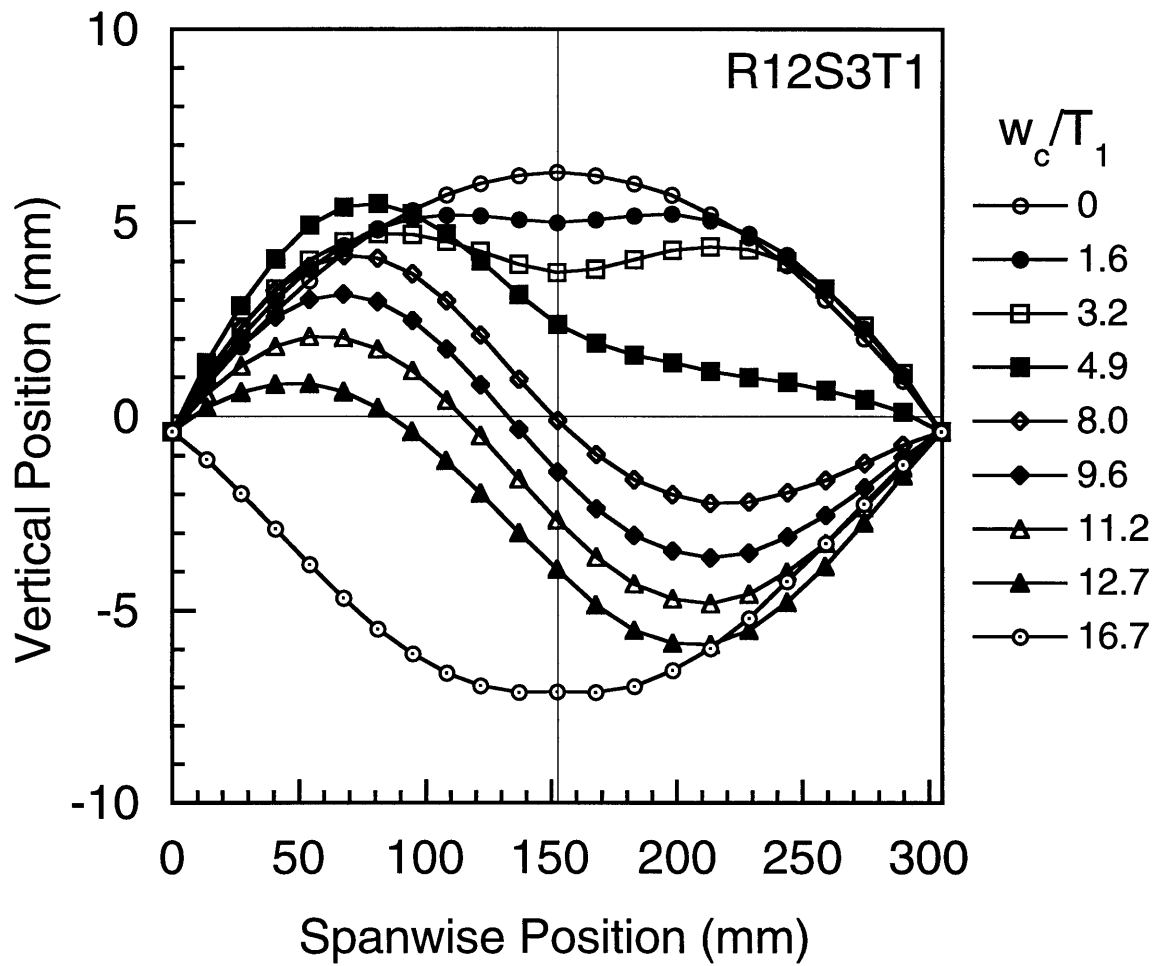


Figure 4.20 Numerical analysis results of central spanwise deformation modes for specimen $R_{12}S_3T_1$ at different values of normalized center deflection.

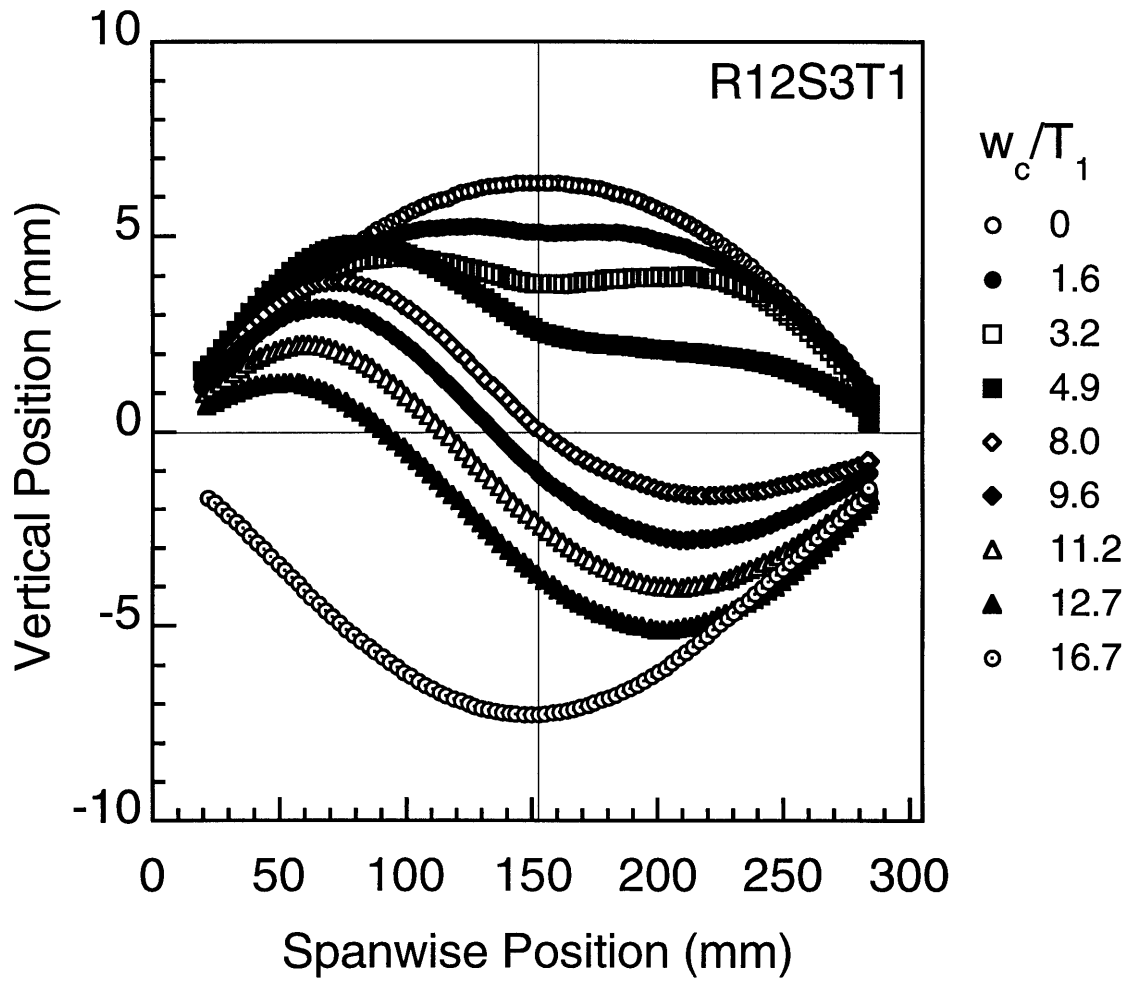


Figure 4.21 Measured [21] central spanwise deformation modes for specimen $R_{12}S_3T_1$ at different values of normalized center deflection.

displacements below the critical bifurcation point in both the numerical and experimental results shown in Figures 4.18 and 4.19, respectively. A dominant asymmetric mode, with respect to the loading in the circumferential direction, is evident only after bifurcation between nondimensional center deflections of 3.1 and 6.3. The same transition, from a primary symmetric mode prior to bifurcation to a dominant asymmetric mode, is also noted for specimen $R_{12}S_3T_1$ between nondimensional center deflections of 3.2 and 4.9 in Figures 4.20 and 4.21. Mode shapes in the axial direction for specimens $R_6S_3T_1$ and $R_{12}S_3T_1$ also reveal good agreement between numerical and experiment results as seen in Figures 4.22 and 4.23, and Figures 4.24 and 4.25, respectively. The experimental data indicates some variation in the axial height of the undeformed specimen which is then evident throughout the specimen response by comparison to the numerical results. In general, excellent agreement between theory and experiment is noted for the deformation modes of specimens $R_6S_3T_1$ and $R_{12}S_3T_1$.

The postbuckling response immediately following bifurcation from the primary equilibrium paths in Figures 4.16 and 4.17 contain several local minima and maxima which deserve further consideration. The majority of specimens analyzed display this behavior near the bifurcation point. The local minima and maxima are associated with axial variations in the shell response which is evident in the deformation mode-shape evolutions near the bifurcation point as shown in Figures 4.26 and 4.27 for specimen $R_6S_3T_1$. The edge mode corresponds to the back (upper right) edge in Figure 4.1. As shown in Figure 4.26, the center of the shell is noted to have an asymmetric (bifurcation) mode at a w_c/T_n value of 5.6 whereas the asymmetric mode is not evident at the shell edge at a w_c/T_n value of 5.6 but is evident at a value of 6.6 (see Figure 4.27). This latter value corresponds to the first local minima. Thus, transition

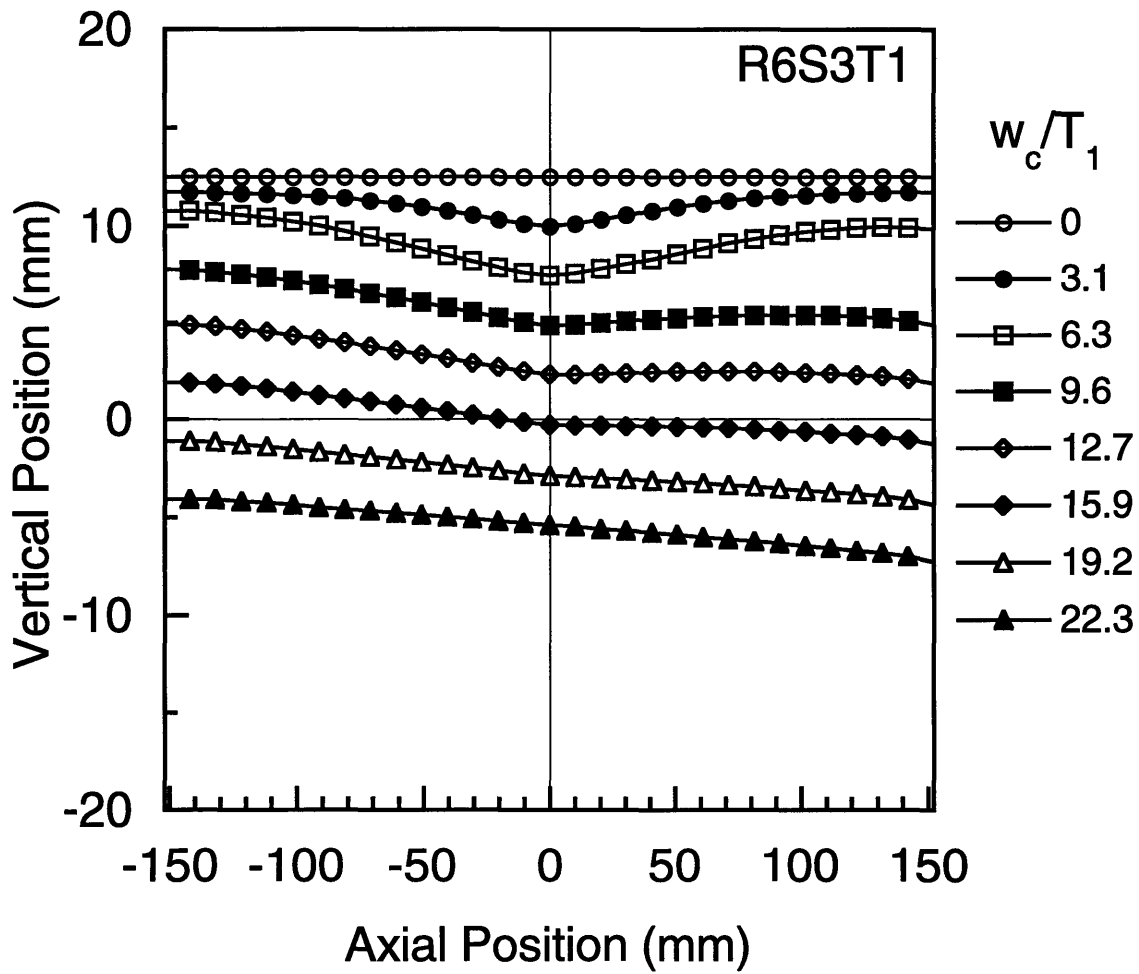


Figure 4.22 Numerical analysis results of central axial deformation modes for specimen $R_6S_3T_1$ at different values of normalized center deflection.

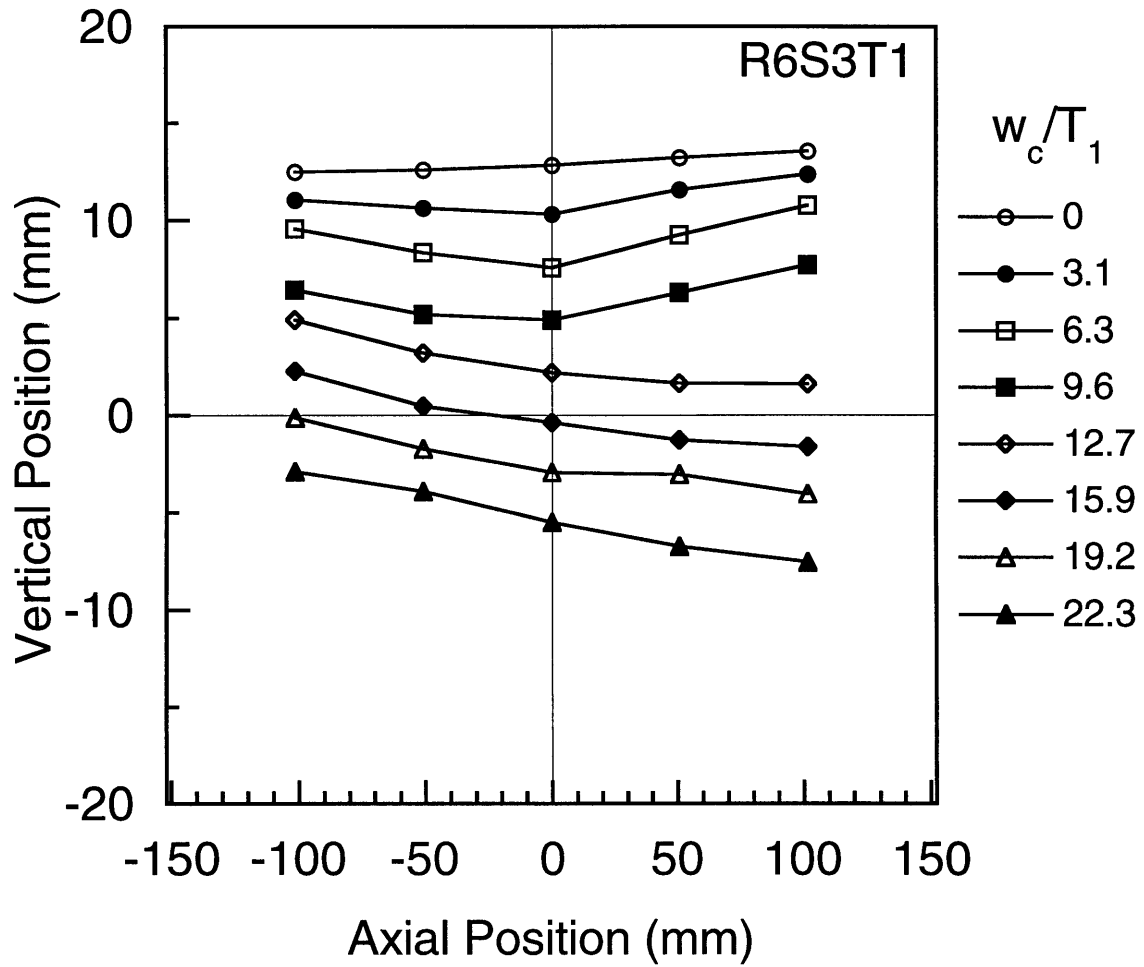


Figure 4.23 Measured [21] central axial deformation modes for specimen $R_6S_3T_1$ at different values of normalized center deflection.

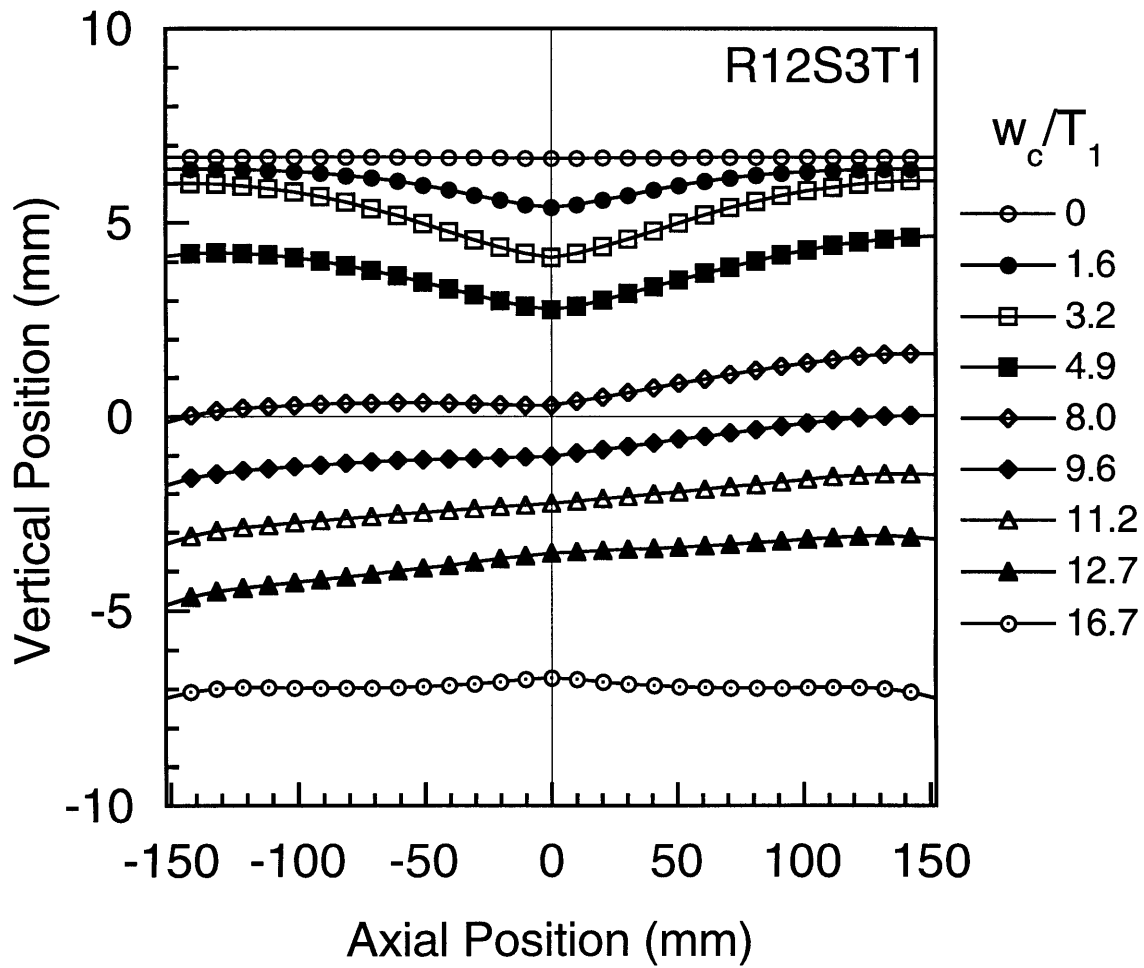


Figure 4.24 Numerical analysis results of central axial deformation modes for specimen $R_{12}S_3T_1$ at different values of normalized center deflection.

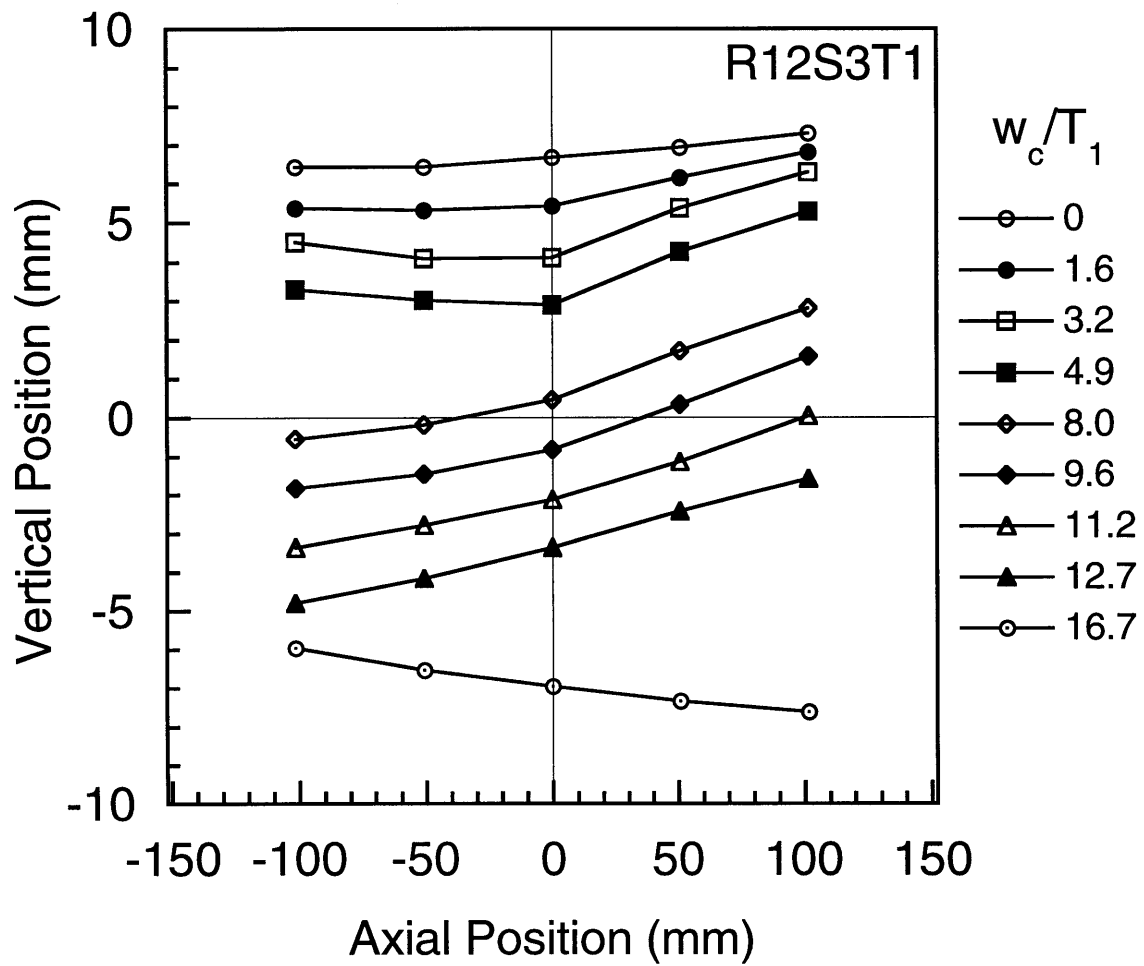


Figure 4.25 Measured [21] central axial deformation modes for specimen $R_{12}S_3T_1$ at different values of normalized center deflection.

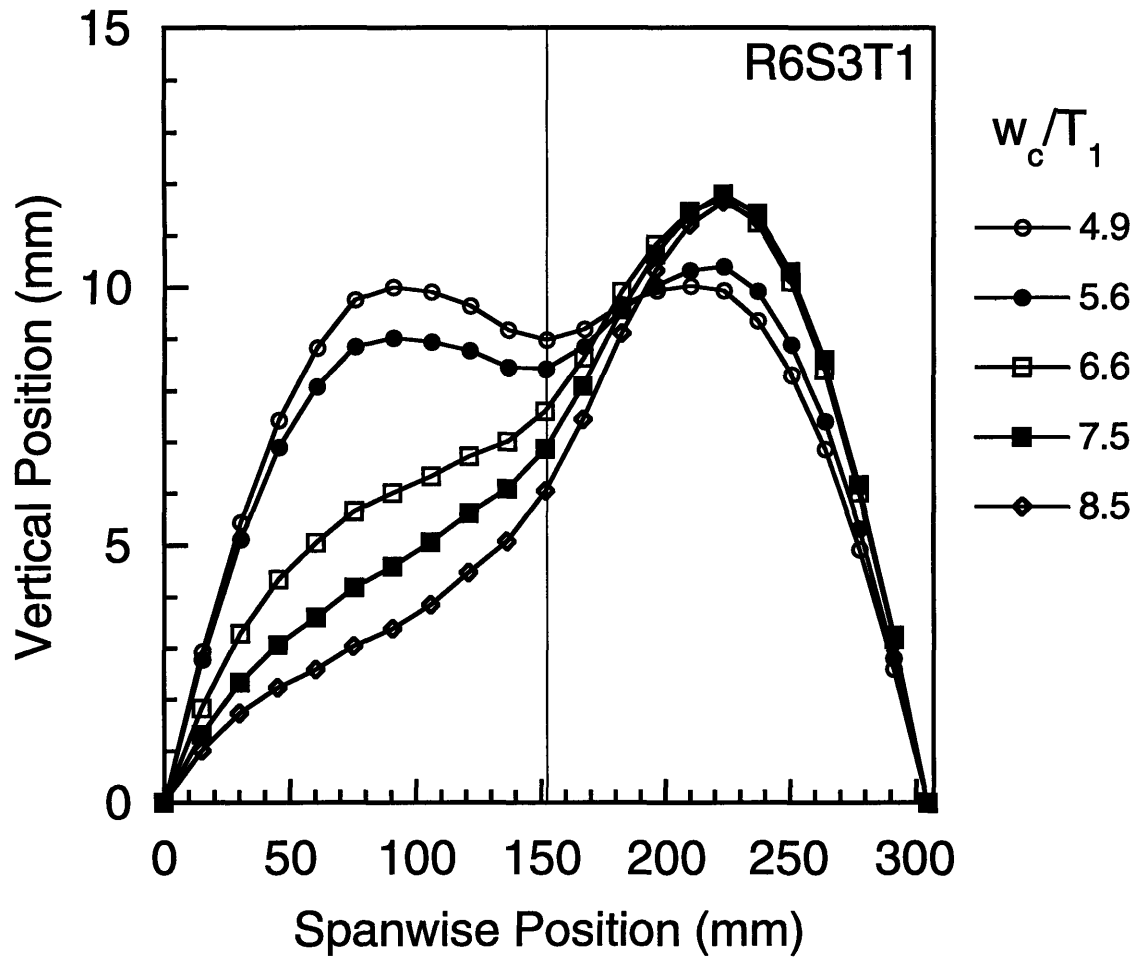


Figure 4.26 Numerical analysis results of central spanwise deformation modes for specimen $R_6S_3T_1$ at different values of normalized center deflection, w_c/T_1 , near the bifurcation point.

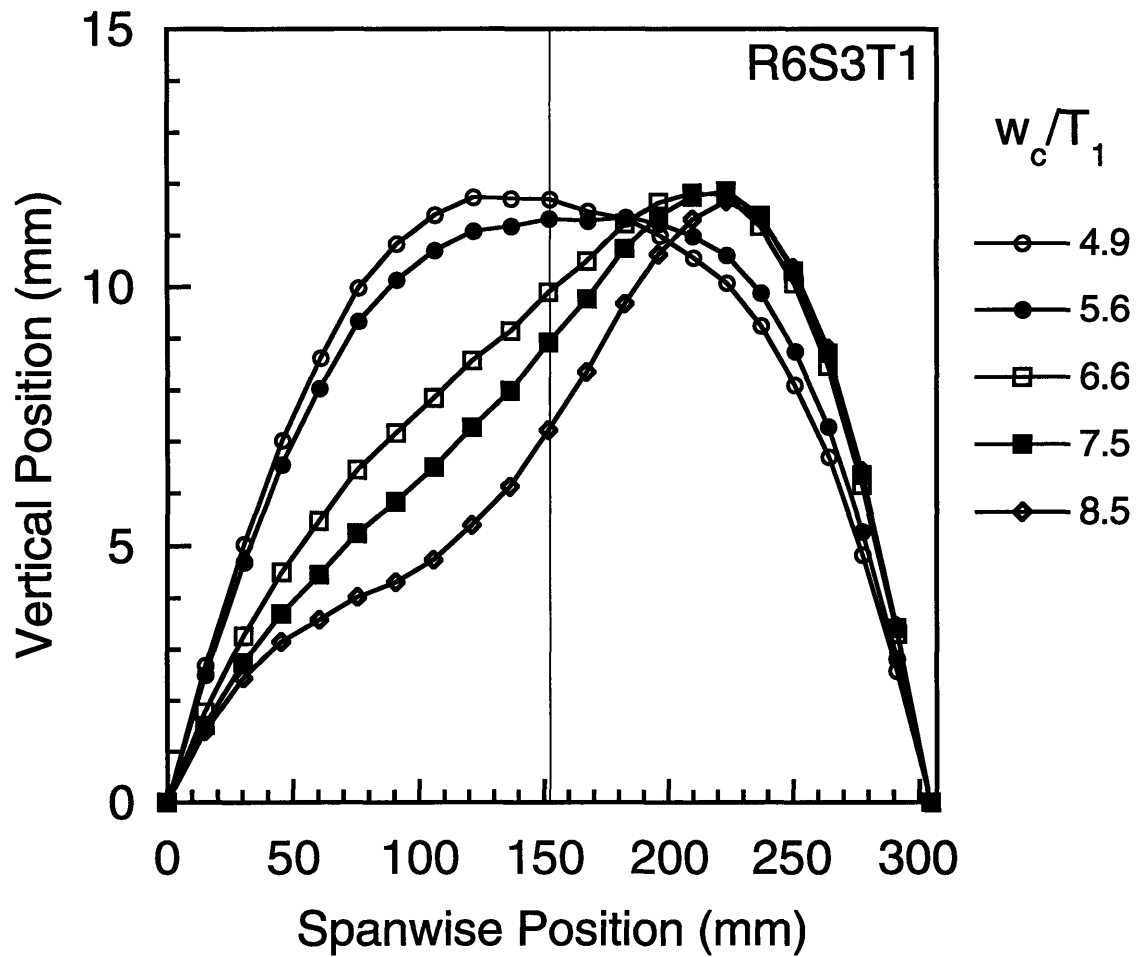


Figure 4.27 Numerical analysis results of edge spanwise deformation modes for specimen $R_6S_3T_1$ at different values of normalized center deflection, w_c/T_1 , near the bifurcation point.

from the first local maxima (near a w_c/T_n value of 5.6) to the first minima (near a w_c/T_n value of 6.6) involves axial propagation of the asymmetric mode from the center to the free shell edges. Using similar considerations, the second local maxima (near a w_c/T_n value of 8.5) is seen to correspond to the shell edge assuming a mode with an inflection point much like the center of the shell.

Due to bending-twisting coupling in the composite laminate, the two shell edges do not deform symmetrically (as in the isotropic benchmark problem). This is evident in the load versus normalized center and edge deflection plots in Figure 4.28. Edge 1 corresponds to the back edge in Figure 4.1, and edge 2 the front (lower left). Initially, the shell edges lag behind the response of the center of the shell but closely follow one another. Only through the postbuckling region are there significant differences between the shell edges where one edge is noted to lag behind the other. On the second stable equilibrium path, as on the first, the shell edges behave similarly and begin to lag behind the center of the shell as the load increases. Thus, asymmetries in the composite shell response are due to bifurcation into an asymmetric mode in the circumferential direction, and also due to bending-twisting coupling in the laminate in the axial direction.

4.4.3 Modeling Assumptions and Experimental Realities

The measured responses of the composite shells are sensitive to imperfections and other experimental realities, such as non-ideal boundary conditions [21, 37], indentation (contact modeling) at the loading point, and damage formation and propagation. These effects have not been accounted for in the elastic models in this work. This is appropriate for many of the shells tested, such as those discussed in section 4.4.2, as illustrated by the excellent

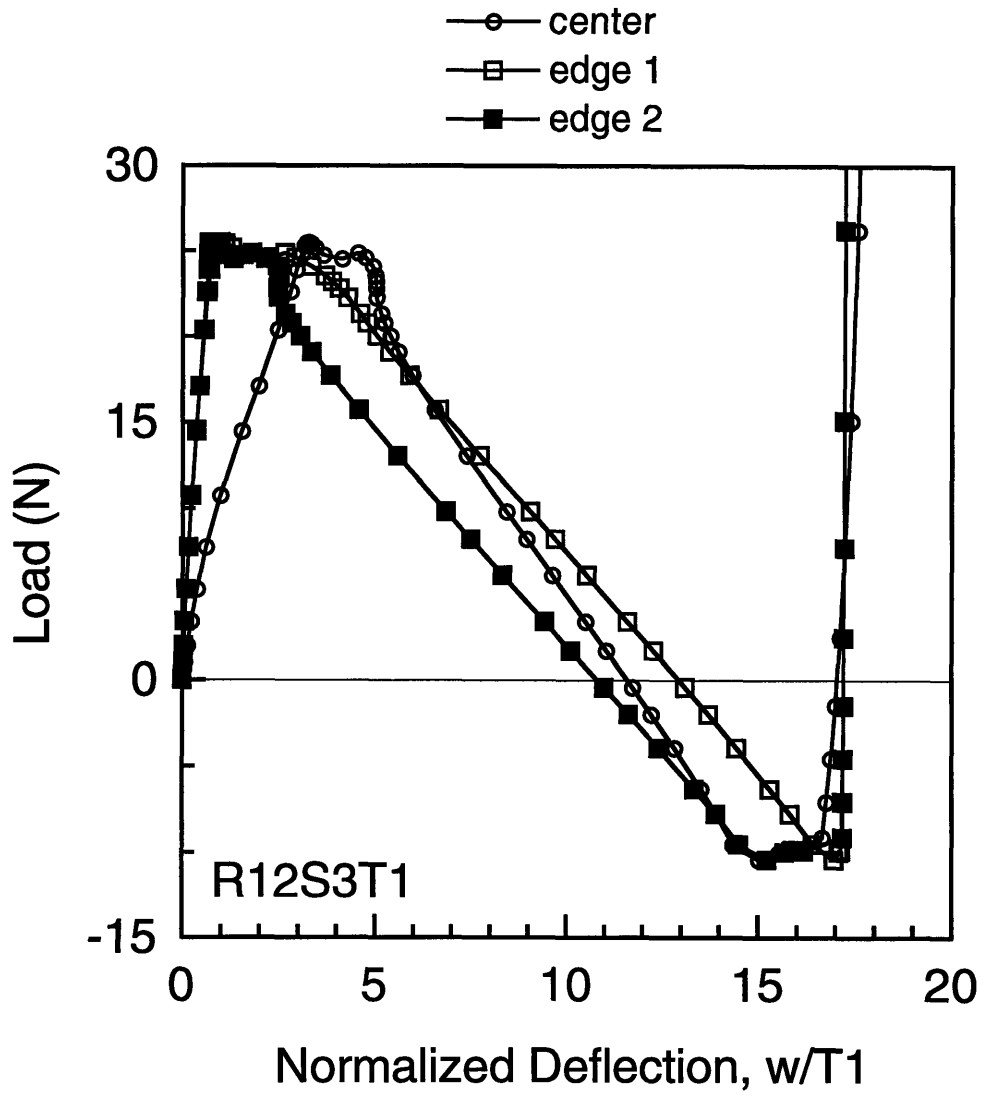


Figure 4.28 Load versus center and edge deflections from numerical analysis of specimen $R_{12}S_3T_1$.

agreement between analysis and experiment. The point-load idealization of the indenter and the mathematical idealization of the hinged boundary condition are justified for specimens $R_6S_3T_1$ and $R_{12}S_3T_1$ as the analysis and experiments agree. Likewise, inevitable imperfections in the specimens and boundary conditions do not seem to affect these shells. However, results from modeling all eighteen of the specimens indicate that experimental realities, particularly boundary conditions, need to be considered in some cases. In general, experimental load-deflection curves are more compliant than those predicted. This has been attributed to compliance in the test fixture which interacts with the shell response through the hinged boundary condition [21]. Test fixture compliance of this kind has been discussed by previous authors in relation to nonlinear collapse of arches at limit points [42, 52]. Fixture compliance acts to soften the structural response and reduce, or even eliminate, limit points in arches.

In the experiments, because the load is introduced under deflection control, compliance of the test fixture in the direction of loading ($-z$ direction) is unimportant. However, compliance of the test fixture perpendicular to the applied loading will couple to the response of the specimen. Compliance of the test fixture thus refers to the in-plane boundary condition of the hinged support. Rather than being fixed, as in the numerical idealization, there is a stiffness associated with the in-plane constraint. The compliant behavior of the experimental data relative to the numerical models is evident in Figure 4.29 where analysis and experiment are compared for specimen $R_{12}S_3T_2$. To investigate the effect of test fixture compliance, a lower bound for the effect of the test fixture is considered by allowing the shell to have a traditional simple-support rather than a hinge. Thus, rather than being rigid (or fixed), the in-plane restraint is free. In arch analyses, a simple support such as this allows

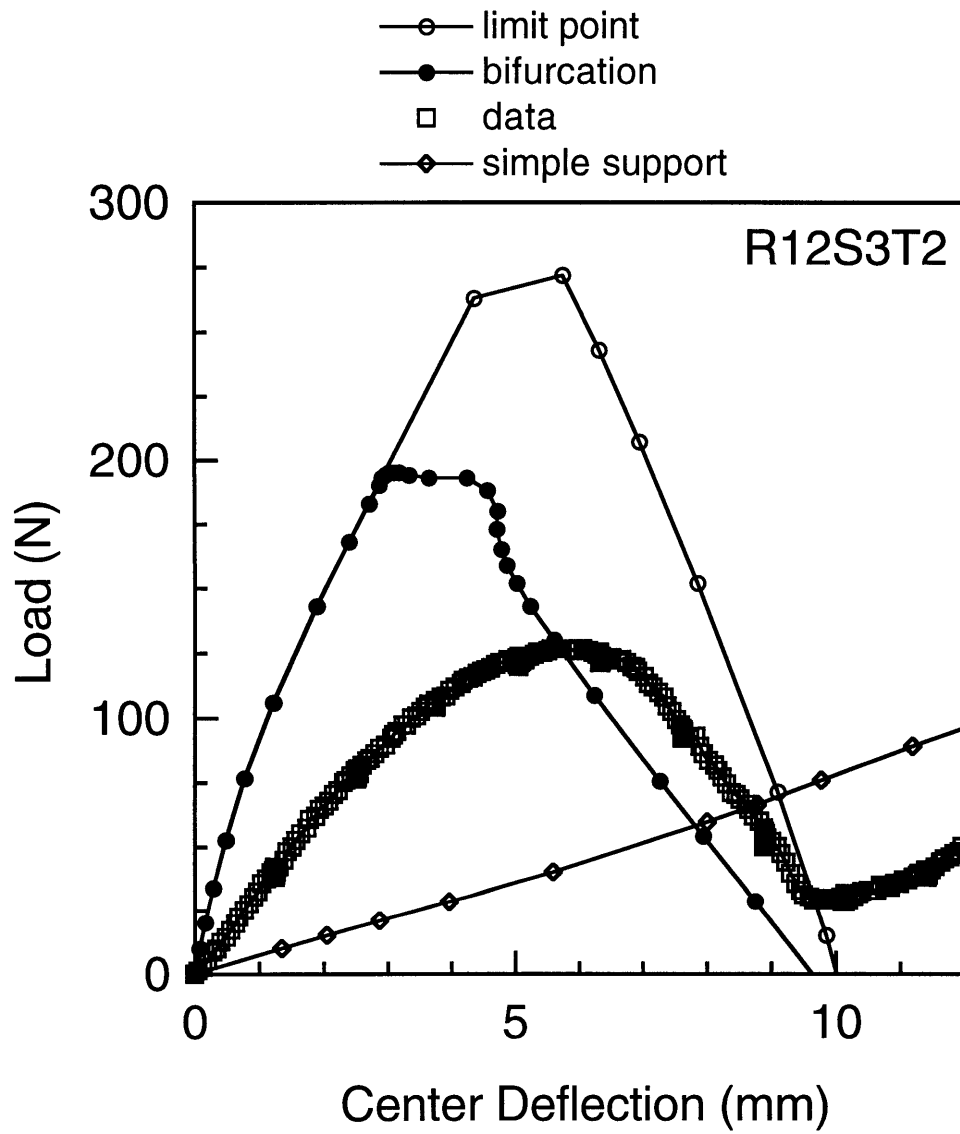


Figure 4.29 Central load-deflection results from numerical analyses and experiment [21] for the transverse buckling response of composite shell specimen $R_{12}S_3T_2$.

the arch to deform continuously with no critical buckling load. The experimental response should thus lie between the two extremes of hinged and simply-supported. This is in agreement with the results obtained for the shells analyzed here as illustrated in Figure 4.29. The simple-support results are much more compliant than the hinged results and act as a lower bound to the measured response with regard to this aspect of the boundary condition. In reality, the test fixture will behave somewhere between a hinge and simple support, roughly acting as a spring in series with the stiffness of the shell. Simple-support results are included in Appendix B for comparison to the experimental results. The simple-support results are generated using an asymmetric mesh (10x6 / 10x5) in Figure 4.29 and Appendix B. Note that symmetric and asymmetric mesh results using the simple-support condition are identical, *i.e.*, bifurcation does not occur. These analyses show that the hinged and simple-support analyses generally bound the behavior as expected. Detailed comparisons of the numerical predictions with the experimental data are given in Reference [83].

A second plausible explanation for more compliant experimental results is that specifics of the contact between the indenter and the shell needs consideration. Contact modeling of shell structures with typical indentation laws for composites have been used, *e.g.*, [84], but other work has indicated that those laws are valid only for a very small region of initial loading of the shell [18]. These contact models act as a nonlinear spring in series with the shell which would reduce the measured structural stiffness in load-deflection plots. In general, contact also acts to soften the structural response by acting as a nonlinear spring in series with the elastic structural response (and the elastic response of the boundary condition). Damage formation will also act to soften the measured structural response. However, only one specimen,

$R_6S_3T_3$, was damaged during testing. Thus, damage did not affect the response of any of the specimens presented in this chapter. Lastly, the models do not include transverse shear in the finite element formulation. While the shells considered in this work are relatively thin, transverse shear may need to be included in the analysis near the point of load introduction, particularly for thicker (T_2 and T_3) specimens. As with the other mechanisms described in this section, inclusion of transverse shear will also tend to make the response more compliant, *e.g.*, [64].

4.5 Summary

Finite element modeling techniques for analyzing composite shells under transverse loading, including bifurcation response, have been presented in this chapter. A technique (AMT) for inducing bifurcation which involves asymmetric meshing has been verified and validated *vis-a-vis* a benchmark problem and comparison with composite shell data. The elastic models are in excellent agreement with other techniques for evaluating bifurcation and the experimental data. The technique enabled all tested specimens from previous work to be analyzed and the bifurcation response, if it exists, to be identified (all results in Appendix B). Unlike the standard techniques, the tangent stiffness matrix does not need to be monitored nor is it necessary to initiate a branch switch – the bifurcation point and postbuckling path are found directly. In using this technique to induce bifurcation, care must be taken when refining the mesh, but it is immediately obvious when an asymmetric mesh finds the bifurcation path by comparison to the limit-point (symmetric mesh) response.

Experimental realities which are not considered in the idealized models, notably compliance of the test fixture, can contribute to a measured response which is more compliant than the predicted response. In cases where test

fixture compliance or contact behavior is important, the models will require additional complexity such as contact elements or Lagrange constraints. However, the basic scheme for the AMT modeling will not change.

Overall, predictive capabilities, particularly with regard to bifurcation, of the models and the AMT have been demonstrated within assumptions of the models.

CHAPTER 5

EXPERIMENTS

Experimental procedures followed in this research are presented in this chapter. The specimen manufacturing process, test fixture, and methods for damage characterization are covered in detail. Results from specimen surveys used to evaluate manufacturing procedures are also presented.

5.1 Manufacturing Procedures

The manufacturing procedure for composite shells is outlined in this section and roughly follows standard TELAC procedures [85]. An assessment of specimen quality is given in section 5.2. As for plates, the manufacture of shells consists of layup, placement on molds, curing, postcuring, and final specimen preparation.

5.1.1 Graphite/Epoxy Prepreg Layup

The AS4/3501-6 material is received in pre-impregnated (prepreg) form on a 1.524 m (5 foot) wide roll and subsequently cut into 305 mm (12") wide rolls for use in laminate manufacture. The AS4/3501-6 prepreg is a net-resin material system with an uncured areal weight of 149 g/m^2 and 36% resin content. Nominal cured ply thickness is 0.134 mm. To begin laminate manufacture, the prepreg tape material is removed from freezer storage and allowed to warm up in the sealed storage bag for a minimum of 45 minutes. Removal in this fashion prevents moisture in the ambient air from condensing

on the cold prepreg.

Plies are cut with a utility-knife utilizing Teflon-covered templates manufactured previously for use in TELAC. The templates are used to form plies with matrix, but not fiber (discontinuous fibers), joints. Plies are cut such that a 343 mm by 330 mm (13.5" x 13") laminate can be created. The individual plies are then put together to form a flat laminate. To complete the layup process, the laminates are sandwiched between two layers of peel-ply (Teflon fabric) release cloth.

5.1.2 Curing

The preparation for curing of composite shells does not have a standardized manufacturing procedure, but previous work [18, 21] in TELAC with shells has yielded an acceptable procedure which is described here. Cylindrical molds are constructed from 6061 aluminum and consist of bulkheads, a baseplate, topsheet, and clamping bars. The entire mold assembly is depicted in Figure 5.1. Five 9.53 mm (3/8") thick bulkheads, each having a radius of 1.829 m (72"), are used with a 9.53 mm (3/8") thick, 737 mm by 838 mm (29" x 33") baseplate. The bulkheads (from previous work [21]) are bolted onto the baseplate 178 mm (7") apart to form a frame. Two 6061 aluminum sheets, 0.794 mm (1/32") thick, are then placed over the bulkheads and clamped to the baseplates using two clamping bars. Two topsheets, rather than a single sheet [18, 21], are used to minimize the impression in the mold surface caused by the bulkheads when the clamping bars are tightened. The load from the bulkheads is dispersed by the lower topsheet before it is transferred to the upper topsheet. The upper topsheet acts as the actual mold surface for the composite. The lower topsheet is cut such that it exactly matches the arclength of the bulkheads. The clamping bars are 737 mm long,

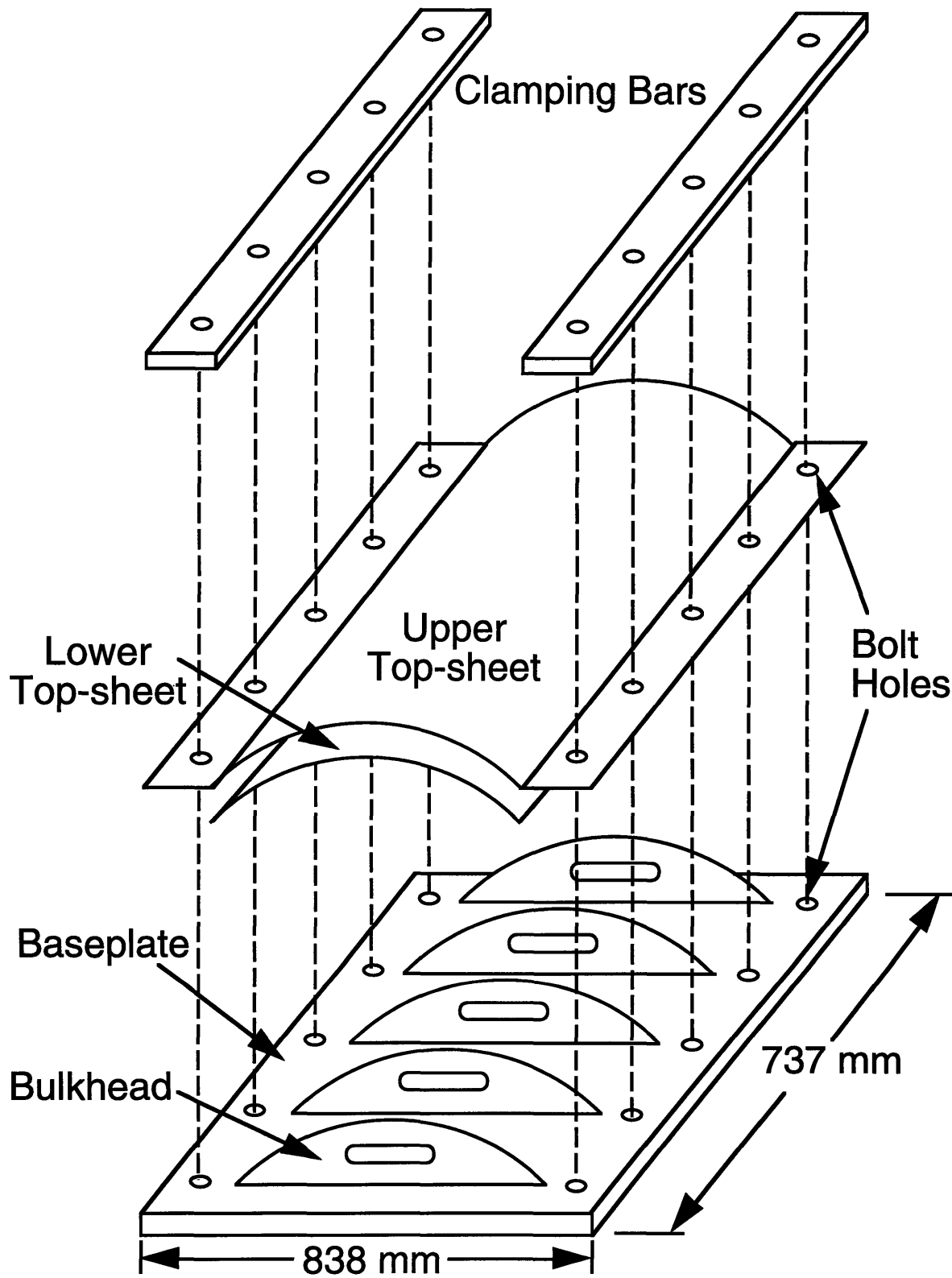


Figure 5.1 Illustration of cylindrical mold.

102 mm wide, and 9.53 mm thick (29" x 4" x 3/8"). Five 6.37 mm (1/4") bolts aligned with the bulkheads are used to tighten down each clamping bar until the topsheets conform to the bulkheads thus forming a cylindrical mold surface. Prior to assembling the molds, it was found helpful to bend the upper topsheet, using a sheet metal forming tool, at the sharp juncture where the bulkheads and baseplate meet. The bulkheads have center cutouts which allow equal pressure on both sides of the mold (aluminum topsheet) during autoclave pressurization. This prevents collapse of the molds during curing.

The next step in the manufacturing process is to setup the laminates on the cure assembly. Small modifications to the standard TELAC cure preparation procedure for the AS4/3501-6 material system were necessitated by the curved geometry of the molds. The cure procedure is thus discussed in detail and the modifications noted. Two shells are manufactured during each cure cycle. Details of standard TELAC procedures for this material system can be found in [85] and supplement the description found in this section.

The mold surface (aluminum sheet) is carefully cleaned and then approximately 25.4 mm (1") of each shell edge is taped off. The uncovered section of the mold surface is then sprayed with Mold Wiz[®], a commercial mold release agent, prior to placement of cure materials. The mold release agent facilitates cleaning of the aluminum topsheets after curing. The tape is removed from the edges and guaranteed nonporous Teflon (GNPT) is flash-taped to the upper aluminum topsheet. The GNPT covers the cylindrical section of the mold leaving about 25.4 mm (1") of aluminum topsheet uncovered on all four edges. The uncovered portion of the topsheet is later used to attach the vacuum bag. Dams made from 25.4 mm (1") wide, 3.18 mm (1/8") thick cork tape are used to create an enclosure on the curved topsheet in which the laminates are placed. To align the laminates on the mold surface, a

T-square is used to lay down the first piece of cork tape in the center of the mold. This part of the enclosure separates the two shells on the mold and thus serves as a reference line for laminate placement. The peel-ply-covered laminates are placed on the mold and enclosed on the remaining three sides with cork tape. Two layers of cork tape are used so that the cork enclosures are higher than the assembled laminates and cure materials.

A cross-section of the cure assembly is illustrated in Figure 5.2. The peel-ply-covered laminates are conformed to the mold by hand on top of the GNPT and between the cork-dam enclosures. The laminates are covered with porous Teflon, and then nonporous Teflon as in Figure 5.2. Top-plates are placed over this configuration. Top-plates for plate specimens are normally 9.53 mm (3/8") thick aluminum plates. For the curved molds, a different approach was needed as in previous work [18, 21]. 6061-T6 aluminum sheets having the same planar dimensions as the specimens and thicknesses of 0.79 mm (1/32") are used as top-plates. The top-plates are placed over the laminates and flash-taped to the cork dams in the circumferential direction to remain fixed until vacuum is pulled. A second layer of GNPT is placed over the entire cure assembly to prevent excess resin from reaching the breather material and vacuum port. Fiberglass air breather is placed over the GNPT to allow a vacuum to be pulled over both laminates. After all cure materials are on the mold, vacuum bag material is vacuum-taped over the entire cure assembly and a vacuum port with rubber gasket installed in a slit cut in the bag. The vacuum is usually pulled through a port cut in the cure plate (mold) when plate specimens are manufactured. This completes the cure assembly.

The cure and postcure cycles are standard for this material system and details can again be found in [85]. Laminates are processed using the standard manufacturer's cure cycle, illustrated in Figure 5.3, of a one-hour flow stage at

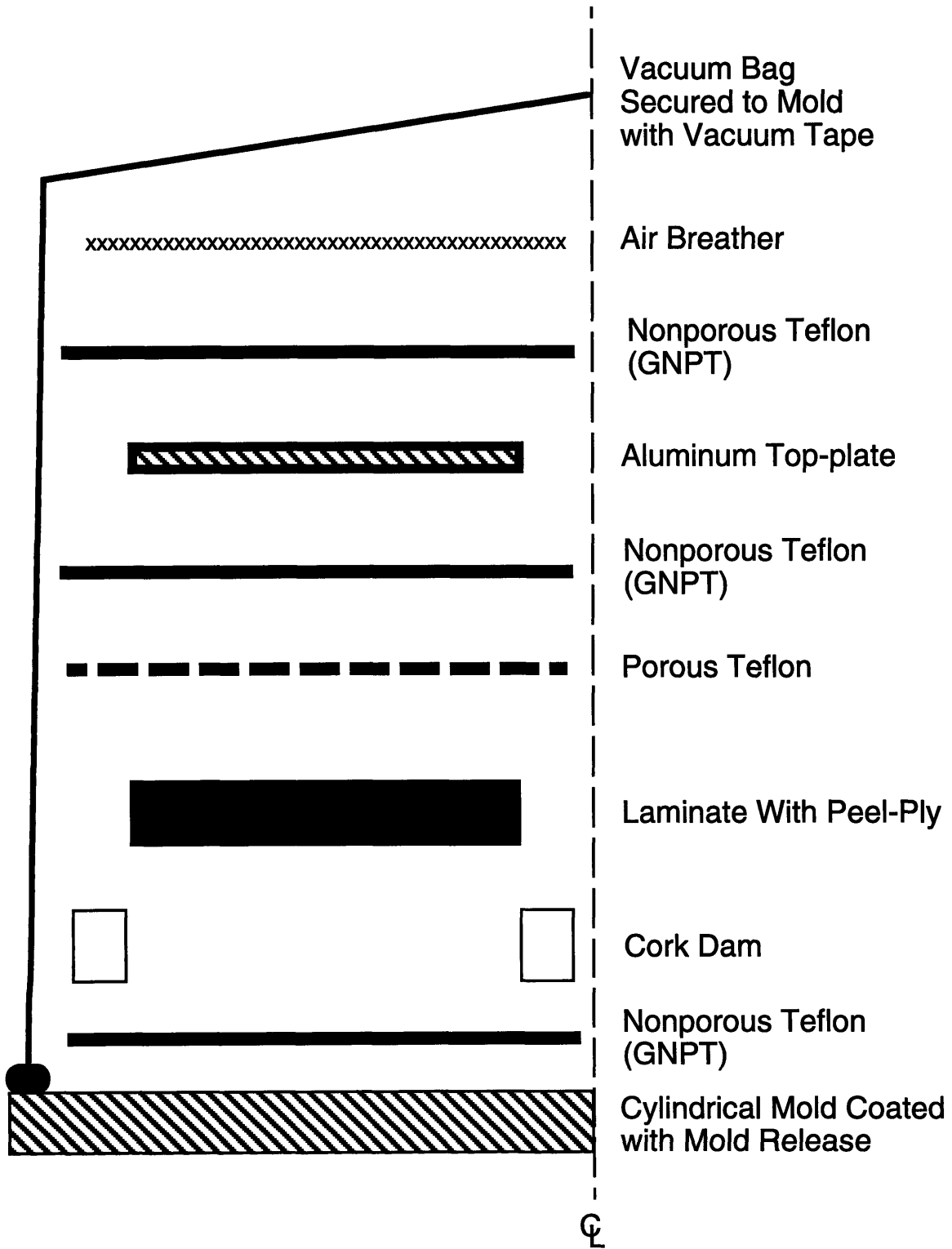


Figure 5.2 Cure assembly.

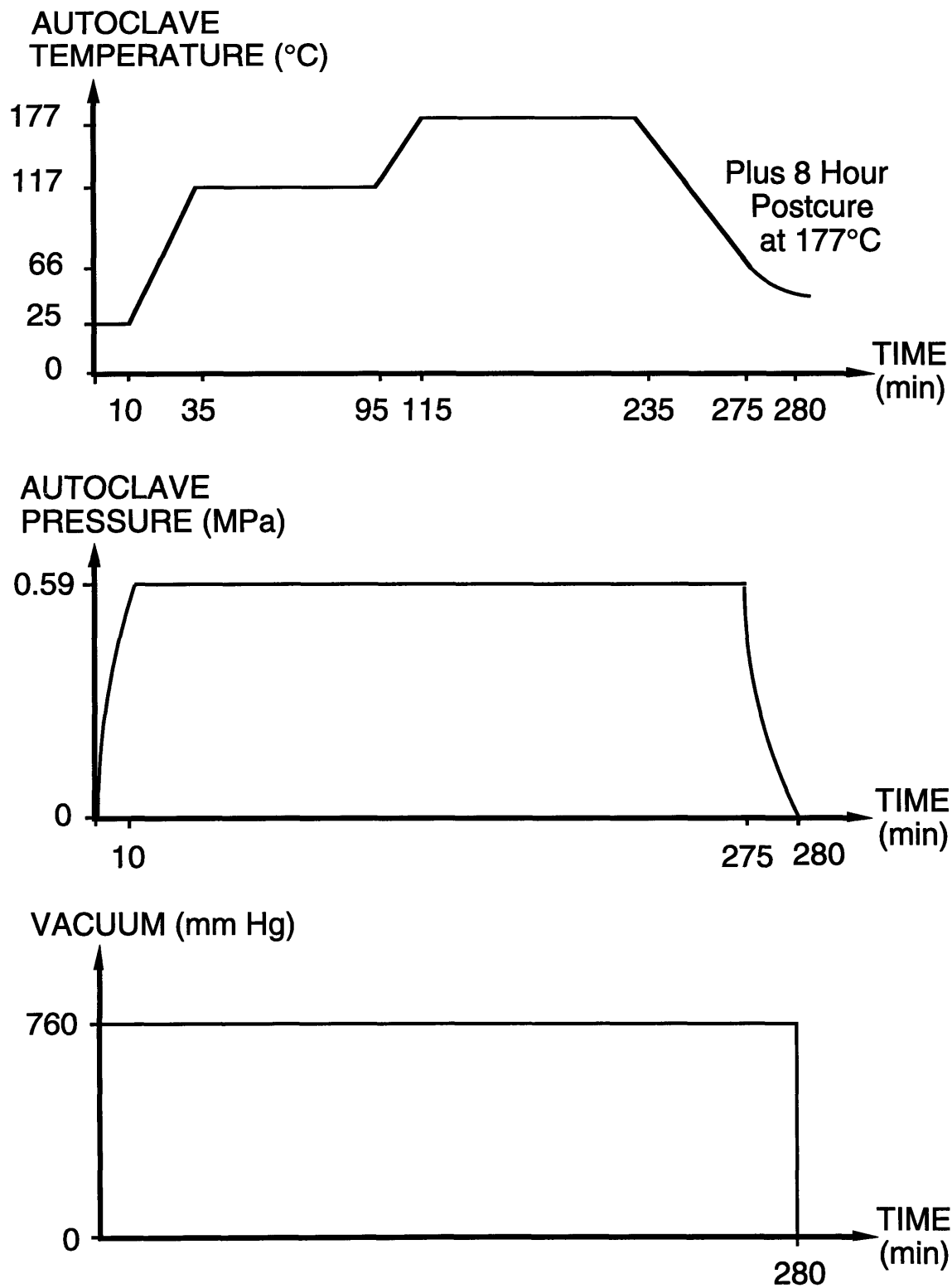


Figure 5.3 Nominal temperature, pressure, and vacuum profiles for cure cycle.

116°C and a two-hour set stage at 177°C. This was conducted in an autoclave under vacuum with 0.59 MPa external pressure. Laminates were postcured in an oven at 177°C for eight hours.

5.1.3 Final Specimen Preparation

Plate specimens are typically cut to the appropriate size for testing or to remove 'ridges' from epoxy and fiber washout. This is done using a water-cooled, diamond-grit cutting wheel mounted on a milling machine. The 220 grit, 1.52 mm (0.060") thick, 254 mm (10") diameter cutting wheel spins at 1100 rpm. Specimens are fed into the wheel at 4.7 mm/s (11"/minute). This same basic procedure is used for shells. Each shell is supported during trimming by a thick (2.412 mm) graphite/epoxy shell which was previously manufactured and has the same nominal dimensions as those being trimmed. All shells were trimmed to yield 305 mm (span direction) by 314 mm wide (12" x 12 3/8") specimens for testing. The span dimension refers to a straight line between the shell boundary conditions, *i.e.*, not the arclength, as in Figure 3.1. Specimen dimensions are maintained within 0.25 mm (0.01") of the nominal values.

Deflection measurements require the black composite shells to be painted white on the concave side for compatibility with the laser displacement transducer used. Shells are placed on an axial edge and painted with Krylon flat-white spray paint (as in [21]). The can of spray paint is held approximately 305 mm (6") from the shell and swept from side to side with each pass appropriately overlapping the previous pass. If necessary, specimens were painted twice in this manner to adequately cover the shell.

5.2 Curvature and Thickness Mapping

In this work, cylindrical shell specimens are characterized by radius of curvature, twist, thickness, and planform dimensions. To evaluate the manufacturing process, mapping schemes were utilized to determine the radius, twist, and thickness of each shell. Planform dimensions were discussed in the previous section. Nine points on each shell were used to determine an average shell thickness. The approximate location of these nine points is illustrated in Figure 5.4 where the distances indicated refer to the shell surface. Thickness was measured before the shells were painted using a deep-throat micrometer with a resolution of 0.01 mm.

A heuristic, developed previously [18], was used to calculate the curvature at three locations along the axis of the shell and the twist along the axial and circumferential directions using distance measurements made from a reference plane. The heuristic is reviewed here to include the use of a noncontacting laser transducer in place of the (previously used) linearly variable differential transformer (LVDT) contacting displacement transducer. No panel deflection is induced by the noncontacting laser which eliminates one source of error in the previous curvature measurement heuristic. Shells are placed on an axial edge and lightly held in a vise which is mounted on a milling machine table with a digital traverse. Resolution on the digital traverse is 13 μm (0.0005"). A laser displacement transducer with a spot diameter of 1 mm is mounted in the milling machine head to measure shell depth. The traverse motion is perpendicular to the laser beam as depicted in Figure 5.5. The Keyence LB-11/70 transducer has a resolution of 10 μm in the range of 60 mm to 140 mm. Using simple geometric considerations, the curvature at a station (y -location) of a shell can be calculated by measuring the x - and z - location of

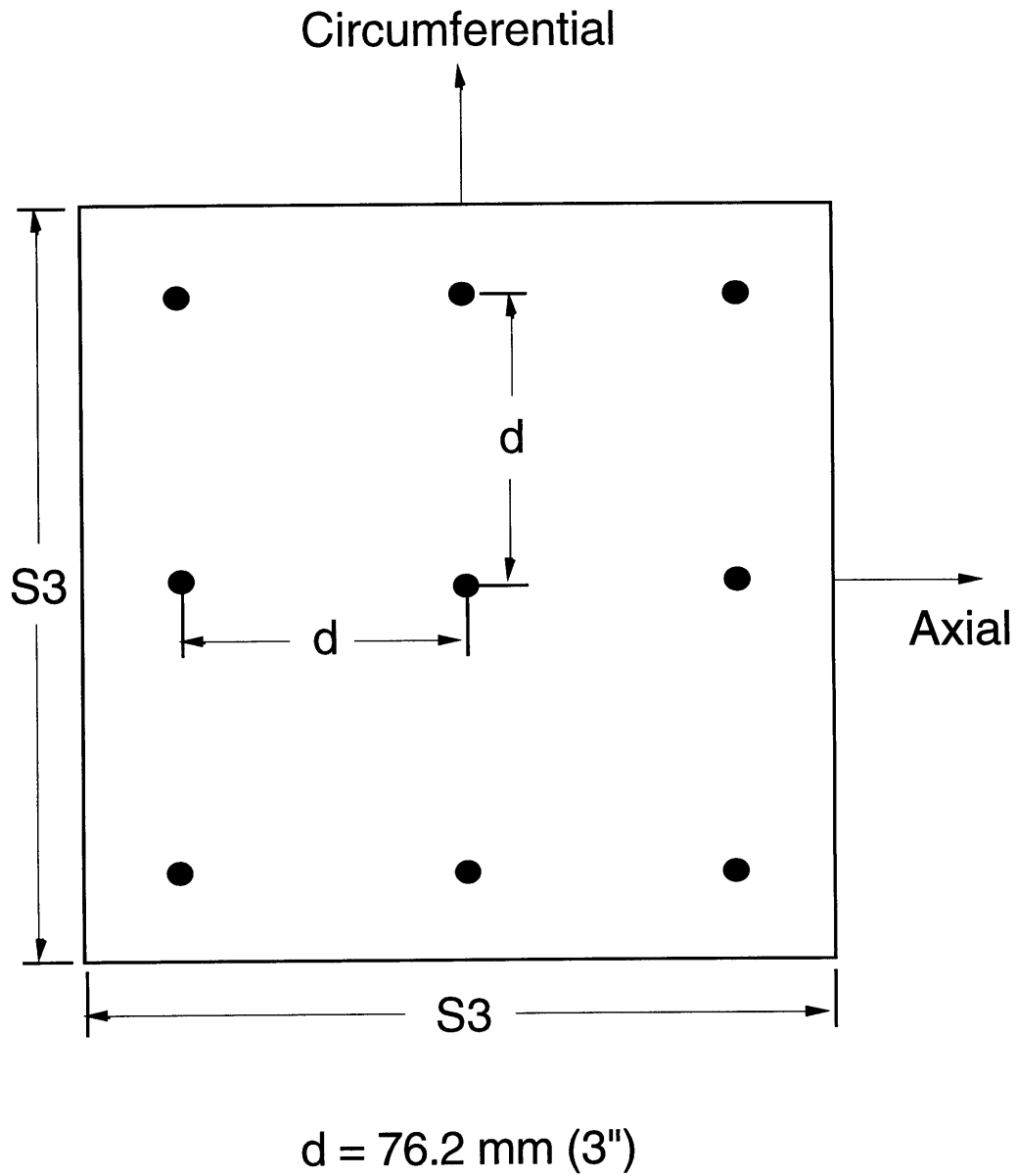


Figure 5.4 Locations used for mapping shell thickness.

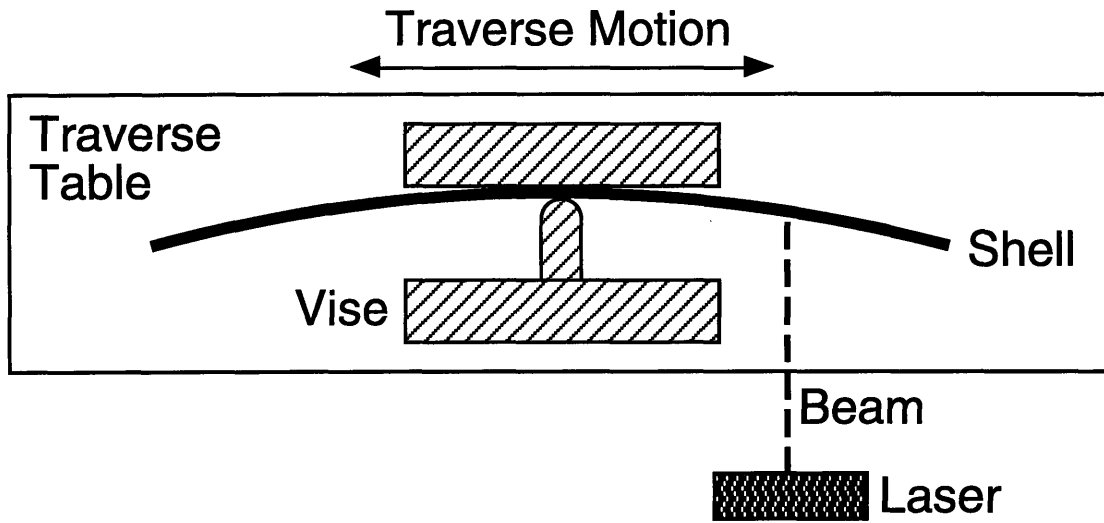


Figure 5.5 Illustration of overhead view of curvature measuring setup.

three points on the shell (see Figure 5.6). The x - and z - locations are given by the digital traverse and laser, respectively.

Using Figure 5.6, radii are calculated with equation 5.1:

$$R_i = \frac{\left(\frac{x_i}{2}\right)^2 + (z_{ic} - z_i)^2}{2(z_{ic} - z_i)}; \quad i = 1, 2, 3 \quad (5.1)$$

where R_i is the radius at y -location i . The distance x_i changes at each y -location either because the shell is twisting or because the radius changes between each y -station. The origin for all measurements is chosen near the circumferential edge along the first y -station as indicated in the upper right of Figure 5.6. There are three y -locations (y_1 , y_2 , and y_3 in Figure 5.6) where measurements are taken for each shell. The three y -locations are marked on the white shell surface with a ruler. The three points at each y -location are measured in the following way, using y_1 as an example: the origin is defined as

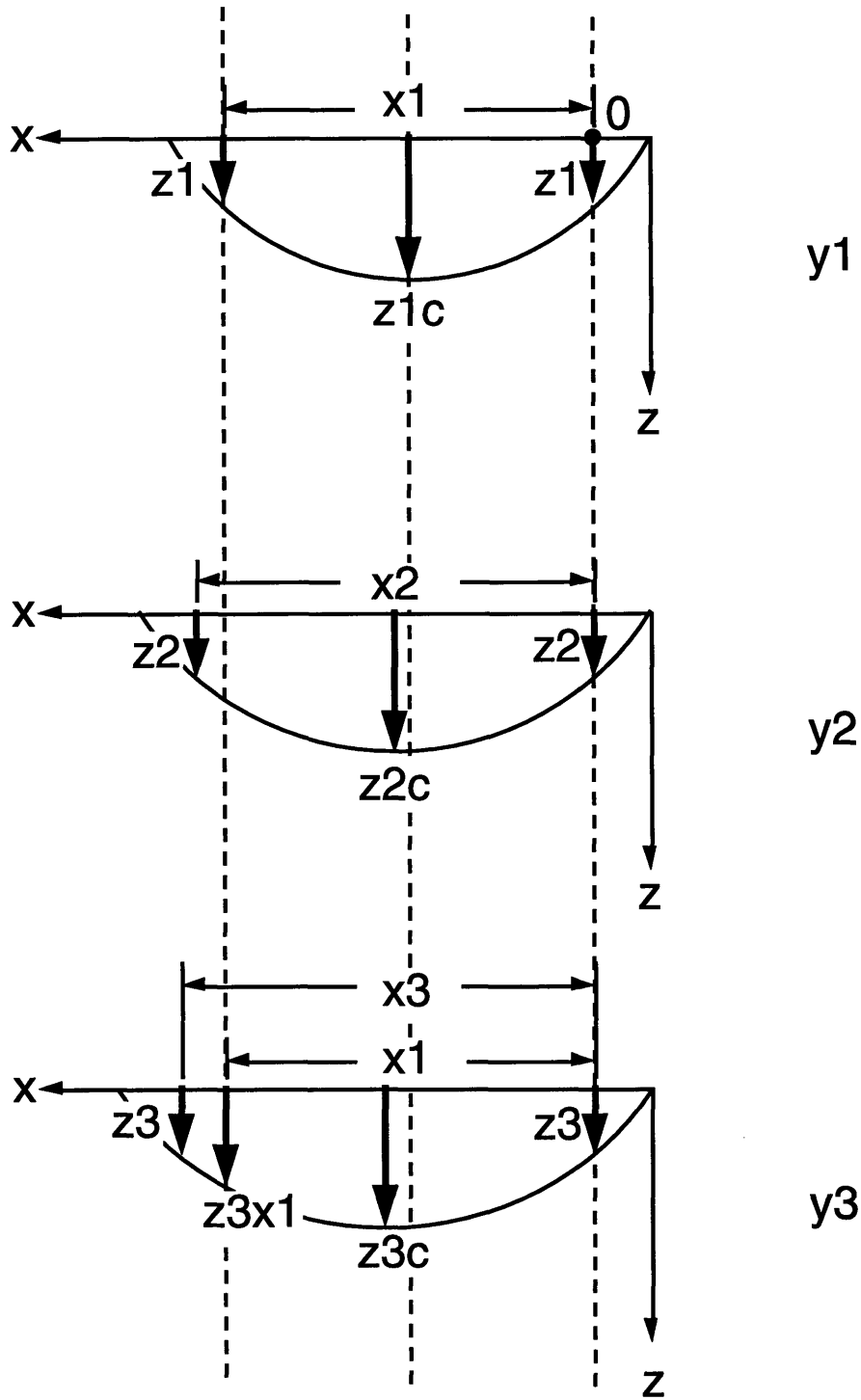


Figure 5.6 Measurements and associated locations used in radii and twist calculations.

above and the distance (x_1) across the shell to an equivalent depth (z -direction) is measured. This determines a straight line across the shell that is level with the milling machine table and traverse. The height (z_{1c}) at the midpoint of the line is measured next completing all the necessary measurements to calculate the radius at the first y -location. The same procedure is followed at stations y_2 and y_3 where the x - location of the starting point is kept constant (equal to 0). The distance between y -stations is equal to the distance d in Figure 5.4. As an example, the radius increases at each y -location in Figure 5.6 to illustrate how the radius can vary.

The twist of each shell can also be calculated about the x - and y -axes given in Figure 5.6. The straight line defined at y_1 , and the straight line between the y_1 and y_3 stations are useful for calculating axial and spanwise twist, respectively. As an example, at the third y -location (y_3) the change in height ($z_{3x1} - z_3$) of the line defined at y_1 can be used to calculate the twist of the shell along the y -axis. This change in height indicates the rotation of the straight line about the y -axis (axial twist). A similar change in height can be defined to calculate twist about the x -axis. Therefore, spanwise and axial twist are given by equations 5.2 and 5.3, respectively:

$$\gamma = \tan^{-1} \left(\frac{z_{3x1} - z_1}{x_1} \right) \quad (5.2)$$

and

$$\beta = \tan^{-1} \left(\frac{z_{3x1} - z_3}{y_3 - y_1} \right) \quad (5.3)$$

where γ is the spanwise twist and β is the axial twist, in radians. The height at x_1 at the third y -location, designated as z_{3x1} , is used to calculate both twist metrics.

For each nominal value of radius and thickness, the average and

coefficient of variation over all test specimens was calculated and is given in Table 5.1. Detailed information on the radius and thickness measurements for each specimen is given in Appendix A. Nominal values for radius and thickness, as well as the percent difference of the average radius and thickness from the nominal values, are also given in Table 5.1.

The manufacturing data in Table 5.1 indicates that the manufacturing process utilized in this research is adequate. Average thickness values are all within 3% of nominal values with acceptable coefficients of variation (less than 4%). The average radius of curvature is within 7% of the nominal (desired) value with an acceptable coefficient of variation. All twist angles are below 1° and are considered negligible. The average twists, gamma and beta, are -0.01° and -0.06° respectively.

5.3 Test Fixture (Boundary Conditions)

The boundary conditions for testing, as described in chapters 3 and 4, are pinned/no in-plane sliding (hinged) on the circumferential edges and simply-supported (with in-plane sliding) on the axial edges. A specially designed test

Table 5.1 Results of Thickness and Curvature Mapping

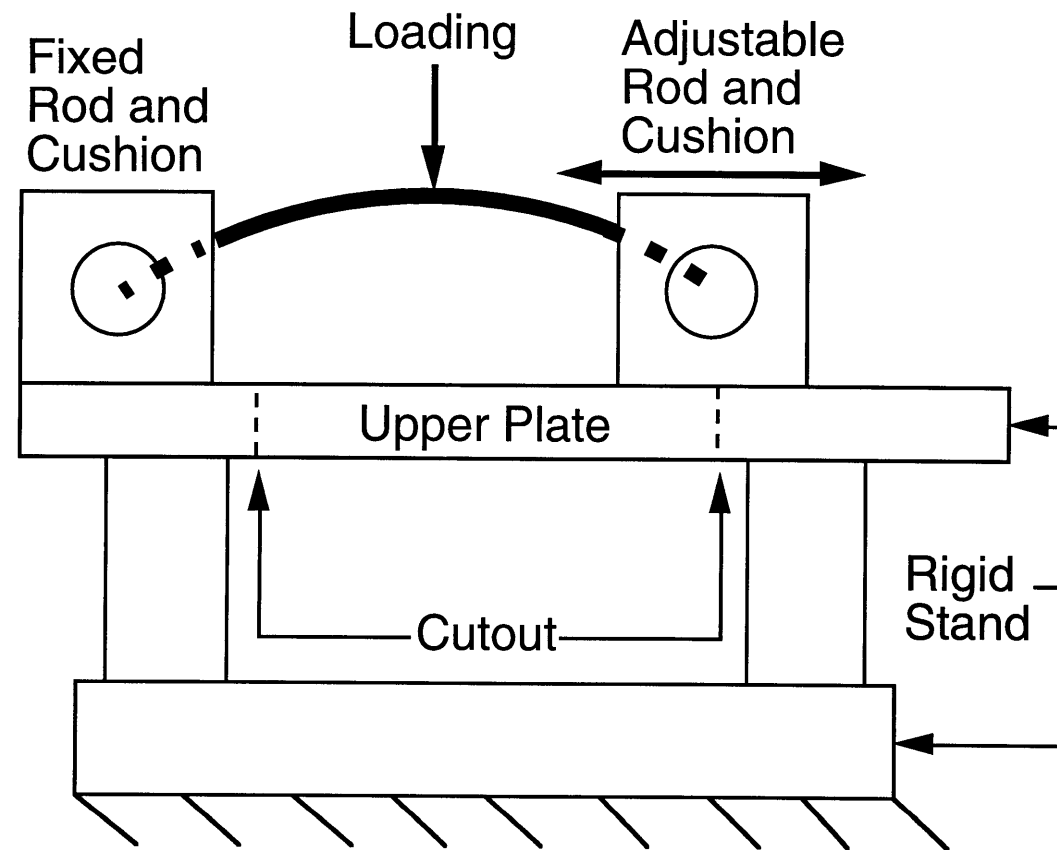
Metric	Average	C. V. ^a	Nominal	Difference
T_1	0.829 mm	1.2 %	0.804 mm	+ 3.1 %
T_2	1.580 mm	3.7 %	1.608 mm	-1.7 %
T_3	2.414 mm	3.4 %	2.412 mm	+0.1 %
R_{12}	1954 mm	4.0 %	1829 mm	+6.8 %

^a Indicates coefficient of variation.

fixture [18, 21] was modified for use in this work, preserving many of the essential features. The original test fixture allowed free axial shell edges and thus was modified to achieve the simply-supported/in-plane sliding condition on the circumferential edges desired in this work.

A side-view illustration of the original test fixture is shown in Figure 5.7. The convex shell is loaded in the center and restrained on the circumferential edges by the rod/cushion assemblies. Although not necessary in this work, the rods can be rotated in the cushions prior to testing to accept different shell geometries before being fixed in place with clamps and 12.7 mm (1/2") diameter threaded steel rods, as shown in Figure 5.8. The cushions mount to the upper plate of the rigid test stand and provide a continuous support for the rods. The two rod/cushion assemblies are mounted on the upper plate, one being fixed and the second being adjustable in the spanwise direction (see Figure 5.7). The upper plate of the rigid stand has a 318 mm (axial dimension) by 292 mm (12.5" x 11.5") cutout in its center to allow for shell buckling into an inverted configuration as well as deflection measurements. The circumferential shell edges rest in grooved inserts which are bolted to the rods, as illustrated in Figure 5.9 [21]. The groove in the steel inserts has a radius of 1.59 mm (1/16") which allows rotation at this boundary. A consequence of this design is the inability to resist "pull-out" of the shell after the shell instability. In this loading region the shell experiences tensile membrane forces in the circumferential direction. However, as discussed in chapter 3, the response of interest in this work occurs before pull-out.

Modifications to the test fixture were necessary to restrain the axial edges of the shell specimens. The boundary condition is achieved using upper and lower axial supports with 'knife' edges which support the axial shell edges on 4.76 mm (3/16") radius rounded corners as illustrated in Figure 5.10. One



NOTE: Not to scale

Figure 5.7 Side-view illustration of original test fixture.

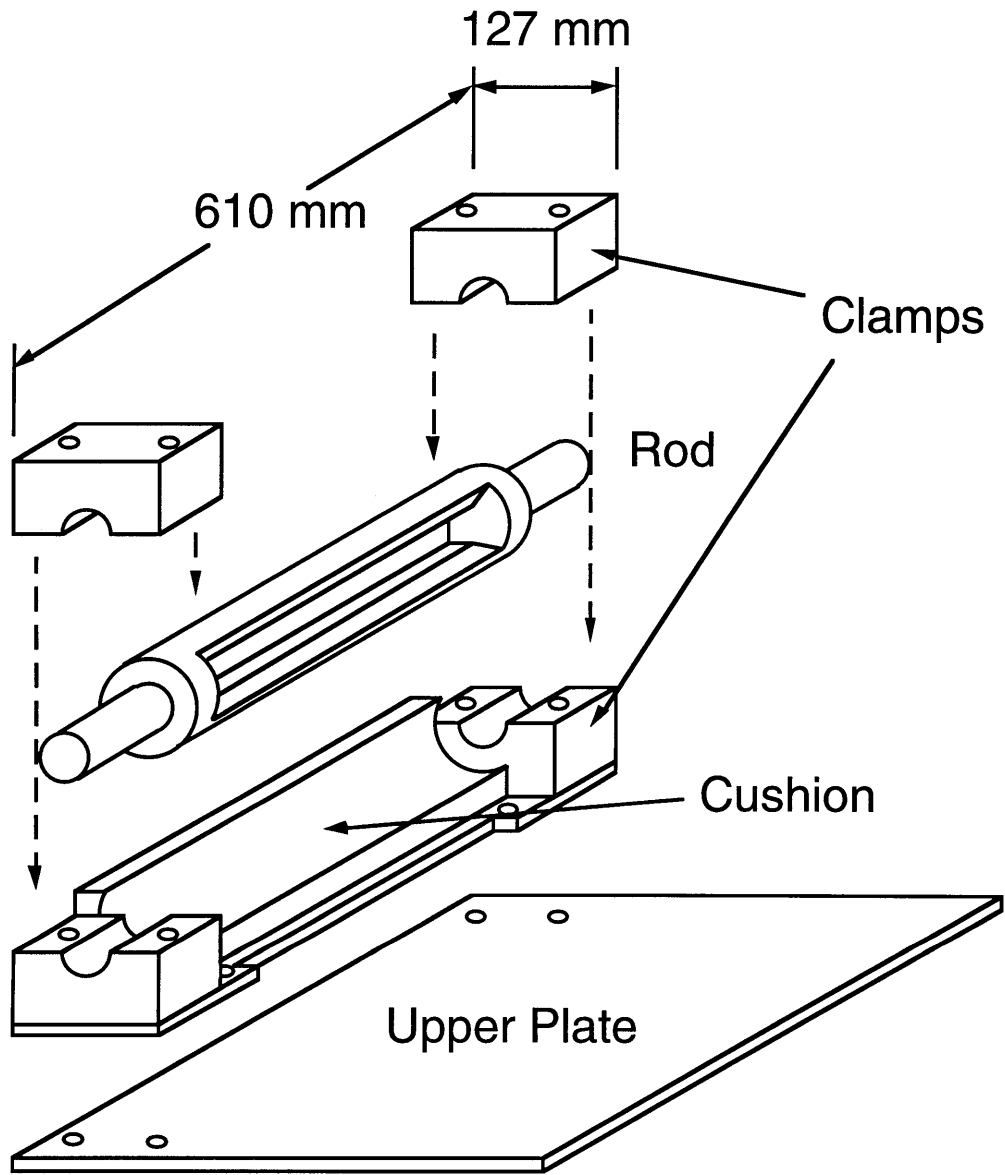


Figure 5.8 Illustration of rod/cushion assembly.

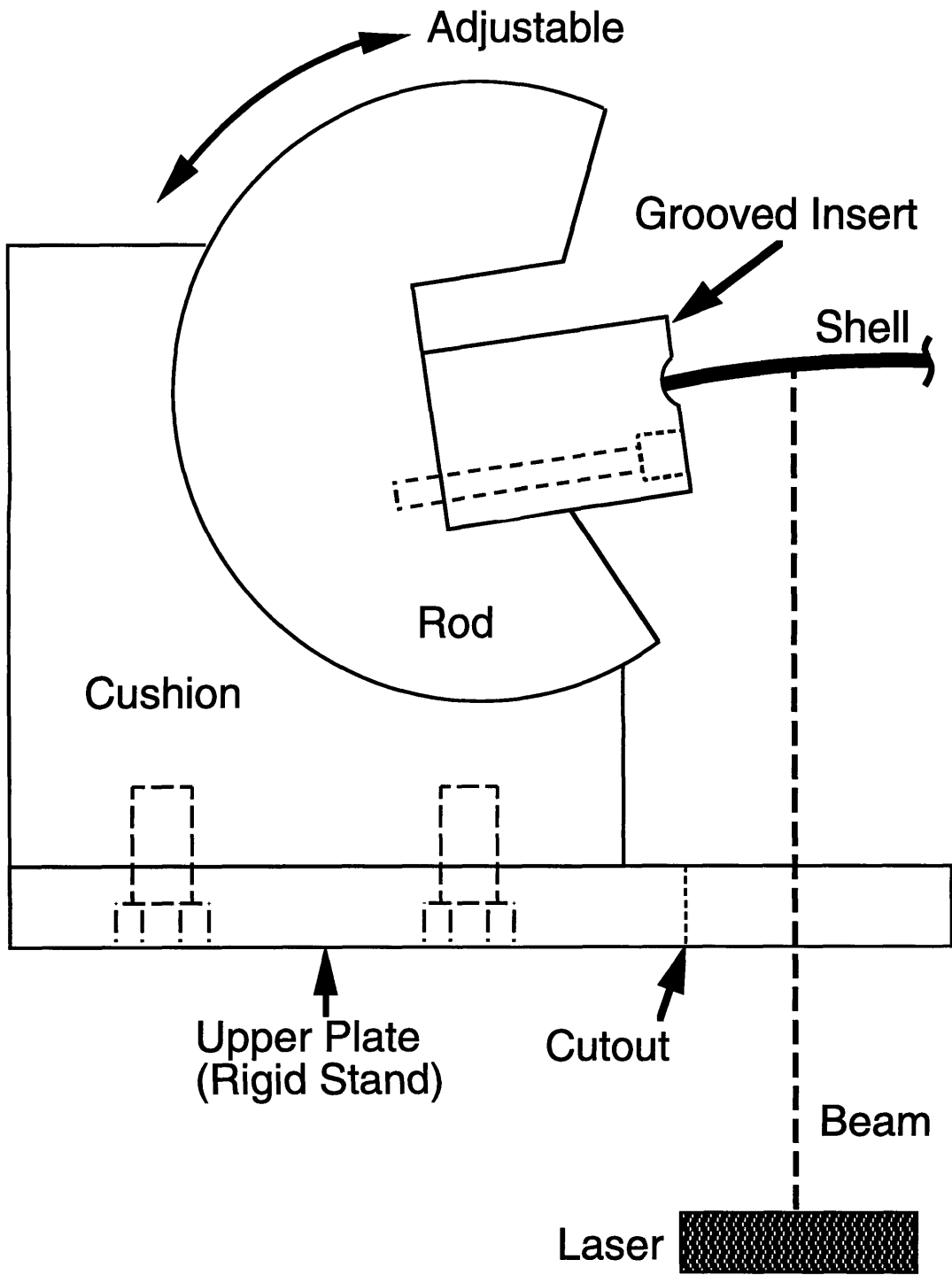
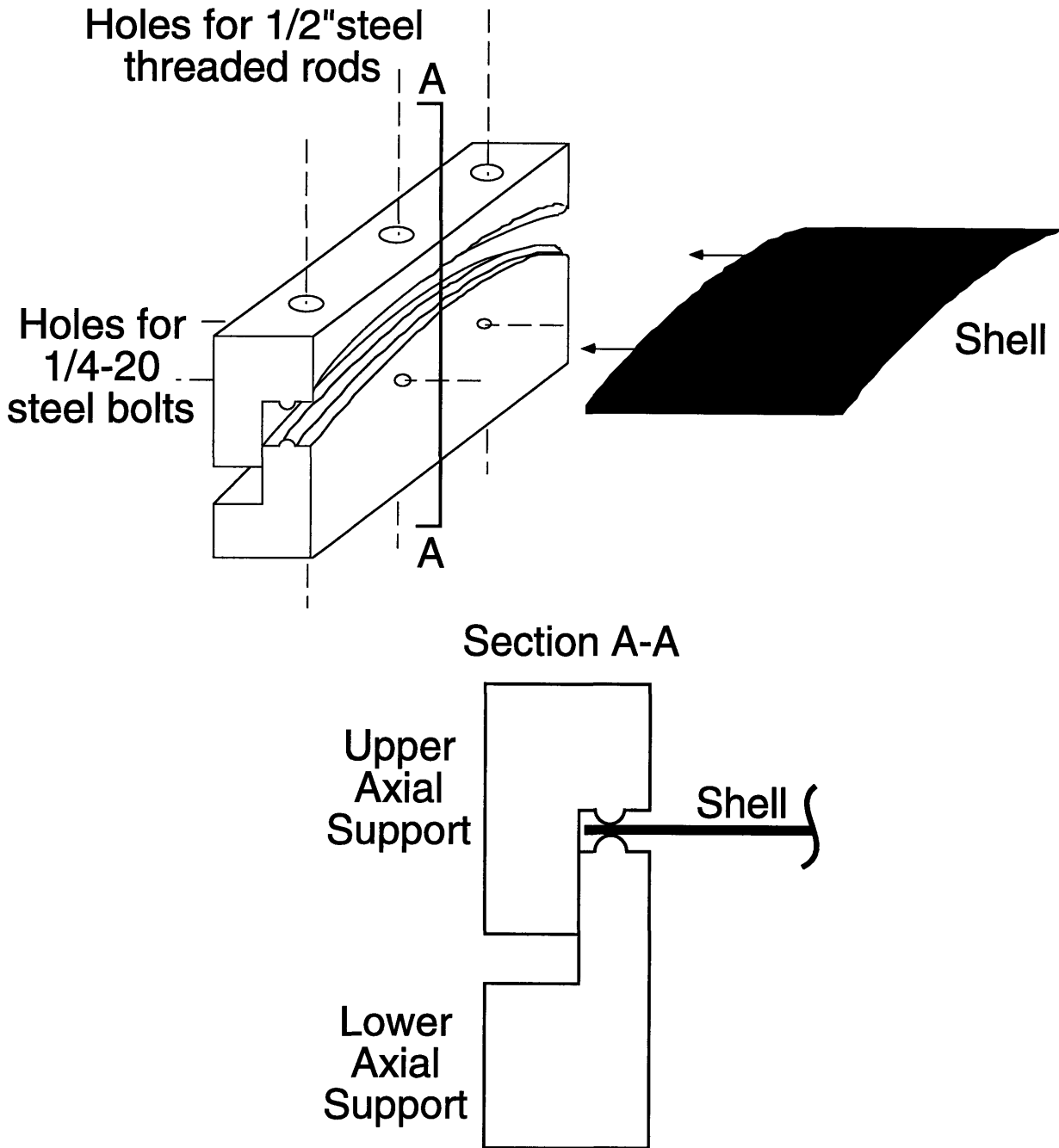


Figure 5.9 Illustration of laser operation and grooved insert in the rod-cushion assembly.



NOTE: Not to scale

Figure 5.10 Illustration of test fixture modification used to restrain axial shell edges.

set (of two) of 6061-T6 aluminum axial supports are shown schematically in Figures 5.11 and 5.12. The axial shell edge rests between the upper and lower knife-edge constraints so that transverse displacement is restricted but rotation and in-plane displacement are allowed.

Each lower axial support is mounted to the upper plate of the test fixture between the two rod/cushion assemblies (see Figure 5.7) using three 12.7 mm (1/2") diameter steel threaded rods. Each upper axial support is bolted to these same three steel rods and additionally restrained with two 1/4-20 steel bolts that attach to the lower axial support in the axial direction as in Figure 5.10. All tolerances on the upper and lower supports were maintained to ± 0.127 mm (± 0.005 "). The 4.76 mm (3/16") radius cut on the knife edge(s) was made using a radius tool and this dimension is considered exact.

Preliminary STAGS analysis of the worst-case loading for this work (T_3 shell, 2500 N loading, factor-of-safety of two on resulting axial edge load), coupled with a simple Hertzian contact law, predicts the deflection of the axial support to be less than 0.025 mm (1 mil). This deflection is small relative to the panel thicknesses and specimen deflection and is thus considered acceptable.

5.4 Testing Procedures

In this section, the experimental procedures used in the testing of the composite shells are described. General procedures associated with the test fixture (i.e. mounting the specimens) are reviewed before testing procedures, including deflection mode-shape evaluation, are described.

Two types of testing are conducted: overall loading response and mode-shape tests. The overall loading response tests are performed first to experimentally characterize the loading response over the entire regime of

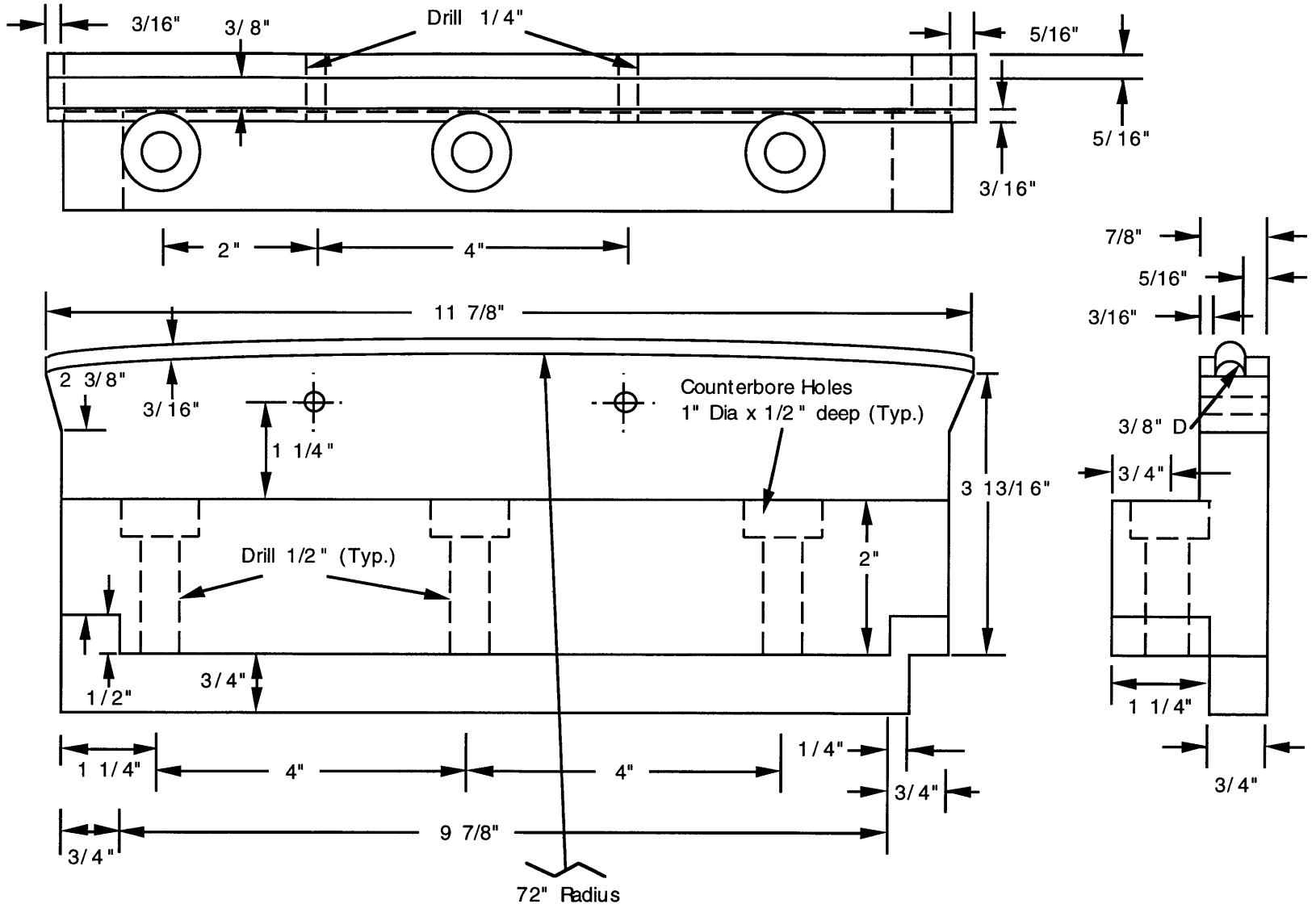


Figure 5.11 Three-view schematic (to scale) of lower support for axial shell edge. (Note: all dimensions in inches)

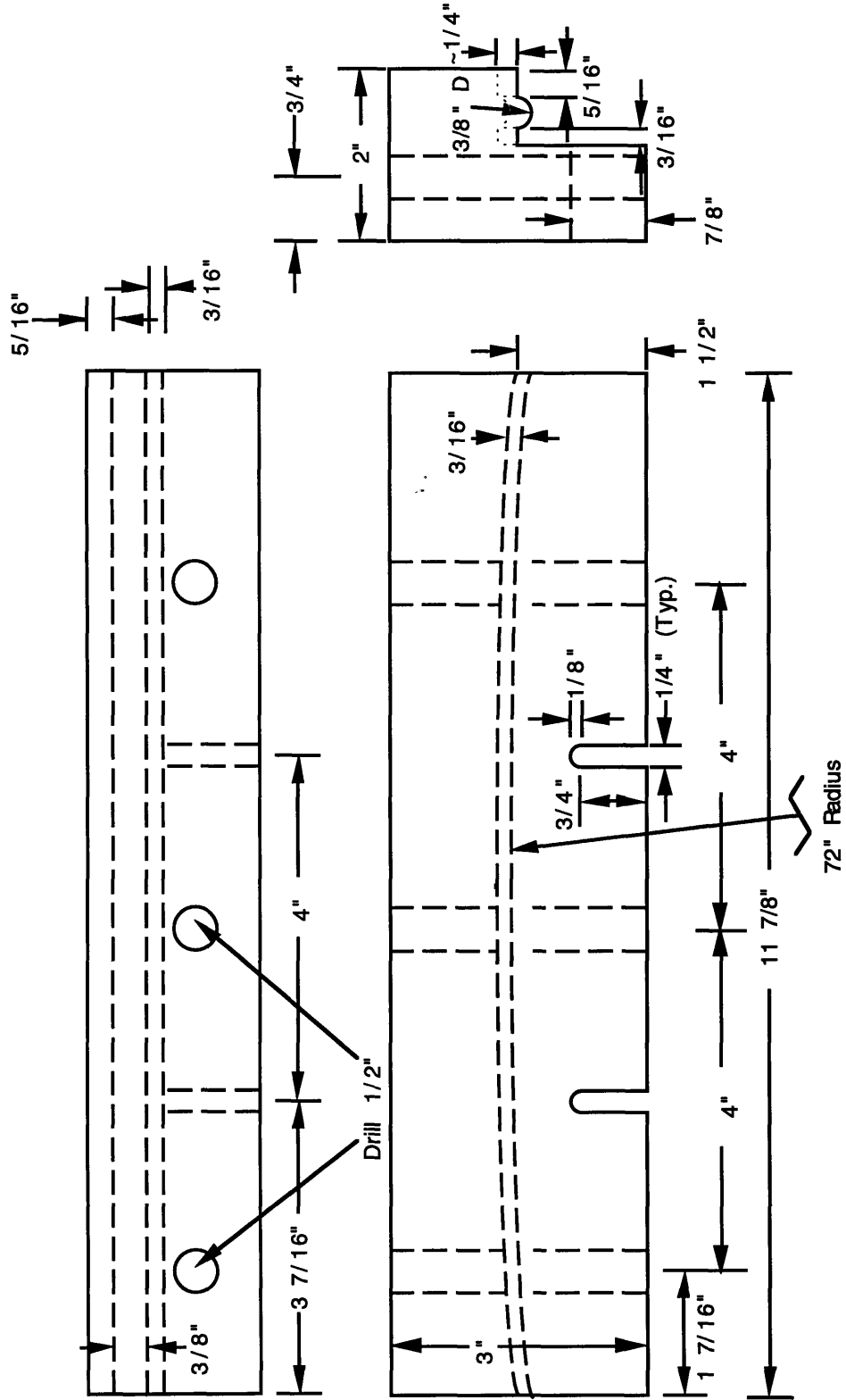


Figure 5.12 Three-view schematic (to scale) of upper support for axial shell edge. (Note: all dimensions in inches)

interest. The regime of interest includes all behavior until an instability is observed or until large-scale damage is observed. If an instability occurs during loading, the test is terminated because the test fixture is not able to restrain the circumferential shell edges during postbuckling. Instabilities are observed during testing by monitoring a real-time plot of load versus elapsed test time. As stroke increases linearly during the test, this is the same as observing a load-deflection plot. Instabilities are indicated by a gradual reduction in the slope of the load versus time plot until the load decreases. Large-scale damage formation, such as penetration, is to be avoided because of the interest in barely visible impact damage (BVID) as discussed previously. Damage formation is indicated by loud cracking and popping noises during testing as well as the formation of visible matrix cracks on the concave surface of the shell directly under the indenter. Mode-shape tests are performed to give deflection mode-shape evolutions during the buckling process. In these tests, stroke is held at predetermined positions so that mode shapes can be assessed. These positions are determined using the overall loading response data as discussed in chapter 3.

5.4.1 Specimen Set-up in Fixture

Specific procedures were maintained to consistently place each shell in the proper position for testing. First, both rods are rotated in the cushions so the shell, when put in place, will impinge perpendicular to the grooved steel insert as in Figure 5.9. The known nominal slope at the circumferential shell edge is matched to within ± 0.3 degrees using gradations marked on the outer surface of the rods. The fixed rod and cushion (see Figure 5.7) are then bolted to the upper plate. Next, the two lower axial supports are mounted 305 mm (12") apart on the upper plate of the test fixture with 12.7 mm (1/2") diameter

steel threaded rods. A T-square is used to ensure that the lower axial supports are perpendicular to the long direction of the steel insert in the fixed rod. The shell is placed so that it rests on the lower axial supports with a 4.76 mm (3/16") overhang on both axial sides. The shell (circumferential edge) also rests against the grooved insert of the fixed rod/cushion assembly.

The second rod/cushion assembly is spanwise adjustable (see Figure 5.7). This assembly is moved toward the shell in the spanwise direction until the shell impinges on the grooved insert of the second rod. The second rod/cushion assembly is carefully adjusted so that the shell is seen to make contact all along the length of the steel insert, thus ensuring proper adjustment (parallel) relative to the fixed rod/cushion. The adjustable rod/cushion assembly is fixed to the upper plate, again with 12.7 mm (1/2") diameter steel threaded rods. The shell is now supported on all edges but rests only lightly against the lower axial support knife edges.

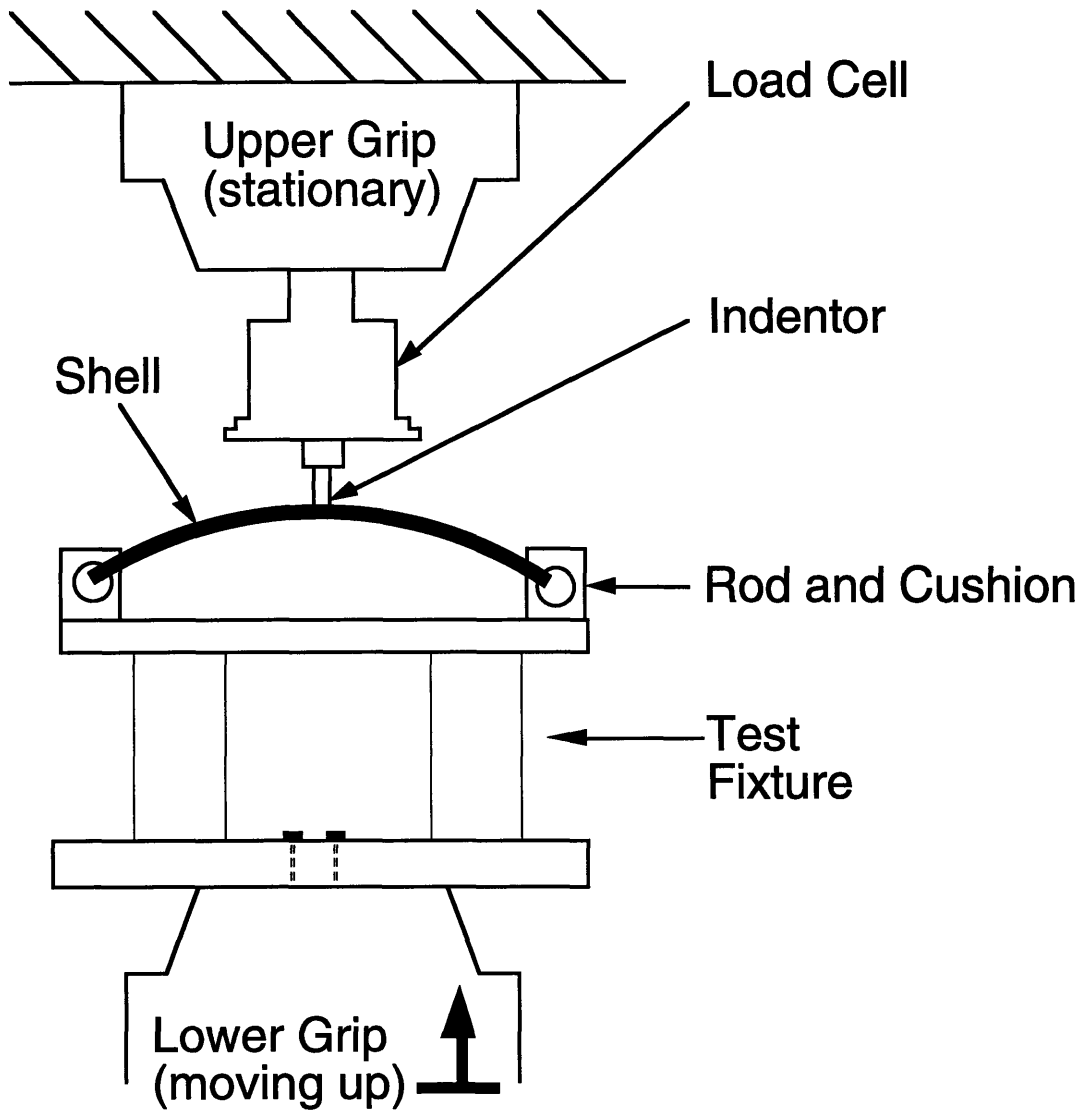
In the last step, the upper axial supports are placed on the three steel threaded rods extending up from each lower axial support. The shells, having radii which nearly match (see Table 5.1) the 1.829 m (72") radius machined on the axial supports, can be easily seated onto the lower axial supports. The shells are seated by moving the upper and lower knife edges (axial supports) together using the three bolts on top of each upper axial support. These bolts are tightened to 0.5 N-m using a torque wrench so that the shell makes intimate contact with the knife edges on both the upper and lower axial supports, thereby conforming the specimen to the 1.829 m radius of the axial boundary condition. The torque of 0.5 N-m was found to effectively seat all the shell types (thicknesses) in this investigation. The shell is now in contact with the upper and lower axial supports (axial boundary condition) along the entire axial boundary and impinges on the steel inserts of each rod (circumferential

boundary condition) as desired.

5.4.2 Quasi-static Testing and Mode-shape Measurement

Mounting of the shell in the test fixture has been described in the previous section. The next step before testing is to align the shell with the indenter. Before being mounted in the test fixture, masking tape is placed on the shell and the center of the shell marked with a 0.5 mm pen on both surfaces. The center marks on the top and bottom (concave side) of the shell are used later to align the indenter and laser, respectively. A cone-shaped center finder is used in place of the indenter to align the center of the shell directly under the indenter. Bolts which hold the test fixture to the lower crosshead are loosened and the test fixture adjusted so the shell is properly aligned with the indenter. Spanwise adjustment of the shell is accommodated by slots in the base of the test fixture. Adjustment in the axial direction, typically less than 1 mm, is accommodated because the bolt diameter is smaller than the width of the slots in the test fixture base. After aligning the shell with the indenter, the mounting bolts are again tightened. The center finder is replaced with the hemispherical indenter and the masking tape used to mark the shell center on the convex surface is removed.

All tests are run in stroke control on an MTS-810 uniaxial hydraulic testing machine with an Instron 8500+ digital controller. Stroke resolution on the controller is 10 μm . Shells are indented using a 12.7 mm (1/2") diameter hemispherical steel indenter. A PCB model 208A04 22240 N (5000 lb) force transducer with resolution of 0.09 N (0.02 lb) is mounted in series with the indenter in the upper grip of the test fixture. The upper grip is stationary during testing and the shell is pushed in stroke control into the indenter by the lower grip as shown in Figure 5.13. All data is acquired with LabVIEW



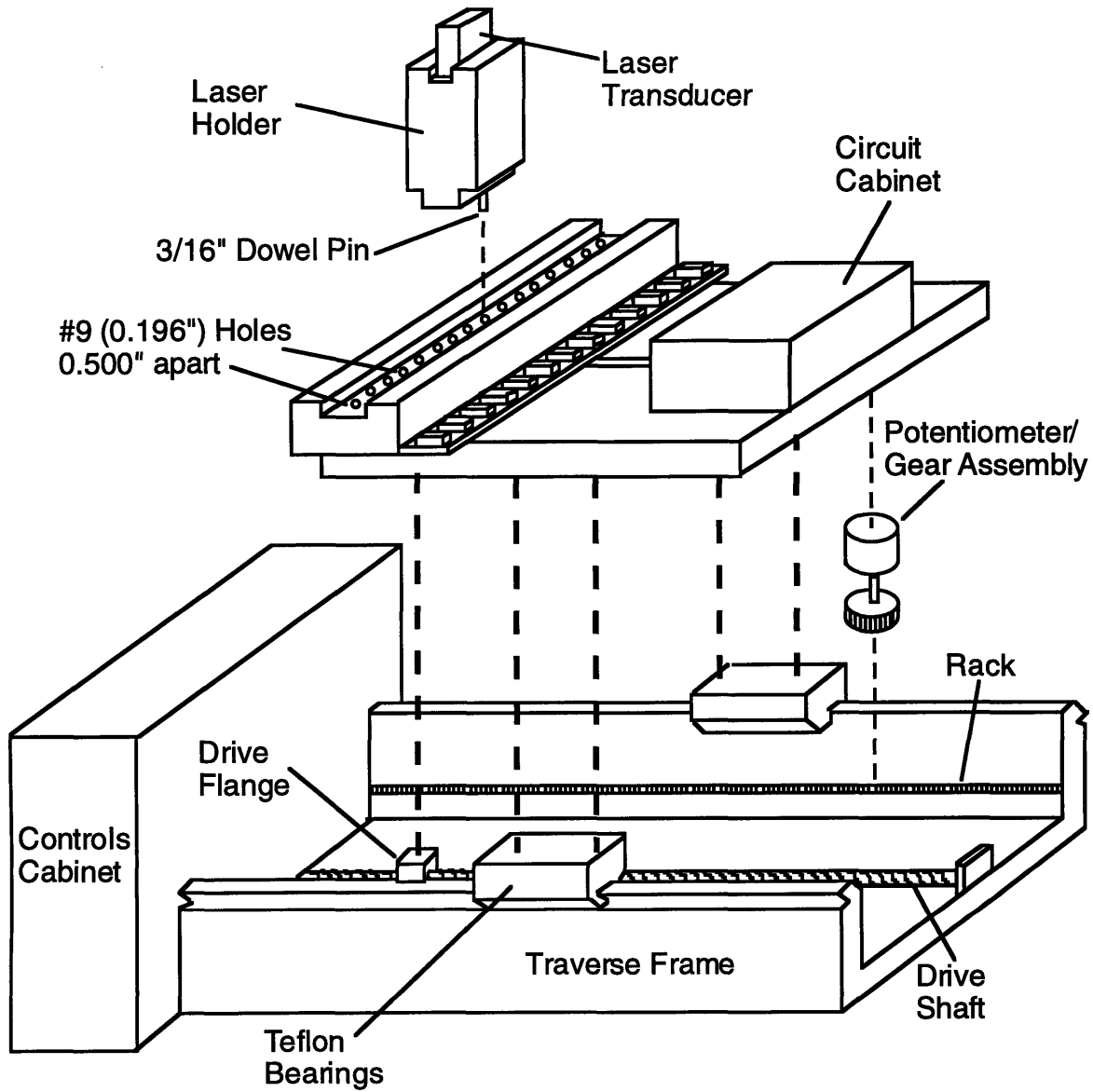
NOTE: Not to scale, axial support not pictured

Figure 5.13 Illustration of test fixture and shell mounted in testing machine.

software on a Power Macintosh computer via an A/D board. Discretization of the analog data by the A/D board limits the recorded load resolution to 0.27 N (0.06 lb) but does not limit the stroke resolution of 10 μm . Preliminary analysis of the specimen response indicates approximately 15 mm of deflection at the instability point. A stroke rate of 0.05 mm/s is used with a data (load and stroke) sampling rate of 1 Hz to allow the tests to proceed quasi-statically and the response to be adequately characterized. The chosen stroke rate allows 18 mm of deflection to be obtained in 6 minutes.

The same noncontacting laser transducer discussed in section 5.2 is used to survey shell deflection mode shapes during testing. The laser has a beam spot of 1 mm and resolution of 10 μm . The laser is mounted on a traverse assembly specifically designed to assess mode shapes during testing of shells [21]. The traverse assembly is mounted to the base of the test fixture such that the laser shines against the concave shell surface as in Figure 5.9. The laser/traverse assembly is designed such that the laser beam is perpendicular to the plane defined by the spanwise and axial directions (x - and y -directions in Figure 5.6), equivalent to being perpendicular to the upper plate in Figure 5.7. Prior to each test, but after the shell has been mounted in the fixture, the laser position is finely adjusted so that it is centered (axially) under the shell center. This is done by aligning the visible laser beam spot with the center of the shell. The masking tape used to mark the shell center is then removed.

The traverse, pictured in Figure 5.14, has continuous movement in the spanwise (shell) direction and discrete axial positions in 12.7 mm (1/2") intervals. Mode shapes were evaluated at three axial locations: along the axial centerline (directly under the indenter) and at 76.2 mm (3") on either side of the centerline. During testing, the mount for the laser, pictured in Figure 5.14, is



NOTE: Not to scale

NOTE: Not to scale

Figure 5.14 Deflection-measurement assembly.

manually moved between axial stations to take the three different mode shapes. The discrete axial location of the laser is known at all times but the spanwise position, being the direction of continuous movement, must be measured. This is done with a rack-and-pinion system connected to a potentiometer which provides a linearly varying voltage with spanwise position. Using the data acquisition system previously described, spanwise position is known within 0.5 mm and the shell height within 10 μm .

After the shell is mounted in the test fixture and the laser and indenter aligned with the shell center, testing is ready to begin. Before loading, the initial shape of the shell mounted in the fixture is assessed which defines the configuration of the unloaded shell. The test is begun by raising the lower crosshead (grip) which moves the test fixture, traverse, and specimen toward the stationary indenter. This is done by manually adjusting the stroke until a preload of not more than 1 N is seen. Stroke is then linearly increased at 0.05 mm/s until the test is either stopped manually (in the case of a loading response test) or automatically at a predetermined value of stroke (as in the case of a mode-shape test). Unloading occurs at the same stroke rate of 0.05 mm/s until the indenter loses contact with the specimen.

5.5 Damage Evaluation

All specimens were evaluated for damage after testing. Visual inspection of damage is undertaken directly after testing. On the convex surface, contact with the indenter typically leaves a smooth or shiny region with dimensions smaller than the indenter diameter. This is typical of previous indentation work with composite shells and has been characterized as a marred region [18]. On the concave surface, matrix cracks at the center of the shell in the 45° direction can be seen during and after testing. However, it is

unclear whether the cracks occur only in the white paint or are manifestations of actual matrix cracks in the bottom 45° ply.

Two further methods were used to evaluate damage: x-radiography and sectioning. Dye-penetrant enhanced x-radiography provides a view of the damage state, typically matrix cracks and delaminations, that is integrated through-thickness. After testing, a 0.79 mm (1/32") diameter hole is drilled through the thickness of the specimen at the center of the loading site. Flash tape is applied to the concave side of the specimen and a dye is injected with a syringe into the hole on the convex surface. The x-ray opaque penetrating dye is 1,4 Diiodobutane (DiB) which seeps into cracks and delaminations in the specimens through capillary action. A small excess bubble of DiB is maintained on the specimen for approximately half an hour. This allows the DiB to fully penetrate into the damaged region. The excess dye bubble and flash tape are removed and the specimen x-rayed. A Scanray® Torrex 150D X-ray Inspection System used in "TIMERAD" mode and 50 kV potential is used to x-ray the specimens with 260 mR (milliRoentgens) of radiation along with Polaroid Type 52 PolaPan film.

DiB soaked portions of the shell specimens show up as dark areas in the x-rays. A sample x-ray photograph showing a large delamination is provided in Figure 5.15. The x-ray photograph is of the damage state looking down at the convex side of the shell. The 0° direction in Figure 5.15 is along the vertical axis of the page (circumferential shell direction) and positive angles are taken counterclockwise from that axis. All x-ray photographs in this work maintain this orientation and are shown to scale. The large damage (delamination) axis is along the 45° ply in this particular figure. The small, light, circular region at the center of the x-ray in Figure 5.15 is the hole drilled through the center of the impact site to inject the penetrating dye. The large light region in the photo is

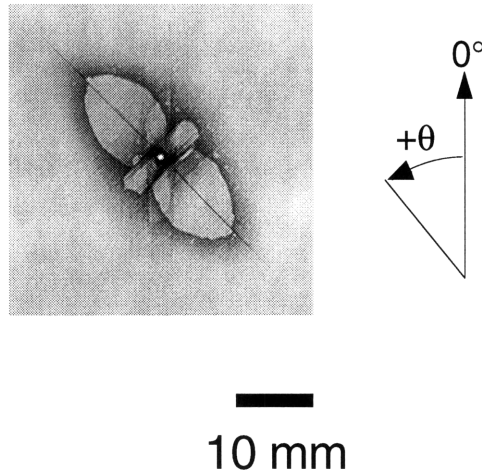


Figure 5.15 Sample planar x-ray picture showing damaged region.

characteristic of a delamination. In this photo, a larger delamination can be seen at 45° and a much smaller one at -45° . The dark line at 45° is a long matrix split in the ply on the concave side of the shell. Shorter matrix splits can also be seen at -45° and 0° . X-radiographs are a planar projection of a curved surface resulting in a smaller damage length in the photograph. This reduction in damage length is less than 0.2% in the circumferential direction (maximum effect) which is negligible.

Sectioning allows through-thickness damage details to be examined so that damage away from the loading point can also be investigated. The specimen is cut into four sections at the three axial locations where the mode shapes are evaluated. The cuts are made with the diamond-grit cutting wheel as described in section 5.1.3, taking into account that the blade thickness removes approximately 1.5 mm of the specimen. The sectioned axial edges are then buffed with a felt bob rotating in a drill press using a slurry of $0.7 \mu\text{m}$ grit powder and water. This creates a polished surface needed to identify through-

thickness damage with a microscope. An Olympus SZ-Tr Zoom stereo microscope is used to examine the shell edges under a magnification of 30-40X. Matrix cracks appear as light lines through the darker matrix and delaminations appear as lightened areas between plies (or ply groups). A sample cross section near the loading point for a T_2 shell is given in Figure 5.16. Crazeing in the upper half of the 45° ply group, delaminations between the lower 0° and -45° , and the -45° and 45° ply groups, and matrix cracks in the lower -45° and 45° ply groups are clearly visible in the photographs. The white paint (see section 5.1.3) on the lower concave shell surface is also visible. These features are even more clearly visible in the magnified view in the lower picture. A single matrix crack on the right in the 45° ply group is visible, and another on the left in the -45° group. A delamination between the two -45° plies, visible in the upper-left corner of the magnified view, is noted to terminate at the matrix crack in the -45° ply group.

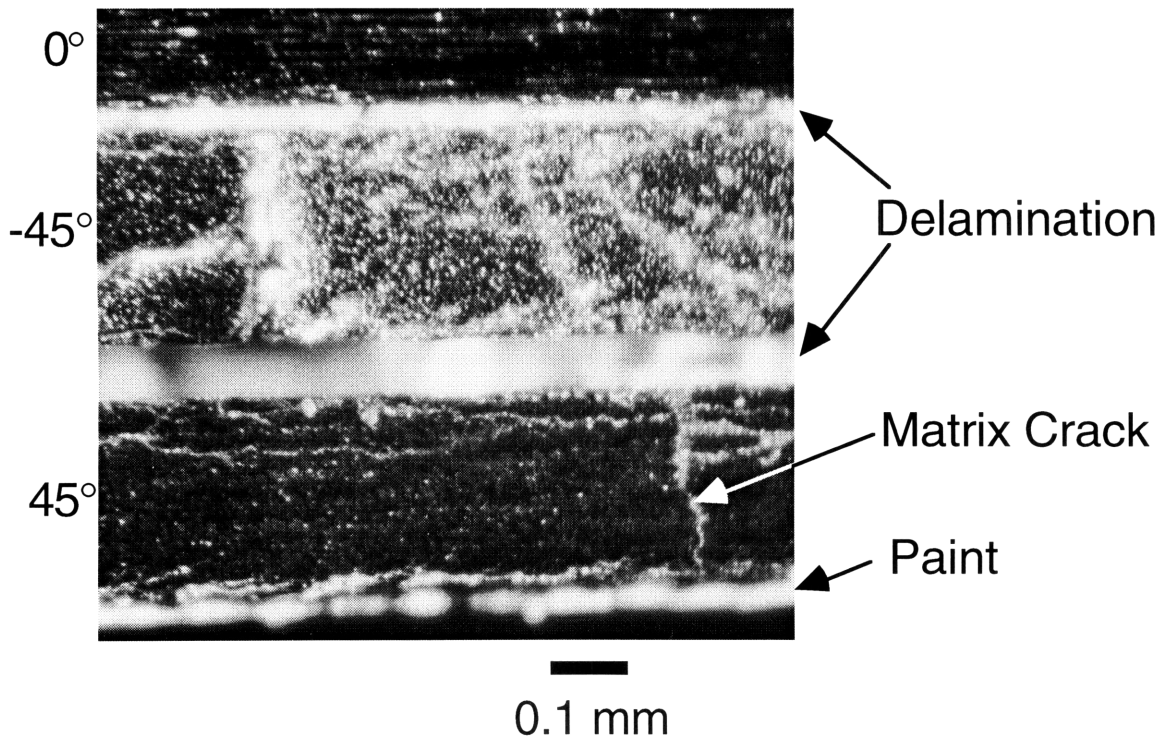
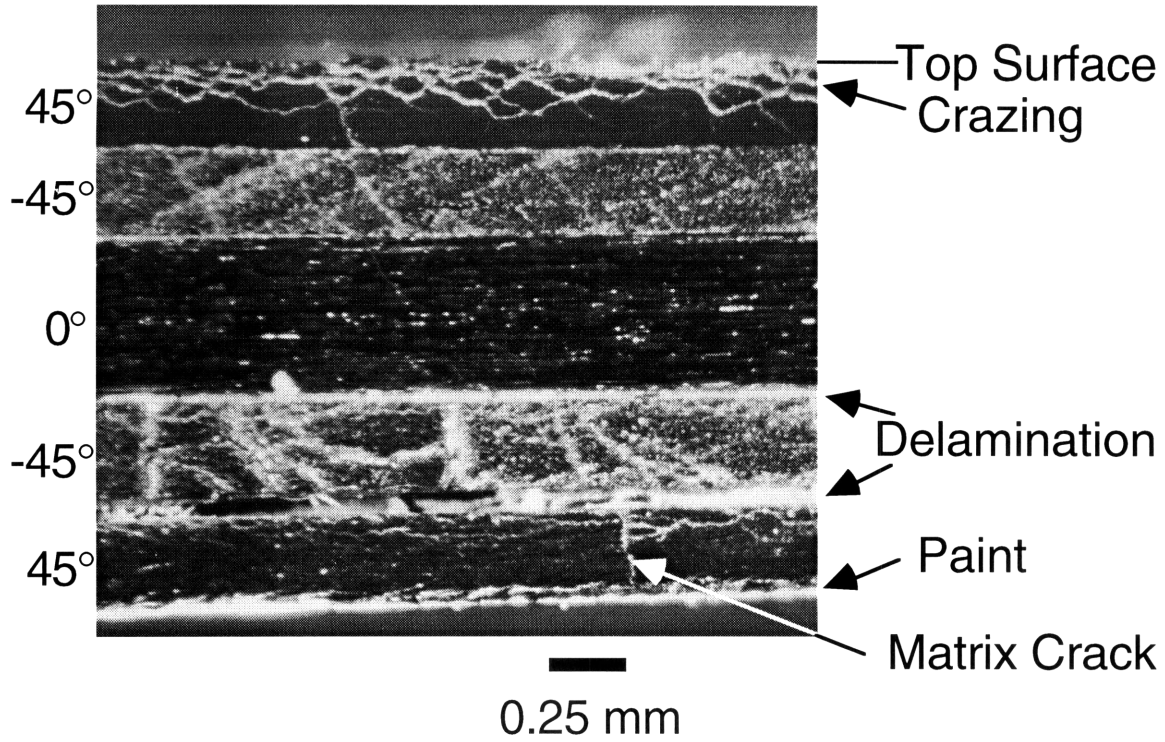


Figure 5.16 Examples of visible damage in cross-sections of a T_2 shell: (*top*) entire specimen thickness, and (*bottom*) magnified view of lower right corner.

CHAPTER 6

RESULTS

Results from testing and numerical analysis are presented in this chapter for specimen configurations tested in this work utilizing the boundary conditions discussed in chapter 5. Experimental results include load-deflection data, deflection mode-shape evolutions, and x-radiographs of damage. Numerical results computed with the STAGS finite element code include load-deflection histories and deflection mode-shape evolutions.

6.1 Experimental Observations

As discussed in section 5.4, two types of testing were conducted – overall loading response and mode-shape tests. The overall loading response tests are used to experimentally characterize the loading response over the entire regime of interest. Mode-shape tests are used to characterize deflection mode-shape evolutions during the shell response, including the buckling process. After testing, specimen damage is evaluated for all specimens using the x-radiography technique.

6.1.1 Loading Response

The loading response is characterized by plotting the load versus the applied stroke (deflection). Two load-deflection results are available for each specimen geometry (thickness) from the two types of tests conducted. Specimens are referenced by the type of test as follows: *-1* after the specimen

type identification refers to the overall loading tests (*e.g.*, specimen $R_{12}S_3T_1-1$), and -2 refers to the damage tests. The tests differ only in that loading was terminated at different peak loads, as described in chapter 3. Specimens of a given type (thickness) are nominally identical although small differences are noted in the experimentally determined radii (see chapter 5). Data from both types of tests are presented in this section for comparison.

Two types of audible phenomenon were noted during testing: a popping noise, and a cracking/crunching noise. 'Cracking' is a sharp, brittle sound, whereas 'popping' is louder and not as sharp. The cracking/crunching noise has been observed previously for transversely-loaded composite plates and shells and is associated with damage formation [18]. Damage formation is often associated with load drops in the load-deflection data, *e.g.*, [86], and therefore load drops frequently occur in association with cracking/crunching. Load drops, not due to damage formation, are noted at points in the load-deflection response where 'popping' was observed. The 'popping noise' is therefore believed to be associated with an instability point in the shell response. These two audible phenomena were monitored during testing, and the approximate stroke value at which they occurred was noted within ± 0.5 mm by observing real-time output of the stroke data.

Load-deflection data from the overall loading response and mode-shape tests for specimen type $R_{12}S_3T_1$ are presented in Figures 6.1 (specimen $R_{12}S_3T_1-1$) and 6.2 (specimen $R_{12}S_3T_1-2$), respectively. Hysteresis in the loading response in Figures 6.1 and 6.2 is typical of load-deflection curves observed in this work and has been found in previous work with similar shells [21]. In Figure 6.1, the shell response first experiences a period of load-softening below approximately 3 mm of applied center deflection. Above 3 mm, the response stiffens slightly until the load suddenly drops at a center

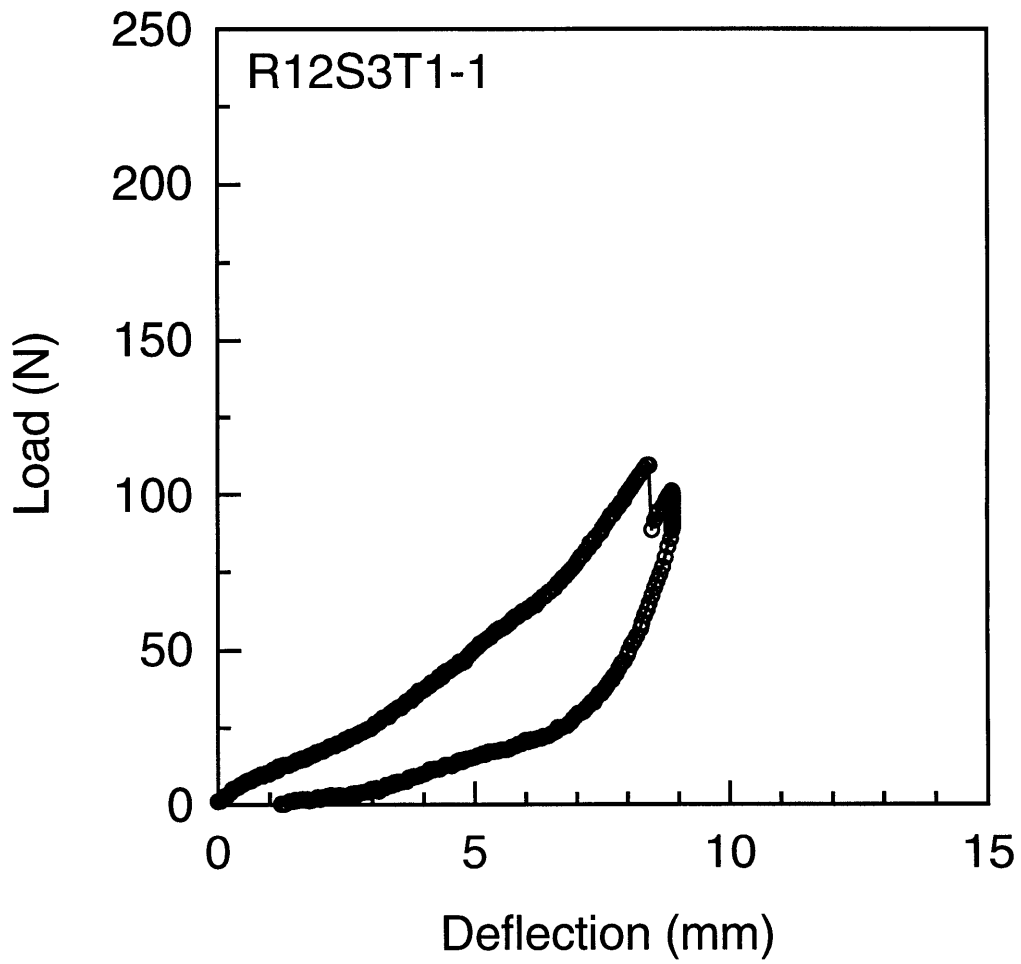


Figure 6.1 Experimental load-deflection response for specimen $R_{12}S_3T_1-1$.

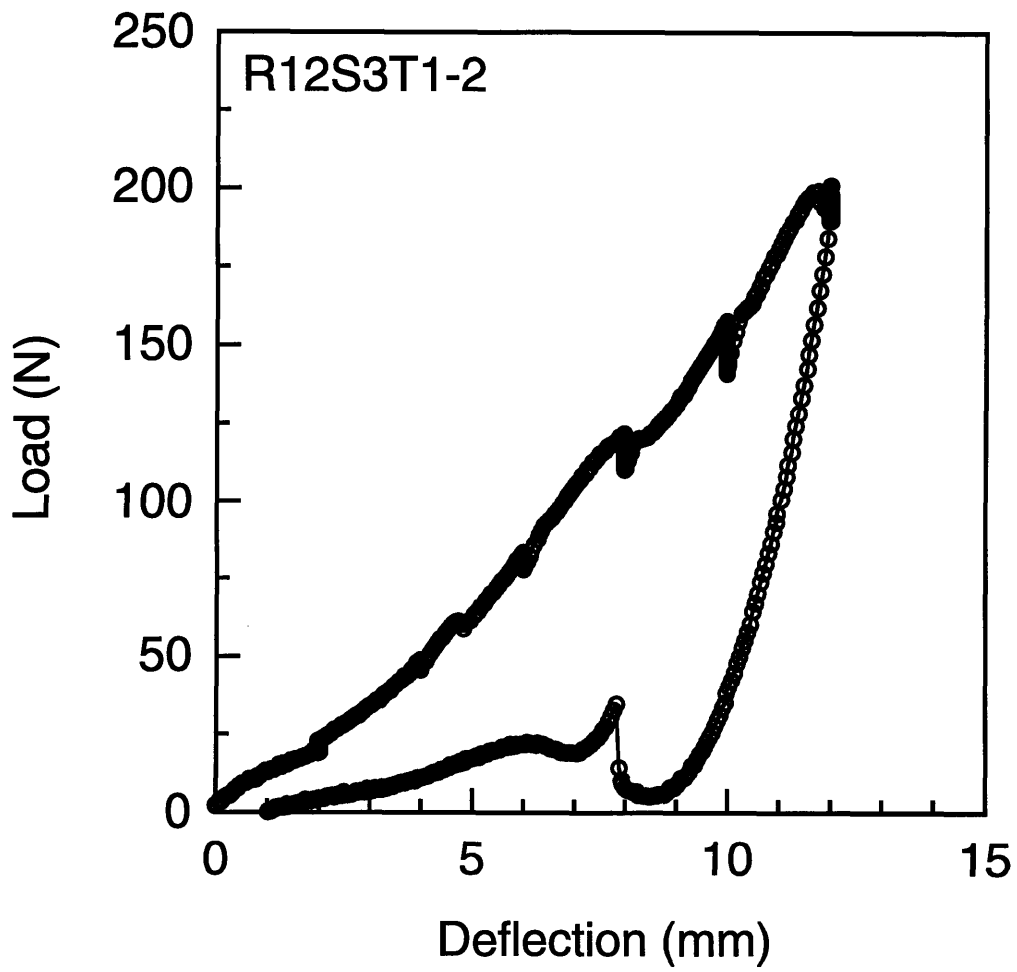


Figure 6.2 Experimental load-deflection response for specimen $R_{12}S_3T_1-2$.

deflection value of 8.5 mm. At the load drop, the shell audibly 'popped' during testing and the test was manually stopped and held at 8.9 mm of deflection in order to take mode-shape measurements. The specimen was subsequently unloaded. As this specimen was undamaged, the sudden load drop and associated 'popping' is attributed to dynamic buckling at the critical point. The dynamic nature of buckling at this point will be further discussed in section 6.2 and chapter 7.

The loading portion of the response for specimen $R_{12}S_3T_{1-2}$ in Figure 6.2 is similar to the loading portion in Figure 6.1. The most notable difference in the response for specimens $R_{12}S_3T_{1-1}$ and $R_{12}S_3T_{1-2}$ are the small deviations in smooth response where stroke was held for mode-shape measurements to be taken in the latter. In Figure 6.2, mode shapes were taken at values of applied center deflection (stroke) of 2.0 mm, 4.0 mm, 6.0 mm, 8.0 mm, 10.0 mm, and 12.0 mm. Deviations at held-stroke values were noted for all specimens. However, as in previous work [21], the load generally returns to the original path making the load-deflection curves smooth apart from the held-stroke datapoints. These points are therefore not considered important and are justifiably ignored in further discussion. Specimen $R_{12}S_3T_{1-2}$ in Figure 6.2 was loaded to a higher load than specimen $R_{12}S_3T_{1-1}$. No damage was observed in specimen $R_{12}S_3T_{1-1}$ so additional mode shapes were pursued in the second test to gain insight into postbuckling. Note that in Figure 6.2, no drop in load associated with buckling at 8.5 mm is observed as in Figure 6.1. However, audible 'popping' was noted near a center deflection value of 5.0 mm and during the hold at 10.0 mm. Additionally, after the held-stroke position at 8.0 mm, the response does not return to the original path as is typically the case. During unloading of specimen $R_{12}S_3T_{1-2}$, the shell is noted to remain in a postbuckled state (load value of approximately 5 N) between applied center deflection

values of approximately 8 mm and 9 mm. Loading of the shell abruptly decreases at a stroke value of 7.9 mm. The abrupt loading was heard audibly as a large 'pop' during the test indicating a dynamic unloading phenomenon, likely due to an instability point. Dynamic unloading of this type has previously been reported for similarly loaded composite shells [18].

The load-deflection responses of specimen type $R_{12}S_3T_2$ for the two test types are presented in Figures 6.3 ($R_{12}S_3T_2-1$) and 6.4 ($R_{12}S_3T_2-2$). Again, the two loading portions of the curves are noted to be similar. Audible 'cracking' was noted at applied center deflections of approximately 10.0 mm, 11.5 mm, 14.0 mm, 16.0 mm, 16.5 mm, 17.5 mm, and 19.0 mm for specimen $R_{12}S_3T_2-1$. A drop in load is noted in the loading response at a center deflection value of 16.6 mm which may correspond to this observed 'cracking'. For specimen $R_{12}S_3T_2-2$, audible 'cracking' was noted at a center deflection of 12.5 mm, and mode shapes were evaluated at applied center deflection values of 2.0 mm, 4.0 mm, 6.0 mm, 8.0 mm, 12.0 mm, and 16.0 mm. Loading was terminated at 16.0 mm to obtain damage information prior to the load drop observed for specimen $R_{12}S_3T_2-1$ at a center deflection of 16.6 mm.

Good agreement is again noted for the loading portions of both specimen responses presented in Figures 6.5 and 6.6 for specimen type $R_{12}S_3T_3$. During loading of specimen $R_{12}S_3T_3-1$, 'cracking' was noted at applied center deflection values of 8.0 mm, 10.0 mm, 12.5 mm, 14.0 mm, and 16.5 mm. Multiple 'cracking' was observed at the latter three deflection values, with a significant load drop (~300 N) noted at the peak deflection (16.7 mm). Given the 'cracking' noted at a center deflection of 14.0 mm, the load drop at 13.9 mm is likely associated with damage formation. However, the load drop at a center deflection of 11.2 mm was not associated with any audible event. Unloading occurs smoothly for both specimens. Mode shapes were evaluated at stroke

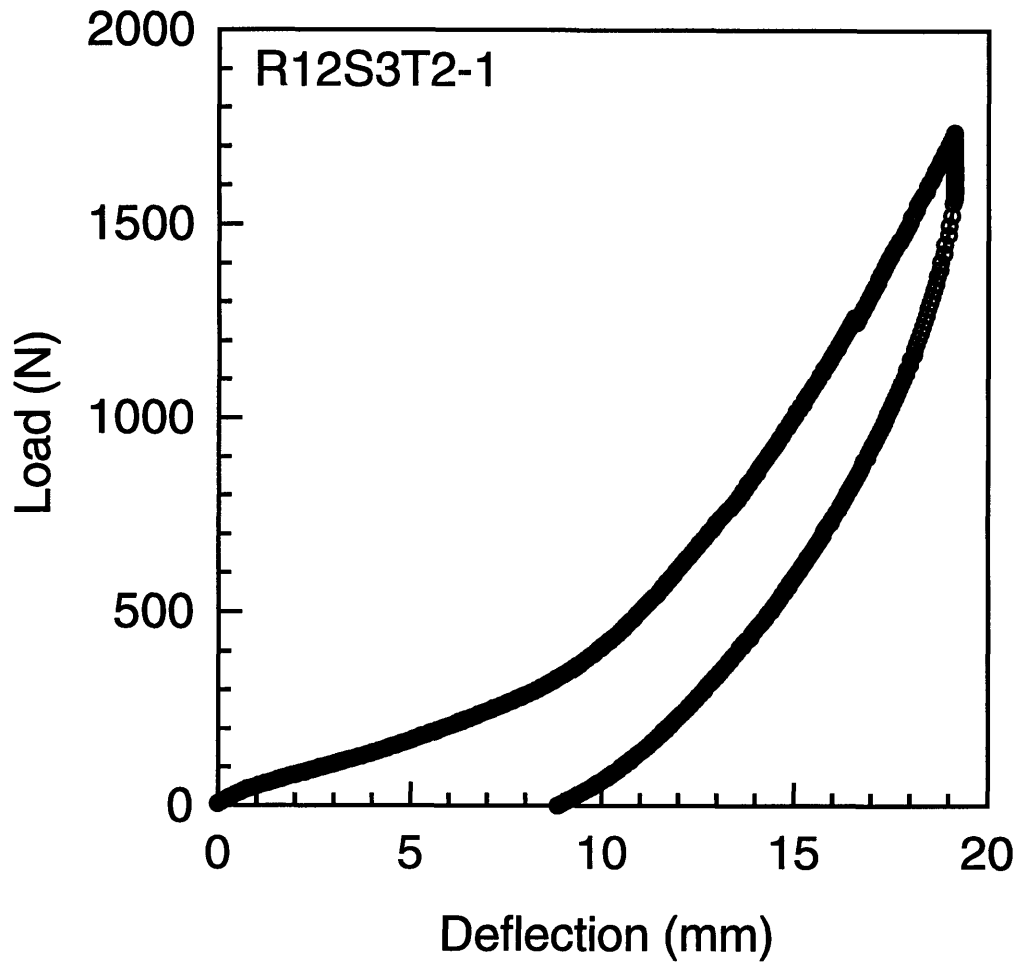


Figure 6.3 Experimental load-deflection response for specimen $R_{12}S_3T_2-1$.

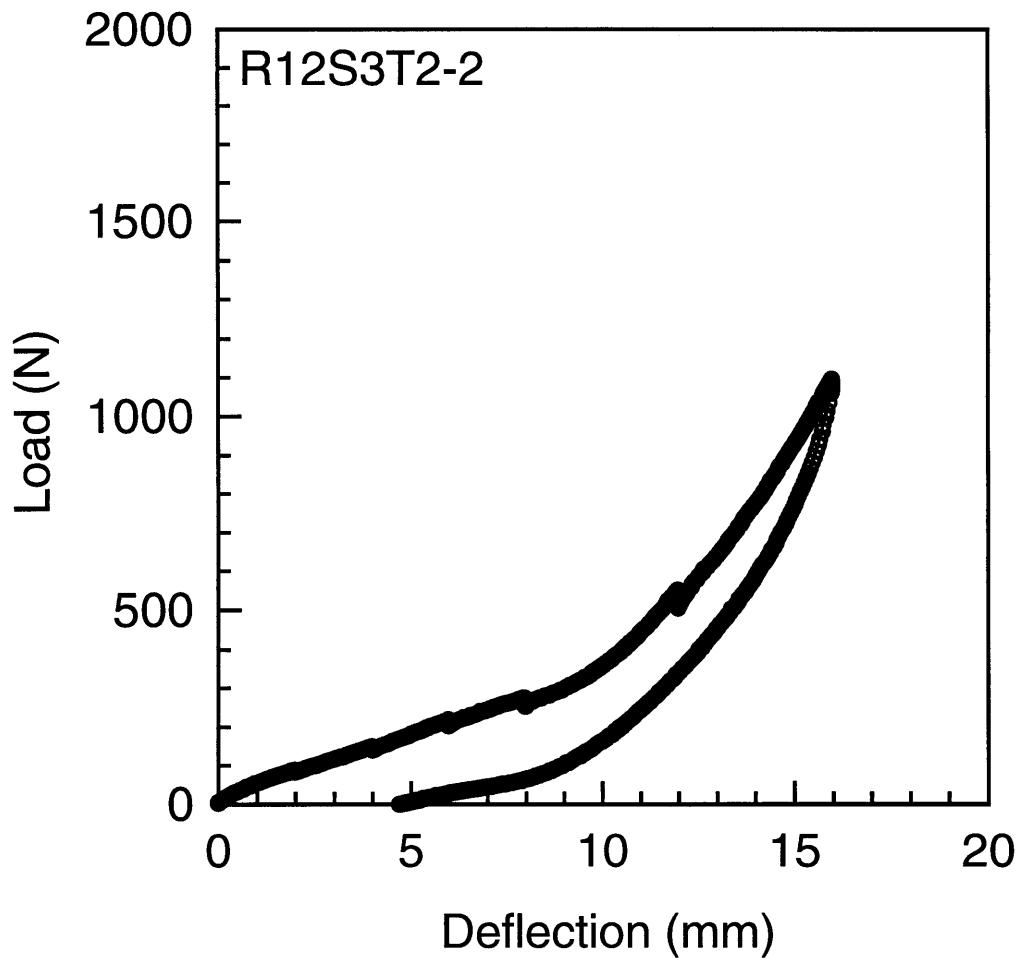


Figure 6.4 Experimental load-deflection response for specimen $R_{12}S_3T_2-2$.

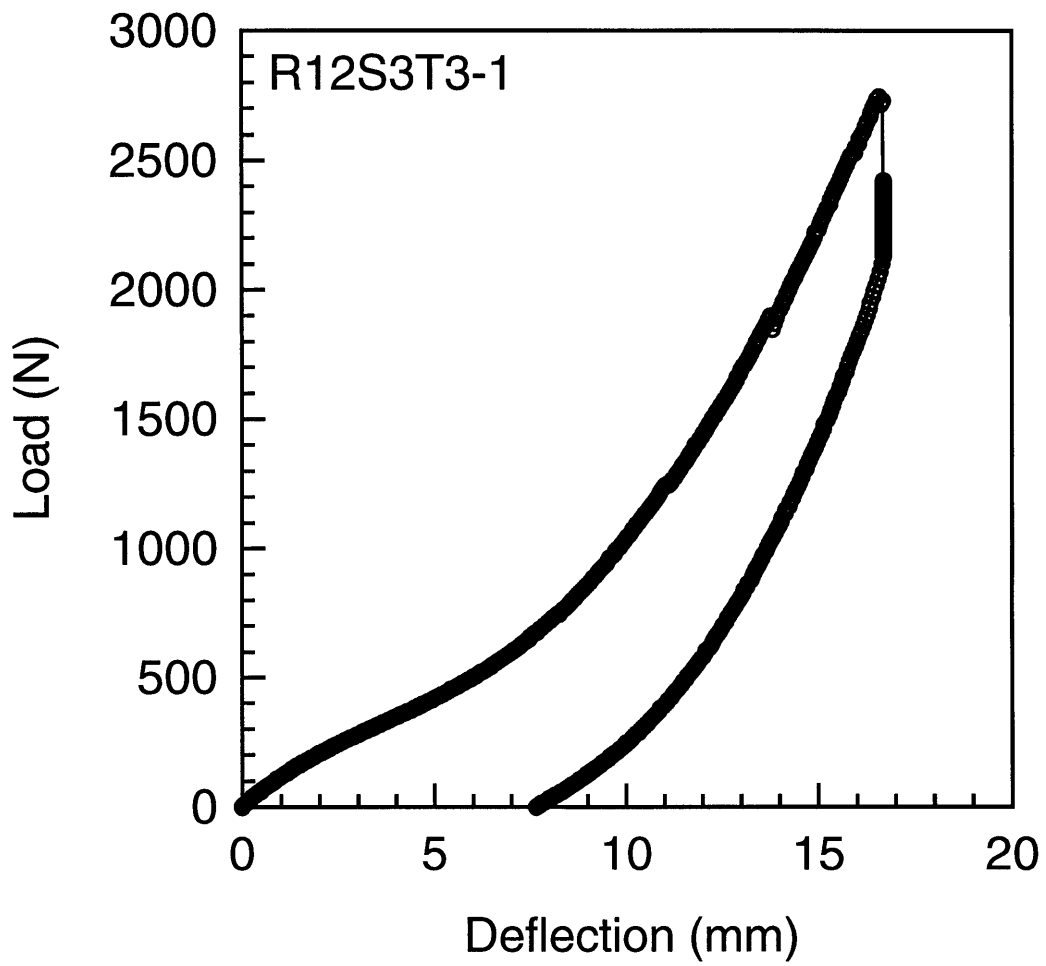


Figure 6.5 Experimental load-deflection response for specimen $R_{12}S_3T_3-1$.

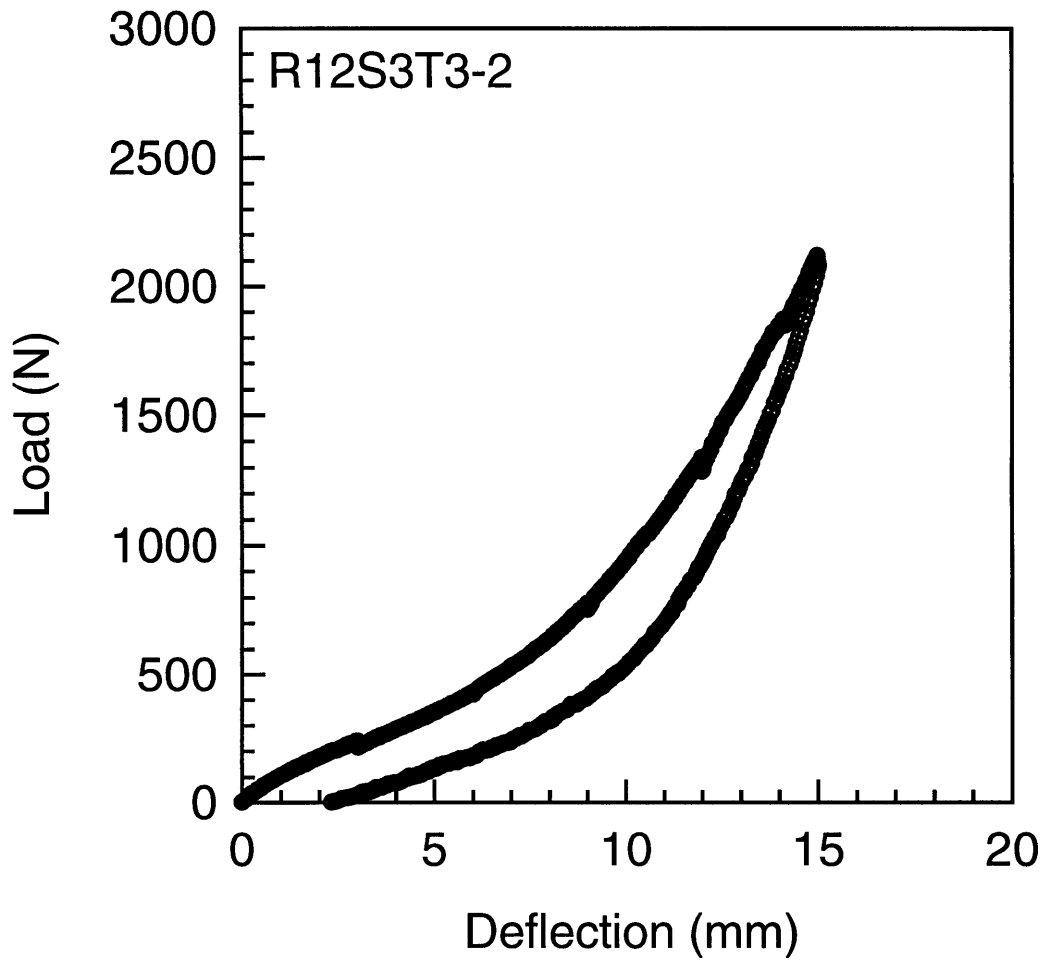


Figure 6.6 Experimental load-deflection response for specimen $R_{12}S_3T_3-2$.

values of 3.0 mm, 6.0 mm, 9.0 mm, 12.0 mm, and 15.0 mm for specimen $R_{12}S_3T_3-2$. Loading for this specimen was terminated at a center deflection value of 15.0 mm to obtain damage data at a load below the peak load for specimen $R_{12}S_3T_3-1$, *i.e.*, intermediate damage data was desired for this specimen type. 'Cracking' was noted at applied center deflection values of 7.5 mm, 9.5 mm, 11.5 mm, 12.5 mm, 13.5 mm, 14.0 mm, and 15.0 mm with multiple (most severe) cracking occurring at 13.5 mm and 14.0 mm. Additionally, 'popping' was heard at a center deflection of 14.0 mm and during the hold at a center deflection of 15.0 mm.

A comparison of the load-deflection response of specimens having different thicknesses is provided in Figure 6.7. The stiffening influence of increased thickness is apparent.

6.1.2 Mode-shape Evolutions

Mode shapes were assessed in the overall loading response tests as well as in the mode-shape tests. Mode-shape evolutions were measured continuously in the spanwise direction at three discrete axial locations as described in chapter 5. Mode shapes in this section are presented by plotting the vertical position of the concave side of the shell versus the spanwise position at different values of applied center deflection (stroke) as done in chapter 4. Also as in chapter 4, the origin is located at the midpoint of the axial (hinged) boundary condition (see Figure 4.1). Central spanwise modes refer to modes where the axial position bisects the shell (through the origin in Figure 4.1). Left and right spanwise modes refer to modes at axial (x -direction in Figure 4.1) positions of -76.2 mm and 76.2 mm, respectively. The axial boundary conditions at ± 152.4 mm (x -direction in Figure 4.1) restrain the shells such that the vertical deflection is zero along these edges. Thus, the left and

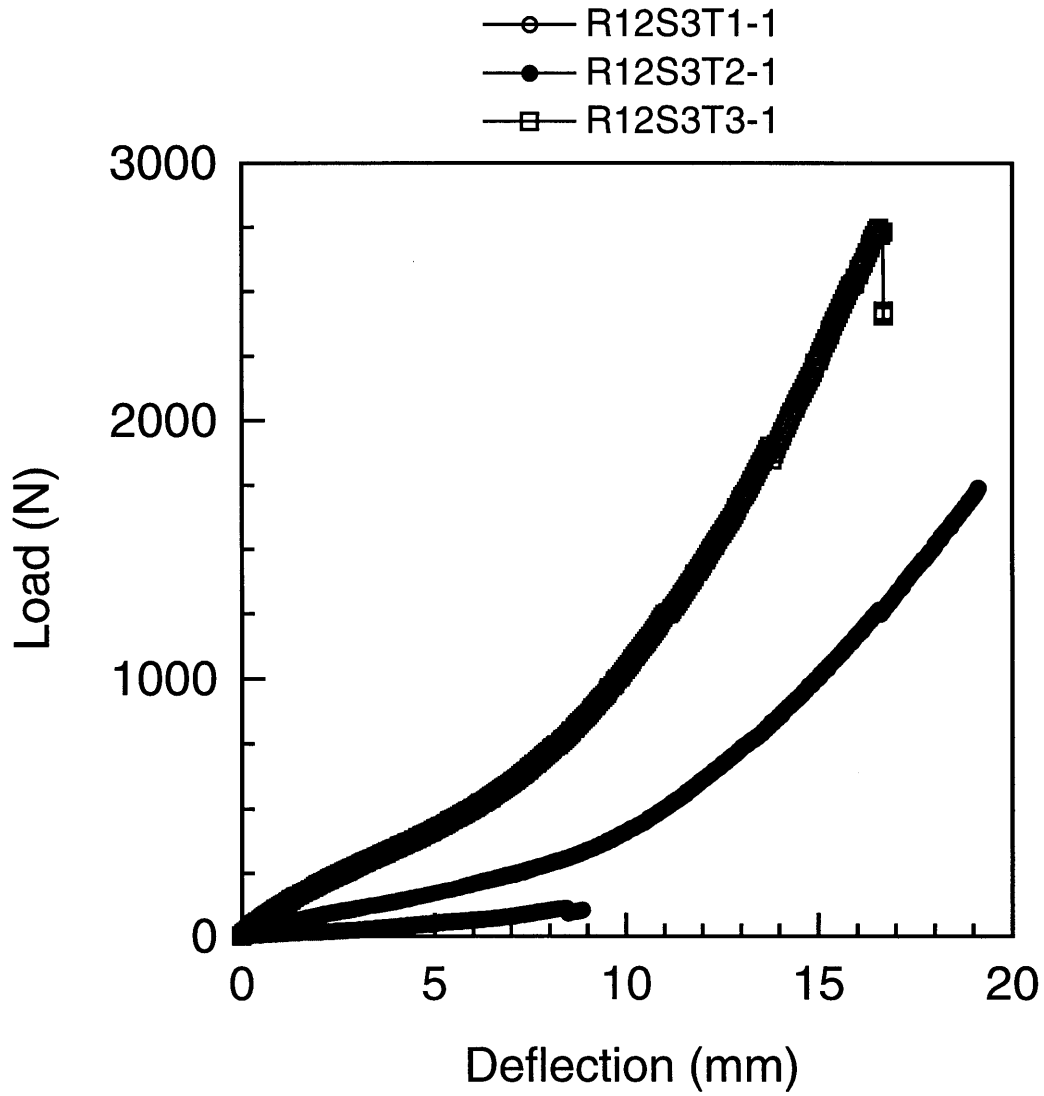


Figure 6.7 Experimental load-deflection responses for specimens of different thicknesses.

right spanwise deformation modes provide modal information midway between the shell center and the axial boundaries. In the overall loading response tests, mode shapes were assessed at three values of applied stroke (w_c): the initial geometry of the shell ($w_c = 0$ mm), the maximum value of center deflection, and the final, unloaded shape of the shell ($w_c = 0$ mm). For the mode-shape tests, mode shapes were measured at predetermined values of applied stroke as discussed in chapter 5.

Central spanwise modes for specimen $R_{12}S_3T_1-1$ (see load-deflection data in Figure 6.1) are presented in Figure 6.8. The initial and final shape of the shell are noted to correspond which indicates that the shell returns to its original configuration upon removal of load. The mode shape at the maximum value of center deflection, 8.9 mm, is noted to be asymmetric in the spanwise direction. As with the composite shell cases in chapter 4, the asymmetry indicates that the shell has bifurcated. Bifurcation occurs prior to loading corresponding to a center deflection value of 8.9 mm. The initial and final conditions of the left and right spanwise mode shapes in Figures 6.9 and 6.10 are also noted to coincide, again indicating that the shell returns to the undeformed configuration after load has been removed. The left and right mode shapes represent a transition from zero deflection at the axial boundary and the response of the central deformation mode. The asymmetry shown in the central spanwise mode is also clearly evident in the right mode. Asymmetry is also noted, to a lesser degree, in the left mode shape. This shell has thus deformed asymmetrically in the axial as well as the spanwise direction. This is further discussed in regard to specimen $R_{12}S_3T_1-2$.

Asymmetries in the mode-shape evolution for this specimen type are more clearly identified in the mode-shape evolutions presented in Figures 6.11 through 6.13 for specimen $R_{12}S_3T_1-2$. The response in the central spanwise

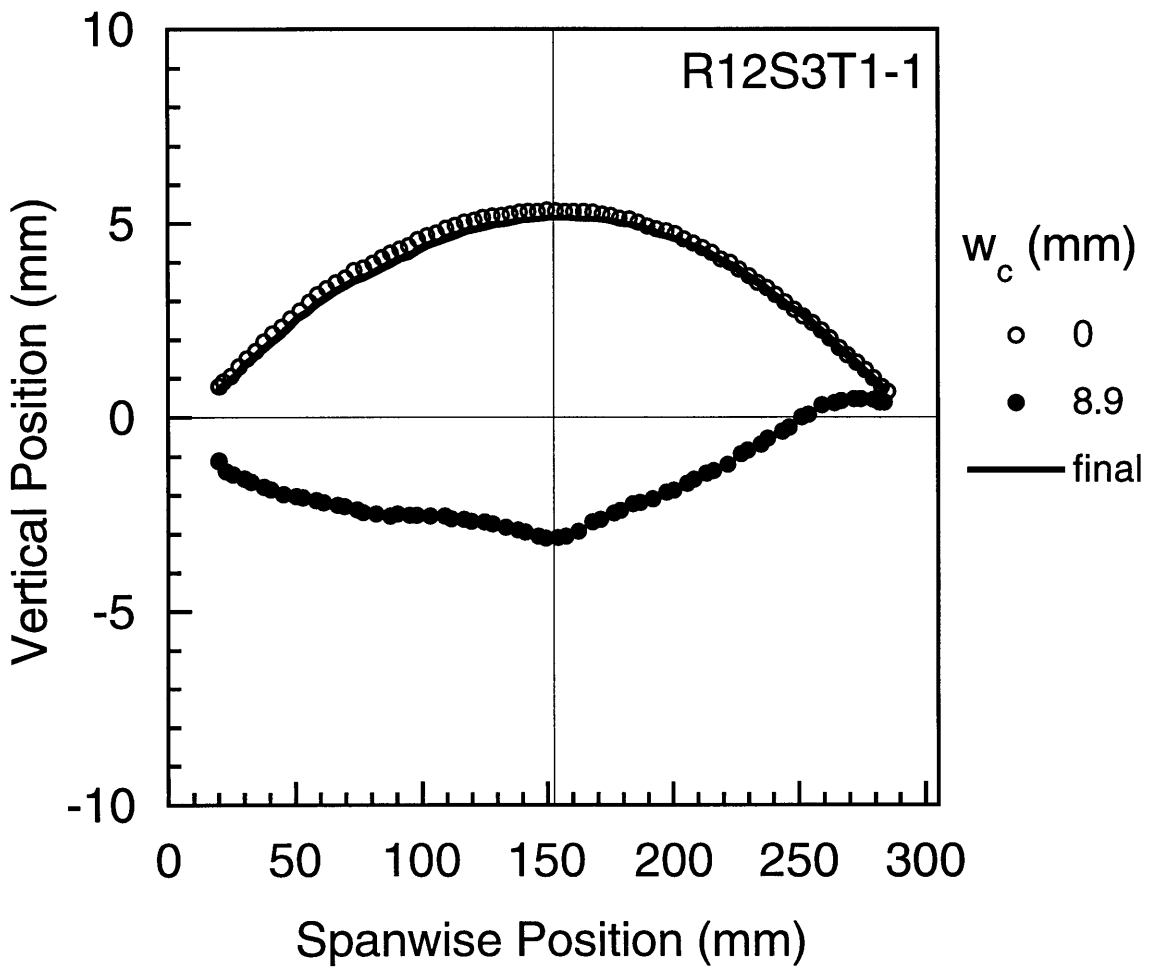


Figure 6.8 Measured central spanwise deformation modes for specimen $R_{12}S_3T_1-1$ at different values of center deflection.

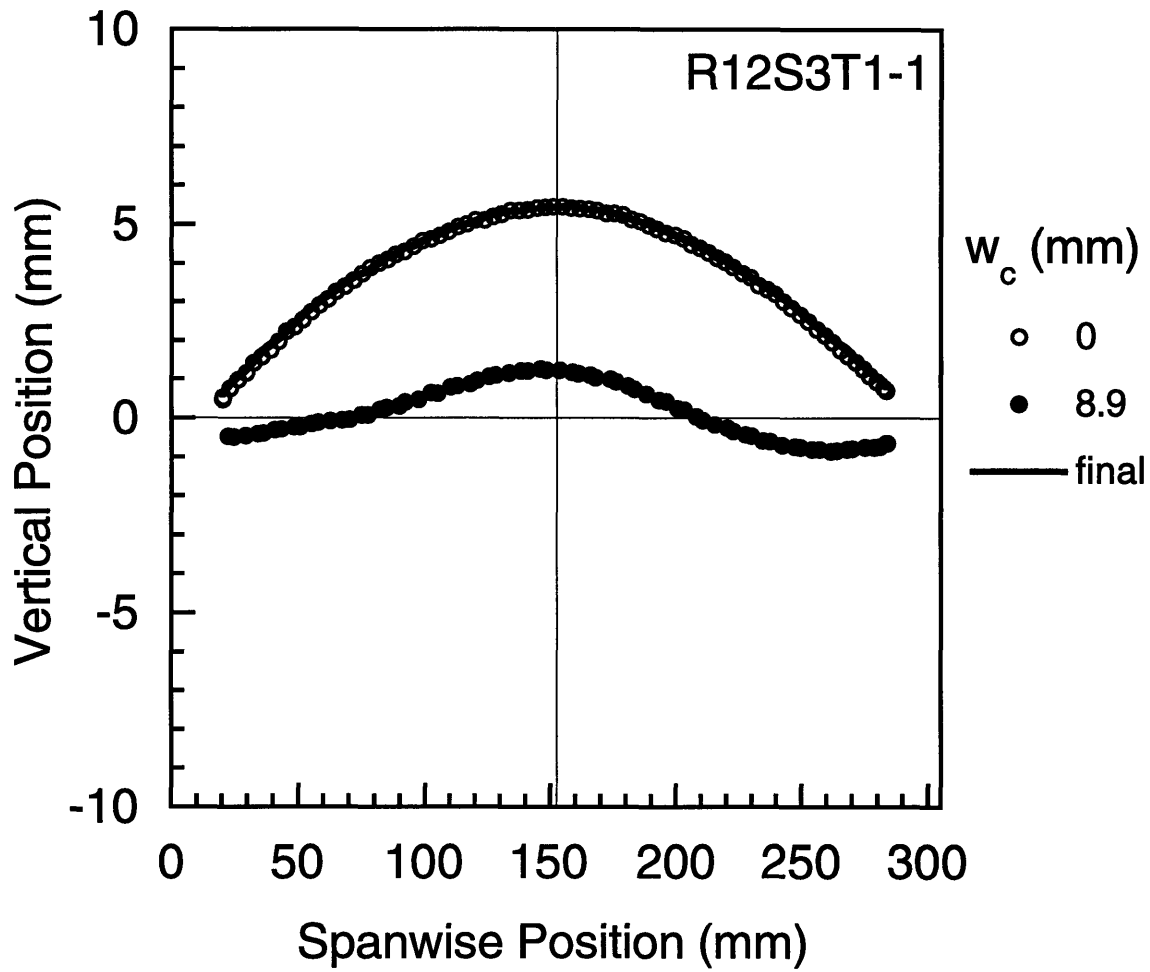


Figure 6.9 Measured left spanwise deformation modes for specimen $R_{12}S_3T_1-1$ at different values of center deflection.

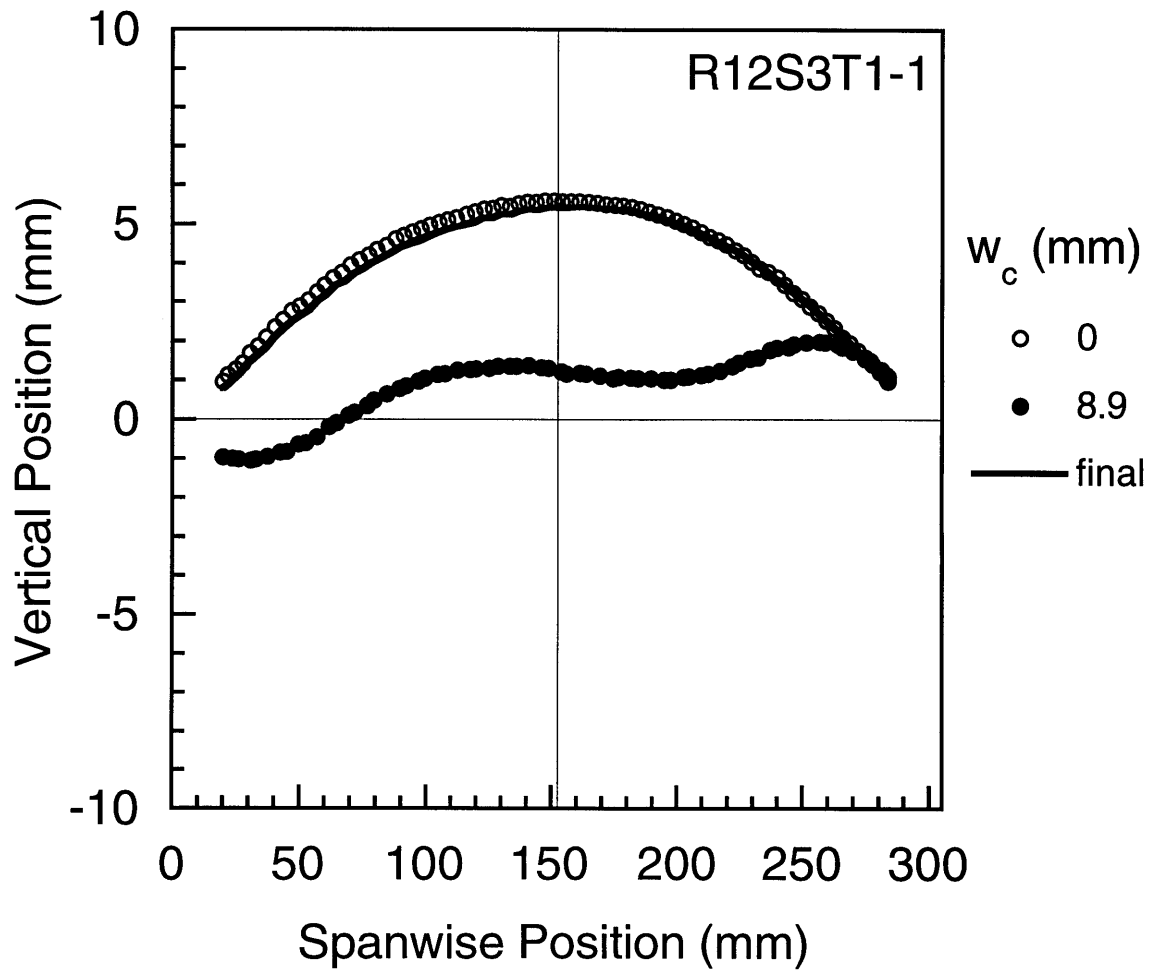


Figure 6.10 Measured right spanwise deformation modes for specimen $R_{12}S_3T_1-1$ at different values of center deflection.

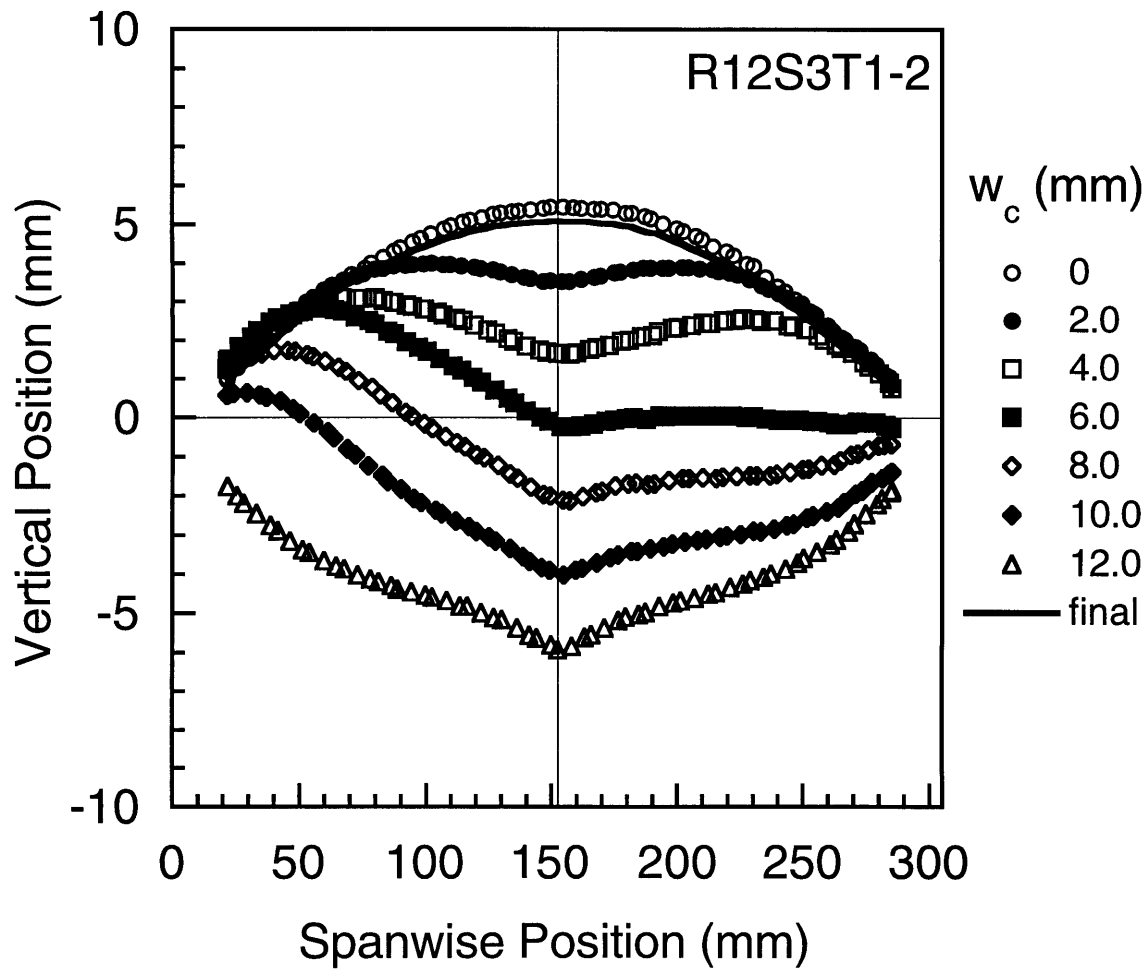


Figure 6.11 Measured central spanwise deformation modes for specimen $R_{12}S_3T_{1-2}$ at different values of center deflection.

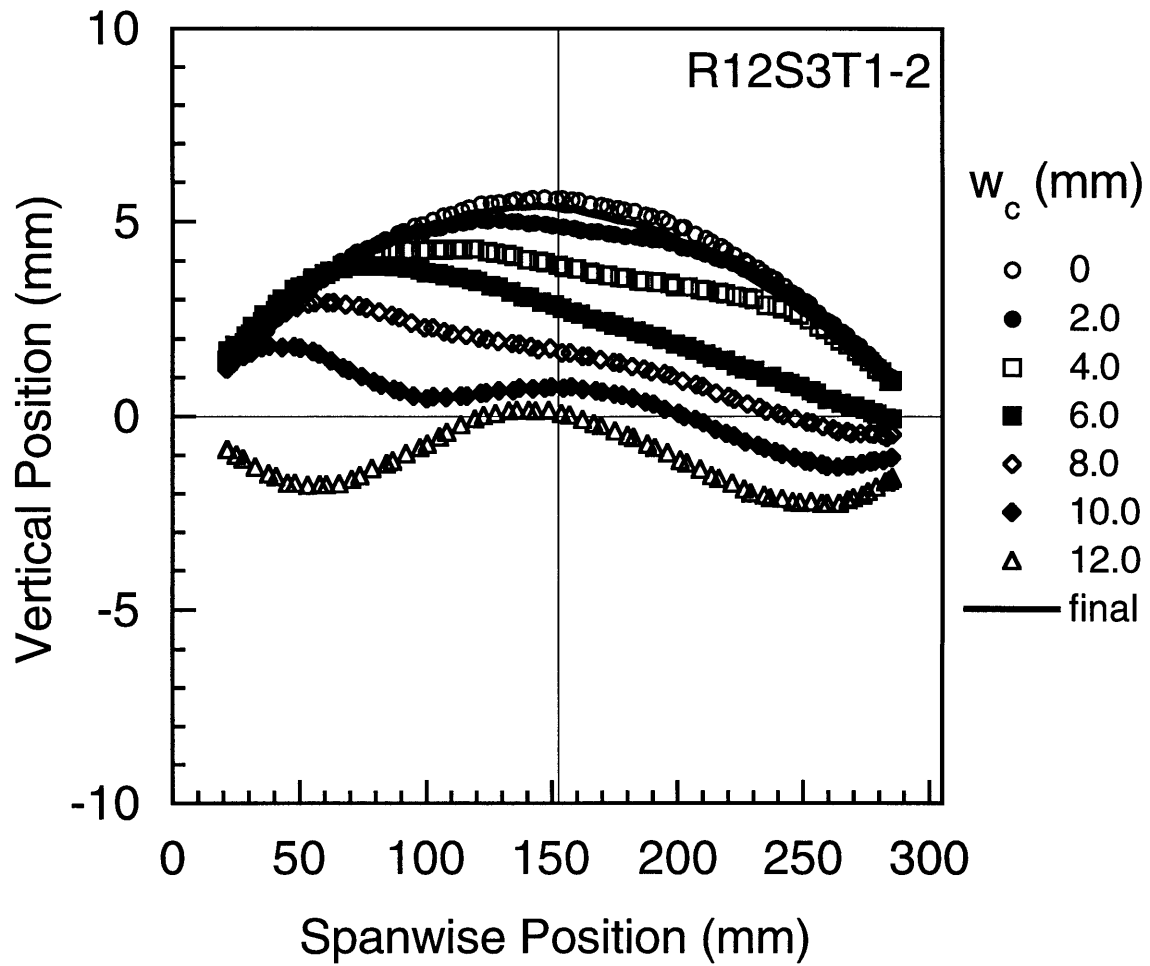


Figure 6.12 Measured left spanwise deformation modes for specimen $R_{12}S_3T_{1-2}$ at different values of center deflection.

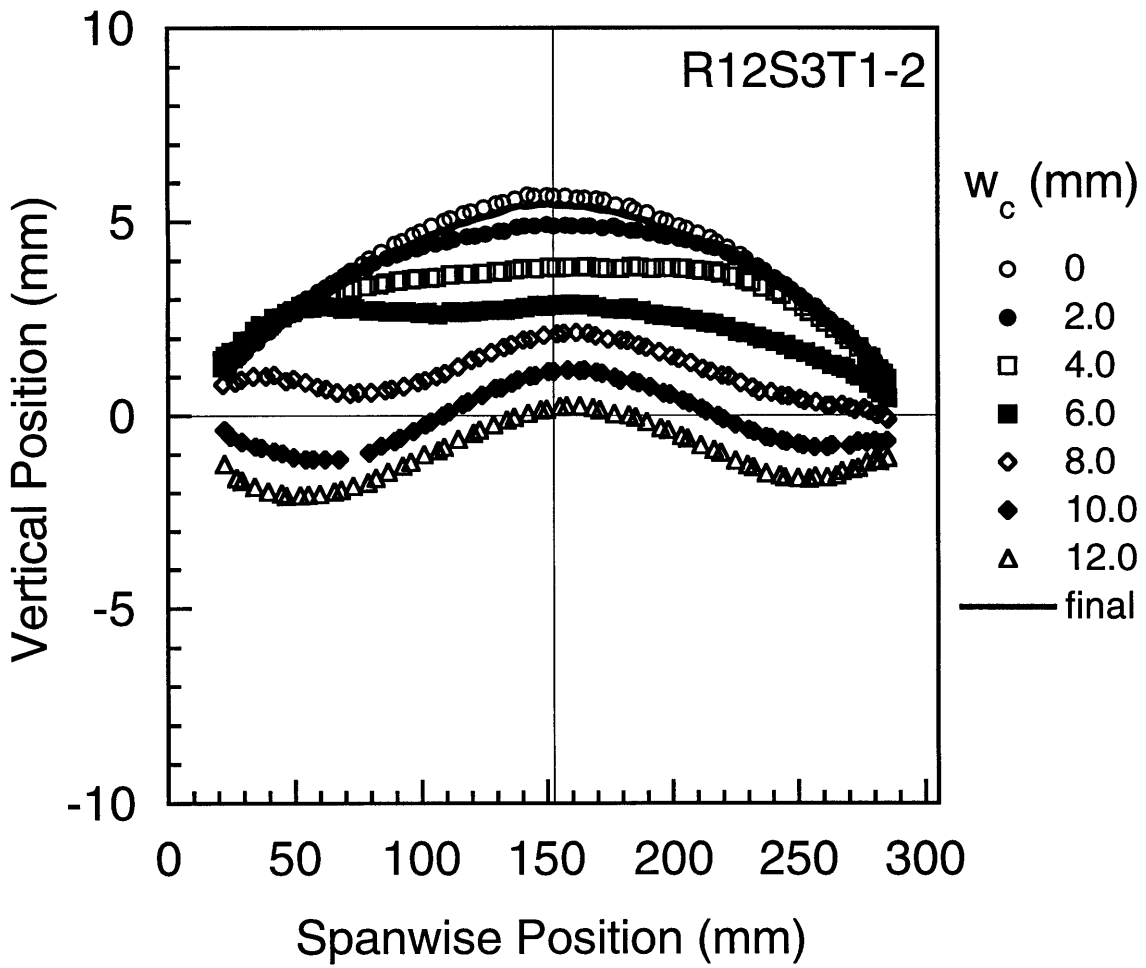


Figure 6.13 Measured right spanwise deformation modes for specimen $R_{12}S_3T_{1-2}$ at different values of center deflection.

modes is noted to be symmetric at a center deflection value of 2.0 mm. The mode at a center deflection of 4.0 mm is dominated by a symmetric component, but there is a slight asymmetry. However, the asymmetry is clearly evident at center deflection values of 6.0 mm, 8.0 mm, and 10.0 mm. These modes indicate that specimen $R_{12}S_3T_{1-2}$ bifurcates between center deflection values of 2.0 mm and 6.0 mm. Symmetry in the deformation mode is regained at a center deflection of 12.0 mm. This is much like the response of composite shells in chapter 4 where the response regains symmetry upon loading onto the second equilibrium path in the inverted configuration. The left and right deformation modes in Figures 6.12 and 6.13 also reflect the transition from a symmetric to asymmetric mode between center deflection values of 2.0 mm and 6.0 mm. An antisymmetric component of deformation in the left and right modes at center deflection values of 2.0 mm, 4.0 mm, and 12.0 mm is evident by comparing Figures 6.12 and 6.13. These modes are all noted to be slightly asymmetric, and antisymmetric with respect to one another (left and right modes). This antisymmetry is discussed subsequently in this section and also in section 6.2.

Excellent agreement is also noted for mode shapes compared for the remaining two specimen types, $R_{12}S_3T_2$ and $R_{12}S_3T_3$. The central, left, and right spanwise deformation modes from the overall loading tests of specimens $R_{12}S_3T_{2-1}$ and $R_{12}S_3T_{3-1}$ are provided in Figures 6.14 to 6.16, and 6.17 to 6.19, respectively. For comparison, the central, left, and right spanwise mode-shape evolutions for the mode-shape tests of specimens $R_{12}S_3T_{2-2}$ and $R_{12}S_3T_{3-2}$ are provided in Figures 6.20 to 6.22, and 6.23 to 6.25, respectively.

Deformations local to the contact area (loading point) at peak applied deflection for the overall loading tests are noted to be quite severe for both specimen types (Figures 6.14 and 6.17). A unique feature of these two mode

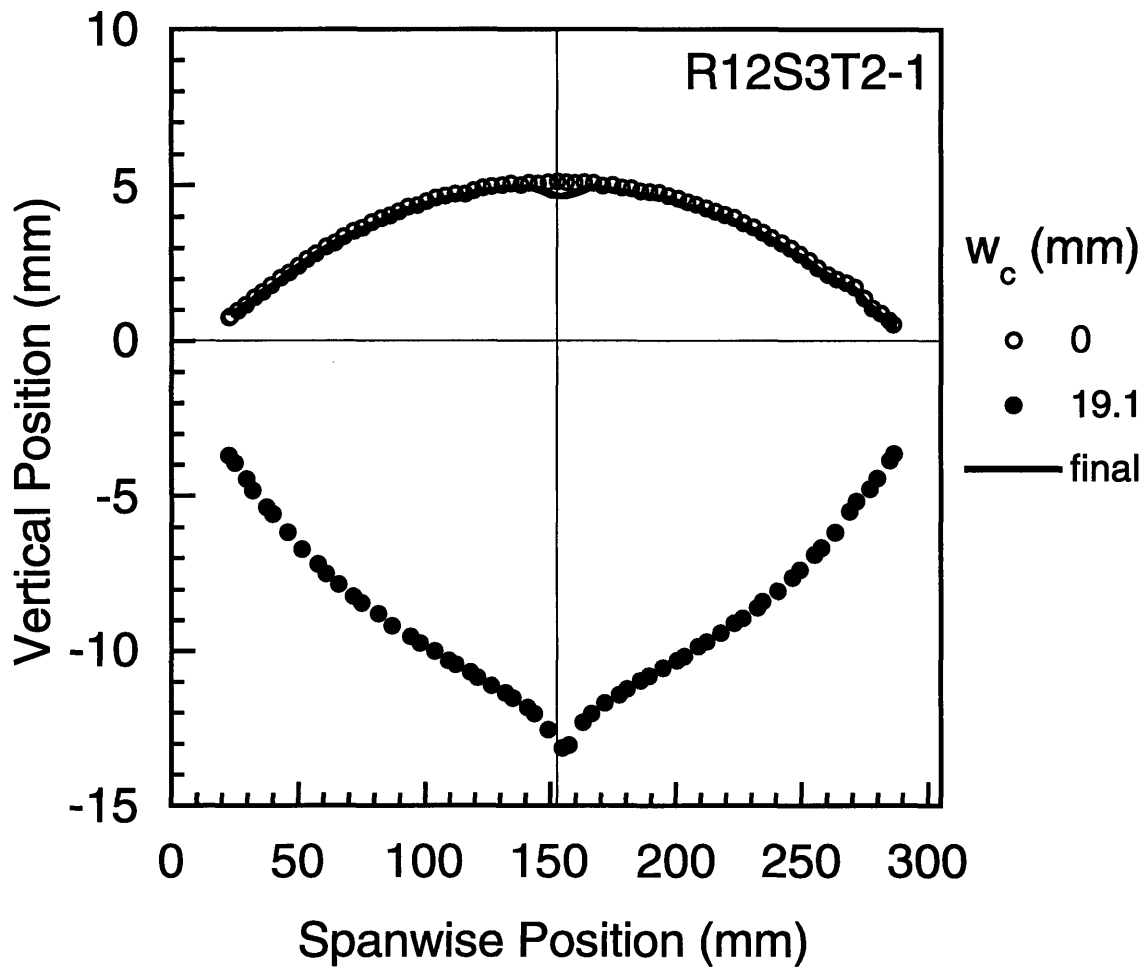


Figure 6.14 Measured central spanwise deformation modes for specimen $R_{12}S_3T_2-1$ at different values of center deflection.

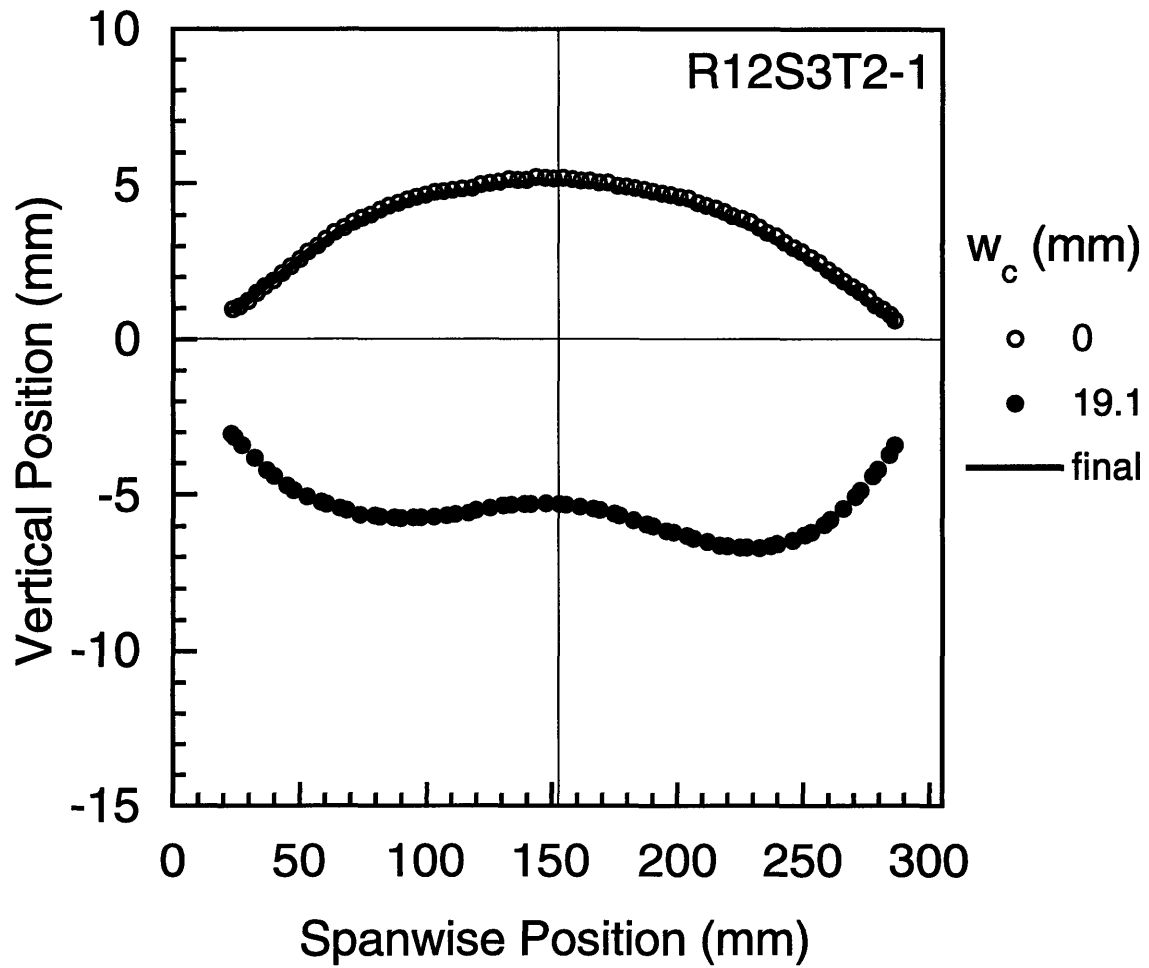


Figure 6.15 Measured left spanwise deformation modes for specimen $R_{12}S_3T_2-1$ at different values of center deflection.

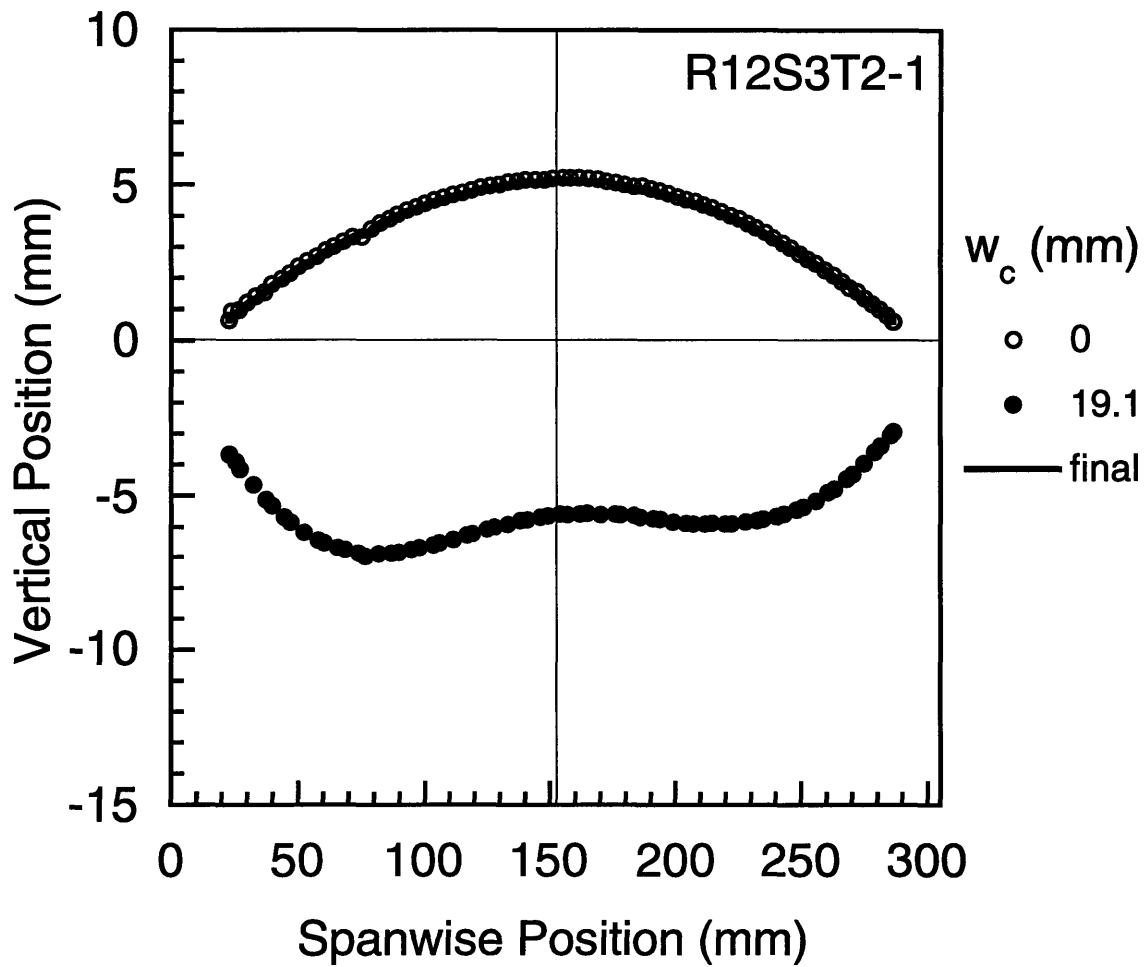


Figure 6.16 Measured right spanwise deformation modes for specimen $R_{12}S_3T_2-1$ at different values of center deflection.

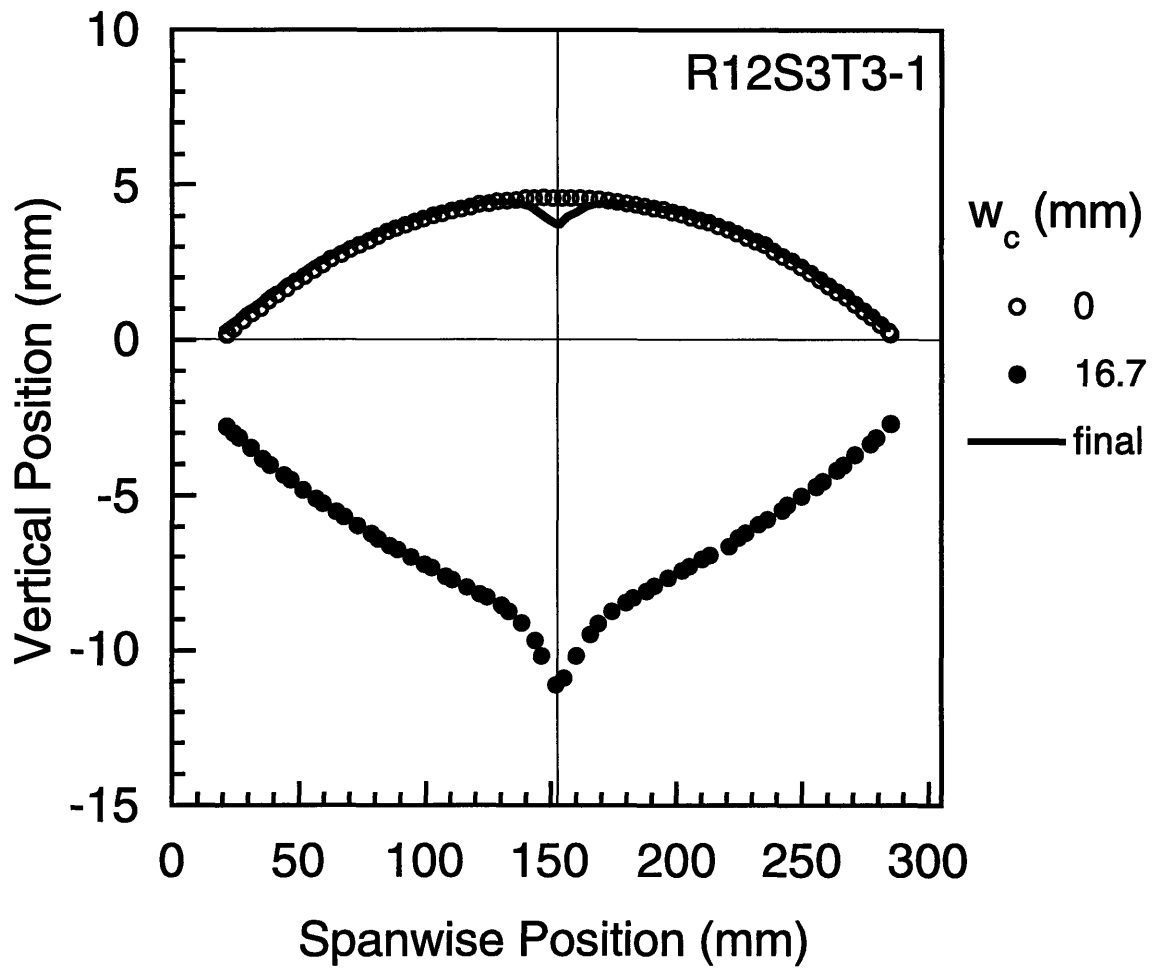


Figure 6.17 Measured central spanwise deformation modes for specimen $R_{12}S_3T_3-1$ at different values of center deflection.

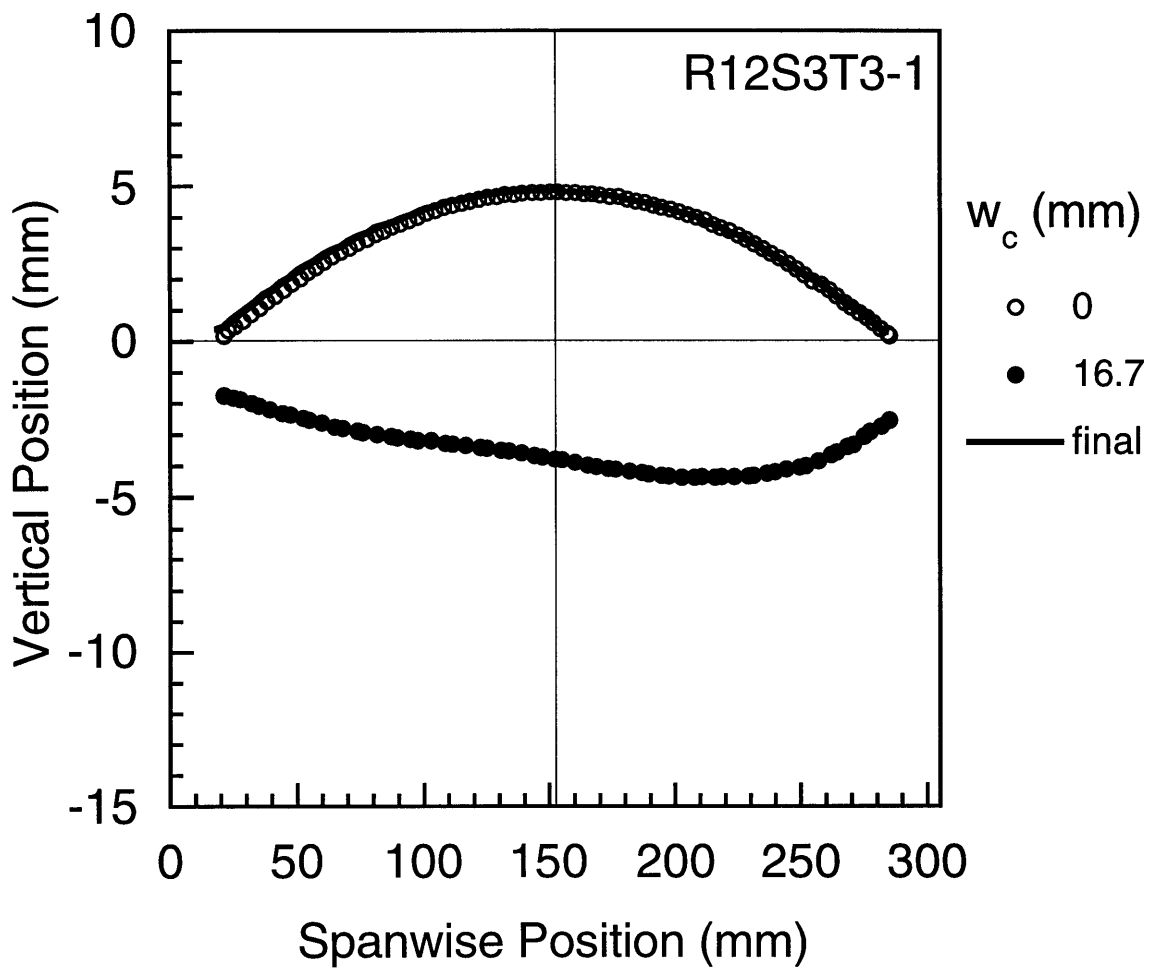


Figure 6.18 Measured left spanwise deformation modes for specimen $R_{12}S_3T_3-1$ at different values of center deflection.

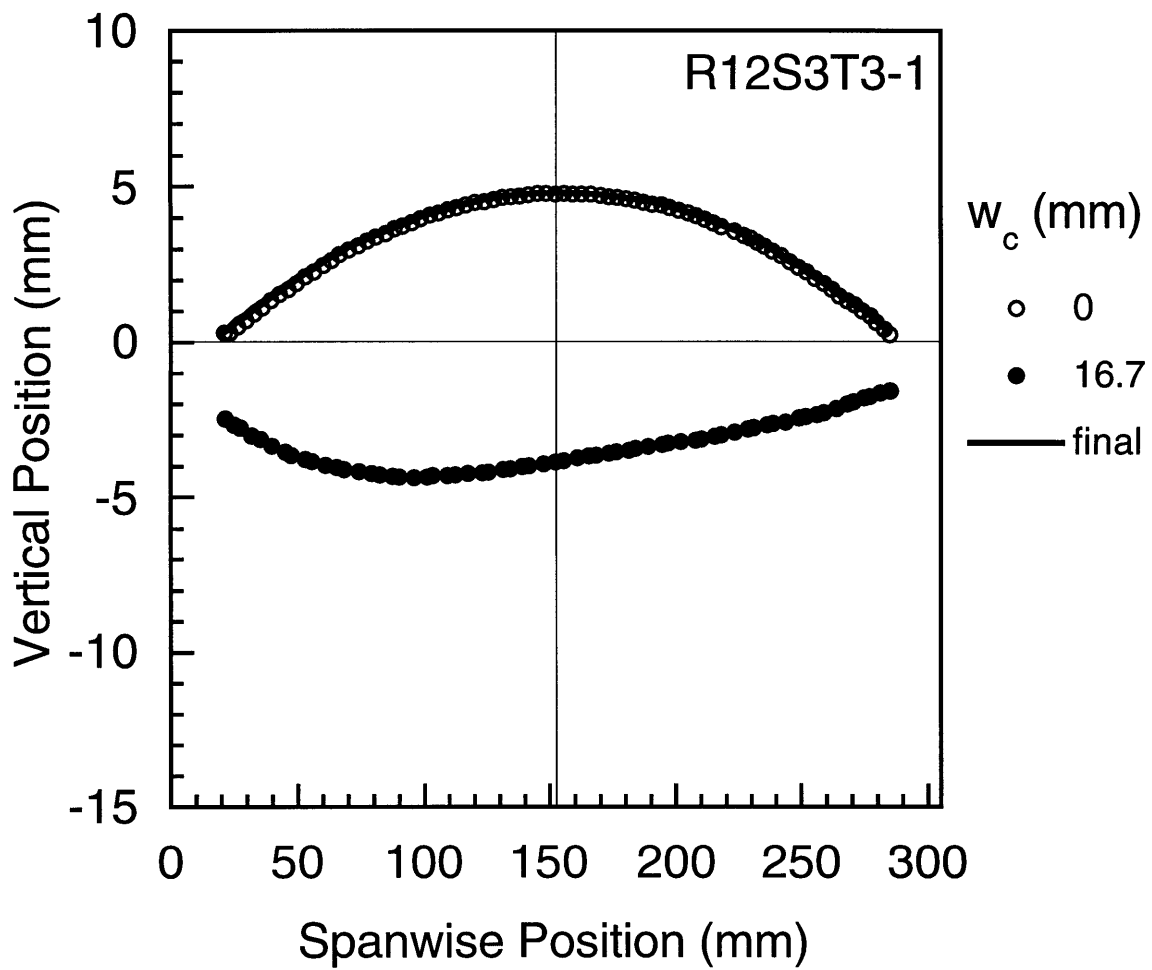


Figure 6.19 Measured right spanwise deformation modes for specimen $R_{12}S_3T_3-1$ at different values of center deflection.

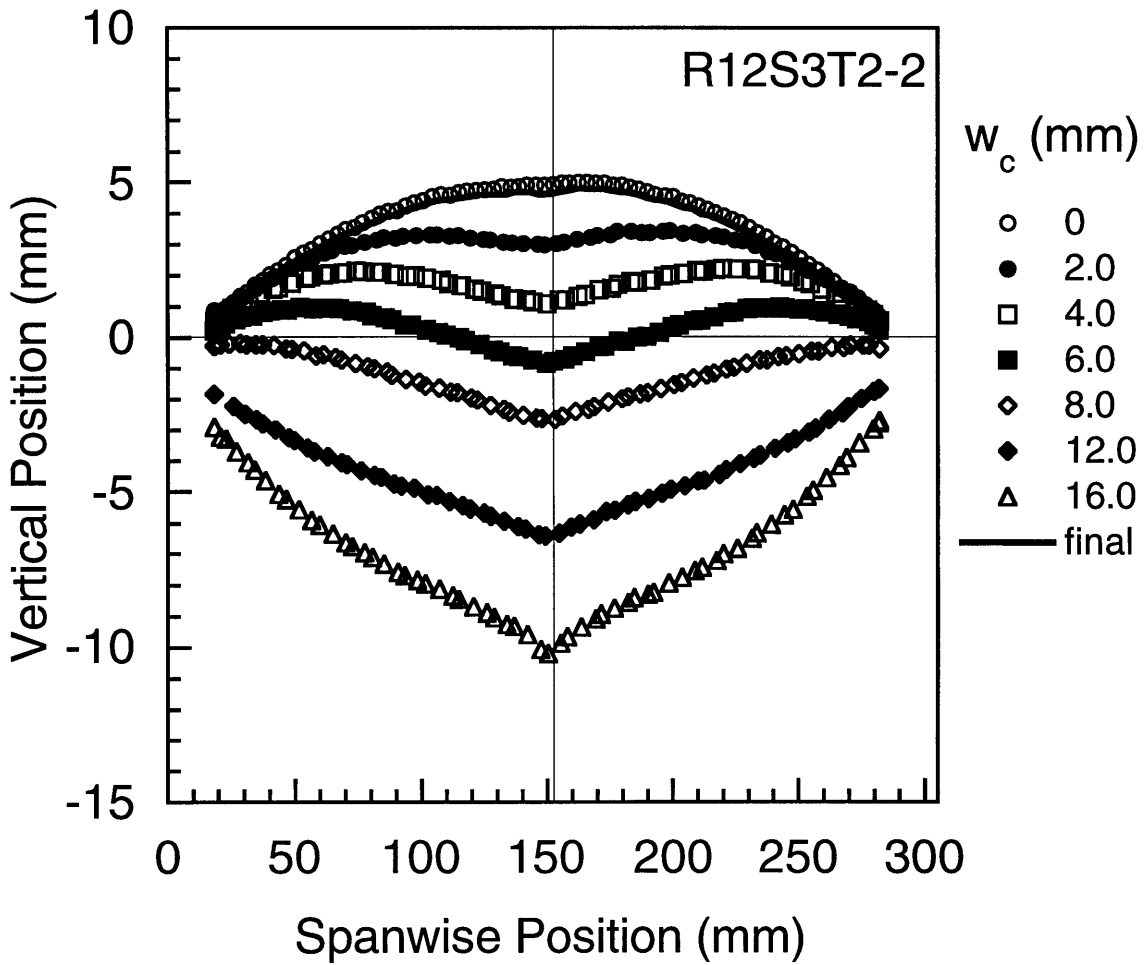


Figure 6.20 Measured central spanwise deformation modes for specimen $R_{12}S_3T_2-2$ at different values of center deflection.

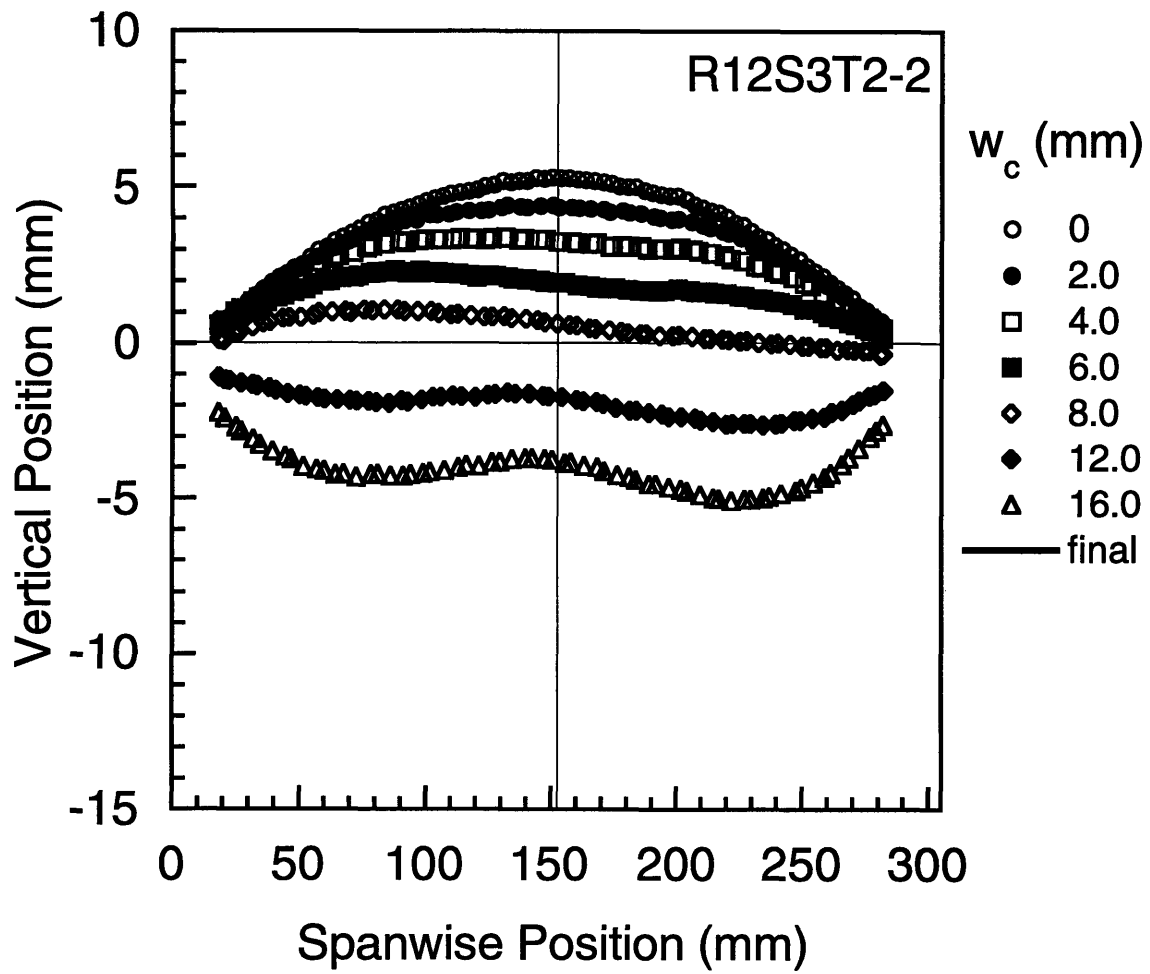


Figure 6.21 Measured left spanwise deformation modes for specimen $R_{12}S_3T_{2-2}$ at different values of center deflection.

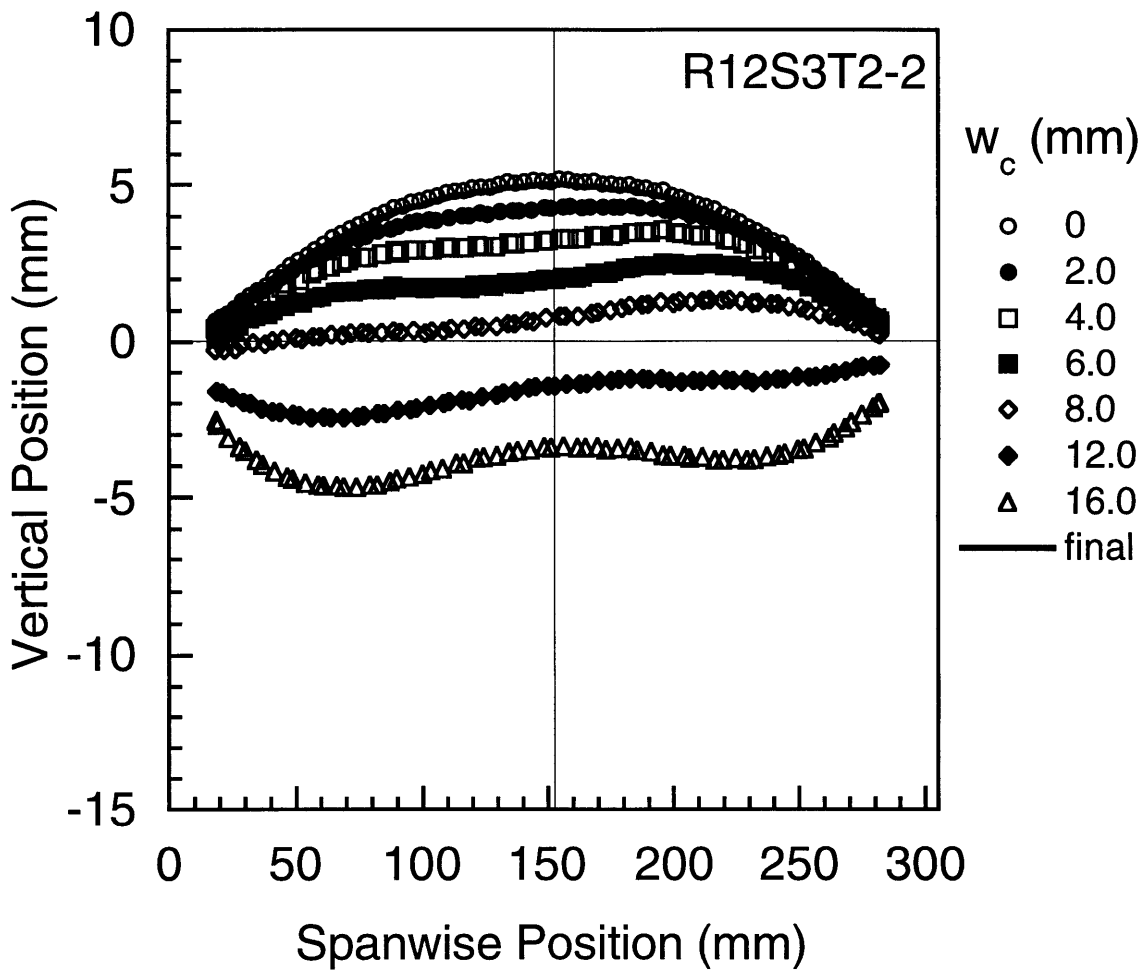


Figure 6.22 Measured right spanwise deformation modes for specimen $R_{12}S_3T_2-2$ at different values of center deflection.

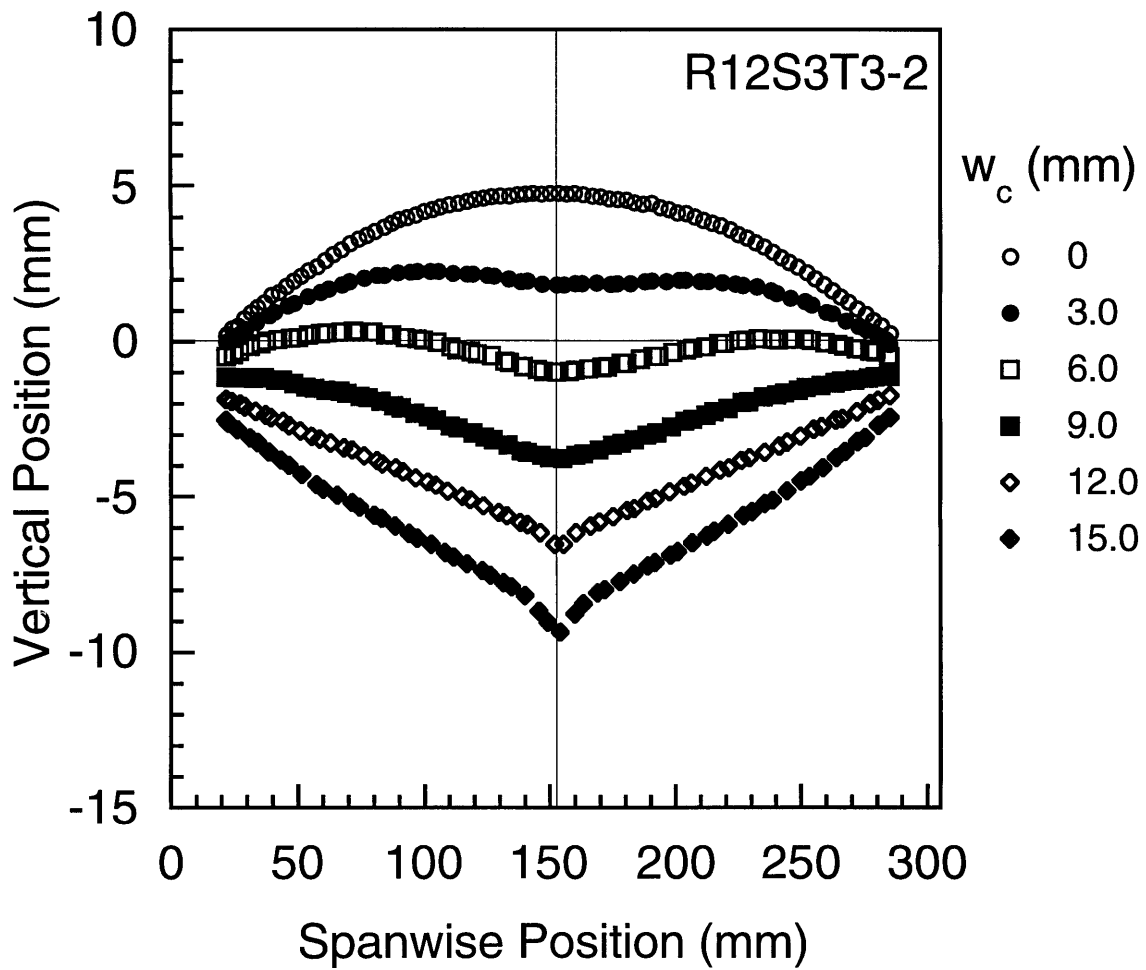


Figure 6.23 Measured central spanwise deformation modes for specimen $R_{12}S_3T_3-2$ at different values of center deflection.

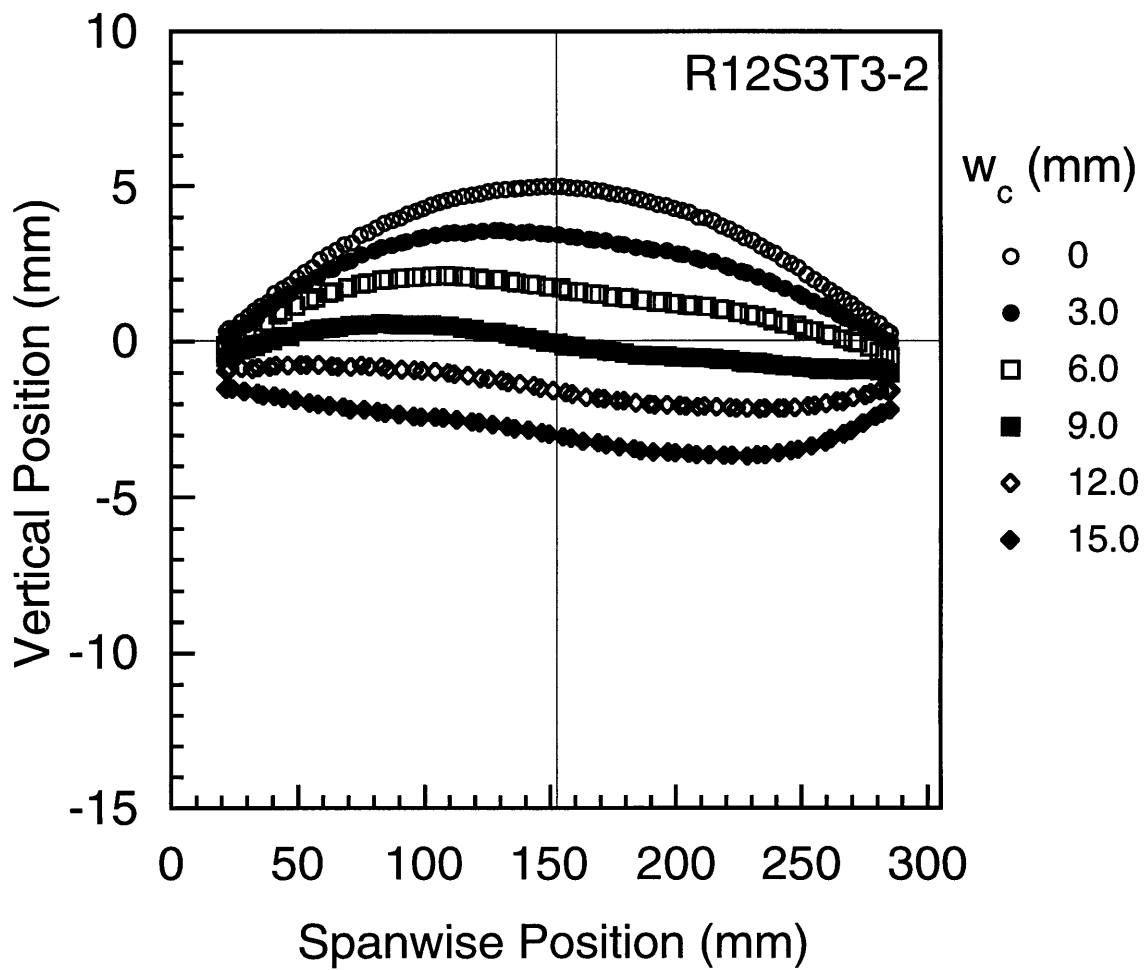


Figure 6.24 Measured left spanwise deformation modes for specimen $R_{12}S_3T_3-2$ at different values of center deflection.

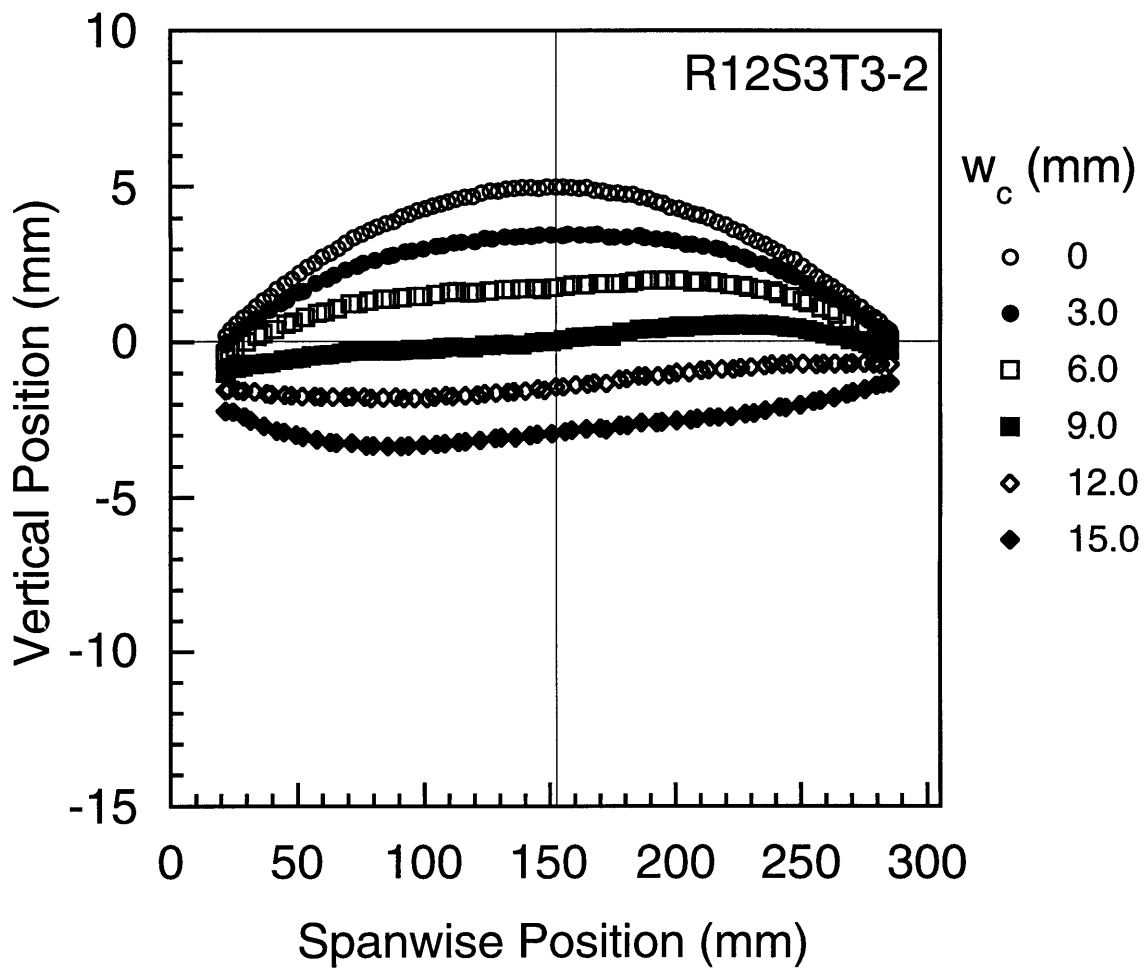


Figure 6.25 Measured right spanwise deformation modes for specimen $R_{12}S_3T_3-2$ at different values of center deflection.

shapes is the residual indentation at the loading site evident in the final, unloaded, mode shape. Both of these specimens were damaged during loading (see section 6.1.3) and the indentation is attributed to damage formation. A description of the severity and modes of damage for all specimens is given in section 6.1.3. The residual indentation is also evident, to a lesser degree, in the final mode shape for specimen $R_{12}S_3T_{2-2}$ in Figure 6.20. This is consistent with the local indentation being attributed to damage as this specimen was loaded to a lower peak deflection (and thus, peak force) than the specimen in Figure 6.14 and therefore was less severely damaged. A final mode shape for specimen $R_{12}S_3T_{3-2}$ in Figure 6.23 is not available because this specimen was inadvertently removed from the test fixture before a final mode shape was assessed.

As excellent agreement is noted between the overall loading and mode-shape deformation data, only evolutions from the mode-shape tests are used for further discussion of the response of specimen types $R_{12}S_3T_2$ and $R_{12}S_3T_3$ (Figures 6.20 to 6.25). The central spanwise deformation modes for both these specimens (Figures 6.20 and 6.23) are dominated by symmetry, *i.e.*, there is no dominant asymmetry indicative of bifurcation such as that observed for specimen type $R_{12}S_3T_1$. A slight asymmetry is discernible in the central mode shapes of specimen $R_{12}S_3T_{2-2}$ at center deflection values of 2.0 mm, 4.0 mm, and 6.0 mm and in those of specimen $R_{12}S_3T_{3-2}$ at center deflection values of 3.0 mm and 6.0 mm in Figures 6.20 and 6.23, respectively. Within fidelity of the mode measurements, it is not possible to determine whether or not these slight asymmetries indicate bifurcation.

The left and right spanwise mode shapes for these specimens shown in Figures 6.21, 6.22, 6.24, and 6.25 are also dominated primarily by symmetric deformations. Considering the left and right mode shapes for specimen

$R_{12}S_3T_2$ in Figures 6.21 and 6.22, a slight asymmetry is noted in both mode-shape evolutions beginning at a center deflection value of 2.0 mm. Comparison of the left and right mode shapes reveals that this asymmetry is antisymmetric with respect to the center of the shell. This same type of antisymmetry was previously noted for specimen type $R_{12}S_3T_1$ beginning at a center deflection value of 2.0 mm. The antisymmetry is also evident in the left and right mode shapes for specimen $R_{12}S_3T_3-2$ in Figures 6.24 and 6.25 beginning at a center deflection value of 3.0 mm. Due to the dominant symmetry in the central mode, and the antisymmetry in the left and right modes, the asymmetric deformations in the left and right mode shapes are attributed to bending-twisting coupling in the laminate. Due to this laminate coupling, bending moments in both the axial and circumferential direction will cause the shell to twist which would be manifested in the left and right mode shapes as antisymmetric modes. Antisymmetric modes due to bending-twisting coupling are further discussed in section 6.2 utilizing numerical modeling results.

6.1.3 Damage Development

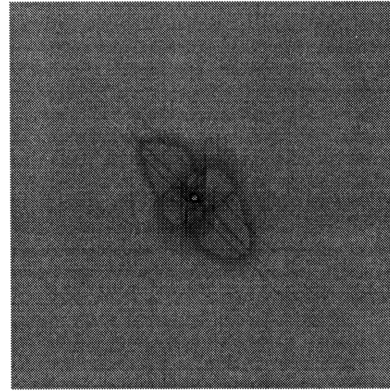
Damage was investigated using sectioning and x-radiography as described in chapter 5. X-radiography was utilized to evaluate damage development at the loading site for a given specimen type at different peak loads (used as a damage resistance metric). As discussed in chapter 2, damage becomes more severe at higher peak loads for composite shells with the *caveat* that the presence of an instability may cause significantly increased damage extent as well as atypical (as compared to plates) damage distributions. As peak load is the primary damage resistance metric, this value has been tabulated for each specimen tested in Table 6.1 along with the corresponding

Table 6.1 Peak Load and Associated Center Deflection

Specimen Type	Test Type	Peak Load	Center Deflection, w_c
$R_{12}S_3T_1-1$	Overall Loading	109 N	8.4 mm
$R_{12}S_3T_1-2$	Mode-shape	201 N	12.0 mm
$R_{12}S_3T_2-1$	Overall Loading	1737 N	19.1 mm
$R_{12}S_3T_2-2$	Mode-shape	1096 N	16.0 mm
$R_{12}S_3T_3-1$	Overall Loading	2746 N	16.6 mm
$R_{12}S_3T_3-2$	Mode-shape	1987 N	15.0 mm

value of center displacement (stroke). Sectioning was utilized to explore the possibility of damage development away from the loading site. Damage formation away from the loading site has been hypothesized due to the asymmetric nature of shell buckling modes.

No damage was found in the x-radiographs for specimen type $R_{12}S_3T_1$ where the peak loads for these two tests were 109 N and 201 N. Previous work has identified a threshold value of peak force of approximately 400 N below which no damage is found for composite shells of the same material, layup, and thicknesses [38]. The data for specimen type $R_{12}S_3T_1$ is therefore consistent with this earlier observation. Also consistent with this observation is that all specimens which reach peak forces above 400 N (specimen types $R_{12}S_3T_2$ and $R_{12}S_3T_3$) are damaged. X-radiographs of the loading site for these two specimen types are provided in Figures 6.26 and 6.27, respectively. The x-radiographs of damage for these shell specimens are typical of damage for composite plate specimens having this layup, with typical delaminations and



10 mm

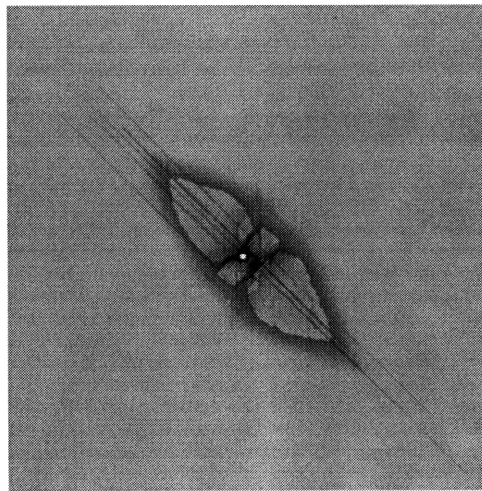
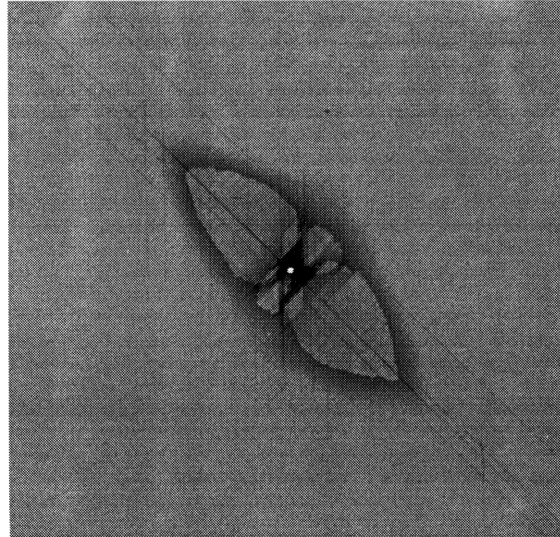


Figure 6.26 X-ray photographs of specimen type $R_{12}S_3T_2$ loaded to: (top) 1096 N ($w_c = 16.0$ mm), and (bottom) 1737 N ($w_c = 19.1$ mm).



—
10 mm

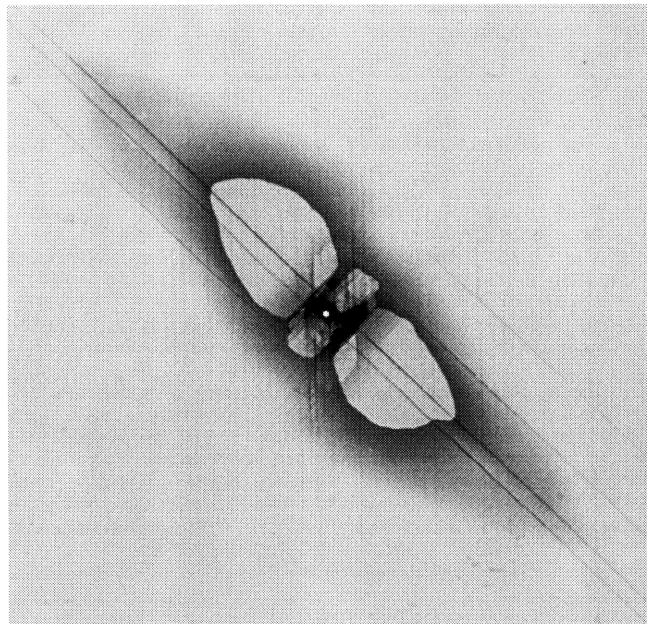


Figure 6.27 X-ray photographs of specimen type $R_{12}S_3T_3$ loaded to: (*top*) 1987 N ($w_c = 15.0$ mm), and (*bottom*) 2746 N ($w_c = 16.6$ mm).

matrix cracks along the ply fiber directions of 45° , -45° , and 0° , with the largest extent in the 45° direction. Sectioning of the specimens through the damaged region also reveals that, as is typical of plates, delamination and matrix cracking occurs on the backface (concave side) of the shell, opposite indentation (see Figure 5.16). This is further substantiated by visually observed 45° matrix cracks on the backface of both specimens directly under the indenter at maximum load and deflection (one matrix crack for specimen $R_{12}S_3T_3-1$ and two for specimen $R_{12}S_3T_3-2$). Also typical of previous findings for plates and shells (with no instability) is the observation that damage extent increases with peak force.

For the three specimen configurations tested, no damage atypical of plate-like damage was observed. Previously observed atypical damage has been attributed to bifurcation into an asymmetric mode. Thus, finding typical damage is not surprising because the two specimen types that were damaged, $R_{12}S_3T_2$ and $R_{12}S_3T_3$, did not have dominant asymmetric modes indicative of bifurcation. The specimen type which did bifurcate, $R_{12}S_3T_1$, was undamaged.

All specimens were sectioned after testing and examined under an optical microscope as described in chapter 5. Sectioning was undertaken to investigate the possibility of damage away from the loading site. This possibility has been hypothesized due to the presence of asymmetric deformation modes during bifurcation buckling. Sectioning of all specimens revealed only damage at the loading site. No additional damage sites were identified through the sectioning process, and the only damage observed was that which emanated from the loading site. Again, this is consistent with the observation that bifurcation into dominant asymmetric modes was observed only for specimen type $R_{12}S_3T_1$ which was undamaged. Thus, all of the damage observed in this work is consistent with previous x-radiograph findings

for the damage resistance of composite plates.

6.2 Numerical Analysis

Results from numerical analysis of the experimental specimens are presented in this section. As for the experimental data in section 6.1, numerical results for load-deflection behavior at the loading point and mode-shape evolutions of the shell during loading are used to characterize the response. Nominal laminate properties given in Table 4.1 and experimentally determined values of radius (see Appendix A) are utilized in the numerical analyses. Experimental and nominal values of span are identical due to the test fixture design. As in chapter 4, the shells are point-loaded at the center. Boundary conditions are modeled as in chapter 4 except for the condition along the (curved) axial edges. Whereas the axial edges were free for the shells analyzed in chapter 4, the shells in this section are restrained out-of-plane. This is accomplished within the finite element analysis by setting the transverse displacement (w) and rotation about the x -axis (R_x) to zero (see Figure 4.1). While the knife edges are designed to allow rotation about the circumferential y -axis (R_y), the upper and lower knife edges restrict rotation about the axial x -axis (R_x). Setting R_x to zero at the axial boundaries in the finite element model reflects this experimental condition. All other aspects of the numerical analyses are identical to those discussed in chapter 4.

6.2.1 Loading Response

As with the experimental results, loading response is characterized by plotting the load versus corresponding deflection (stroke in the experiments). Results from both types of testing (specimens) are presented in this section to determine the effect of the experimentally determined radii on the response.

As with the numerical analysis of specimens in chapter 4, it is instructive to consider both limit-point and bifurcation analyses for each specimen. Comparing both types of response in this way highlights the importance of bifurcation. Limit-point analyses are obtained with symmetric meshes whereas the AMT is used to assess bifurcation (or limit-point behavior if bifurcation does not exist).

All of the shells are found to have a bifurcation point followed by a limit point. This behavior is different than that encountered for the cases discussed in chapter 4 where a single critical point is observed for each shell. Therefore, the response generated using the AMT for specimen type $R_{12}S_3T_1$ is compared with the bifurcation response calculated using two traditional techniques. This is done to validate the new technique with regard to this different type of shell behavior. A converged solution using a symmetric mesh is first undertaken prior to inducing bifurcation using traditional techniques. The equivalence transform and geometric imperfection techniques were previously discussed and used to evaluate shell bifurcation in chapter 4. Finally, bifurcation for these shells is investigated using the AMT.

The response of specimen $R_{12}S_3T_1-1$ utilizing three symmetric meshes is presented in Figure 6.28 to investigate convergence via mesh refinement. The 10x10 mesh is not converged by comparison to the 20x20 and 30x30 meshes. However, the 20x20 mesh is sufficiently refined because it gives a converged solution to the shell limit-point response. The response of this specimen initially softens, then stiffens, and then softens again towards a limit point near a load of 145 N and a center deflection value of approximately 9 mm. Postbuckling after the limit point in these cases causes convergence difficulties for the finite element analysis. Nonconvergence occurs in the numerical solution of the nonlinear shell equations when a solution can not be

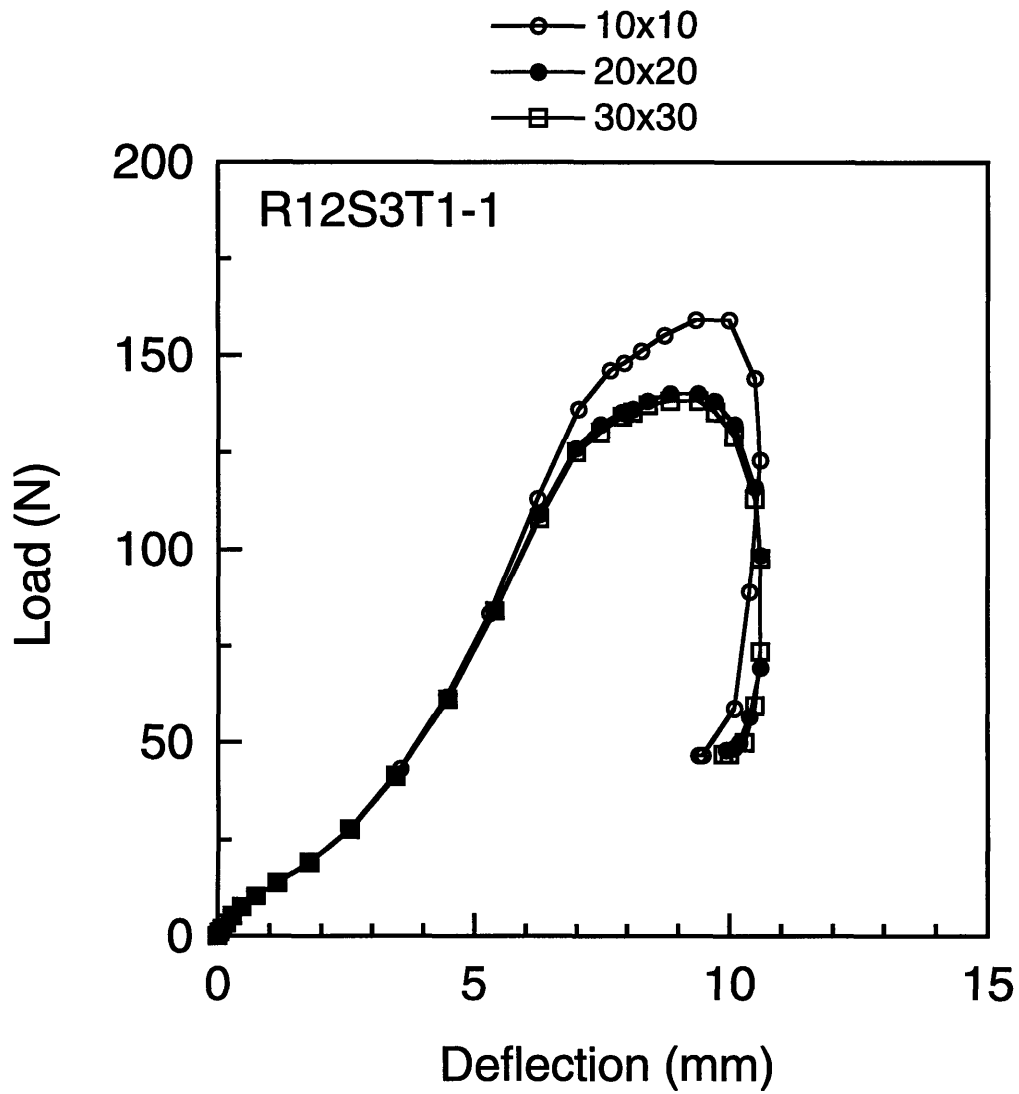


Figure 6.28 Load-deflection results from numerical analyses for specimen $R_{12}S_3T_1-1$ using symmetric meshes.

obtained even upon successive reductions in the load/displacement steps. Convergence difficulties of this sort are oftentimes encountered in practice and are found in this study for specimen types $R_{12}S_3T_1$ and $R_{12}S_3T_2$. Postbuckling for these cases is likely dynamic in nature, and thus an analysis which includes inertia of the composite shell would be required. A transient (dynamic) analysis is typically employed in such cases to characterize the response [73]. Dynamic analyses of this sort are beyond the scope of this work. Furthermore, as discussed in chapter 3, the response prior to this postbuckling is of interest in this work because it addresses the response region where shell behavior differs from plates. Thus, the current analysis is sufficient for the objectives of this work. In addition, postbuckling of specimen types $R_{12}S_3T_3$ will later be shown to be adequately captured by the static analyses. This is interpreted to mean that postbuckling of the thicker specimens is not dynamic, most likely due to the increased bending stiffness of the shell, which acts to resist the dynamic motion.

Bifurcation of specimen $R_{12}S_3T_1-1$ is investigated using the AMT and these results are compared to the limit-point response using a symmetric 20x20 mesh in Figure 6.29. The response calculated using the AMT is noted to bifurcate from the primary path at approximately 130 N, approximately 15 N below the limit-point solution calculated with the converged symmetric mesh. Thus, the shell bifurcates before reaching the limit point. This bifurcation point will be shown, in section 6.2.2, to be associated with a dominant asymmetric mode similar to that encountered for the composite shells discussed in chapter 4. After bifurcation, the response follows a descending path very close to the primary path as both load and deflection decrease to approximately 40 N and 3.8 mm, respectively. At this point, the response is noted to resume loading upon a second equilibrium path which leads to a second

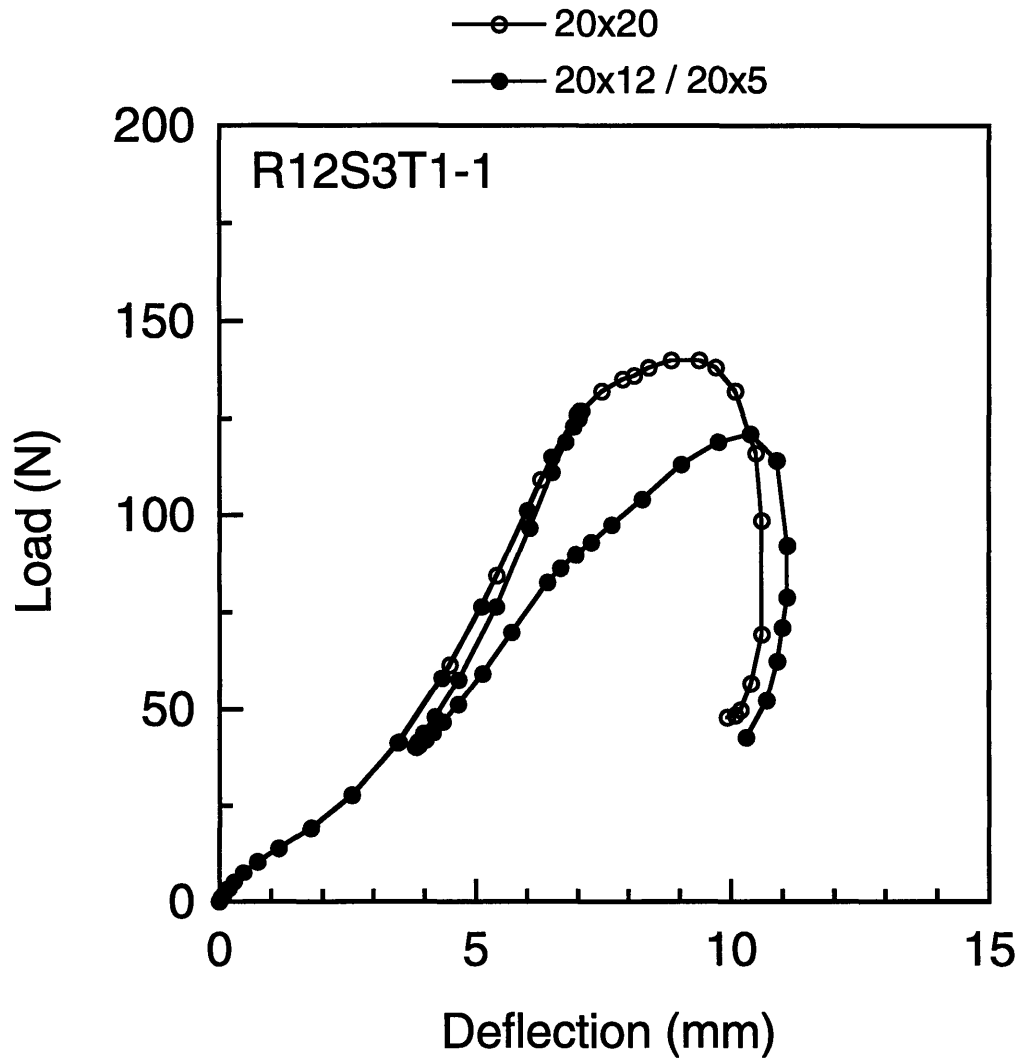


Figure 6.29 Load-deflection results from numerical analyses for specimen $R_{12}S_3T_1-1$ using symmetric and asymmetric meshes.

critical point. This second critical point is a limit point and is not associated with bifurcation. After the second critical point, the response parallels the limit-point path from the symmetric analysis and convergence difficulties are again encountered. Much like the second equilibrium path for the benchmark problem discussed in chapter 4, it is likely that the bifurcation and limit-point postbuckling paths will correspond as the shell snaps through to an inverted configuration and regains load-carrying capability on a third (and final) equilibrium path. This behavior will later be noted for specimen type $R_{12}S_3T_3$ where load-carrying capability is regained on a third such equilibrium path.

Both load and deflection decrease after the bifurcation point on the descending path for specimen $R_{12}S_3T_1-1$ in Figure 6.29. This type of response, where both load and deflection decrease simultaneously, can only be realized in an analysis where the "loading" is a combination of both load and deflection increments (path-parameter). In a load-controlled test, the response at the bifurcation point would "snap" (at a constant load of 130 N) dynamically to the second equilibrium path, just prior to the limit point. In a deflection (stroke)-controlled test, the response at the bifurcation point would dynamically "snap" (at a constant center deflection of 7.1 mm) to the second equilibrium path. Thus, the single response calculated using the path-parameter method allows both the load- and deflection- controlled response of the shell to be evaluated.

Other asymmetric meshes are used to calculate the response of specimen $R_{12}S_3T_1-1$ to evaluate convergence of the bifurcation solution. A very coarse 10x6 / 10x5 mesh is noted to induce bifurcation but the response is not converged by comparison to a more refined 32x18 / 32x7 mesh in Figure 6.30. However, convergence is obtained using the 20x12 / 20x5 mesh in Figure 6.29 which corresponds to the more refined mesh result in Figure 6.30. Asymmetric 20x12 / 20x7 and 32x18 / 32x9 meshes did not induce bifurcation,

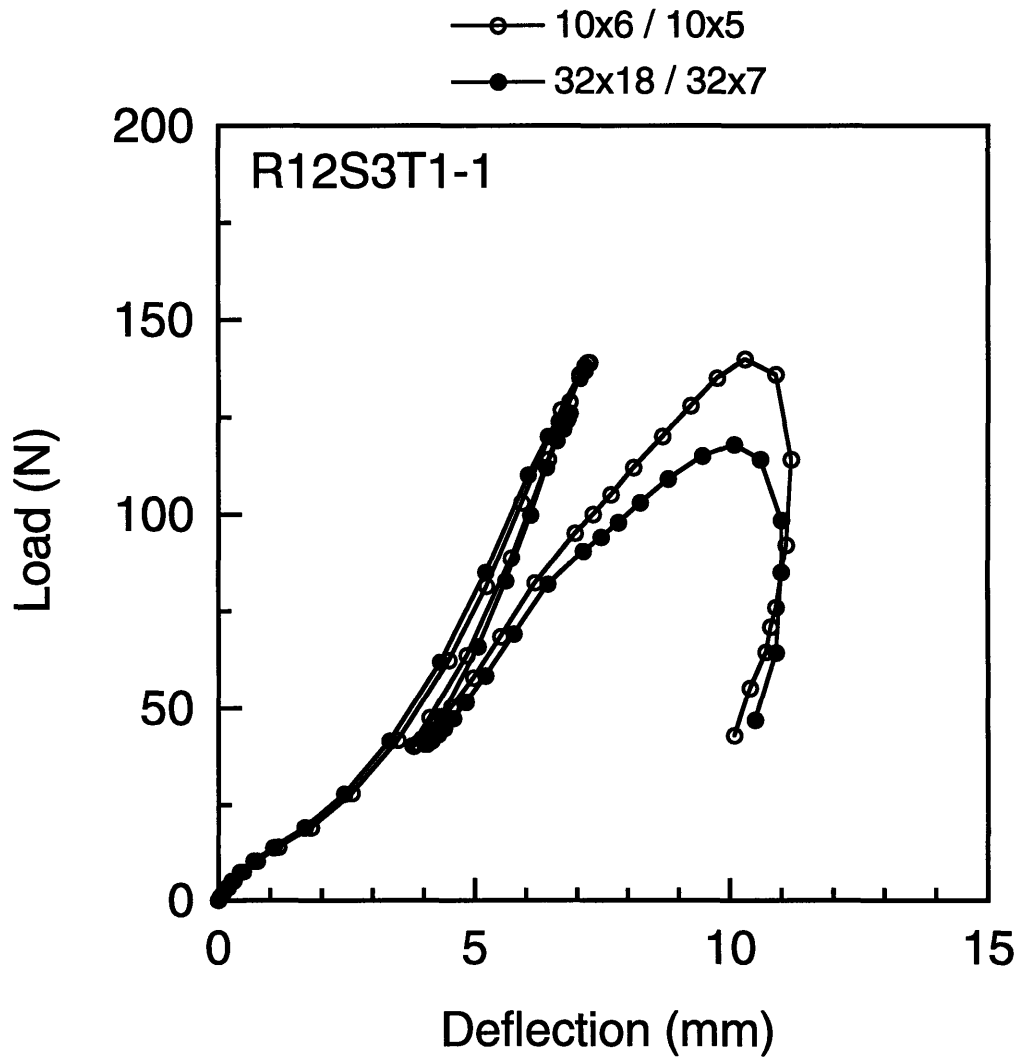


Figure 6.30 Load-deflection results from numerical analyses for specimen $R_{12}S_3T_1-1$ using various asymmetric meshes.

but rather found the limit-point response. Thus, for specimen $R_{12}S_3T_1-1$, a $20 \times 12 / 20 \times 5$ mesh is sufficient to find the converged bifurcation response. These observations are consistent with the discussion of mesh refinement and asymmetric meshing given in chapter 4.

The bifurcation point at a load value of 130 N and a center deflection of 7.1 mm, and the associated postbuckling path, are next evaluated using two traditional methods to verify the AMT solution. Results from the 20×20 and 30×30 symmetric mesh analyses (see Figure 6.28) indicate, by a change in sign of the determinant of the tangent stiffness matrix, that a bifurcation point exists at 129.7 N. The first bifurcation mode at this point on the primary (first equilibrium) path is found to be dominated by an asymmetry much like that encountered in chapter 4 for similar composite shells. A central spanwise plot of this bifurcation mode, scaled to 1000% of the shell thickness, is presented in Figure 6.31 to illustrate the asymmetry. The equivalence transform technique is next utilized to assess bifurcation near the indicated critical (bifurcation) point of 129.7 N. The bifurcation mode is assumed as a solution at 126 N and the load minimized to initiate a branch switch. The technique failed to switch to the bifurcation path over a large range of assumed modal amplitudes (as a percentage of specimen thickness): 1%, 10%, 50%, 100%, 500%, 1000%. In all cases, a switch was not initiated and the response remained on the primary path. A branch switch was next attempted at 129 N using a variety of modal amplitudes for the first eigenmode. Bifurcation did not occur for amplitudes (as a percentage of specimen thickness) of 1%, 5%, 10%, or 25%, but was initiated at 50% and 100%. Numerical results from a successful switch (50% t) are shown in Figure 6.32. By comparison to Figure 6.29, the bifurcation response in Figure 6.32 corresponds to that found previously using the AMT.

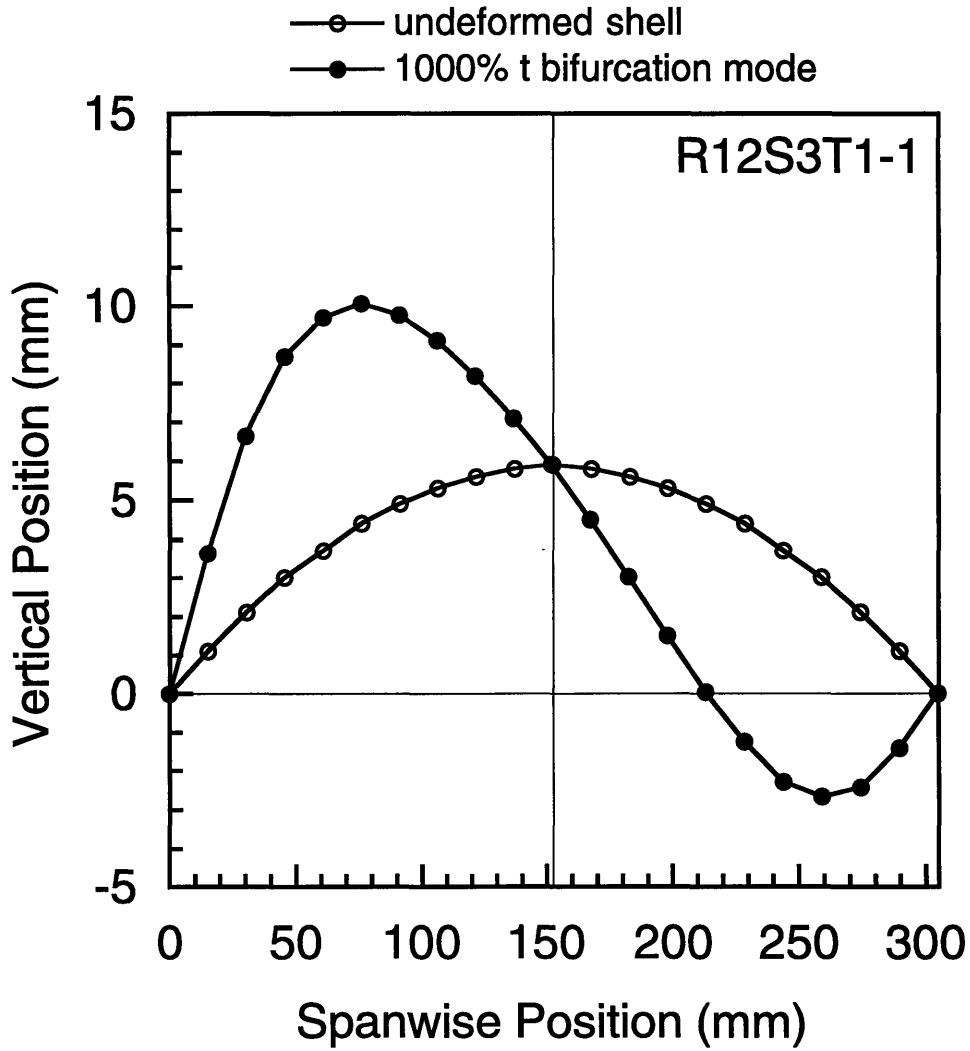


Figure 6.31 Central spanwise bifurcation mode evaluated at 126 N for specimen $R_{12}S_3T_1-1$ using a symmetric (20x20) mesh.

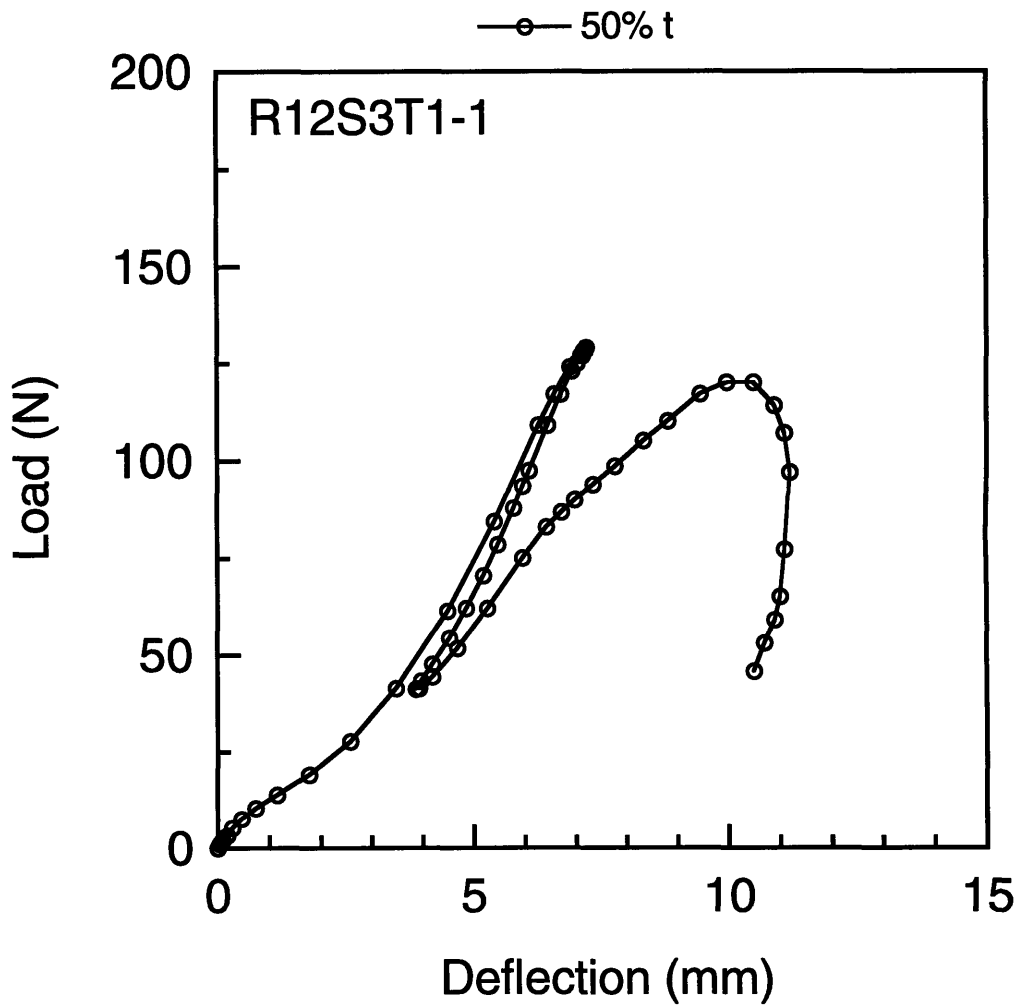


Figure 6.32 Load-deflection results from numerical analyses of specimen $R_{12}S_3T_1-1$ using a 20x20 symmetric mesh incorporating scaled eigenmode deformations (equivalence transform) near the bifurcation point.

As an alternative to the equivalence transform technique, the second traditional technique of introducing geometric imperfections can be used to initiate a branch switch. A geometric imperfection in the form of the first eigenmode calculated near the bifurcation point (load value of 126 N) is introduced into the initial problem geometry to initiate bifurcation. As in chapter 4, the mode is introduced by scaling its largest translational amplitude as a percentage of specimen thickness. Bifurcation is initiated using a geometric imperfection with amplitude of 0.5% of the specimen thickness using a symmetric 20x20 mesh and the results presented in Figure 6.33. The bifurcation response is compared with the limit-point solution using the symmetric 20x20 mesh in Figure 6.33. By comparing Figures 6.33 and 6.29, the solution using the geometric imperfection and the AMT are found to be equivalent. The imperfection amplitude of 0.5% t is very close to the smallest imperfection which will induce bifurcation (an imperfection amplitude of 0.1% t did not induce bifurcation). Larger imperfection amplitudes (50% and 100% of thickness) are introduced to generate the solutions presented in Figure 6.34 and thereby investigate effects of the choice of imperfection amplitude. Increasing the imperfection amplitude is noted to reduce the bifurcation load significantly for a 50% t imperfection. At an imperfection equal to the specimen thickness (100% t), the response is noted to bifurcate from the primary path directly to the second equilibrium path in the bifurcation response of the unperturbed geometry (see Figure 6.29). These large amplitude imperfections are also noted to cause an increase in the value of the second critical point (near a center deflection value of 10 mm). These results indicate that alteration of the original problem (geometry) by these relatively large imperfections has a significant effect on the resulting predicted response. However, results using small geometric imperfections and the equivalence

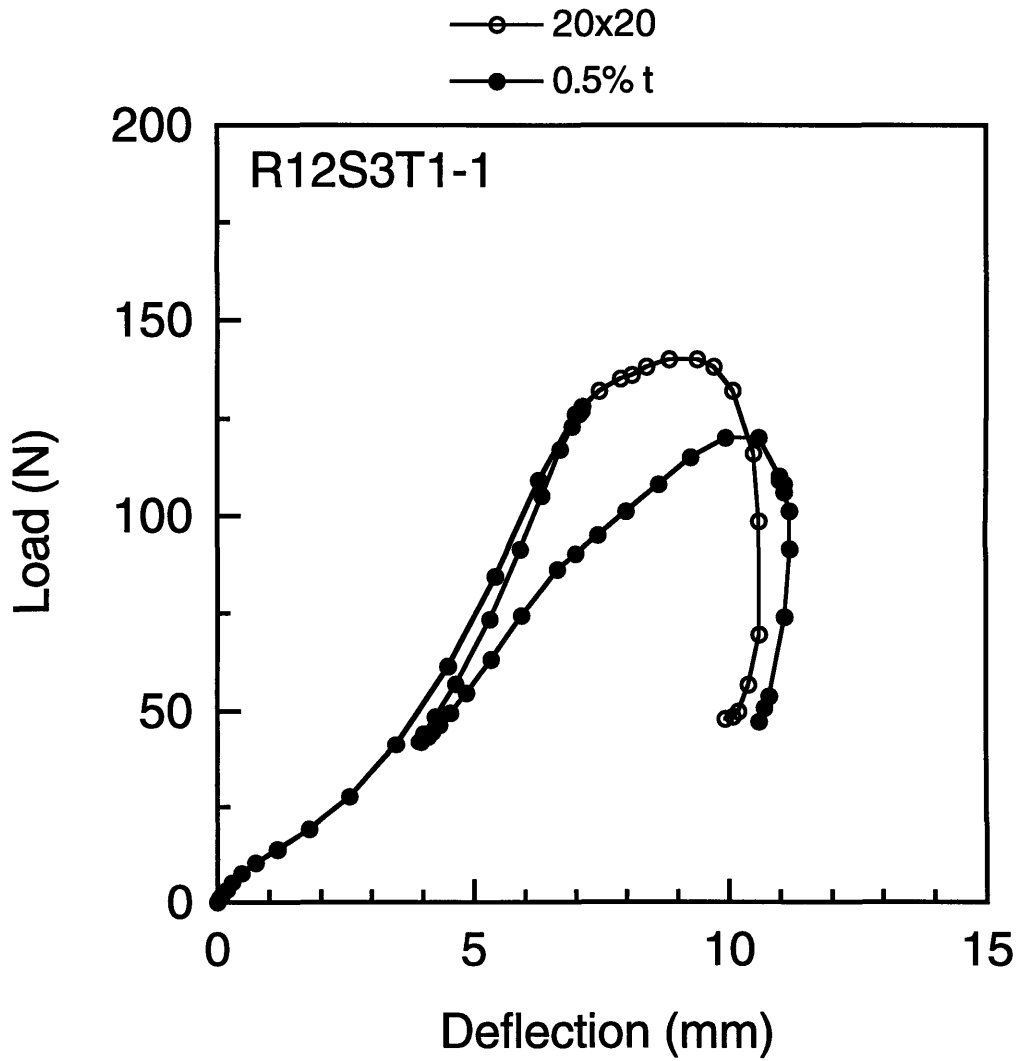


Figure 6.33 Load-deflection results from numerical analyses of specimen $R_{12}S_3T_1-1$ using a 20x20 symmetric mesh and a 20x20 symmetric mesh with a 0.5% t imperfection based on the eigenmode in Figure 6.31.

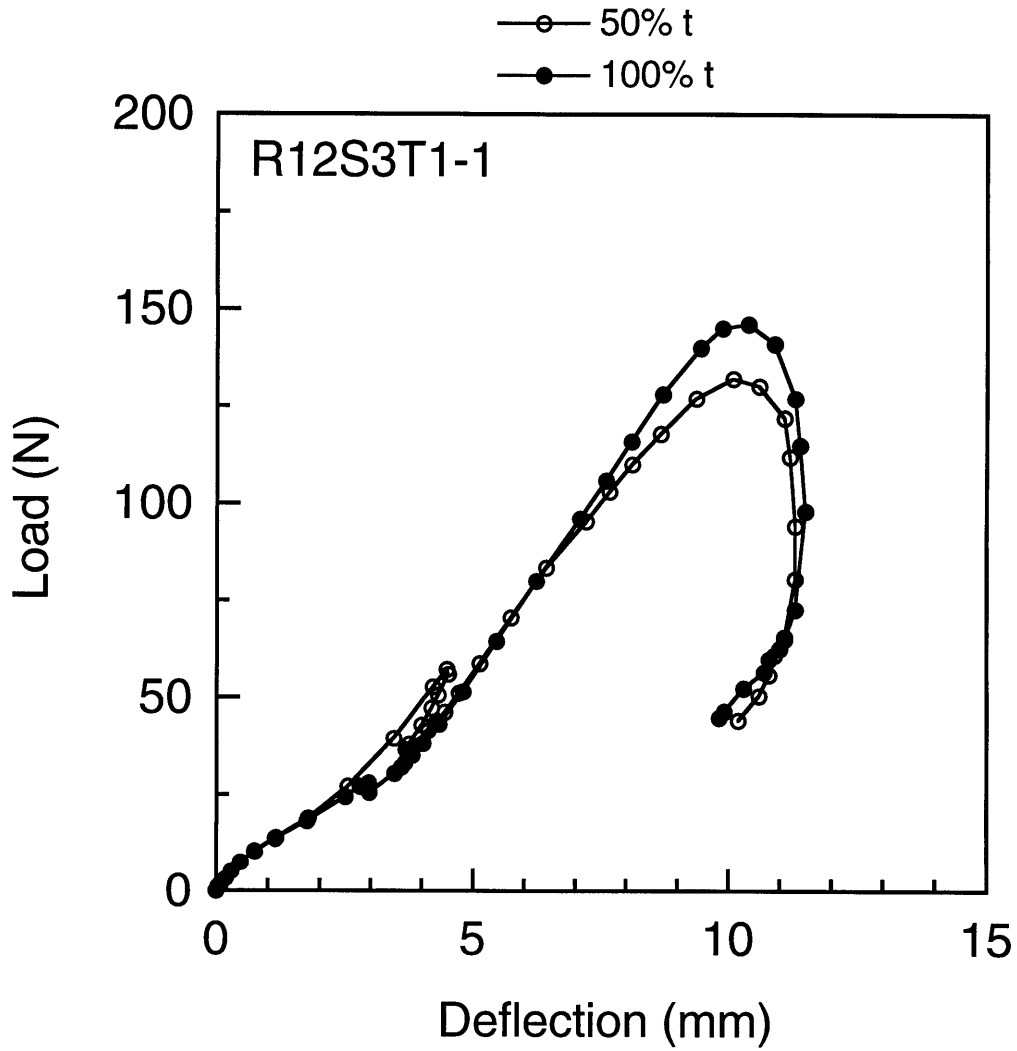


Figure 6.34 Load-deflection results from numerical analyses of specimen $R_{12}S_3T_1-1$ using a 20x20 symmetric mesh with 50% and 100% t imperfections based on the eigenmode in Figure 6.31.

transform technique both verify the AMT bifurcation solution.

The effect of changing the radius, the only difference between specimens $R_{12}S_3T_{1-1}$ and $R_{12}S_3T_{1-2}$, is explored in Figure 6.35. The converged bifurcation response for these two specimens, utilizing asymmetric 20x12 / 20x5 meshes, correspond. Thus, the difference in radius for these two specimens, (1.978 m for $R_{12}S_3T_{1-1}$, and 1.960 m for $R_{12}S_3T_{1-2}$, respectively) does not significantly affect the numerically evaluated bifurcation response.

The limit-point and bifurcation responses of specimen $R_{12}S_3T_{2-1}$ in Figure 6.36 are noted to be qualitatively similar to that of specimen type $R_{12}S_3T_1$. Bifurcation from the primary path is followed by a path characterized by decreasing load and deflection nearly coincident with the primary path. The response then begins loading on a second equilibrium path towards a second critical (limit) point. Although not physically meaningful, the limit-point response is provided for comparison to the bifurcation response. A 20x20 symmetric mesh and a 20x12 / 20x7 asymmetric mesh are found to give converged limit-point and bifurcation solutions, respectively, for this specimen type. As with specimen type $R_{12}S_3T_1$, all solutions (symmetric and asymmetric meshes) for specimen $R_{12}S_3T_{2-1}$ are found to experience convergence difficulties after the second critical point. Also in agreement with the findings for specimen type $R_{12}S_3T_1$ is that the small difference in radius between specimens $R_{12}S_3T_{2-1}$ and $R_{12}S_3T_{2-2}$ has little effect on the numerically predicted response. This can be seen in the results presented in Figure 6.37.

The response of specimen type $R_{12}S_3T_3$ qualitatively differs from those of specimen types $R_{12}S_3T_1$ and $R_{12}S_3T_2$ in two ways: there is only one critical point and, as mentioned previously, there are no convergence difficulties associated with traversing onto the final (third) equilibrium path. The

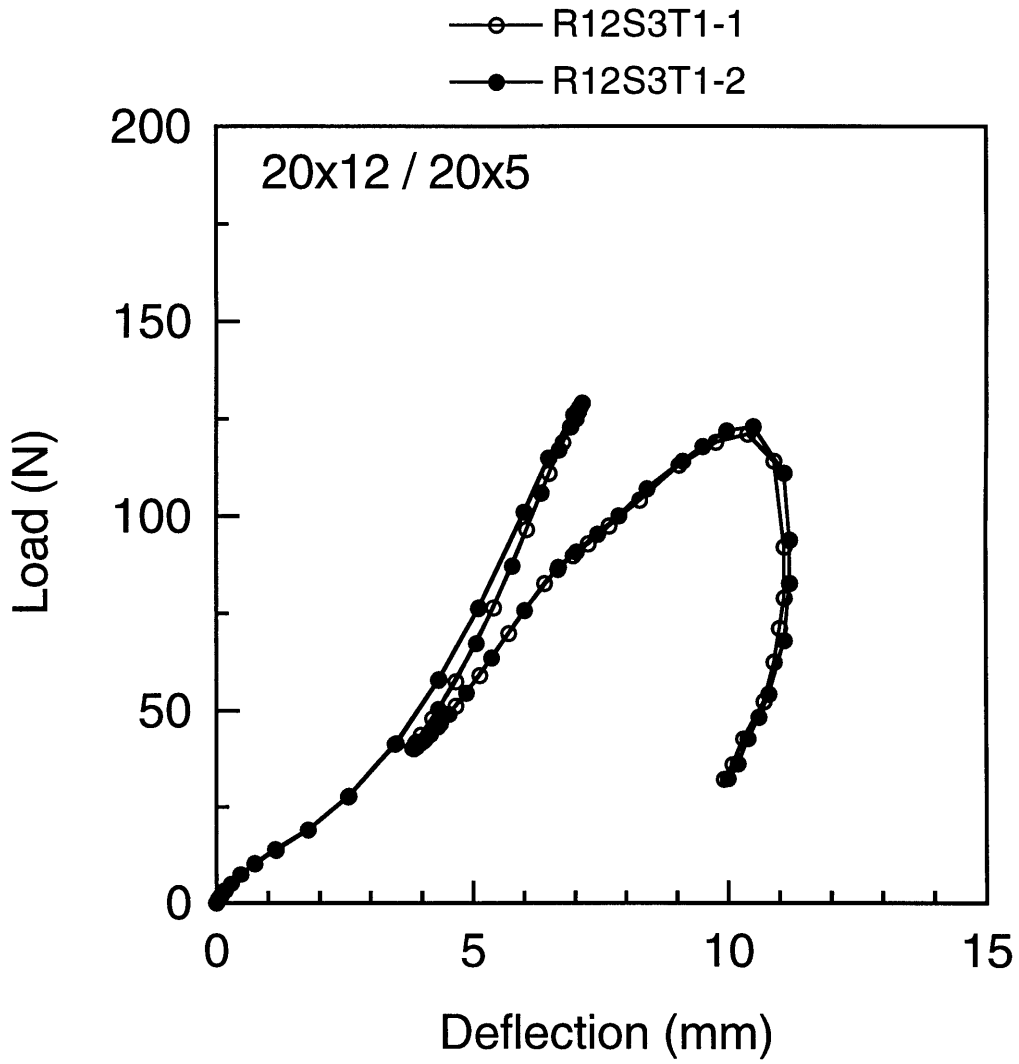


Figure 6.35 Load-deflection results from numerical analyses for specimens $R_{12}S_3T_1-1$ and $R_{12}S_3T_1-2$ using an asymmetric (20x12 / 20x5) mesh.

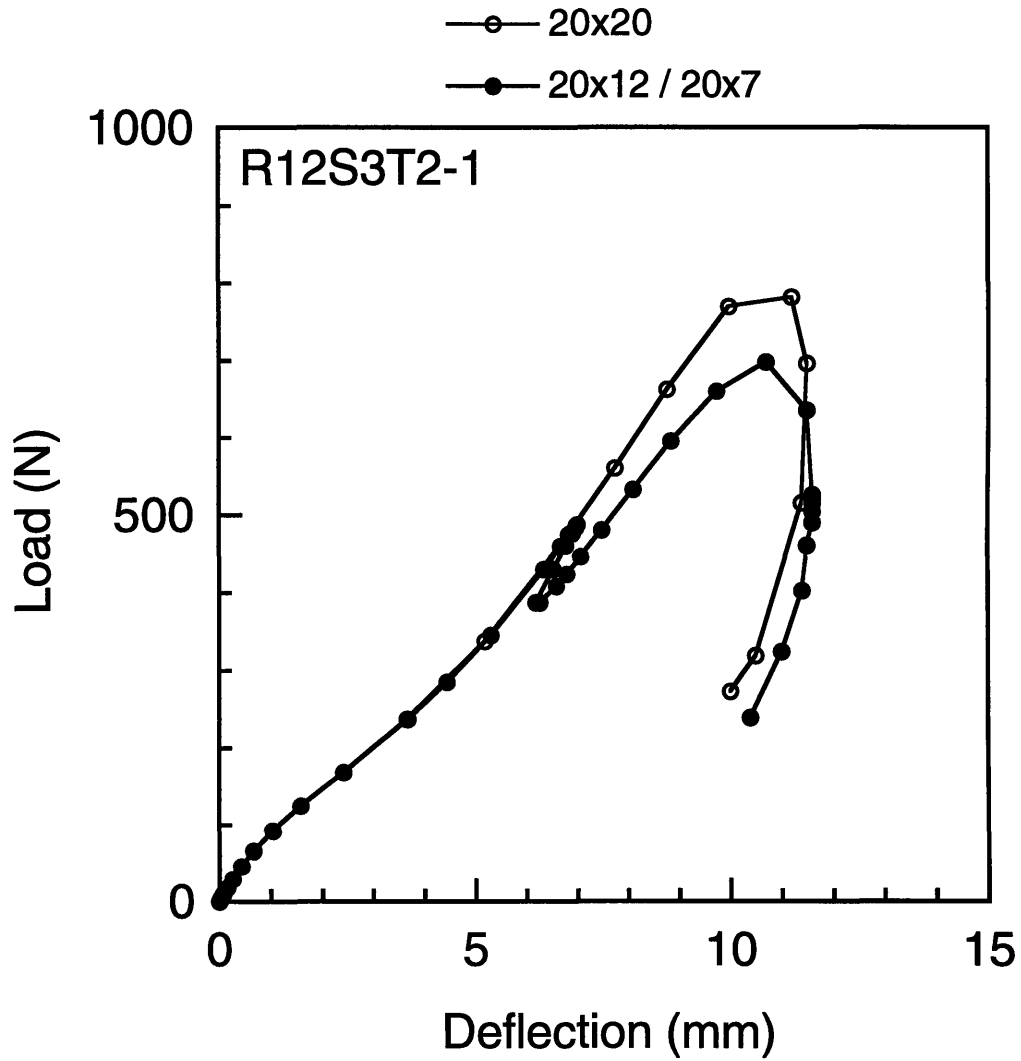


Figure 6.36 Load-deflection results from numerical analyses for specimen $R_{12}S_3T_2-1$ using symmetric and asymmetric meshes.

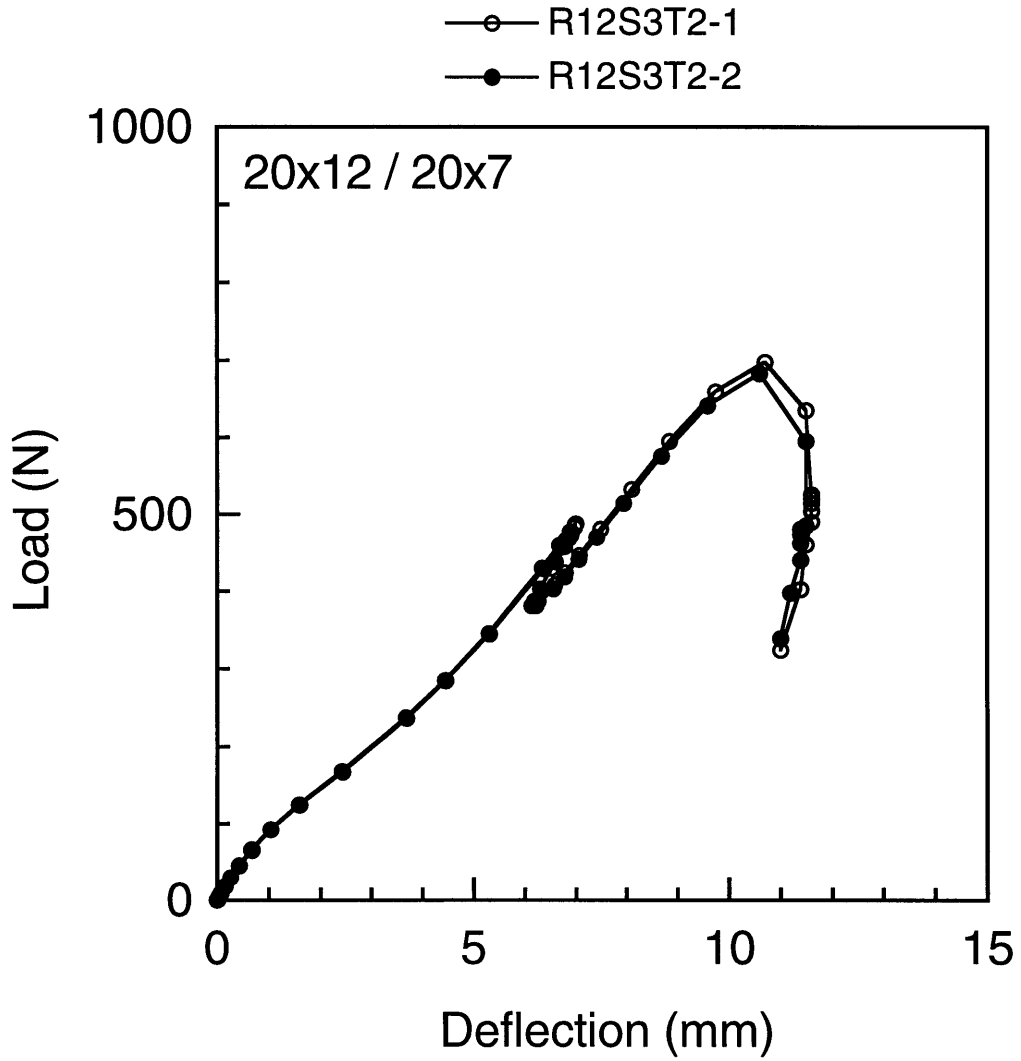


Figure 6.37 Load-deflection results from numerical analyses for specimens $R_{12}S_3T_{2-1}$ and $R_{12}S_3T_{2-2}$ using an asymmetric (20x12 / 20x7) mesh.

converged limit-point and bifurcation responses for specimen $R_{12}S_3T_3-1$ are presented in Figure 6.38 using 20x20 symmetric and 20x12 / 20x7 asymmetric meshes, respectively. The bifurcation response follows the primary response until a center deflection value of 7.1 mm (load value of 1080 N) where bifurcation occurs onto a stable secondary path. The secondary path associated with the bifurcation lies very close to the primary path as shown in the exploded-view of the response in Figure 6.39. The response reaches a critical (limit) point at approximately 1440 N (10.0 mm center deflection). The load drops rapidly after the critical point at a center deflection value of 11.2 mm to a load of approximately 925 N where the response reaches the final postbuckling path and regains its load-carrying capability. Thus, for specimen type $R_{12}S_3T_3$, bifurcation is subtle relative to the other specimen types and there are no convergence difficulties associated with the transition to the final equilibrium path. As with the other two specimen types, the response of specimens $R_{12}S_3T_3-1$ and $R_{12}S_3T_3-2$ in Figure 6.40 reveals that the radius difference (largest of all the specimen types) between these two specimens has little effect on the resulting numerical response.

As with the experimental data (see Figure 6.7), it is instructive to consider the response of the three specimen types relative to one another. The numerical load-deflection response for the three specimens are presented in Figure 6.41 for comparison. It is immediately obvious that thicker panels, as expected, are stiffer both initially and overall. Both the load and deflection range associated with the bifurcation point (instability region) decreases significantly with thickness as can be noted by comparing the responses of specimen $R_{12}S_3T_1-1$ and $R_{12}S_3T_2-1$. This instability region associated with the bifurcation point disappears altogether for specimen $R_{12}S_3T_3-1$. The deflection associated with the critical points at both the first bifurcation point and the

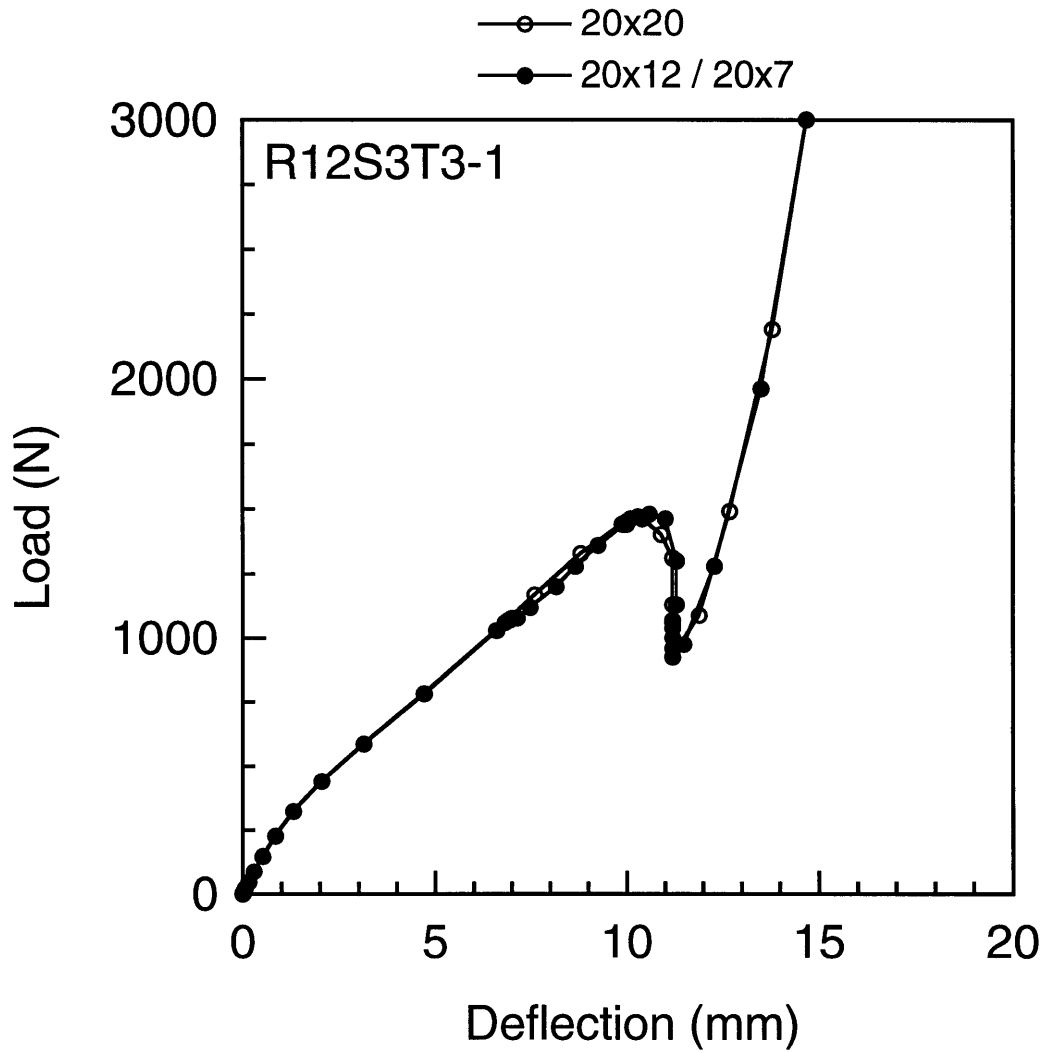


Figure 6.38 Load-deflection results from numerical analyses for specimen $R_{12}S_3T_3-1$ using symmetric and asymmetric meshes.

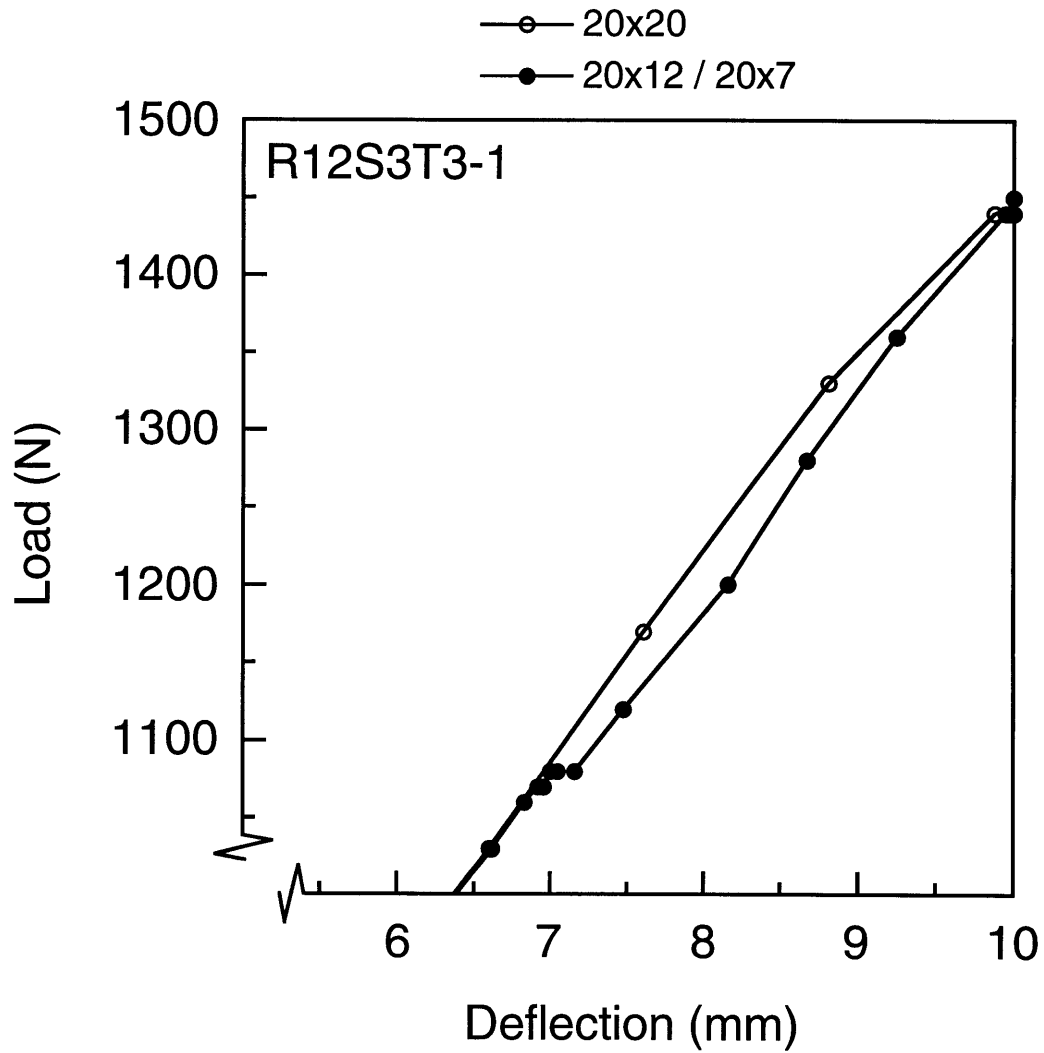


Figure 6.39 Blow-up of Figure 6.38 in area of bifurcation: load-deflection results from numerical analyses for specimen $R_{12}S_3T_3-1$ using symmetric and asymmetric meshes.

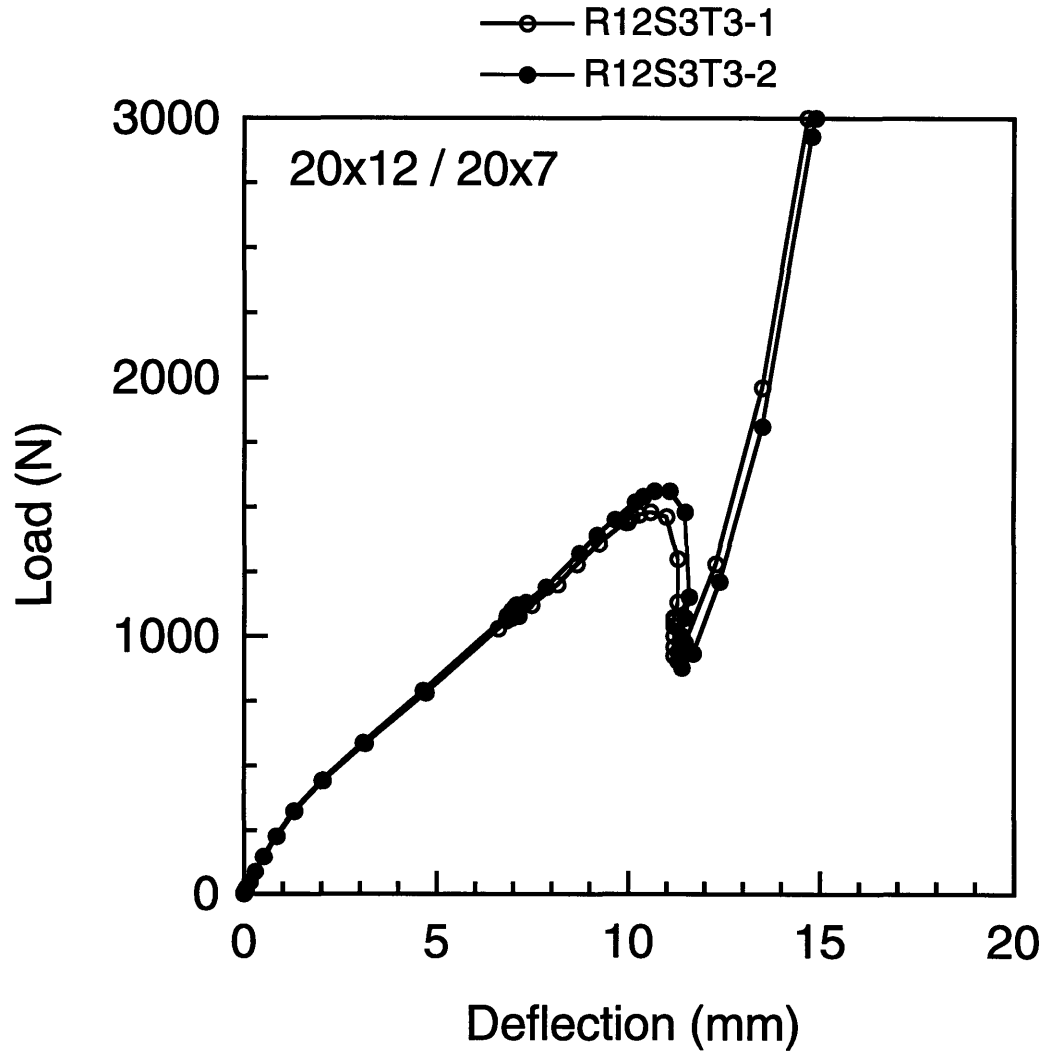


Figure 6.40 Load-deflection results from numerical analyses for specimens $R_{12}S_3T_3-1$ and $R_{12}S_3T_3-2$ using an asymmetric (20x12 / 20x7) mesh.

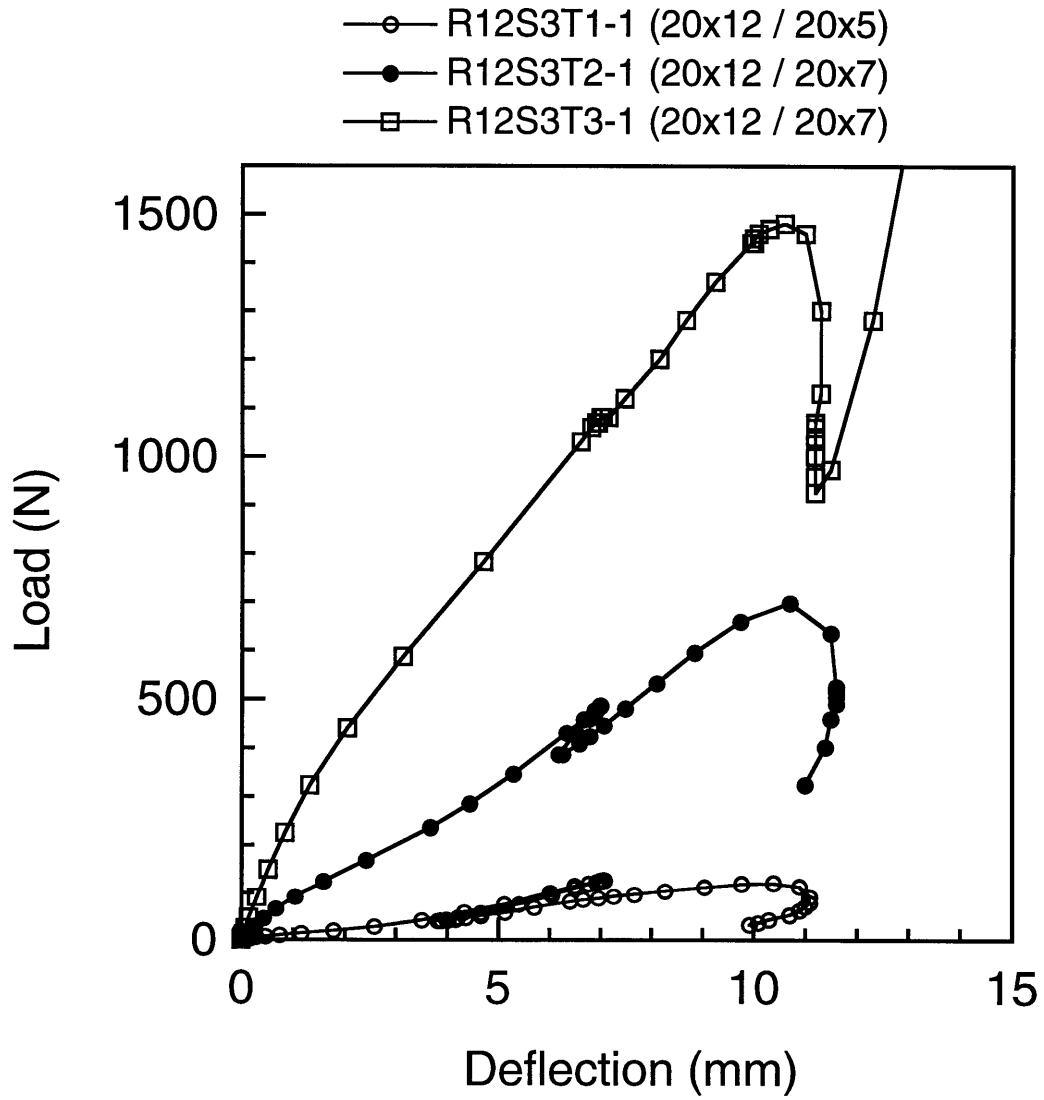


Figure 6.41 Load-deflection results from numerical analyses for specimens $R_{12}S_3T_1-1$, $R_{12}S_3T_2-1$, and $R_{12}S_3T_3-1$ using asymmetric meshes.

second critical (limit) point, are noted to be approximately independent of thickness when radius and span are held constant. Bifurcation occurs at a center deflection of approximately 7.0 mm, and the second local maximum occurs at a value of approximately 10.5 mm for all specimen types. However, the loads associated with these points clearly increase with increasing specimen thickness. The consistent values of deflection associated with buckling for specimens of different thickness has been noted in previous work with arches (*e.g.*, [52]) and is related to the typical shell-height parameter. As a result, shell height is oftentimes used to nondimensionalize transverse deformations of arches and shells, *e.g.*, [33, 54]. Nominal shell height for the shells in this work is 6.4 mm which is slightly less than the displacement corresponding to bifurcation (7.0 mm). However, the out-of-plane deformations vary from a maximum at the shell center to zero at the restrained axial edges. Thus, these shells do not deform as arches, but they do share the geometric characteristic that buckling occurs at a consistent center deflection approximately corresponding to the shell height.

6.2.2 Mode-shape Evolutions

The calculated numerical response for the three specimen types discussed in the previous section, particularly bifurcation versus limit point buckling, can be further elucidated by considering deformation evolutions. As there is little difference in the calculated loading response for specimens of a given thickness, only deformation evolutions for the mode-shape tests ($R_{12}S_3T_n$ -2 specimen types) are presented. Mode-shape evolutions for these specimens are required later for comparison to the experimental data. The mode-shape evolutions are presented in the same format as in section 6.1 for direct comparison in chapter 7. The converged AMT bifurcation solutions for

each specimen type are utilized to construct the mode-shape evolutions. Refinement of these asymmetric meshes are $20 \times 12 / 20 \times 5$ for specimen $R_{12}S_3T_{1-2}$, and $20 \times 12 / 20 \times 7$ for specimens $R_{12}S_3T_{2-2}$ and $R_{12}S_3T_{3-2}$.

The numerically evaluated central, left, and right mode-shape evolutions for specimen $R_{12}S_3T_{1-2}$ are presented in Figures 6.42, 6.43, and 6.44, respectively. Mode shapes are presented at key values in the shell response: the initial (undeformed) shell, near the midpoint of the first equilibrium path, just prior to and just after the bifurcation point, at the start of and near the midpoint of the second equilibrium path, at the limit point, and after the limit point near the midpoint of the postbuckling path. The central deformation mode for this specimen is noted to be symmetric at center deflection values of 2.6 mm and 7.1 mm, the latter being the last point evaluated prior to bifurcation. At a center deflection value of 6.9 mm, just after bifurcation, the mode shape is noted to be slightly asymmetric. The central mode shape is then dominated by an asymmetric mode at a center deflection of 3.8 mm (load value of 40.4 N) corresponding to the local minimum at the beginning of the second equilibrium path (see Figure 6.29). The asymmetry is still clearly evident on the second equilibrium path and at the second critical (limit) point at center deflection values of 7.9 mm (load value of 100 N) and 10.5 mm (load value of 123 N), respectively. The response remains asymmetric into the second postbuckling region at a load and deflection of 82.6 N and 11.2 mm, respectively. Thus, the response along the center of the shell is dominated by symmetry until bifurcation, where an asymmetric mode dominates through the second postbuckling region (after the second critical point).

The left and right mode-shape evolutions in Figures 6.43 and 6.44 of specimen $R_{12}S_3T_{1-2}$ have similar symmetries and asymmetries at the same values of center deflection as the central spanwise mode in Figure 6.42. The

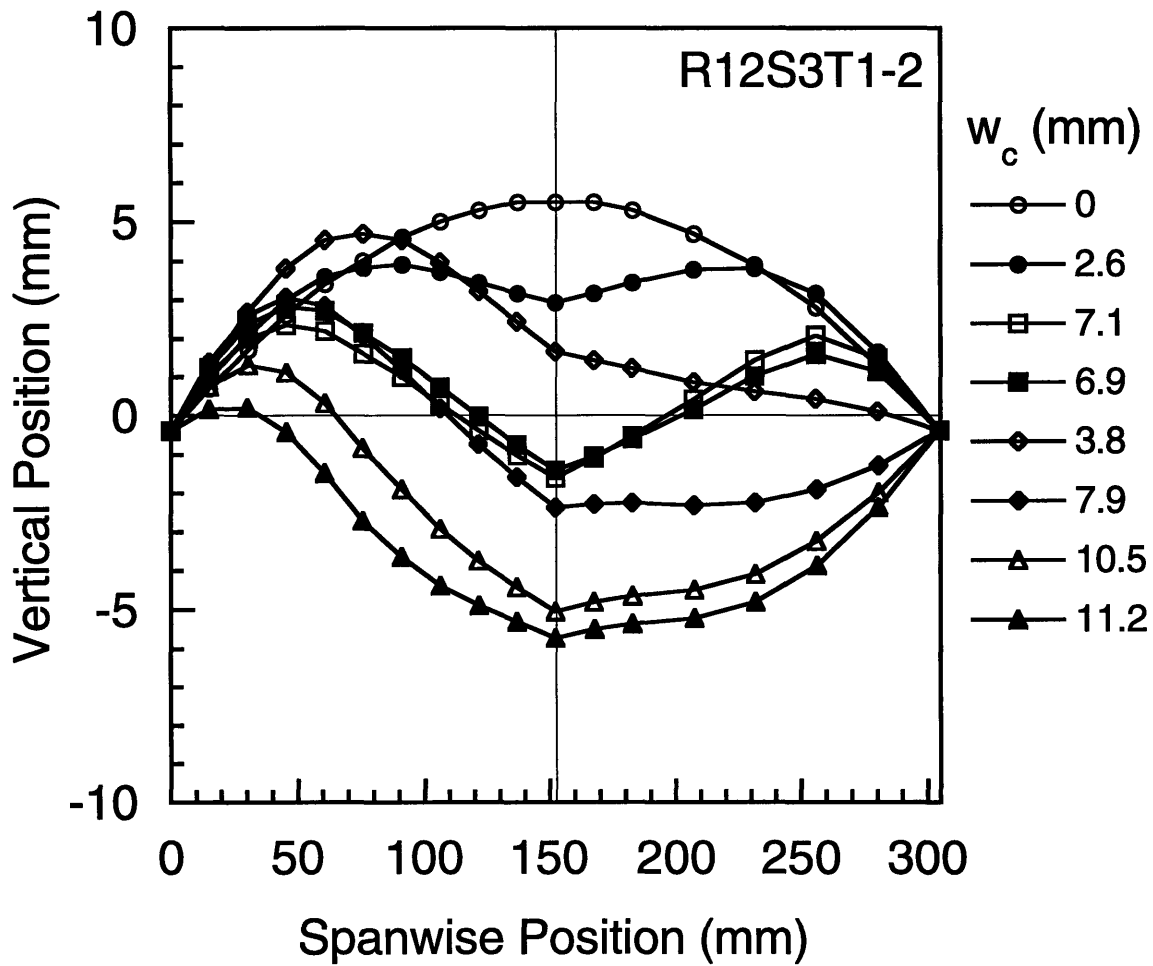


Figure 6.42 Numerical analysis results of central spanwise deformation modes for specimen $R_{12}S_3T_{1-2}$ at different values of center deflection.

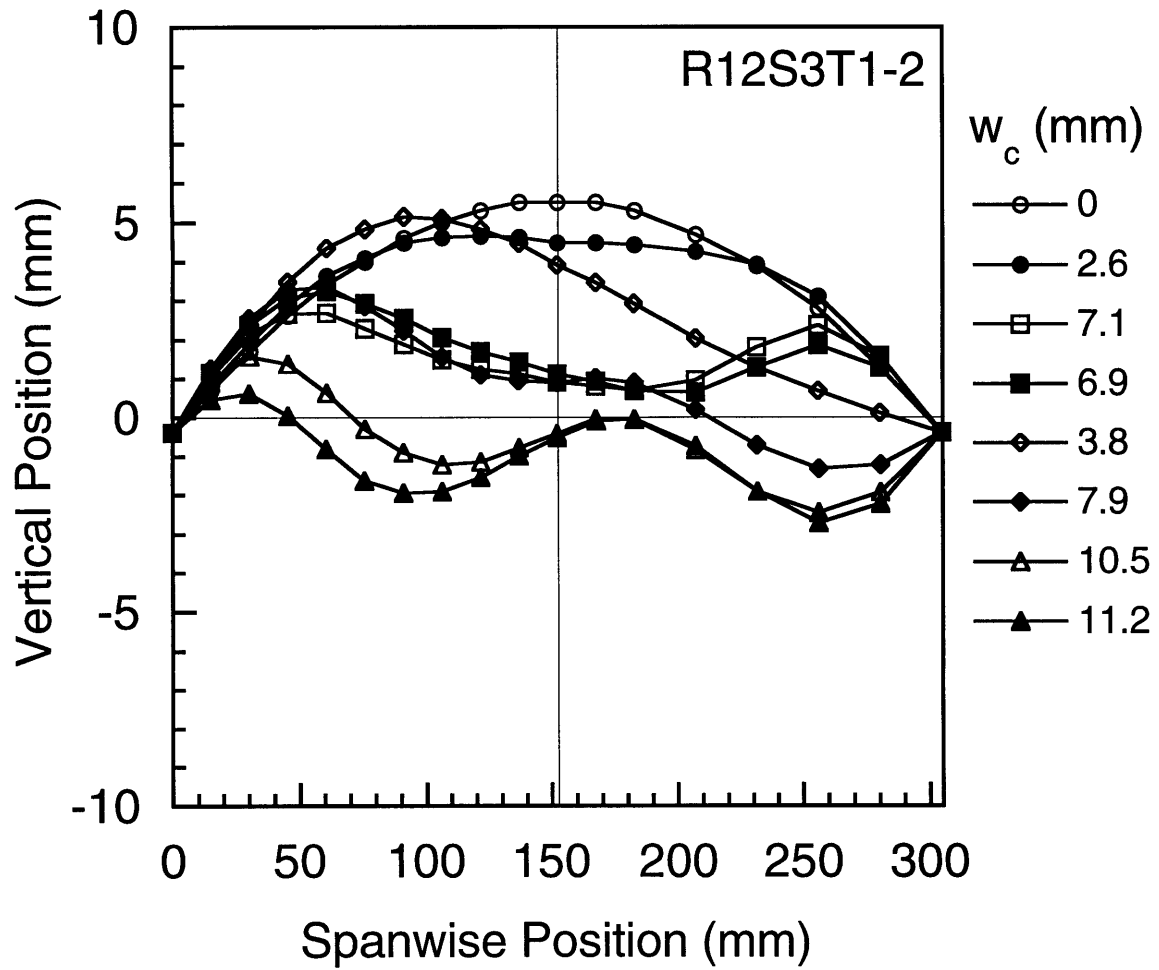


Figure 6.43 Numerical analysis results of left spanwise deformation modes for specimen $R_{12}S_3T_{1-2}$ at different values of center deflection.

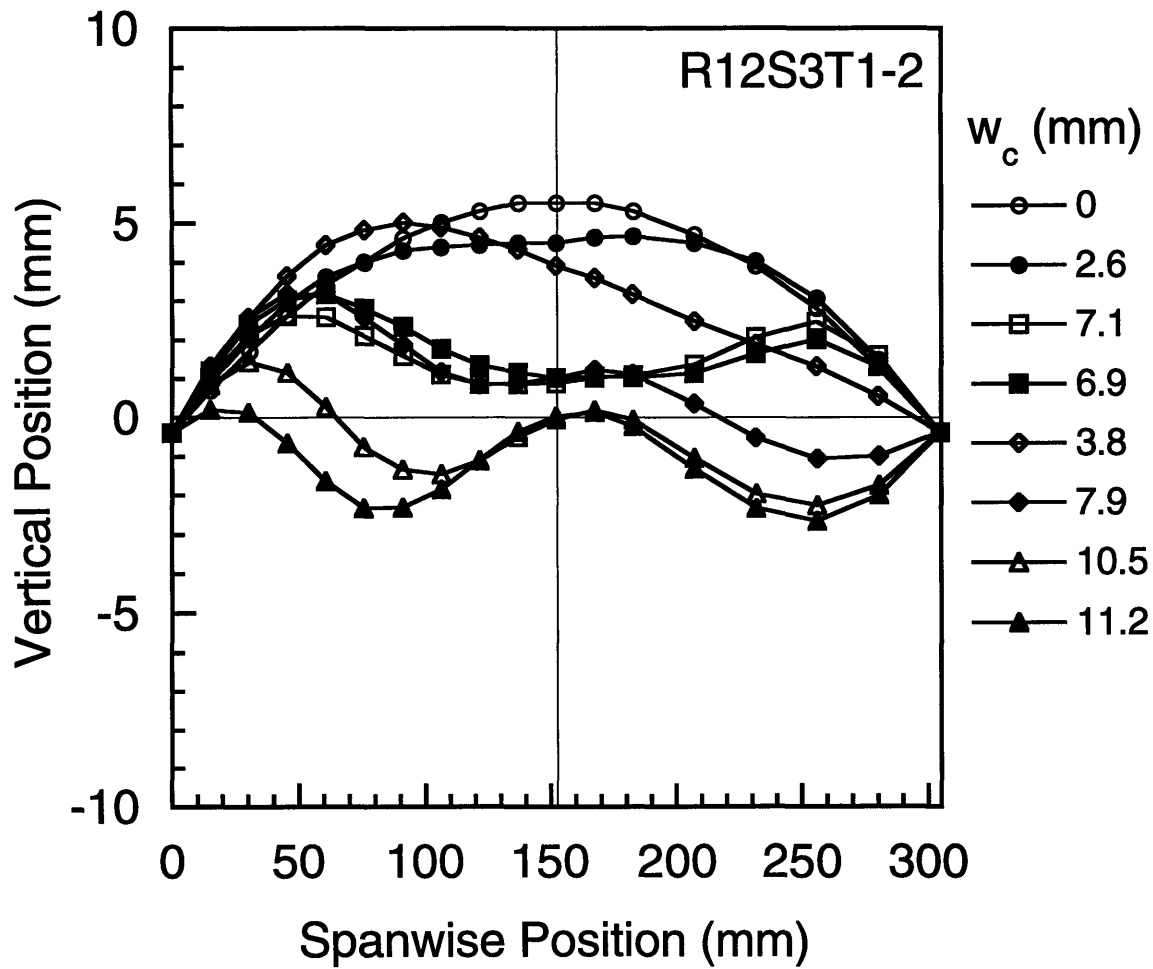


Figure 6.44 Numerical analysis results of right spanwise deformation modes for specimen $R_{12}S_3T_{1-2}$ at different values of center deflection.

left and right mode shapes prior to the second equilibrium path, at center deflections of 2.6 mm, 7.1 mm, 6.9 mm, and 3.8 mm, are similar to those for the central spanwise mode. The modal amplitudes are slightly decreased relative to the central mode because the left and right axial stations represent the midpoint between the center of the shell and the restrained axial shell edge. Although still asymmetric, left and right mode shapes on and after the second equilibrium path are markedly different than those for the central mode. Deformations at the center of the shell are significantly diminished in these later modes as compared to those for the central mode shape. Larger deformations at the center of the central spanwise mode relative to the left and right modes are expected, however, due to load application at the center of the central mode. Lastly, the left and right spanwise modes are noted to be slightly asymmetric (relative to the central mode) and also nearly identical. These modes are dominated by the asymmetric buckling mode but are not identical due to the small antisymmetric effect due to laminate bending-twisting coupling. Antisymmetry is also discernible in the left and right modes at a center deflection of 2.6 mm. This effect has been noted for geometrically similar composite shells in chapter 4, and further evidence and discussion is presented subsequently in the left and right mode shapes for specimen types $R_{12}S_3T_2$ and $R_{12}S_3T_3$.

As with the load-deflection response, the central mode-shape evolution for specimen $R_{12}S_3T_2-2$ in Figure 6.45 displays the same characteristics as specimen $R_{12}S_3T_1-2$ (see Figure 6.42). Mode shapes for specimen $R_{12}S_3T_2-2$ are provided at the same key points in the response: on the first equilibrium path, just prior to bifurcation, just after bifurcation, etc. A similar comparison can be drawn regarding the left and right mode-shape evolutions for specimen $R_{12}S_3T_2-2$ as well (compare Figures 6.46 and 6.47 with Figures 6.43 and 6.44).

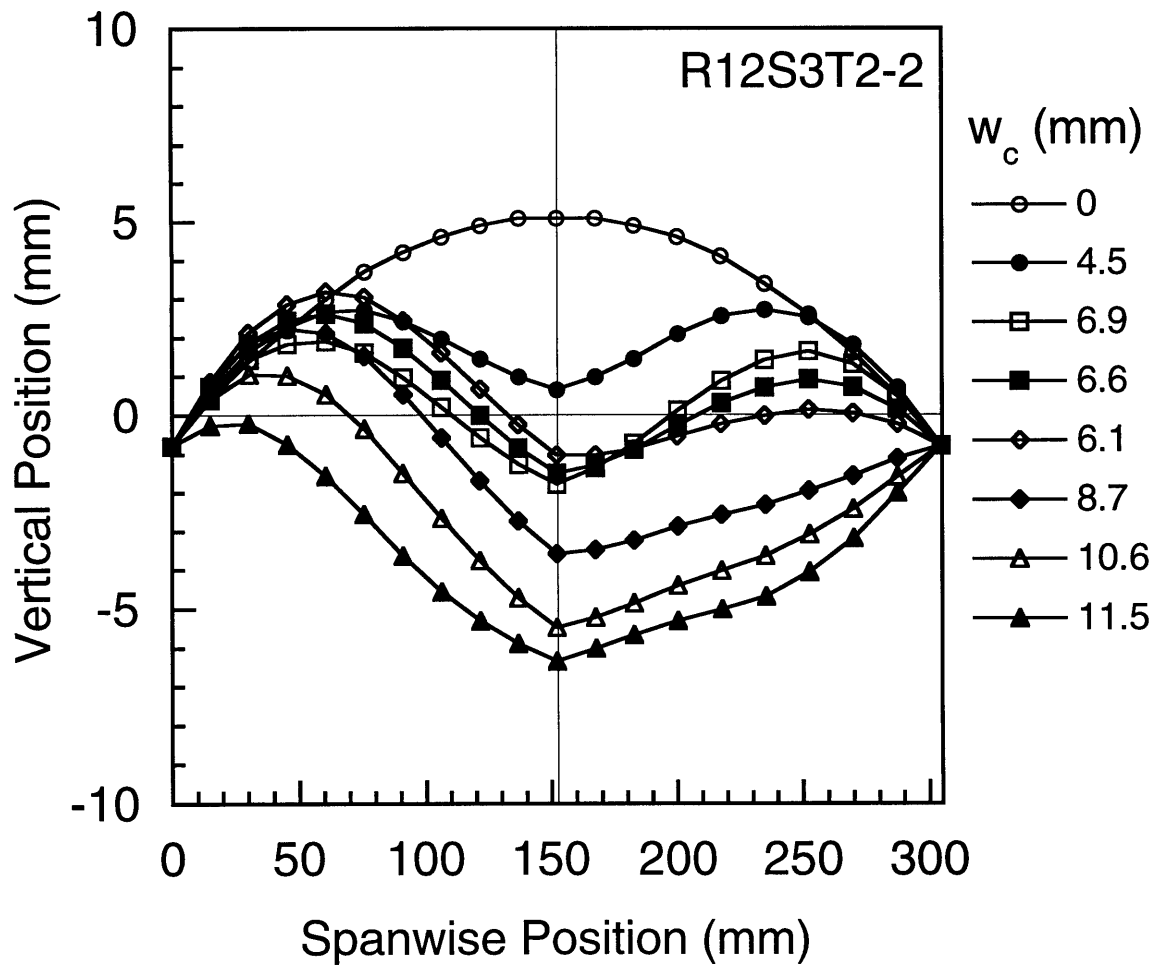


Figure 6.45 Numerical analysis results of central spanwise deformation modes for specimen $R_{12}S_3T_2-2$ at different values of center deflection.

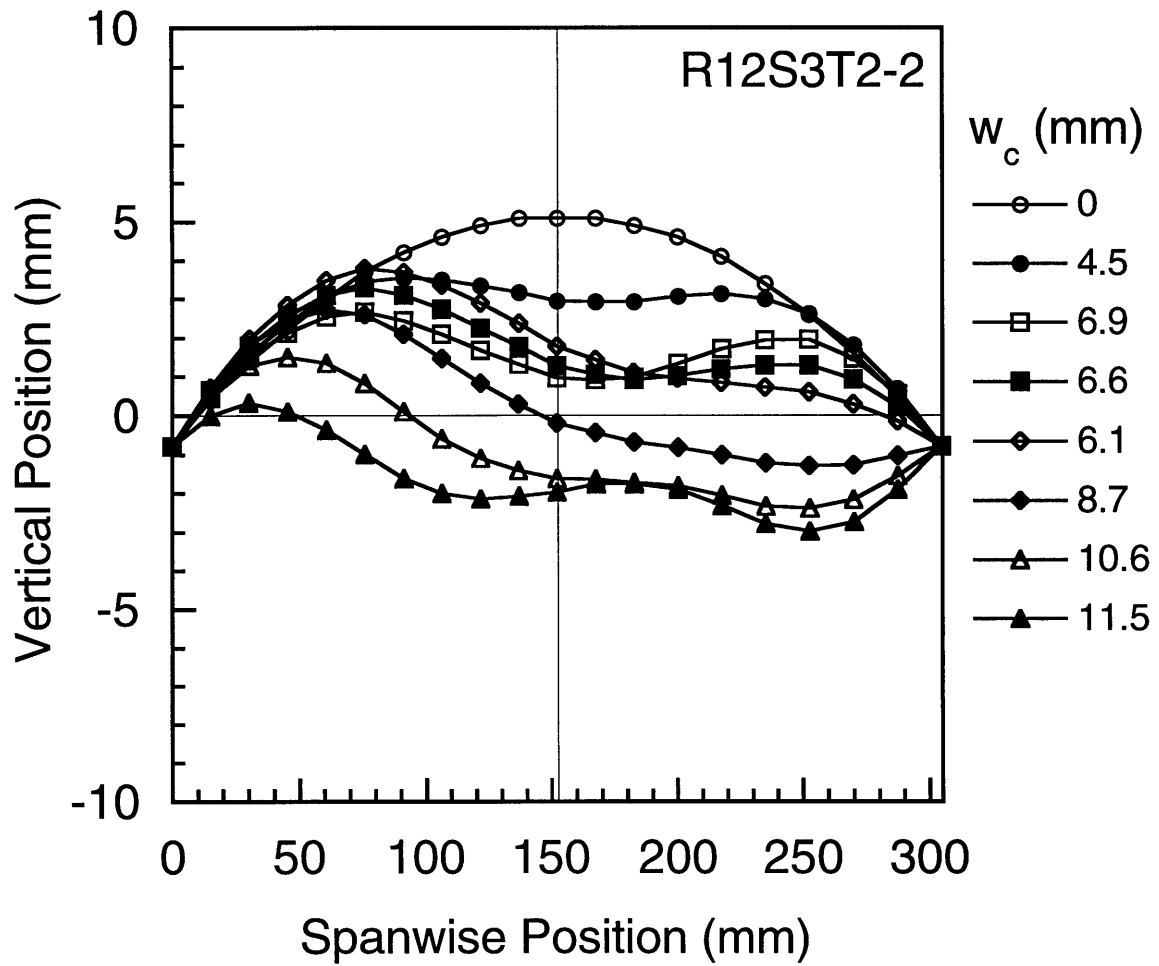


Figure 6.46 Numerical analysis results of left spanwise deformation modes for specimen $R_{12}S_3T_2-2$ at different values of center deflection.

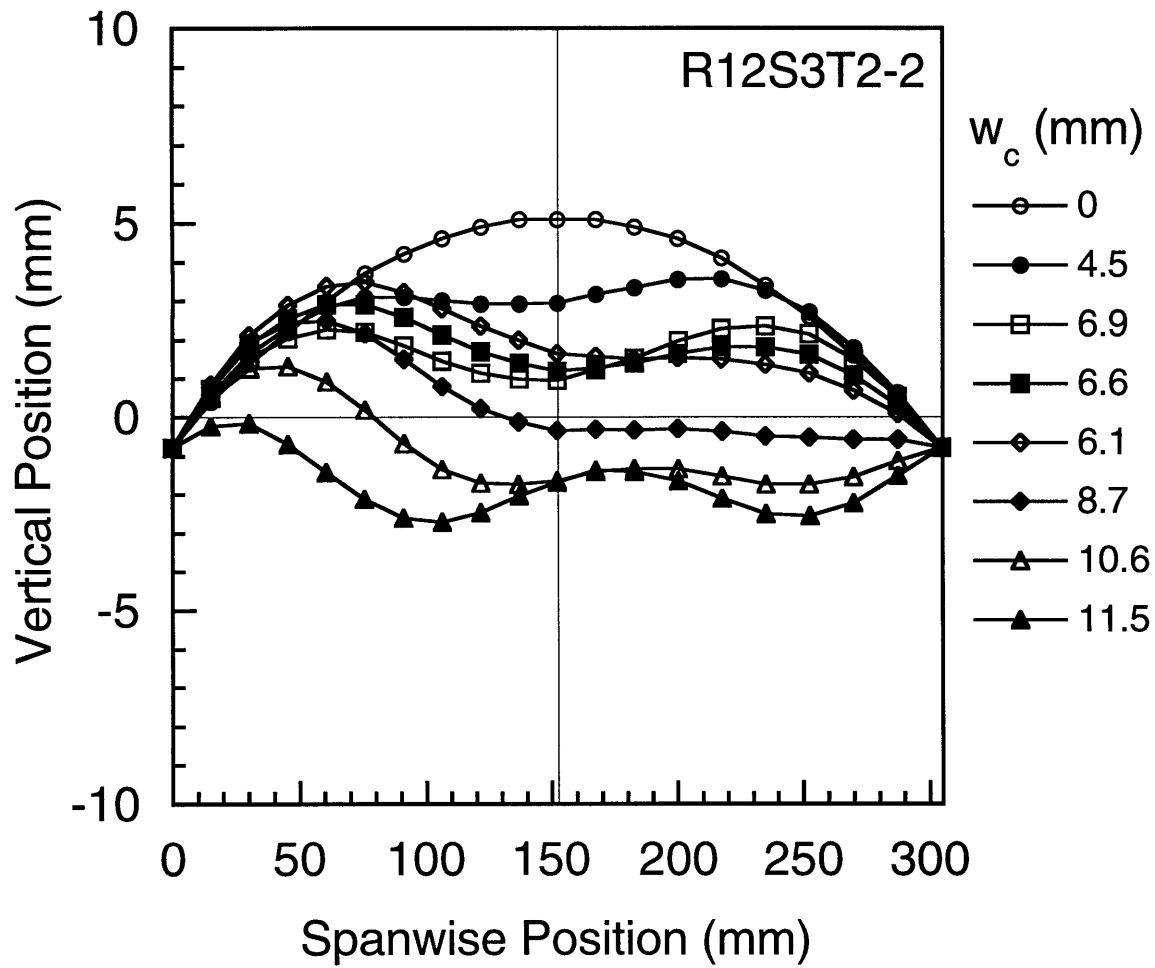


Figure 6.47 Numerical analysis results of right spanwise deformation modes for specimen $R_{12}S_3T_2-2$ at different values of center deflection.

Thus, response characteristics typical of specimen type $R_{12}S_3T_{1-2}$ – symmetric mode shapes prior to bifurcation, asymmetric mode shapes after bifurcation, and a moderate antisymmetric effect in the left and right mode shapes due to bending-twisting coupling – are observed for specimen $R_{12}S_3T_{2-2}$ as well.

The central spanwise deformation modes for specimen $R_{12}S_3T_{3-2}$ in Figure 6.48 also exhibit the transition from symmetric to asymmetric modes at the bifurcation point. The inverted symmetric mode for this specimen upon reaching the final (third) equilibrium path is evident at a center deflection of 11.4 mm (load value of 877 N). The left and right spanwise modes for specimen $R_{12}S_3T_{3-2}$ in Figures 6.49 and 6.50 do not exhibit the symmetry observed in the central spanwise mode on the final equilibrium path (center deflection of 11.4 mm). In contrast, the modes are noted to be asymmetric and also antisymmetric with respect to one another. Again, this is a manifestation of the laminate bending-twisting coupling which induces a greater effect for this layup at larger thicknesses. Further evidence for this antisymmetry is provided by the left and right mode shapes prior to bifurcation at center deflections of 4.7 mm and 7.0 mm which would otherwise be symmetric. The bifurcation mode does dominate the left and right mode-shape responses as evidenced by the loss of antisymmetry after bifurcation, but before the final equilibrium path, at center deflection values of 7.4 mm, 9.2 mm, 11.1 mm, and 11.5 mm. The effect of laminate bending-twisting coupling is noted in the mode-shape evolutions for all specimens, both prior to and after bifurcation, but the effect is more pronounced for thicker specimens as expected.

The mode-shape evolutions for the three specimen types, taken together with the loading response, indicate a consistent progression with regard to thickness. The descending (load and deflection) instability region associated

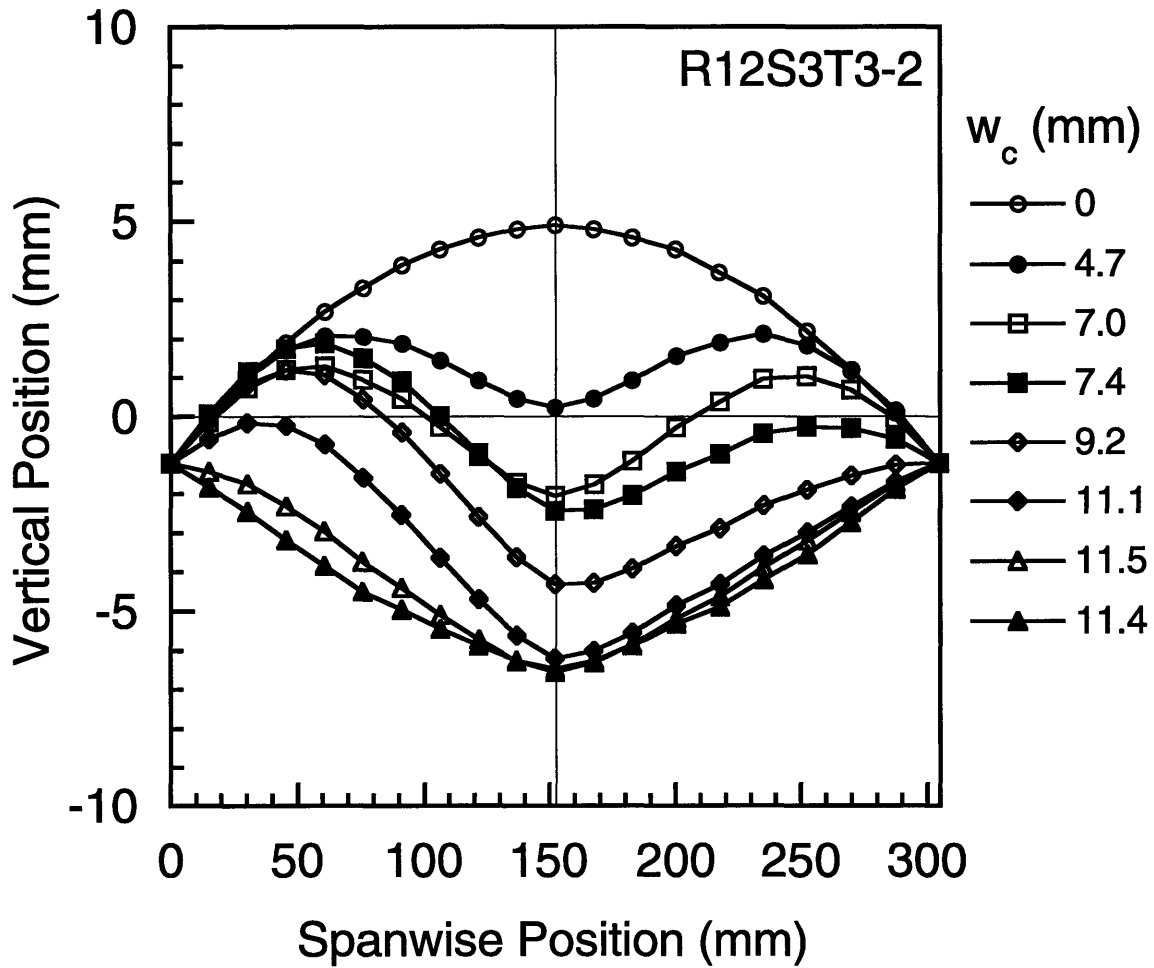


Figure 6.48 Numerical analysis results of central spanwise deformation modes for specimen $R_{12}S_3T_3-2$ at different values of center deflection.

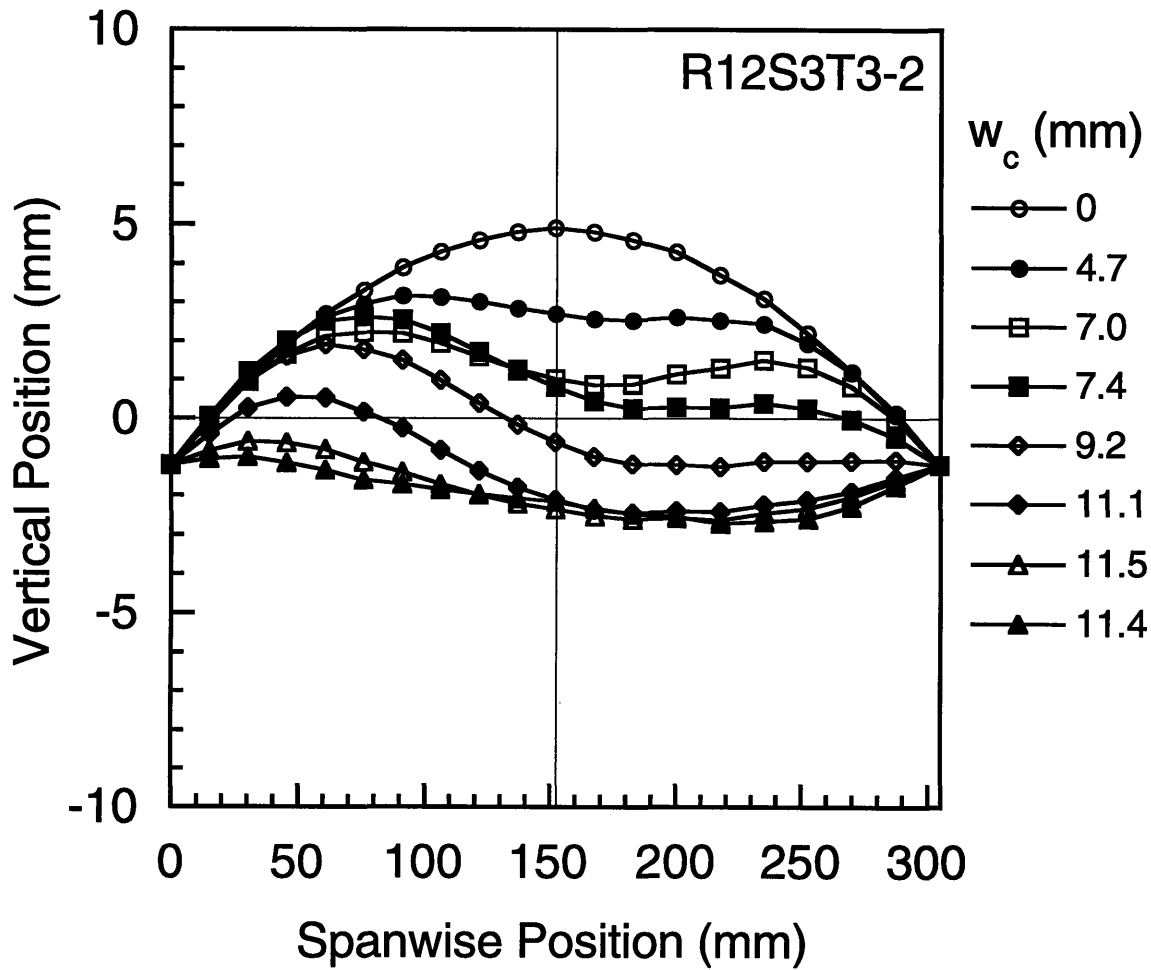


Figure 6.49 Numerical analysis results of left spanwise deformation modes for specimen $R_{12}S_3T_3-2$ at different values of center deflection.

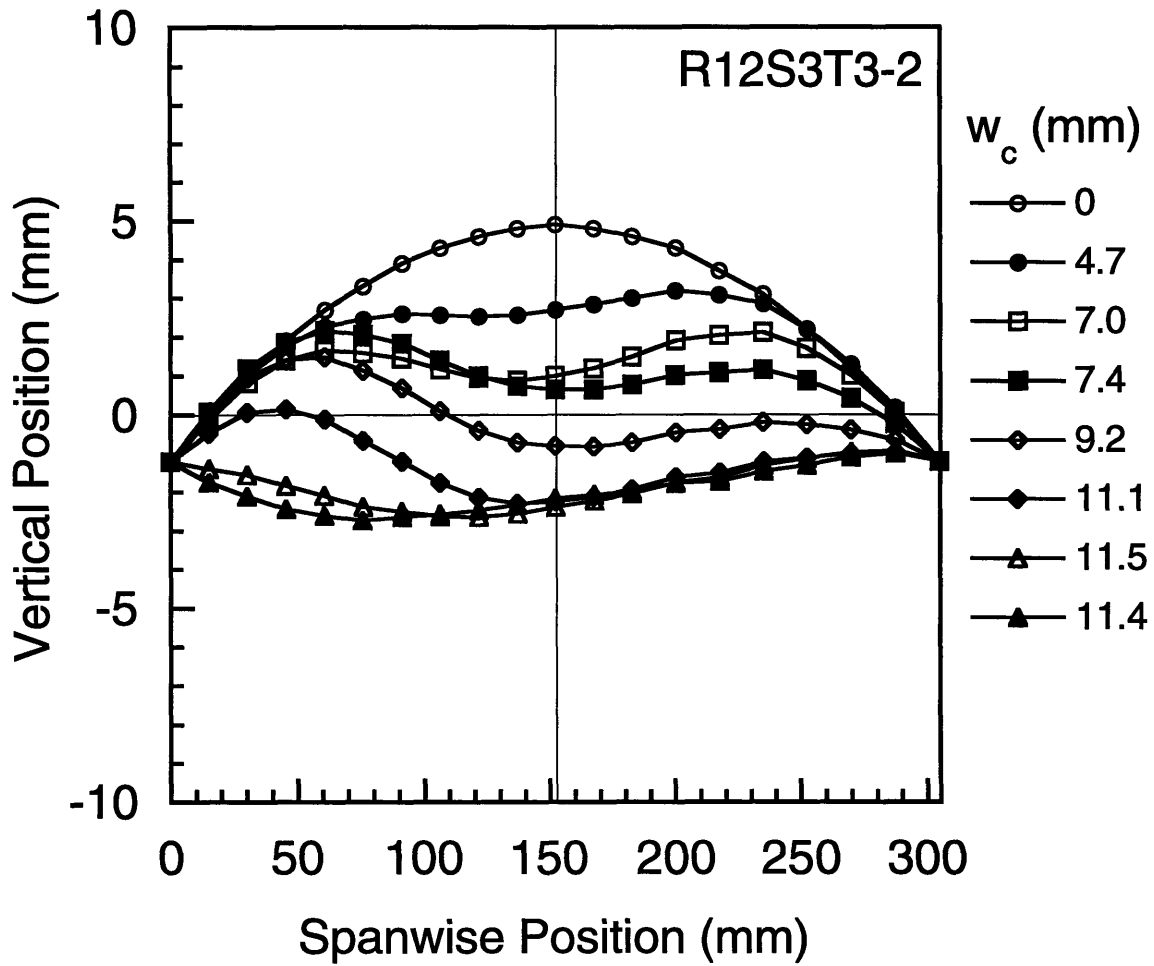


Figure 6.50 Numerical analysis results of right spanwise deformation modes for specimen $R_{12}S_3T_3-2$ at different values of center deflection.

with the bifurcation point is less pronounced as thickness increases until it disappears entirely for specimen type $R_{12}S_3T_3$ where a stable secondary (bifurcation) path is observed. The secondary path, though stable, still has a transition to asymmetric modes shapes associated with the bifurcation point. Furthermore, the third (final) equilibrium path, where symmetric mode shapes are regained for all three specimen types, is able to be characterized by a static analysis for the thickest specimen type ($R_{12}S_3T_3$).

CHAPTER 7

DISCUSSION

Important findings regarding composite shell response from the present work are discussed in this chapter. Results from chapters 4 and 6 are used to motivate the discussion. A comparison between the experimental and numerical results from the specimens tested in this work is provided in section 7.1. Effects of boundary conditions on the predicted and experimentally observed responses are considered in section 7.2. A discussion of damage resistance for the specimens tested in this work is presented in section 7.3 and related to the current understanding of damage resistance of composite shell structures. Lastly, the utility of the asymmetric meshing technique (AMT) in evaluating the bifurcation response of composite shells is considered in section 7.4.

7.1 Experimental and Numerical Comparisons

In this section, experimental data and results from the numerical analysis are used to gain a better understanding of the response of the shells tested in this work. Comparisons of both load-deflection behavior and mode-shape evolutions are particularly useful for gaining insight into the shell response. In all cases, converged numerical bifurcation results using the AMT for each specimen are utilized for comparison to the experimental data.

As discussed in chapter 6, the numerical results allow both load- and deflection-controlled buckling responses to be evaluated. A combination of

both load and deflection (path-parameter) are utilized to "load" the structure in the numerical analysis. In the numerical results for specimen types $R_{12}S_3T_1$ and $R_{12}S_3T_2$, bifurcation involves an unstable postbuckling region wherein both load and deflection decrease simultaneously. In a deflection-controlled test, such as that performed in the experimental portion of this work, the response would (and did) "snap" at constant deflection to the stable second equilibrium path. This deflection-controlled "snap" is illustrated in Figure 7.1 utilizing the numerical results from specimen $R_{12}S_3T_1-1$ (see Figure 6.29). "Snapping" during the deflection-controlled test must be considered when making comparisons to the experimental data. The load-drops and associated 'popping' observed during testing of specimen type $R_{12}S_3T_1$ (see Figures 6.1 and 6.2) are likely associated with "snapping" from the primary path to the second equilibrium path at the experimental bifurcation point.

The numerical and experimental loading responses for specimen $R_{12}S_3T_1-1$ are provided in Figure 7.2. Although the responses coincide initially (center deflections less than 0.5 mm in Figure 7.2), the experimental response is noted to become more compliant than the predicted response as loading increases and the response softens. The experimental loading response for specimen types $R_{12}S_3T_2-1$ and $R_{12}S_3T_3-1$ are also noted to be more compliant than the predicted results in the loading response comparisons presented in Figures 7.3 and 7.4, respectively. The initial experimental response is in good agreement with the numerical results for specimen $R_{12}S_3T_2-1$, but is more compliant than the prediction for specimen $R_{12}S_3T_3-1$.

A characteristic of all the experimental data relative to the numerical predictions is that the data generally represents a more compliant response. This is consistent with findings in chapter 4 for the broad range of composite shells tested previously. Reasons for a more compliant experimental response

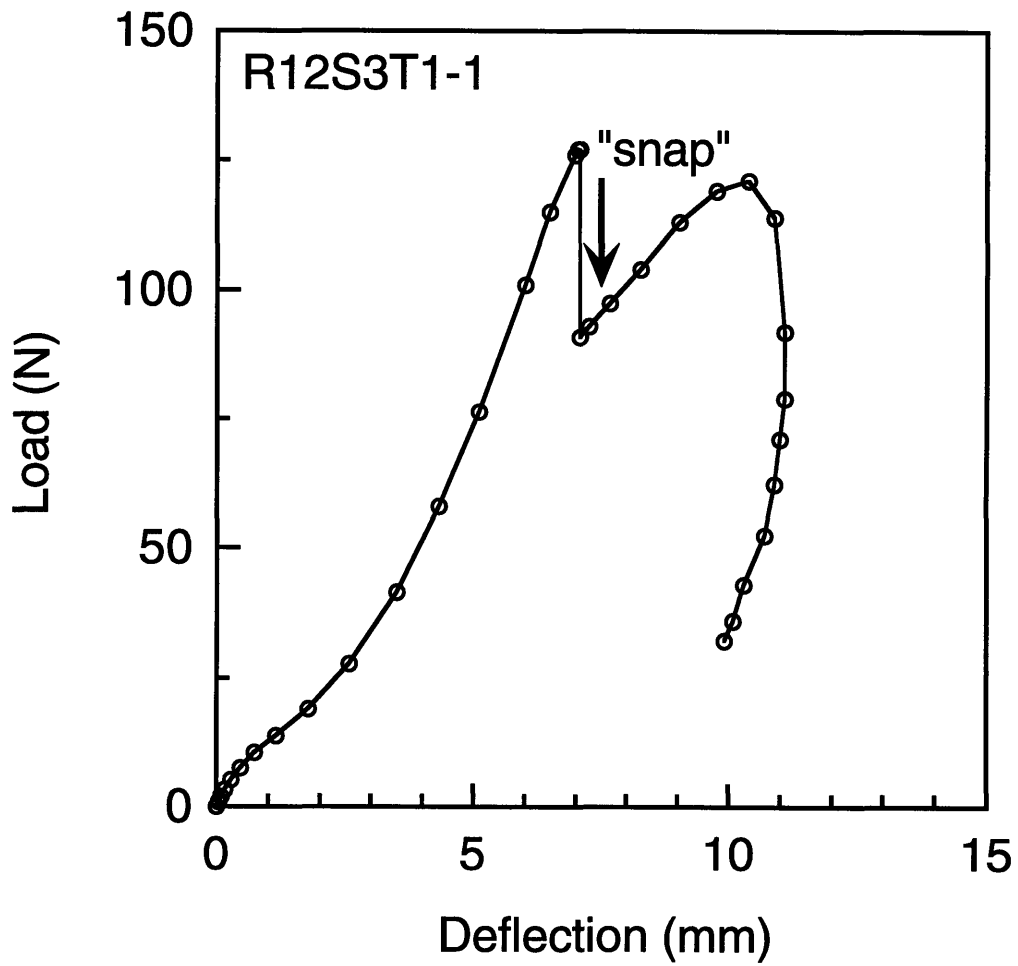


Figure 7.1 Illustration of deflection-controlled "snap" utilizing load-deflection results from numerical analyses for specimen $R_{12}S_3T_1-1$ (see Figure 6.29).

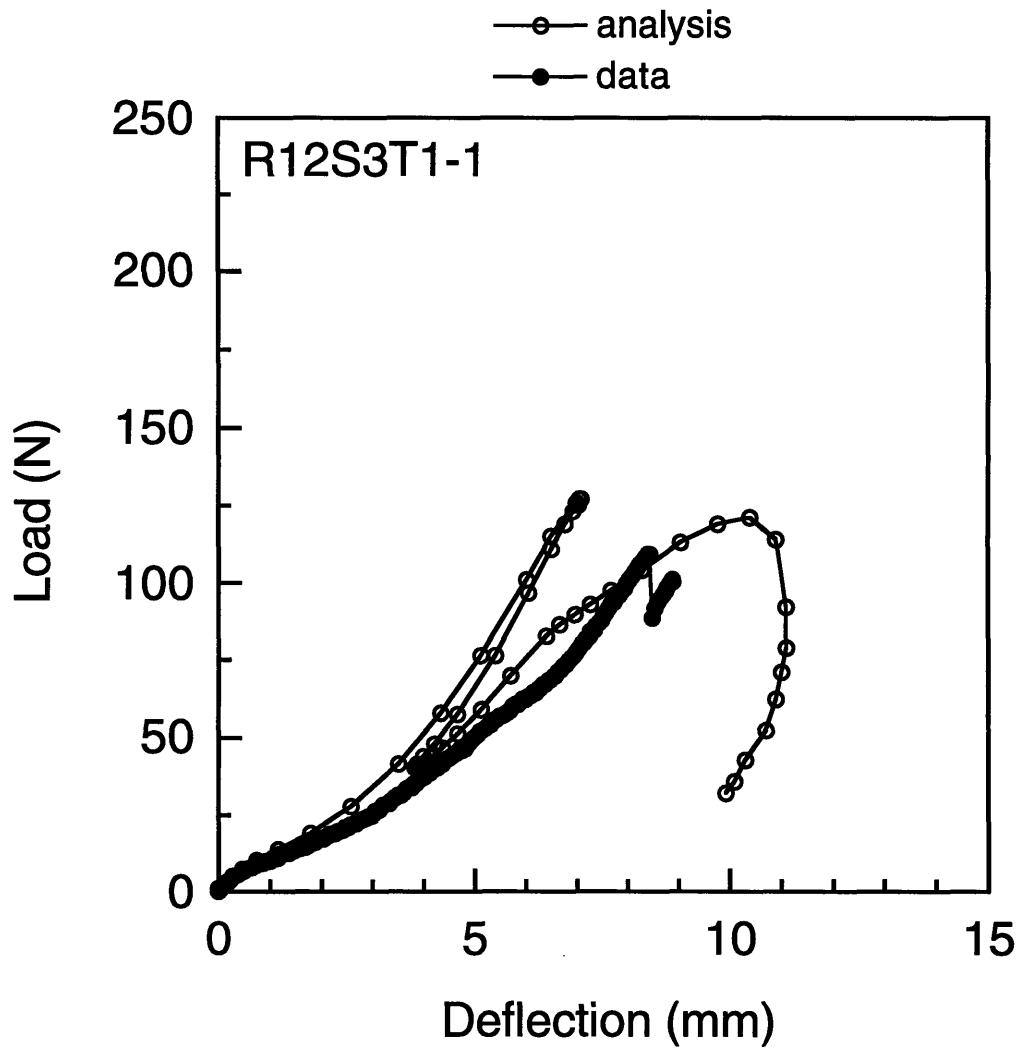


Figure 7.2 Numerical and experimental load-deflection results for specimen $R_{12}S_3T_1-1$.

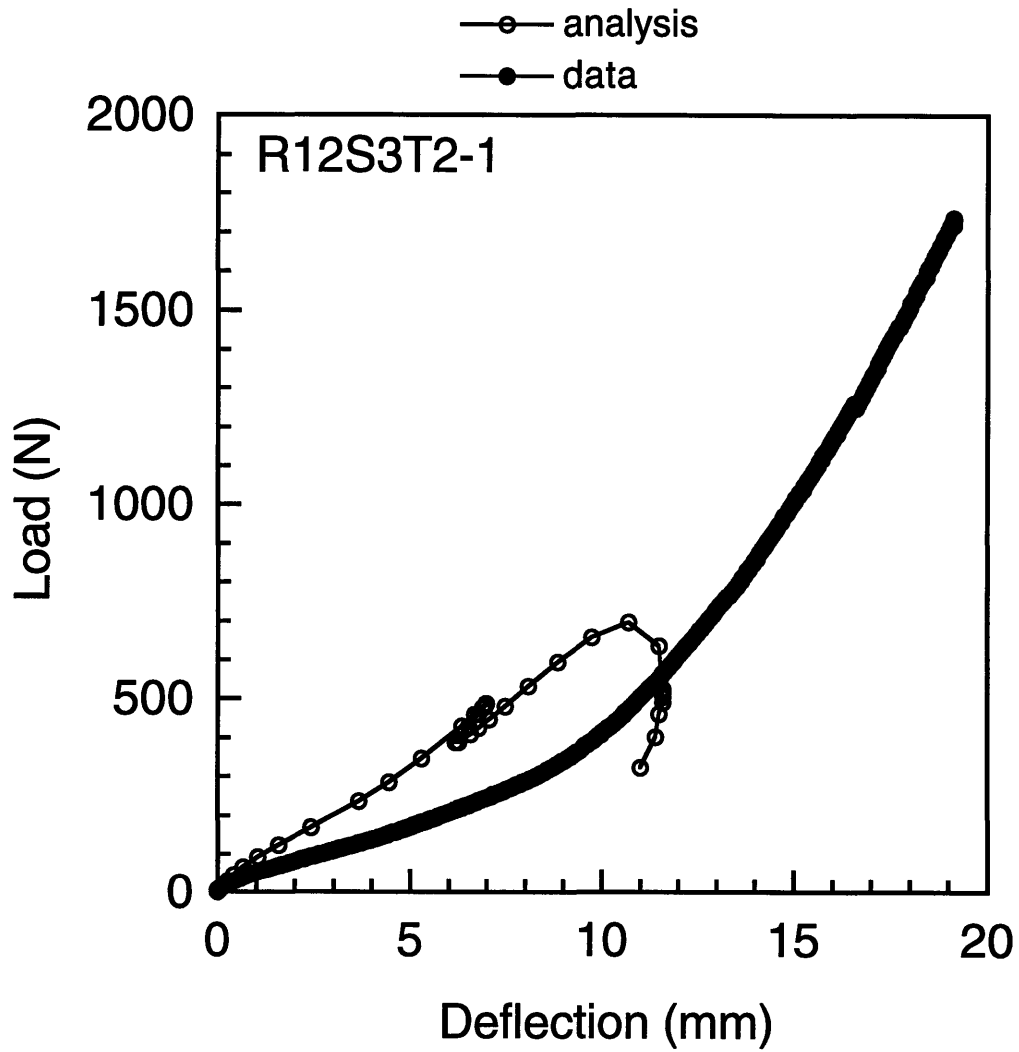


Figure 7.3 Numerical and experimental load-deflection results for specimen $R_{12}S_3T_2-1$.

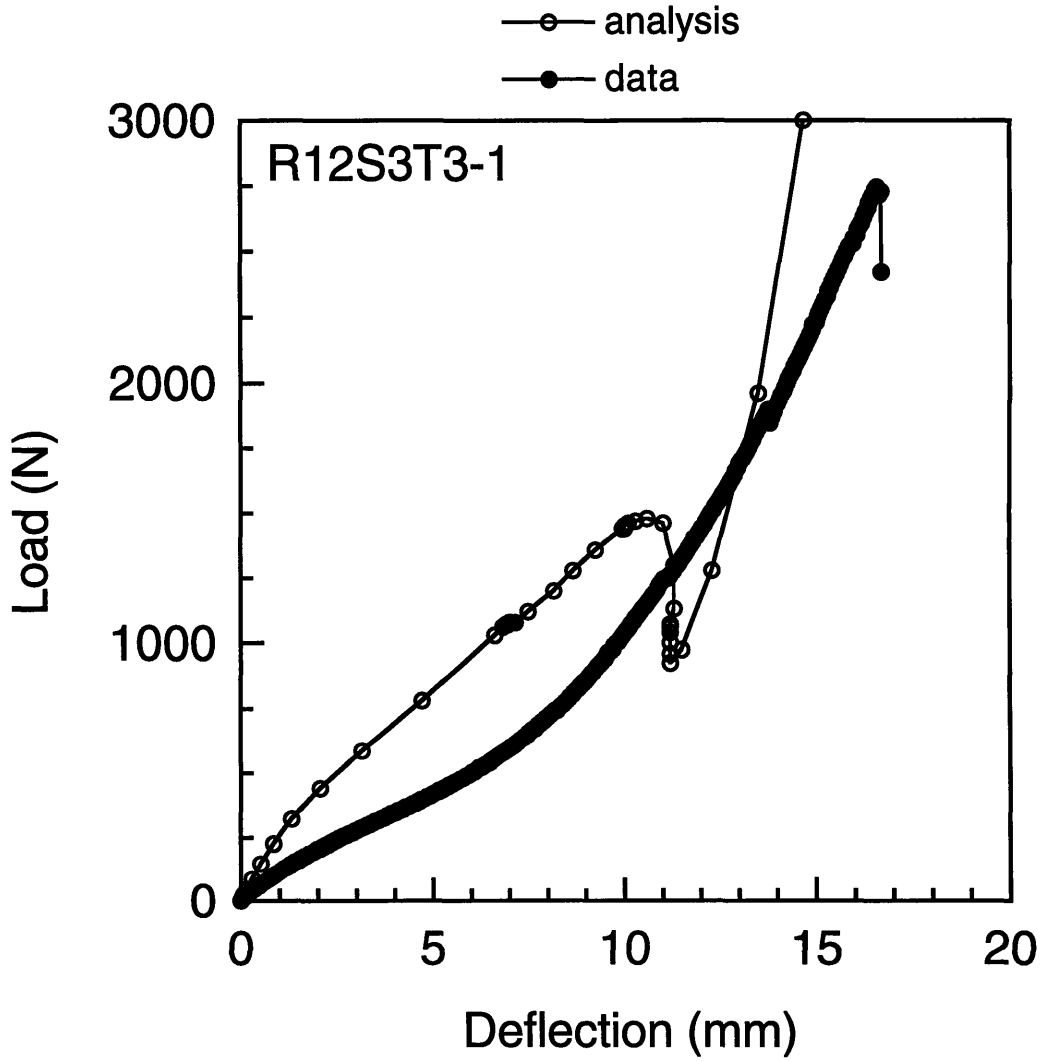


Figure 7.4 Numerical and experimental load-deflection results for specimen $R_{12}S_3T_3-1$.

for these specimens are the same as previously discussed in chapter 4: the analysis does not include transverse shear or account for experimental realities such as compliance of the test fixture (elastic, not rigid, circumferential boundary condition), contact behavior at the loading point, or damage. All of these effects act to make the experimental response more compliant than the numerical results, as well as delaying or eliminating bifurcation entirely. Increased compliance (and disagreement) of the experimental response relative to the numerical predictions as thickness increases can be attributed to many factors. These include a decrease in relative stiffness of the test fixture as compared to the shells, deformation at the loading site due to shear, and seating of the thicker specimens into the grooved circumferential (hinged) supports. It should be noted that thinner specimens fit into the grooved (finite radius) insert utilized here more readily than thicker specimens. Refinements to the analysis, as well as experimental techniques to investigate these different effects, are suggested in chapter 8 as extensions of the current work.

In the numerical results, bifurcation is indicated in a number of ways including a change in path and the development of asymmetric modes. In the experimental data, mode-shape evolutions, particularly the transition from a symmetric to an asymmetric mode, indicate bifurcation. Observed asymmetries in experimental mode-shape evolutions are key to identifying bifurcation in this work. However, it is important to distinguish between modal asymmetry and antisymmetry. In chapter 6, left and right mode shapes for all specimen types (*e.g.*, see Figures 6.24 and 6.25 for specimen $R_{12}S_3T_3-2$) were noted to be asymmetric. However, this asymmetry oftentimes occurred with no corresponding asymmetry in the central mode and, furthermore, the left and right modes were noted to be antisymmetric. This antisymmetry in the left

and right spanwise modes is a result of bending-twisting coupling in the composite laminate and does not indicate bifurcation. This is supported by the numerical analysis results which indicate this type of antisymmetry in the absence of bifurcation. Evidence of antisymmetry in left and right experimental mode shapes is also observed prior to bifurcation and on the final equilibrium path for all specimen types, regions where central deformation modes are symmetric. Thus, the antisymmetry in left and right mode shapes does not indicate bifurcation, but rather reflects a composite laminate coupling. Evidence for this type of antisymmetry due to laminate coupling was also provided in chapter 4 for the composite shells tested previously. This antisymmetric effect is small relative to the asymmetric modes associated with bifurcation. This can be seen for specimen type $R_{12}S_3T_1$.

Mode shapes from numerical analysis for all three specimen types (thicknesses) contain an asymmetric component due to the predicted bifurcation. These asymmetries in the numerically evaluated mode shapes are evident for all three specimen types between center deflection values of approximately 7 mm and 11 mm. However, a dominant asymmetric mode indicative of bifurcation is noted in the experimental data for only one of the three specimen types, $R_{12}S_3T_1$, between center deflection values of 6.0 mm and 10.0 mm. The other two specimen types were not observed to have this dominant asymmetry, although slight asymmetries were noted in the central modes between center deflection values of 2.0 mm and 6.0 mm. As discussed in chapter 6, it is unclear whether the mode-shape data for these two thicker specimens indicate bifurcation or not. Given evidence from chapter 4 and previous work that test fixture compliance acts to inhibit bifurcation (and thus asymmetric modes), it is not surprising that bifurcation is difficult to identify for these thicker specimens. Recommendations for further work to

experimentally determine bifurcation are provided in chapter 8.

Experimental central spanwise mode shapes for specimen $R_{12}S_3T_{1-2}$ are presented in Figure 7.5 for comparison to the numerical spanwise mode shapes evaluated at the same values of applied center deflection in Figure 7.6. Recall that the numerical response is deflection-controlled in this comparison, following the path given in Figure 7.1. Excellent agreement is noted for all mode shapes except for the mode at a center deflection value of 6.0 mm. The experimental mode is noted to be asymmetric, *i.e.*, the shell has bifurcated prior this value of center deflection. The numerical solution, however, is symmetric because bifurcation is not predicted until an applied center deflection of 7.1 mm is reached. Thus, the experimental data indicates bifurcation between center deflection values of 4.0 mm and 6.0 mm whereas it is not predicted to occur until a center deflection value of 7.1 mm. In this range of applied center deflection, the numerical response (primary path) lies very close to the second equilibrium path (with associated asymmetric modes). It is hypothesized that an imperfection (loading, boundary condition, or geometric) causes bifurcation from the primary to the secondary path before the numerical bifurcation point. This has been illustrated in chapter 6 (see Figure 6.34) where a geometric imperfection in the numerical model allowed the response to move directly from the first to the second equilibrium path at a center deflection of 4.5 mm. Apart from this discrepancy in mode shapes at a center deflection of 6.0 mm, the experimental and numerical central spanwise mode shapes for specimen $R_{12}S_3T_{1-2}$ are in excellent agreement.

Numerical and experimental left and right spanwise mode shapes for specimen $R_{12}S_3T_{1-2}$ are provided in Figures 7.7 and 7.8, and 7.9 and 7.10, respectively, for comparison. As with the central spanwise mode shape, bifurcation is evident for the experiments in the asymmetric left and right

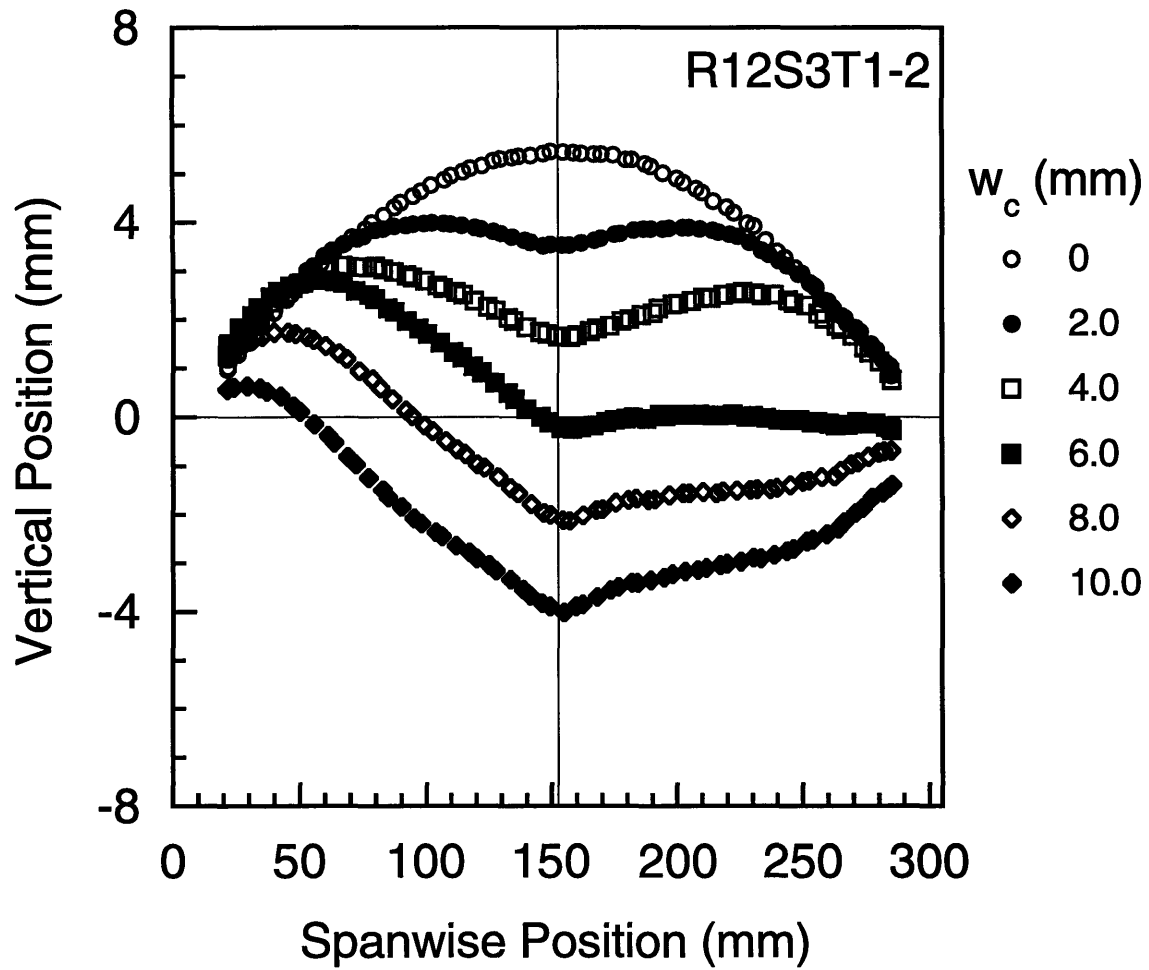


Figure 7.5 Measured central spanwise deformation modes for specimen $R_{12}S_3T_{1-2}$ at different values of center deflection.

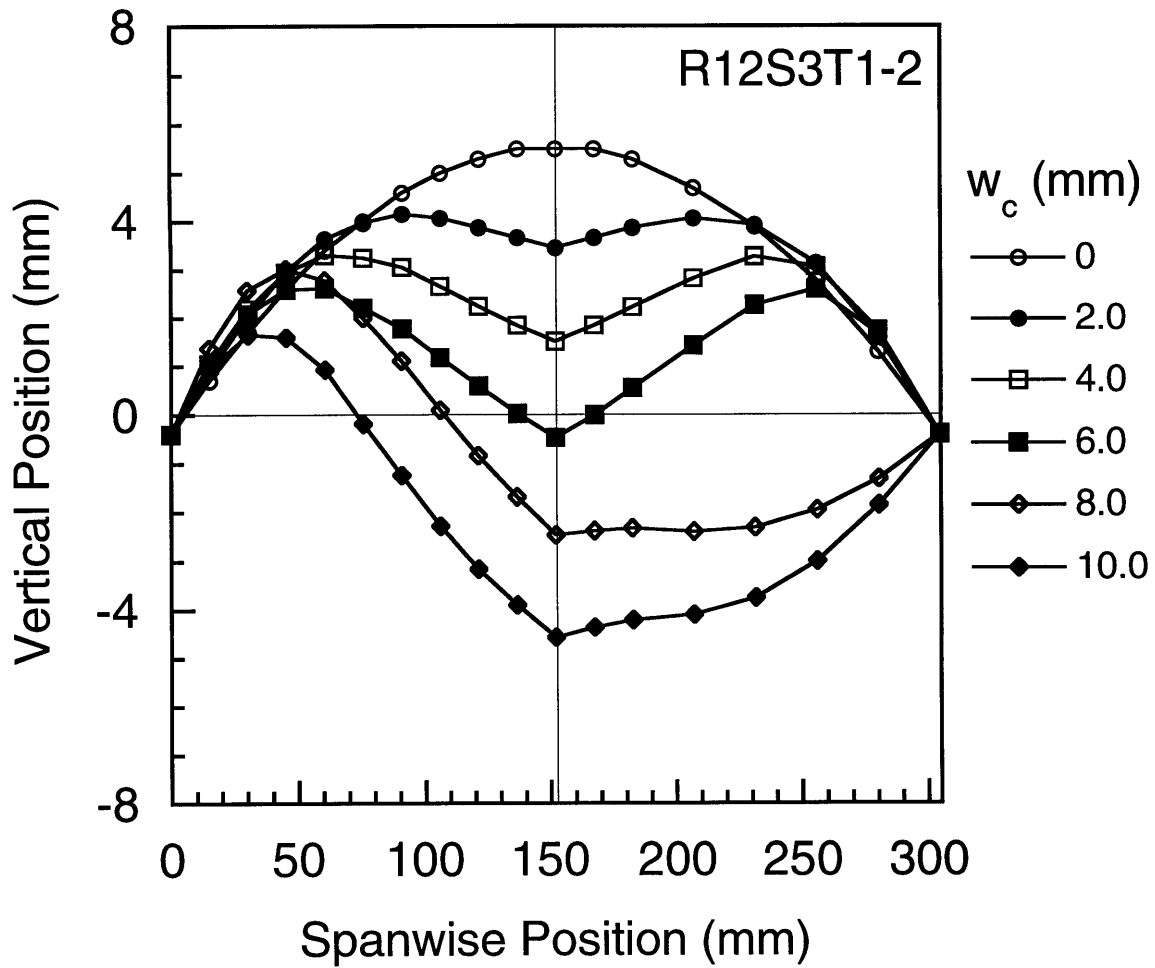


Figure 7.6 Numerical analysis results of central spanwise deformation modes for specimen $R_{12}S_3T_{1-2}$ at different values of center deflection.

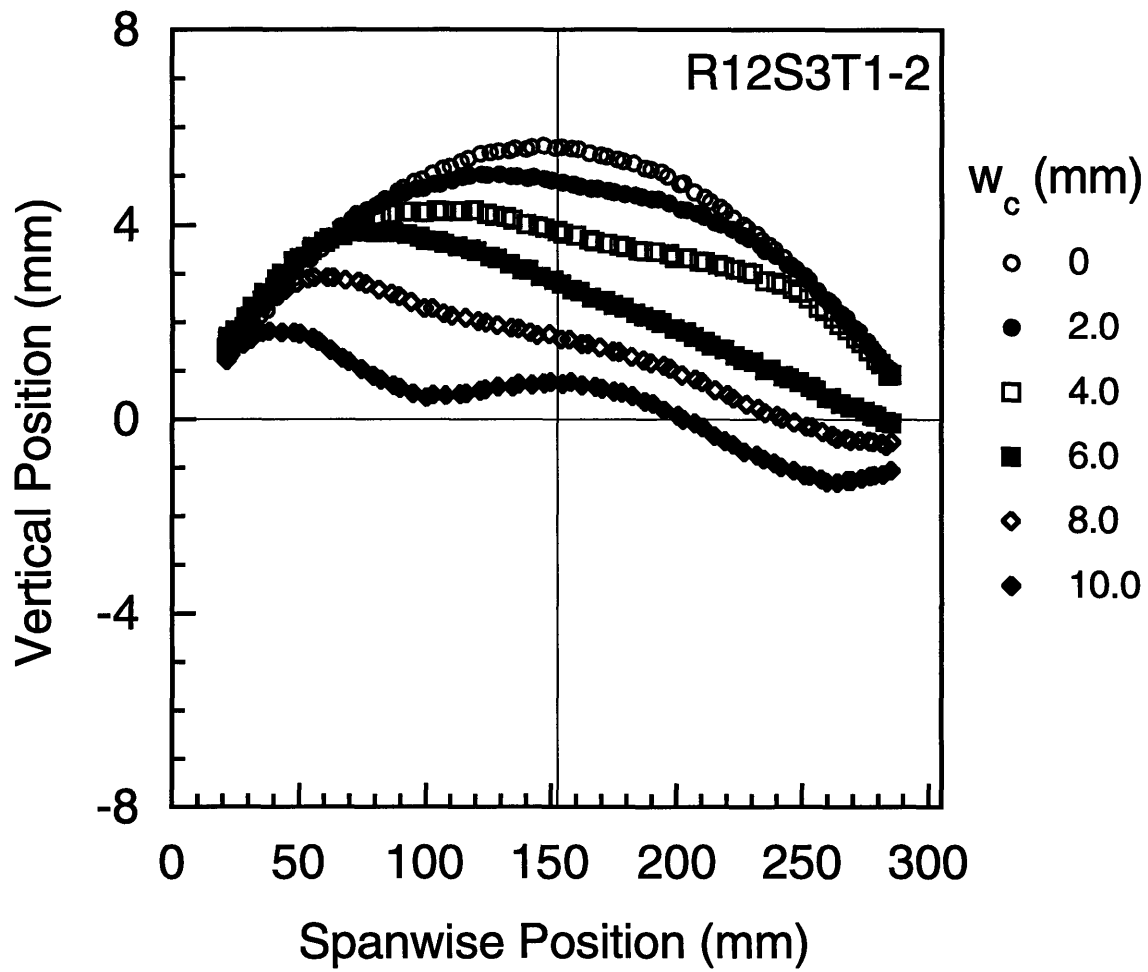


Figure 7.7 Measured left spanwise deformation modes for specimen $R_{12}S_3T_{1-2}$ at different values of center deflection.

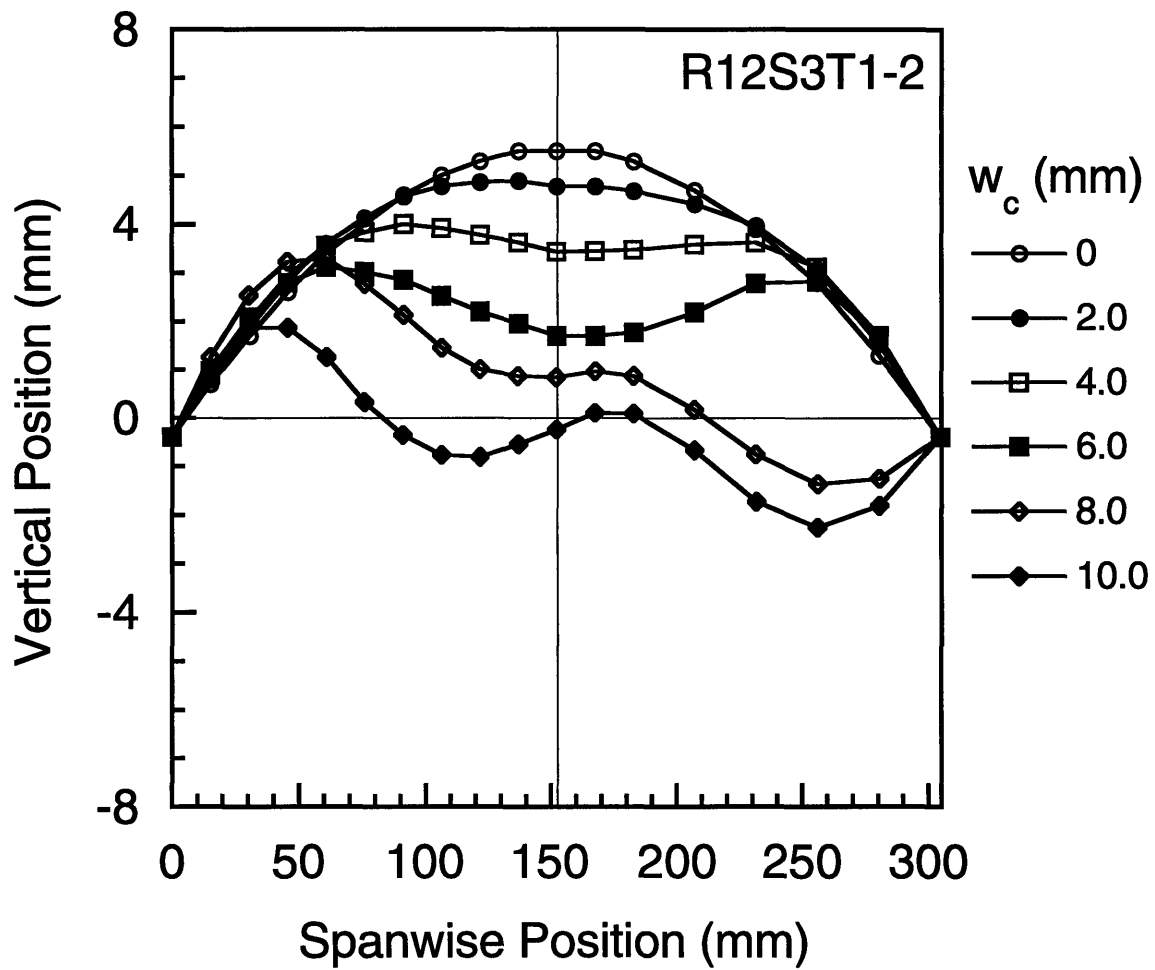


Figure 7.8 Numerical analysis results of left spanwise deformation modes for specimen $R_{12}S_3T_{1-2}$ at different values of center deflection.

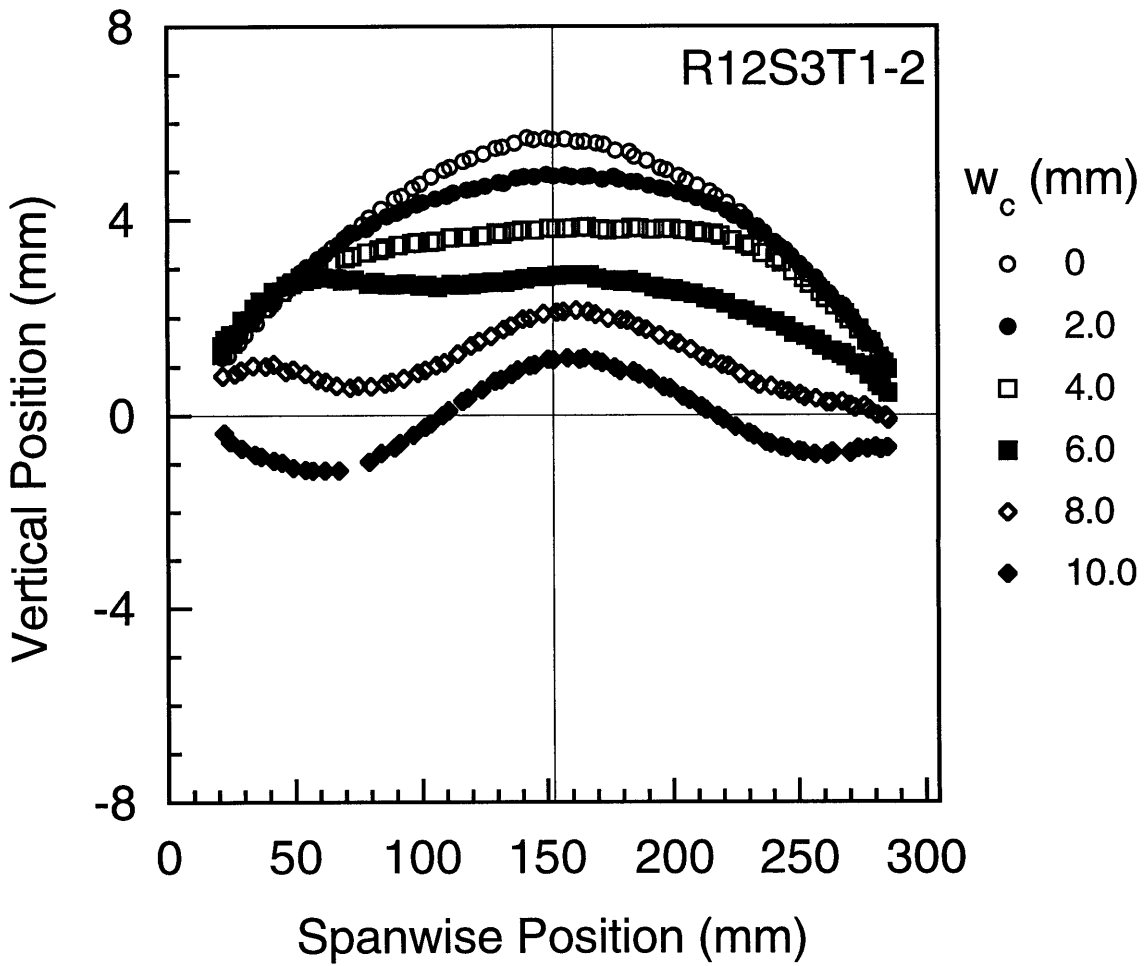


Figure 7.9 Measured right spanwise deformation modes for specimen $R_{12}S_3T_{1-2}$ at different values of center deflection.

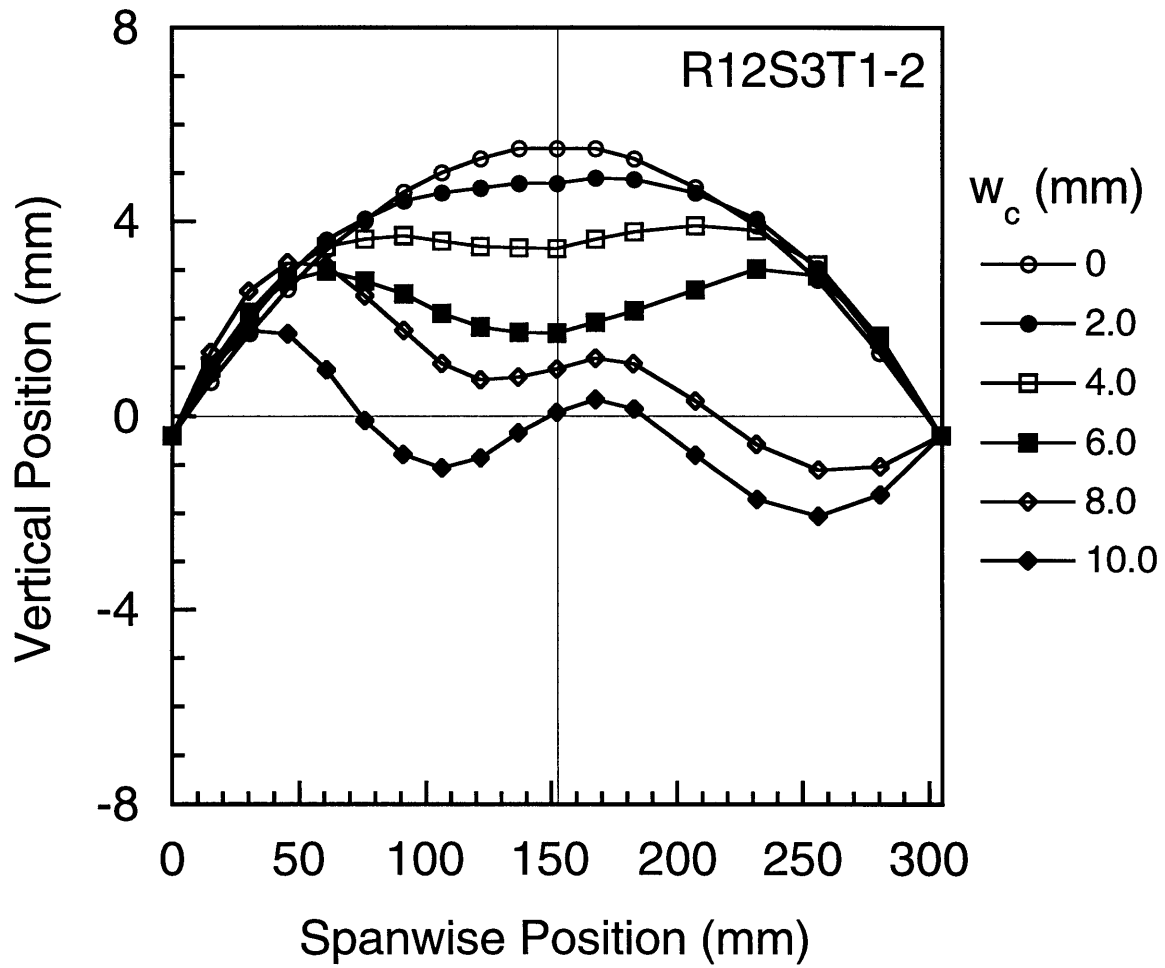


Figure 7.10 Numerical analysis results of right spanwise deformation modes for specimen $R_{12}S_3T_{1-2}$ at different values of center deflection.

spanwise modes at a center deflection of 6.0 mm. Apart from the antisymmetry due to bending-twisting coupling previously discussed, the left and right numerically evaluated modes are similar, *i.e.*, there is symmetry in the axial direction. However, the experimental modes (Figures 7.7 and 7.9, respectively), do not show this same agreement after bifurcation. This is clearly evident in the mode at a center deflection of 10.0 mm where the right mode (Figure 7.9) indicates that the shell edges (at the hinged boundaries) have snapped-through to an inverted configuration whereas the left mode (Figure 7.7) has not inverted at the left boundary (spanwise position of 0 mm). Asymmetry in the axial direction for the experimental results is also evident in the left and right mode for specimen $R_{12}S_3T_1-1$ in chapter 6 (see Figures 6.9 and 6.10). Thus, an axial asymmetry, apart from the bending-twisting antisymmetry, is evident in the experimental data which is not predicted numerically. It is hypothesized that imperfect axial boundary conditions, particularly frictional loading differences between the two axial boundaries, induce this axial asymmetry. Investigation of this behavior is recommended for further work.

As discussed previously, the experimental mode shapes for specimens $R_{12}S_3T_2-2$ and $R_{12}S_3T_3-2$ do not allow bifurcation to be conclusively identified. The experimental and numerical central spanwise modes for both specimens are provided in Figures 7.11 through 7.14 for comparison. The mode shapes for specimen $R_{12}S_3T_2-2$ in Figure 7.11 are largely symmetric, in agreement with the predicted modes in Figure 7.12 at center deflection values of 2.0 mm, 4.0 mm, and 6.0 mm. However, because bifurcation was predicted to occur at a center deflection value of 7.1 mm, asymmetry is noted at a center deflection value of 8.0 mm in the predicted results whereas the experimental mode is symmetric. Furthermore, this last experimental mode indicates that the shell

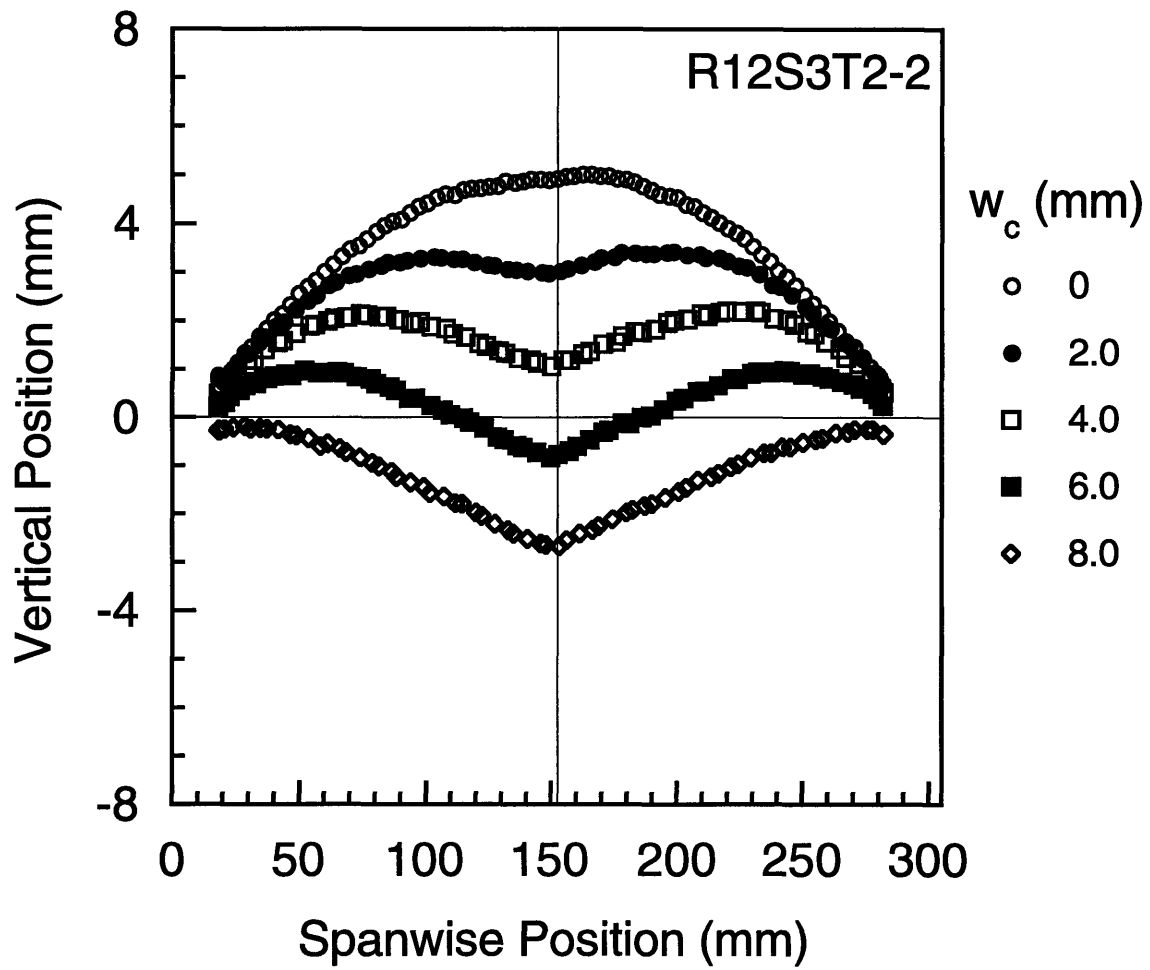


Figure 7.11 Measured central spanwise deformation modes for specimen $R_{12}S_3T_2-2$ at different values of center deflection.

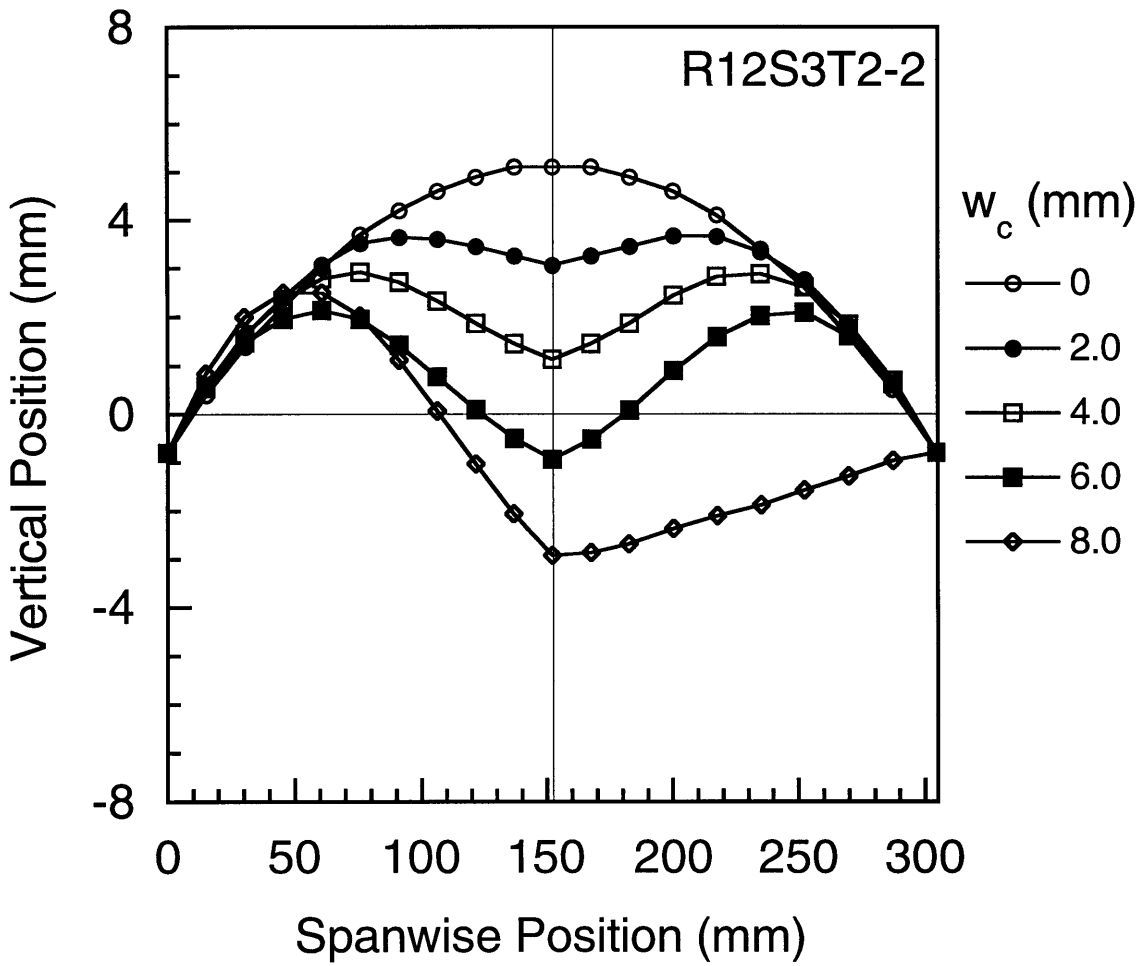


Figure 7.12 Numerical analysis results of central spanwise deformation modes for specimen $R_{12}S_3T_2-2$ at different values of center deflection.

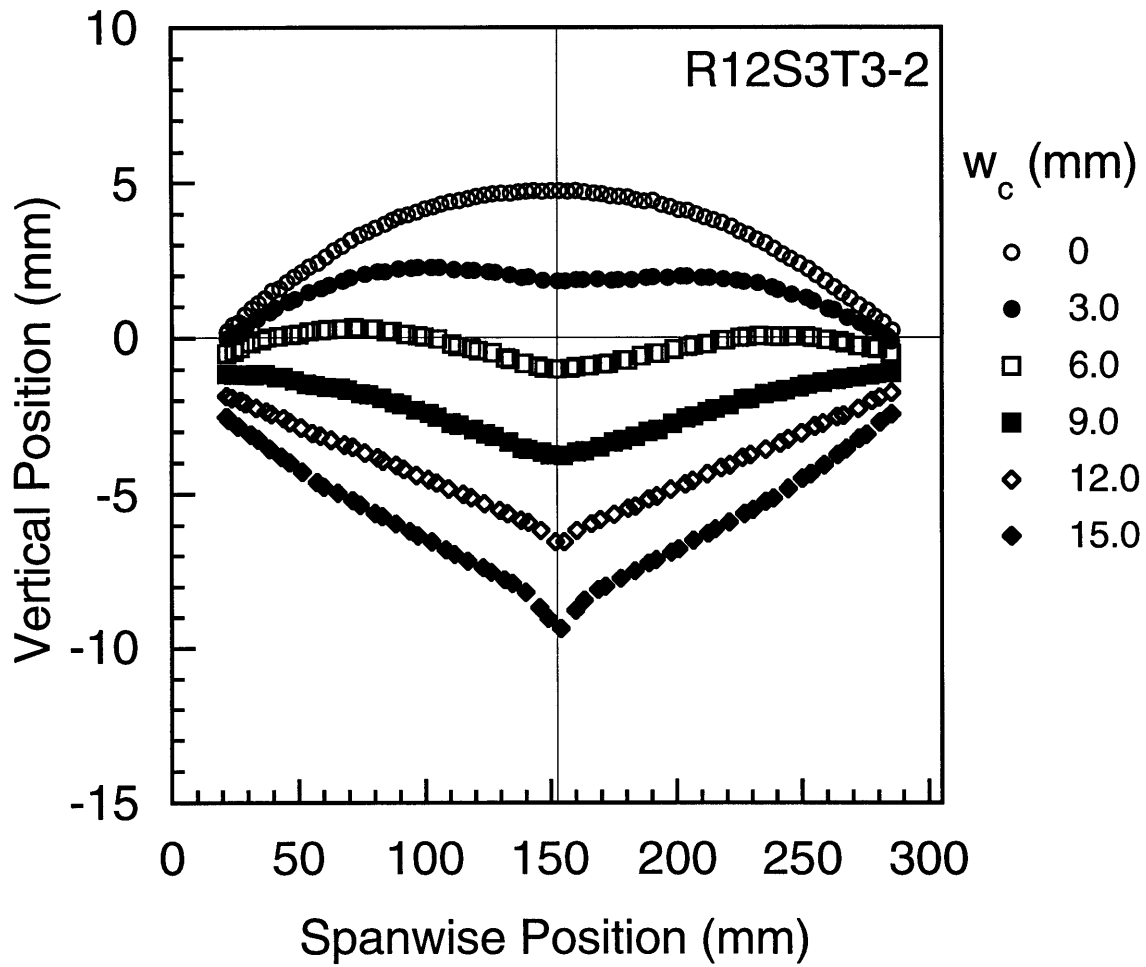


Figure 7.13 Measured central spanwise deformation modes for specimen $R_{12}S_3T_3-2$ at different values of center deflection.

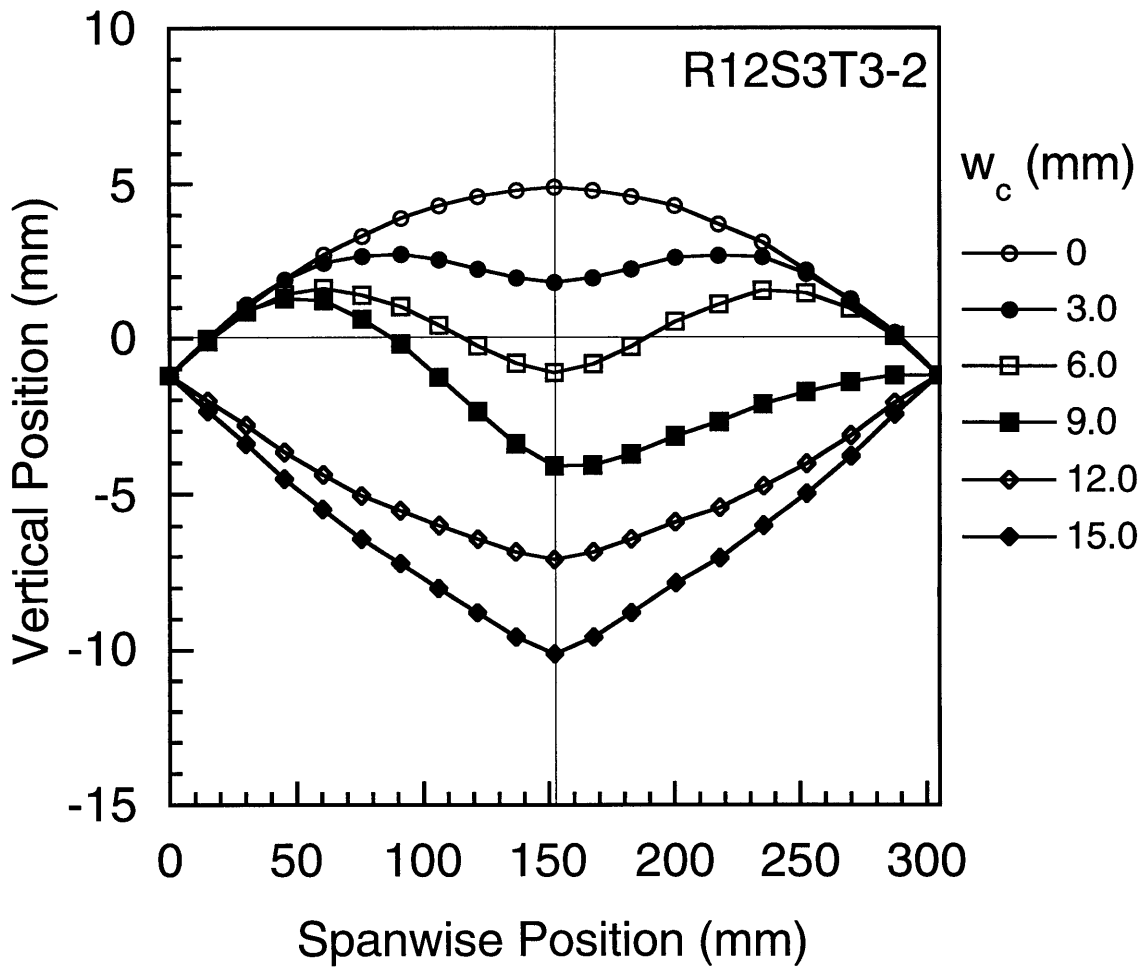


Figure 7.14 Numerical analysis results of central spanwise deformation modes for specimen $R_{12}S_3T_3-2$ at different values of center deflection.

is in an inverted configuration. The analysis would not predict this behavior until loading on the final (third) equilibrium path. This specimen was damaged during loading and it is hypothesized that increased compliance at the loading point due to the incurred damage affects bifurcation into an asymmetric mode. Characteristics of the deformation modes for specimen $R_{12}S_3T_3-2$, which was also damaged during testing, indicate the same type of behavior (see Figures 7.13 and 7.14). Damage at the loading site is believed to induce symmetric deformations and inhibit bifurcation. Thus, it is clearly important to consider the effect of damage formation on the response of these shells, particularly in regard to bifurcation. Suggestions for further experimental work to characterize the effect of damage on the resulting shell response are made in chapter 8.

Results discussed in this section provide a clear picture of the response of the shells tested in this work. Analysis of these specimens shows that all three specimen types, under perfect conditions, would bifurcate (into asymmetric modes) from a primary equilibrium path, then reach a second critical (limit point) before regaining load-carrying capability on a final equilibrium path. Symmetric deformations dominate the response prior to bifurcation and on the final (third) equilibrium path whereas asymmetric modes dominate the transition between these paths. Bifurcation is conclusively observed in the experimental data for specimen type $R_{12}S_3T_1$, but it is unclear whether bifurcation into asymmetric modes occurred for the two thicker specimen types. Numerical analysis predicts that bifurcation is unstable in both load- and deflection-control for specimen types $R_{12}S_3T_1$ and $R_{12}S_3T_2$. Dynamic loading and unloading was observed in the response of specimen type $R_{12}S_3T_1$ but not for specimen type $R_{12}S_3T_2$. Generally, the analysis is in good agreement with regard to predicting initial load-deflection

response and mode-shape evolutions. However, some disagreement is noted at higher load levels due to a more compliant experimental response. The more compliant experimental response is linked to many factors including damage and transverse shear, but primarily to the finite stiffness of the test fixture which is modeled as rigid. Experimental refinements and modeling recommendations are given in chapter 8 to better understand and quantify these various effects with regard to composite shell buckling response and damage resistance.

7.2 Boundary Conditions

In this section, two issues related to boundary conditions are explored. In section 7.2.1, the assumption of zero displacement in the x -direction (u -displacement component, *i.e.*, sliding along the boundary) at each circumferential hinged boundary condition for specimens tested in this work is investigated. This is done to ascertain the effect of this aspect of the boundary condition on the shell response. In section 7.2.2, the effect of adding the axial restraint to the shell response is explored using data from this and previous work, as well as results from numerical analyses.

7.2.1 Modeling Assumption at Circumferential (Hinged) Edge

The numerical analysis results presented in chapters 4 and 6 and section 7.1 assume zero displacement for the u -component of displacement (x -direction) at the circumferential shell edge (hinged condition). However, it is unclear whether the experimental boundary condition at this shell edge maintains zero displacement. Friction at the boundary condition likely makes this displacement boundary condition neither completely fixed (zero) nor completely free. The influence of this boundary condition on the response is

easily bounded numerically by considering the two extremes of completely fixed (zero displacement) or completely free (zero force). Analyses using the zero force assumption at the circumferential boundary condition are identified as "u free". Analyses which utilize the previous assumption of zero displacement at this boundary condition are identified as "u fixed" in this section. As in section 7.1, all results from analysis represent converged bifurcation solutions for the shell response.

The numerical load-deflection response for specimen $R_{12}S_3T_1-1$ using the two assumptions at the hinged boundary are presented in Figure 7.15. The two extreme cases for the u -displacement are noted to have relatively little effect on the predicted response. The "u free" case is slightly more compliant in some regions than the "u fixed" case, but the effect is likely too small to be observed in any experimental data. The change in boundary condition is noted to influence the bifurcation load, however, and the limit-point load to a lesser extent. For specimen $R_{12}S_3T_1-1$, the bifurcation load is reduced from 127 N in the "u fixed" case to 113 N in the "u free" case. Similarly, the limit-point load is reduced from 121 N to 116 N. These reductions in bifurcation and limit-point loads are also noted in the response comparisons for specimens $R_{12}S_3T_2-1$ and $R_{12}S_3T_3-1$ in Figures 7.16 and 7.17, respectively. For these specimens, the bifurcation load is noted to be reduced from 487 N to 436 N, and from 1075 N to 1025 N, respectively. As with specimen $R_{12}S_3T_1-1$, changing the boundary condition is noted to have little effect on the overall response of the thicker shells. Similarly, mode shapes for all specimens are not affected by this change in boundary condition.

The analysis results in this section indicate that, as expected, a more restrained condition at the boundary ("u fixed") results in a stiffer response than the less restrictive "u free" case. The "u fixed" condition results in a

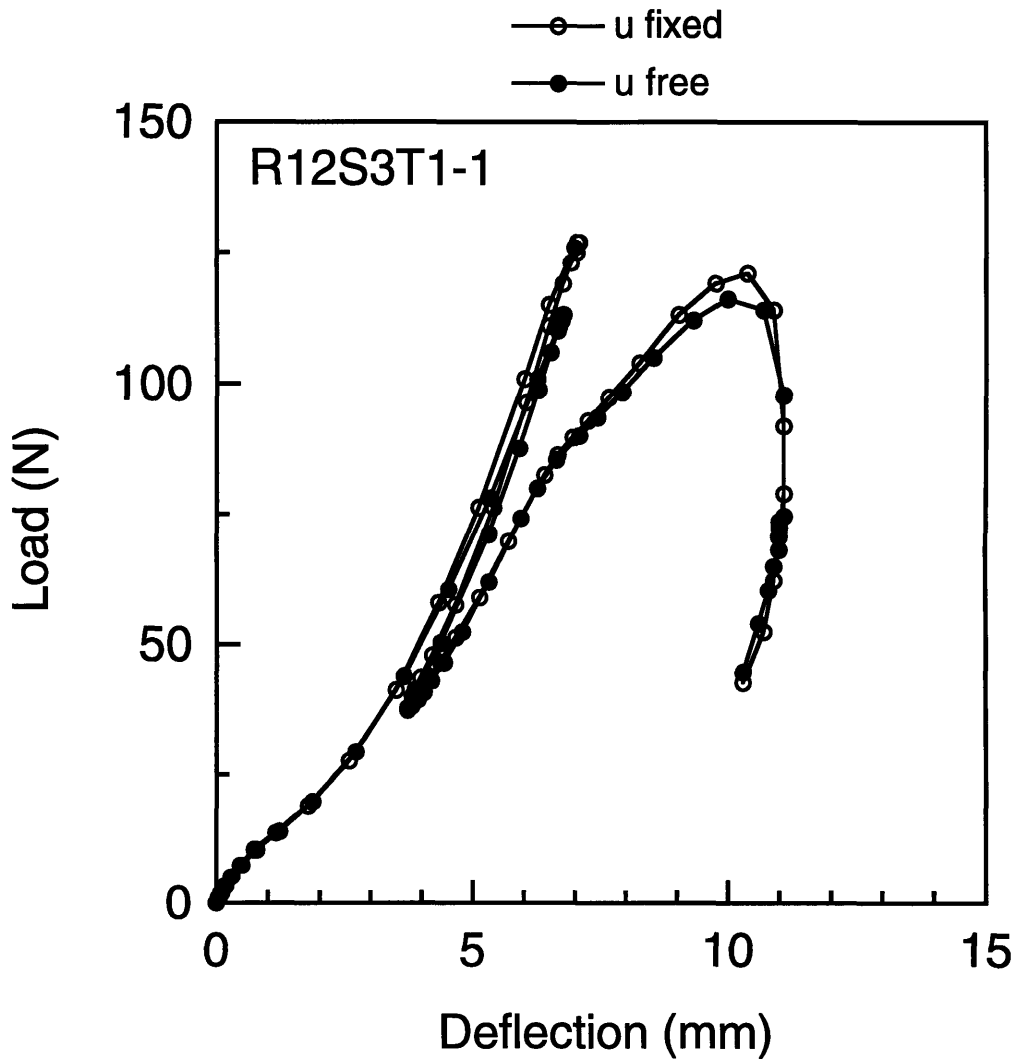


Figure 7.15 Numerical load-deflection results for specimen $R_{12}S_3T_1-1$ utilizing different assumptions on the u -component of displacement at the circumferential boundary condition (hinged).

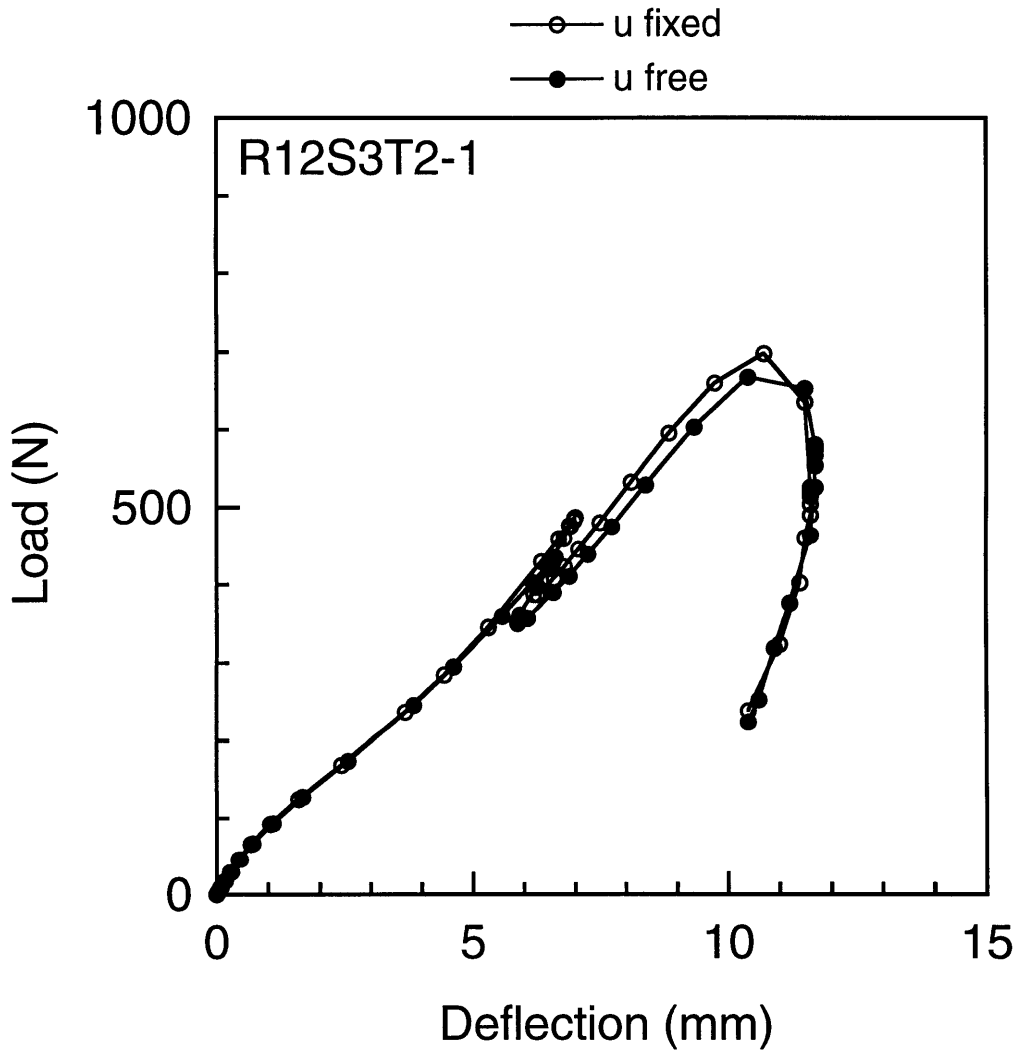


Figure 7.16 Numerical load-deflection results for specimen $R_{12}S_3T_2-1$ utilizing different assumptions on the u -component of displacement at the circumferential boundary condition (hinged).

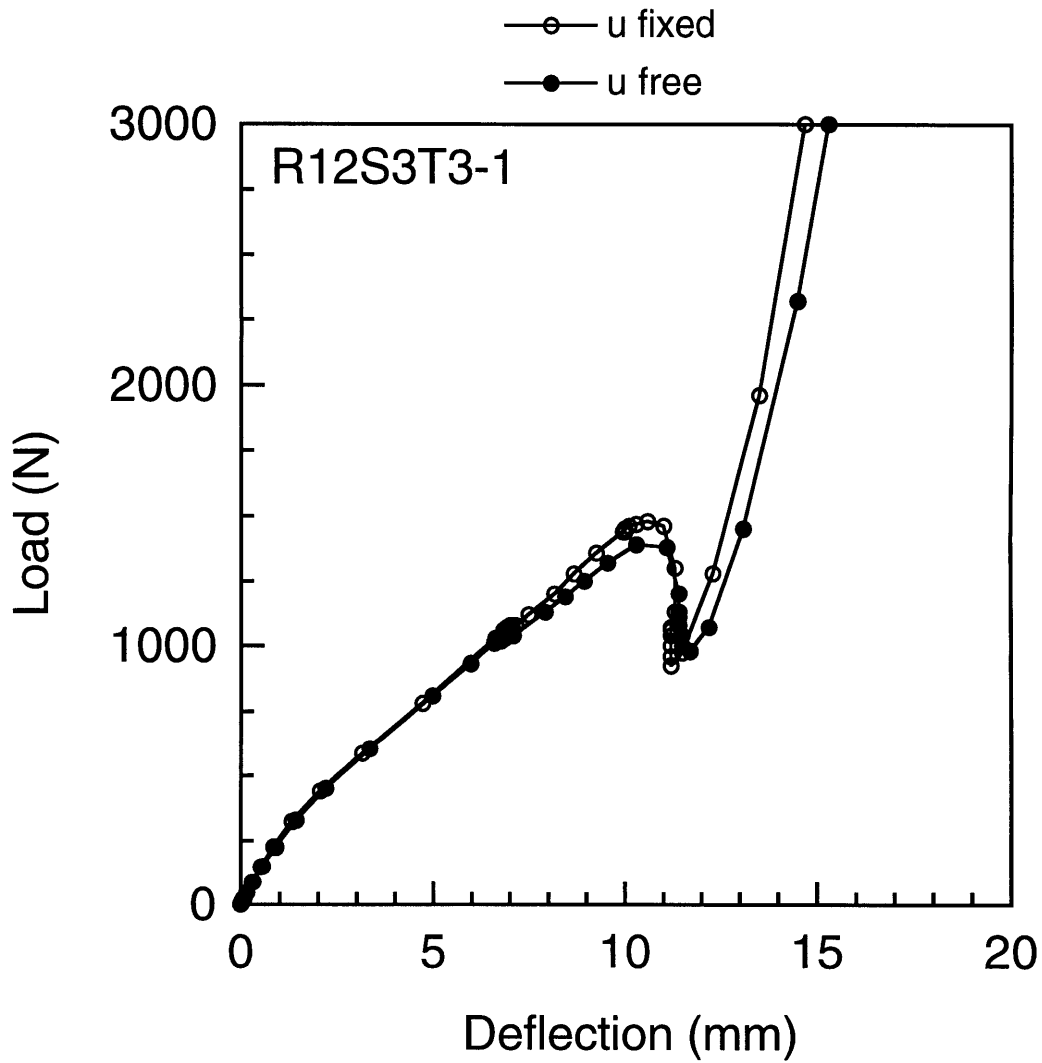


Figure 7.17 Numerical load-deflection results for specimen $R_{12}S_3T_3-1$ utilizing different assumptions on the u -component of displacement at the circumferential boundary condition (hinged).

slightly stiffer response with critical points approximately 10% higher than for the "u free" cases. These results are for both extremes of the boundary condition and result in relatively small changes in shell response. Experimentally, with all other parameters held constant, the response will lie between these two extremes. With regard to differences observed between the experimental and numerical responses discussed previously (see Figures 7.2, 7.3, and 7.4), differences due to this component of the hinged boundary condition are relatively small. Thus, the effect of the u -component of displacement at the hinged boundary condition is relatively unimportant for the shells considered in this work.

7.2.2 Effect of Axial Edge Restraint

One of the objectives of the experimental work is to explore the effect of restraining the axial edge on the shell response. In the previous work [21] with geometrically identical composite shells (discussed in section 4.4), the axial edges were free of traction. In the experimental component of the current work, these edges were restrained as described in chapter 5. Restraining the axial edges is more representative of the condition for a fuselage structure than free edges. The actual boundary condition in a fuselage, due to a frame or stringer, will lie somewhere between this restrained case (simple support) and fully clamped. The knife edges which restrain the shell along the axial edges in the experiments are intended to restrain out-of-plane displacement. This boundary condition is modeled (see section 6.2) by setting the out-of-plane displacement, w , and x -axis (axial direction) rotation, R_x , equal to zero in the numerical analyses. In this section, the response of geometrically identical shells having free and restrained axial boundary conditions are compared. The different responses are compared using both experimental data (from this and

previous [21] work) and numerical analysis results. For the purposes of discussion, specimens which are not restrained (free) on the axial edges are denoted by using *-free* after the specimen type designation (e.g., $R_{12}S_3T_1$ -free) while those with the axial edge restrained are denoted by using *-restrained*. The "free" and "restrained" designations thus refer to the axial edge boundary condition which is the only difference between specimens of a given geometry as considered here. The effect of these two axial boundary conditions on damage resistance is discussed in section 7.3.

The experimental loading responses for specimen type $R_{12}S_3T_1$ utilizing the two different axial boundary conditions are presented in Figure 7.18. The two load-deflection responses are in excellent agreement until the response of specimen $R_{12}S_3T_1$ -free diverges (prior to bifurcating) at a center deflection of approximately 3.0 mm. Results from numerical analysis in Figure 7.19 of the same specimens also indicate excellent agreement prior to bifurcation of the "free" specimen. The axial-edge restraint has very little effect on the response of this specimen type prior to bifurcation of the "free" specimen. Numerical axial deformation mode shapes from chapter 4 (see Figure 4.24) for specimen $R_{12}S_3T_1$ -free provide further insight into this observation. Prior to bifurcation for specimen $R_{12}S_3T_1$ -free, the axial shell edge is noted to deform out-of-plane very little (0.7 mm) relative to the center of the shell (2.6 mm) where load is applied. The axial variation in deformation prior to bifurcation for specimen $R_{12}S_3T_1$ -free is similar to that for specimen $R_{12}S_3T_1$ -restrained. Therefore, in the region of loading prior to bifurcation, shells with these two different axial restraints deform similarly which explains the loading response agreement prior to bifurcation of specimen $R_{12}S_3T_1$ -free.

Similar agreement is generally noted prior to buckling for the other two specimen types, $R_{12}S_3T_2$ and $R_{12}S_3T_3$, as shown in the experimental and

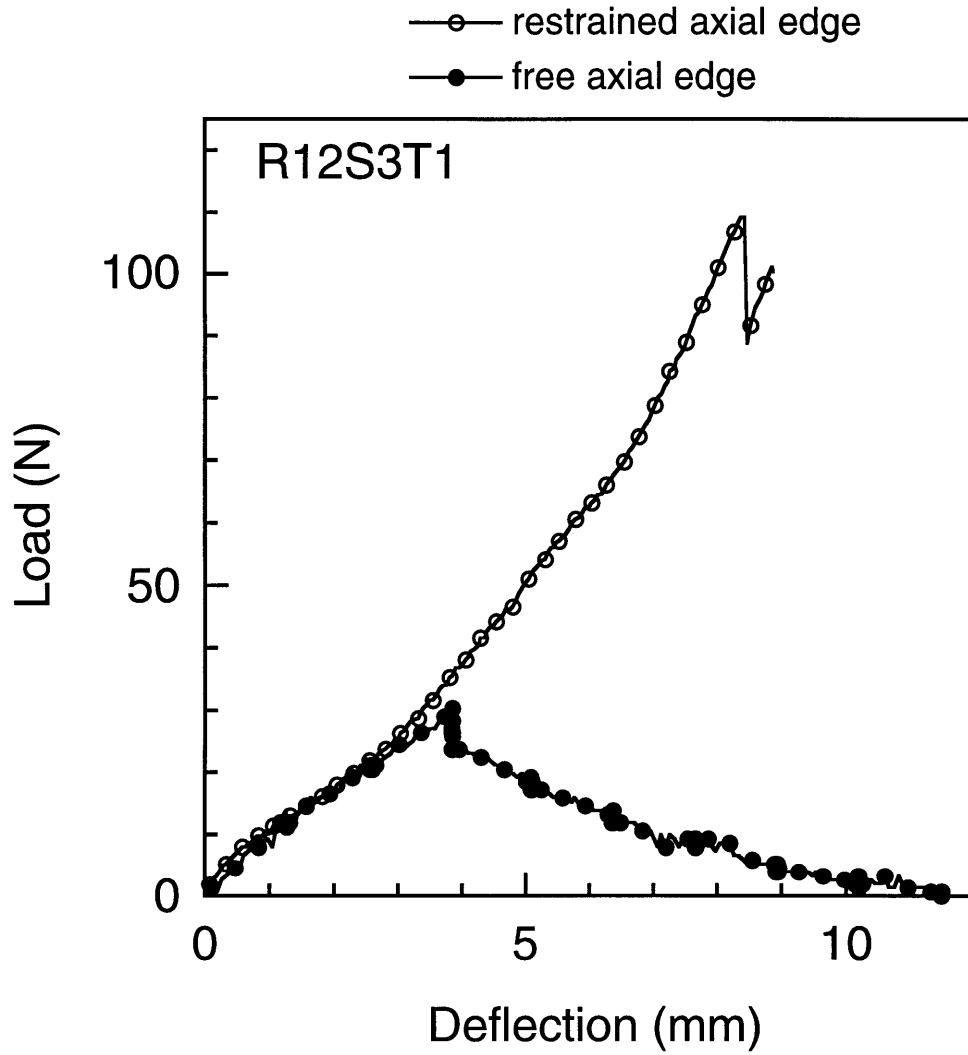


Figure 7.18 Experimental load-deflection response of composite shell $R_{12}S_3T_1$ with axial edges restrained and free [21].

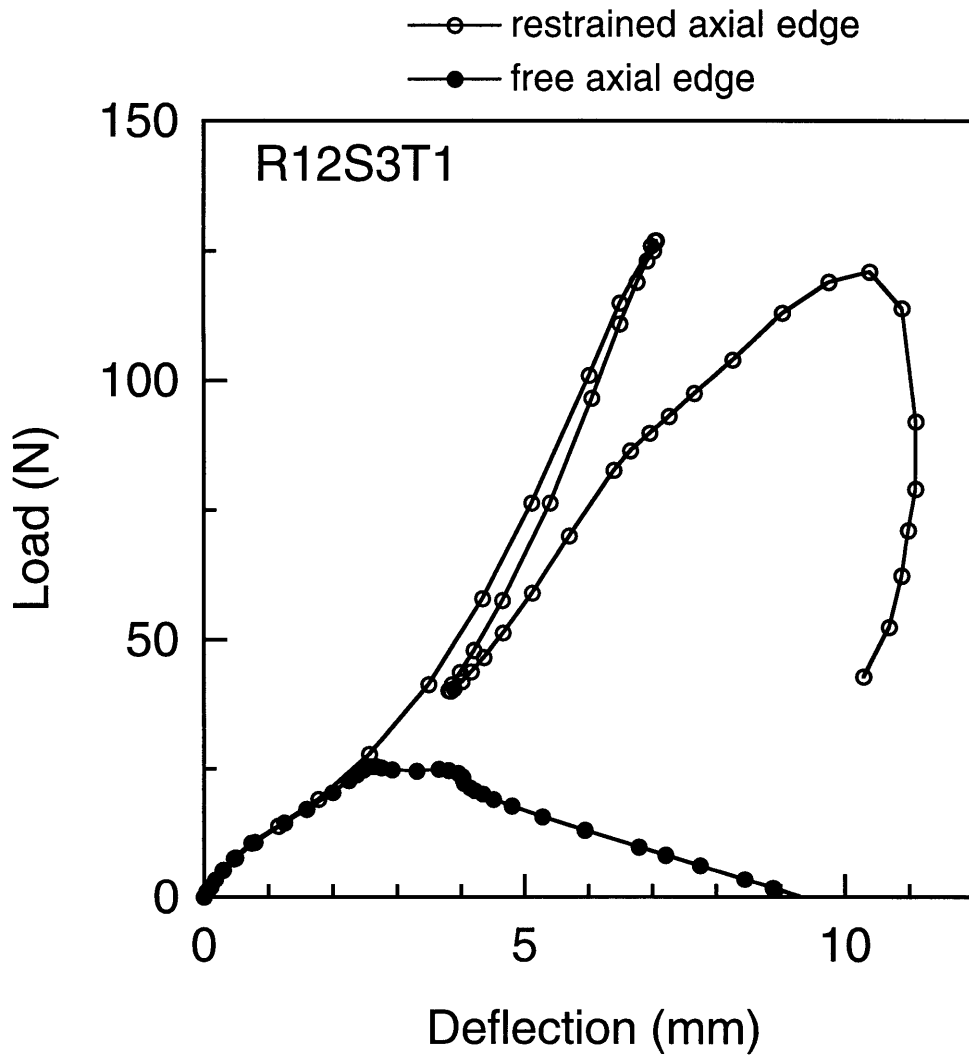


Figure 7.19 Numerical load-deflection results for composite shell $R_{12}S_3T_1$ with axial edges restrained and free.

numerical response comparisons in Figures 7.20 through 7.23. However, the experimental response in Figure 7.22 for specimen $R_{12}S_3T_3$ -free is more compliant than the response of specimen $R_{12}S_3T_3$ -restrained, including the response prior to bifurcation. It is hypothesized that this is due to the test fixture compliance at the circumferential boundary condition (hinged) described in section 4.4.3. Test fixture compliance would less strongly affect specimen $R_{12}S_3T_3$ -restrained because a percentage of the load is reacted through the axial restraints rather than entirely through the (compliant) hinged restraint. In general, however, the numerical and experimental responses for all three specimen types indicate that prior to buckling for the "free" specimens, the response of specimens with "restrained" and "free" axial constraints are quite similar. Implications of this observation for composite shell damage resistance are further discussed in section 7.3.

The response comparison for specimen type $R_{12}S_3T_1$ in Figures 7.18 and 7.19 are typical of those for the other two specimen types with regard to differences caused by the axial boundary condition. The responses are similar prior to bifurcation for the "free" specimen, but the critical (bifurcation) load for the "restrained" specimens are noted to be much higher than for the "free" specimen, *e.g.*, 127 N versus 25 N for specimen type $R_{12}S_3T_1$ in Figure 7.19. The bifurcation point for the "restrained" specimens has associated with it a secondary (bifurcation) path which is unstable in both load- and deflection-control. This is not observed for the "free" specimens which have a response (*e.g.*, as in Figure 7.19) which is unstable only in load-control. In the numerical results for all "restrained" shells in this work, bifurcation occurs from the primary path (symmetric deformation modes) to a secondary path (asymmetric deformation modes) before collapsing at a limit point. In contrast to the "free" shells, asymmetric modes are associated with the limit point for

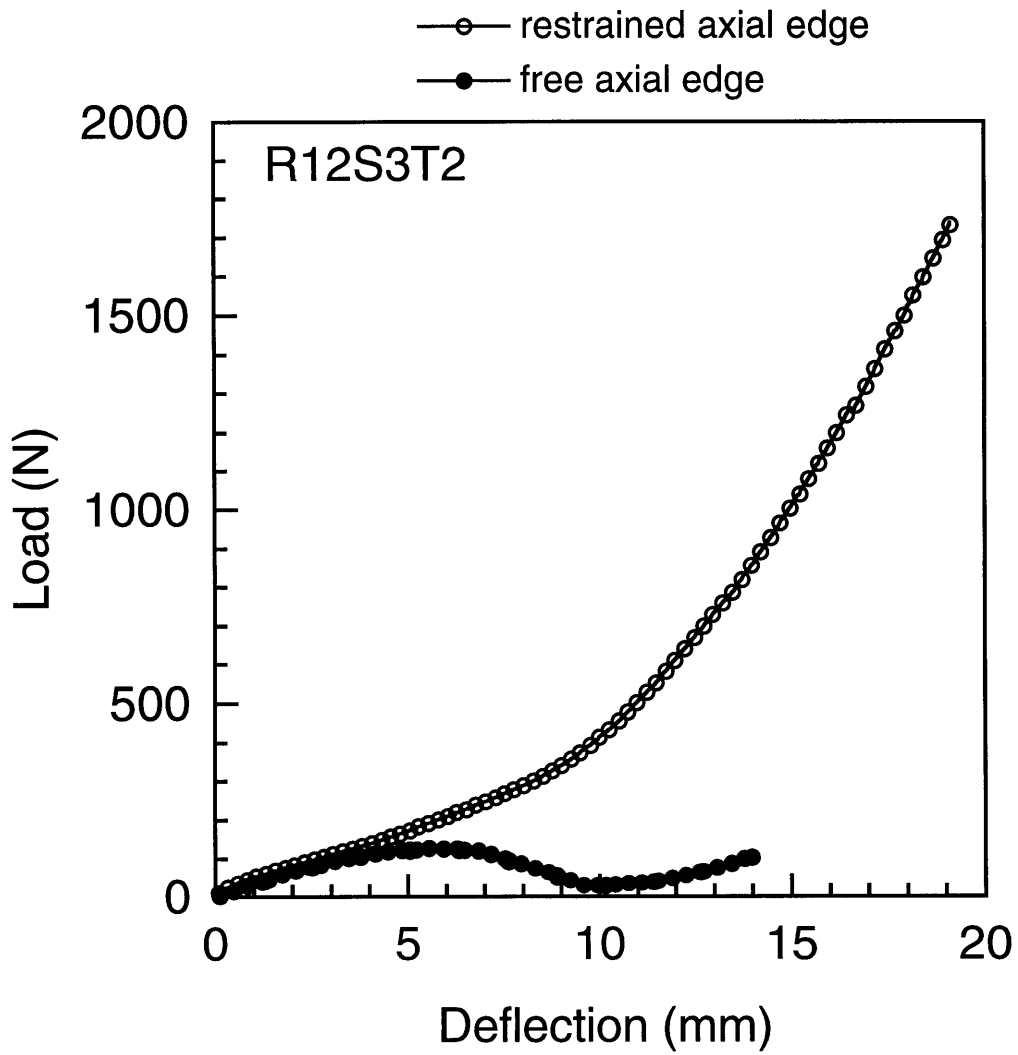


Figure 7.20 Experimental load-deflection response of composite shell $R_{12}S_3T_2$ with axial edges restrained and free [21].

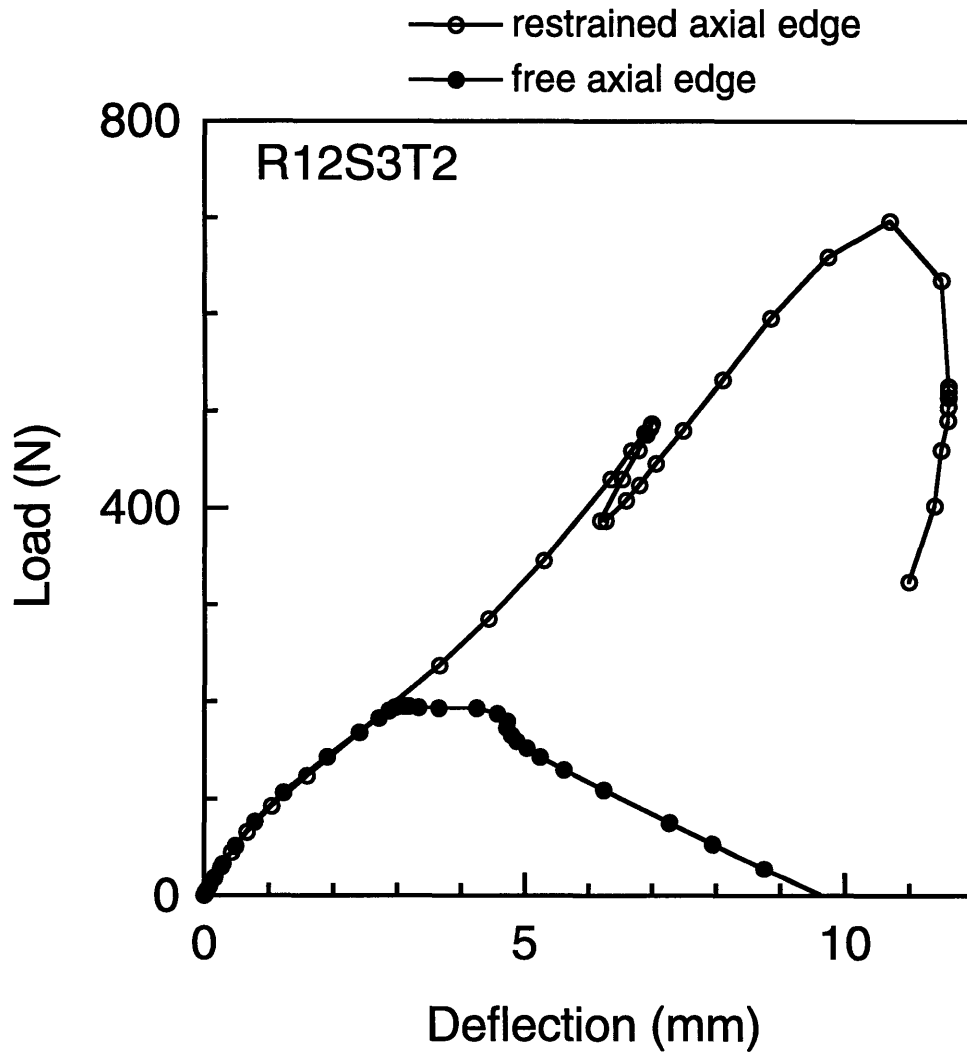


Figure 7.21 Numerical load-deflection results for composite shell $R_{12}S_3T_2$ with axial edges restrained and free.

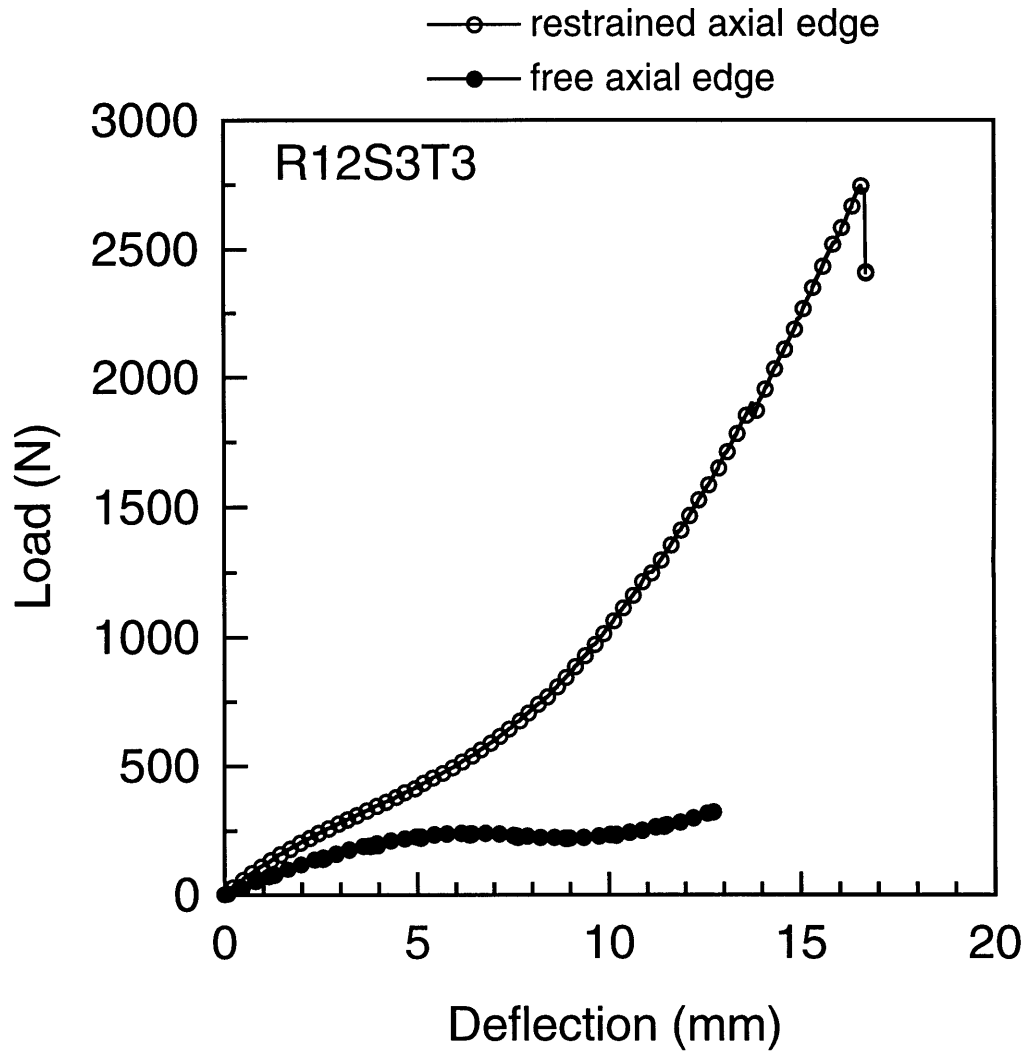


Figure 7.22 Experimental load-deflection response of composite shell $R_{12}S_3T_3$ with axial edges restrained and free [21].

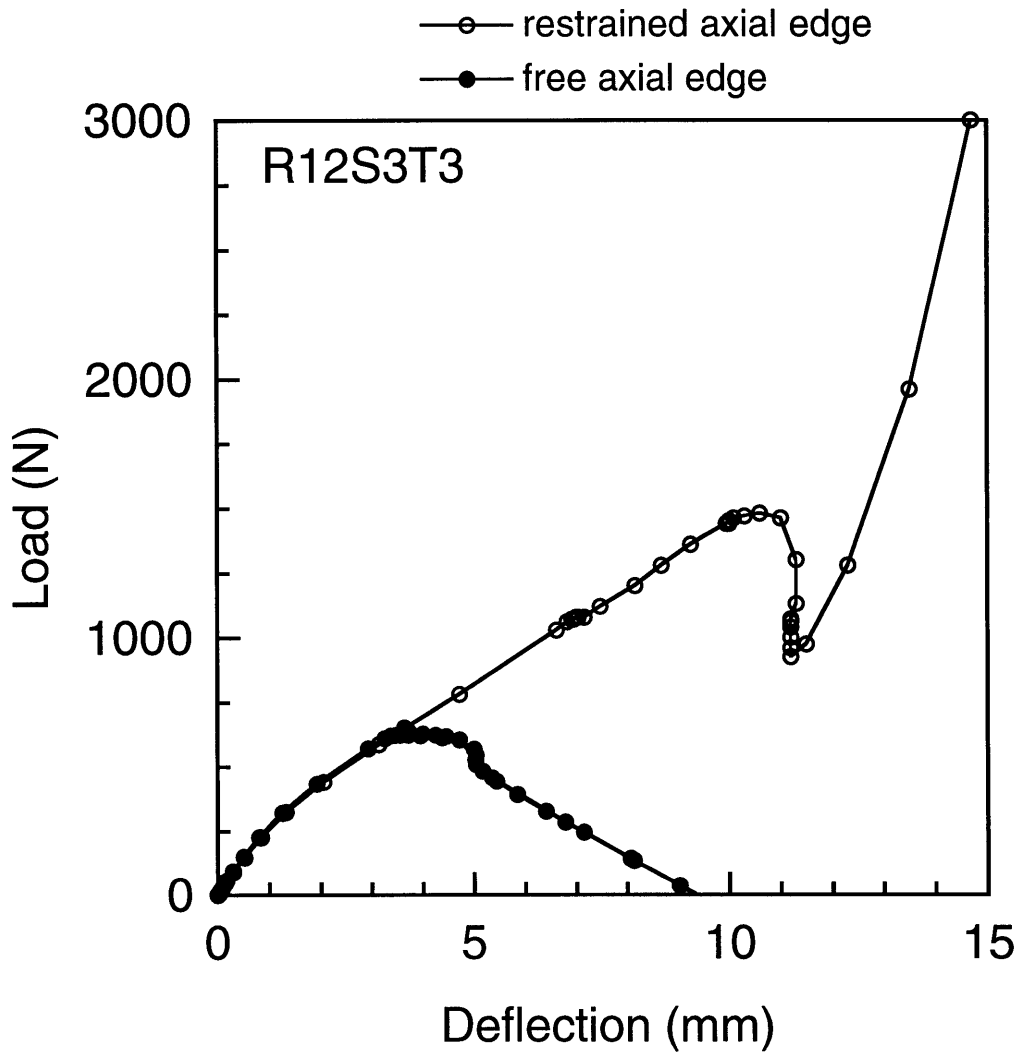


Figure 7.23 Numerical load-deflection results for composite shell $R_{12}S_3T_3$ with axial edges restrained and free.

the "restrained" shells due to the prior bifurcation. In both the "free" and "restrained" cases, the shells reach an inverted configuration on a stiffening final equilibrium path having associated symmetric deformation modes. In the "free" case, the final path is the second stable equilibrium path whereas for the "restrained" cases this is the third stable path (due to bifurcation and a limit point). In general, the response of the "restrained" shells is more complex (bifurcation and limit-point buckling) and has higher critical loads than the response of shells with "free" axial edge constraints.

A direct experimental comparison of the central spanwise mode shapes, including bifurcation, can be made for specimen type $R_{12}S_3T_1$ having "free" and "restrained" axial boundary conditions. The central spanwise modes for specimen $R_{12}S_3T_1$ -free are provided in Figure 7.24 for comparison to those in Figure 7.5 for specimen $R_{12}S_3T_1$ -restrained. As with the loading responses, the (symmetric) mode shapes for these two cases are in excellent agreement prior to bifurcation of the "free" specimen. A dominant asymmetric mode is evident in the "free" response at a center deflection of 3.9 mm whereas an asymmetric mode is not evident in the "restrained" case until a center deflection of 6.0 mm. As with the loading response, numerically evaluated mode shapes for the "restrained" specimen are in excellent agreement with numerically evaluated mode shapes for the "free" case before the two responses diverge near the bifurcation point of the "free" response (compare Figures 4.20 and 7.6).

The axial restraint also influences the form of the asymmetric shell bifurcation mode. The influence of the axial restraint on the bifurcation mode of specimen $R_{12}S_3T_1$ -restrained is evident in Figure 7.5 for center deflections of 6.0 mm, 8.0 mm, and 10.0 mm by comparison to the bifurcation modes for specimen $R_{12}S_3T_1$ -free in Figure 7.24. Bifurcation modes in Figure 7.24 are sinusoidal (antisymmetric with respect to the shell center) as for an arch. In

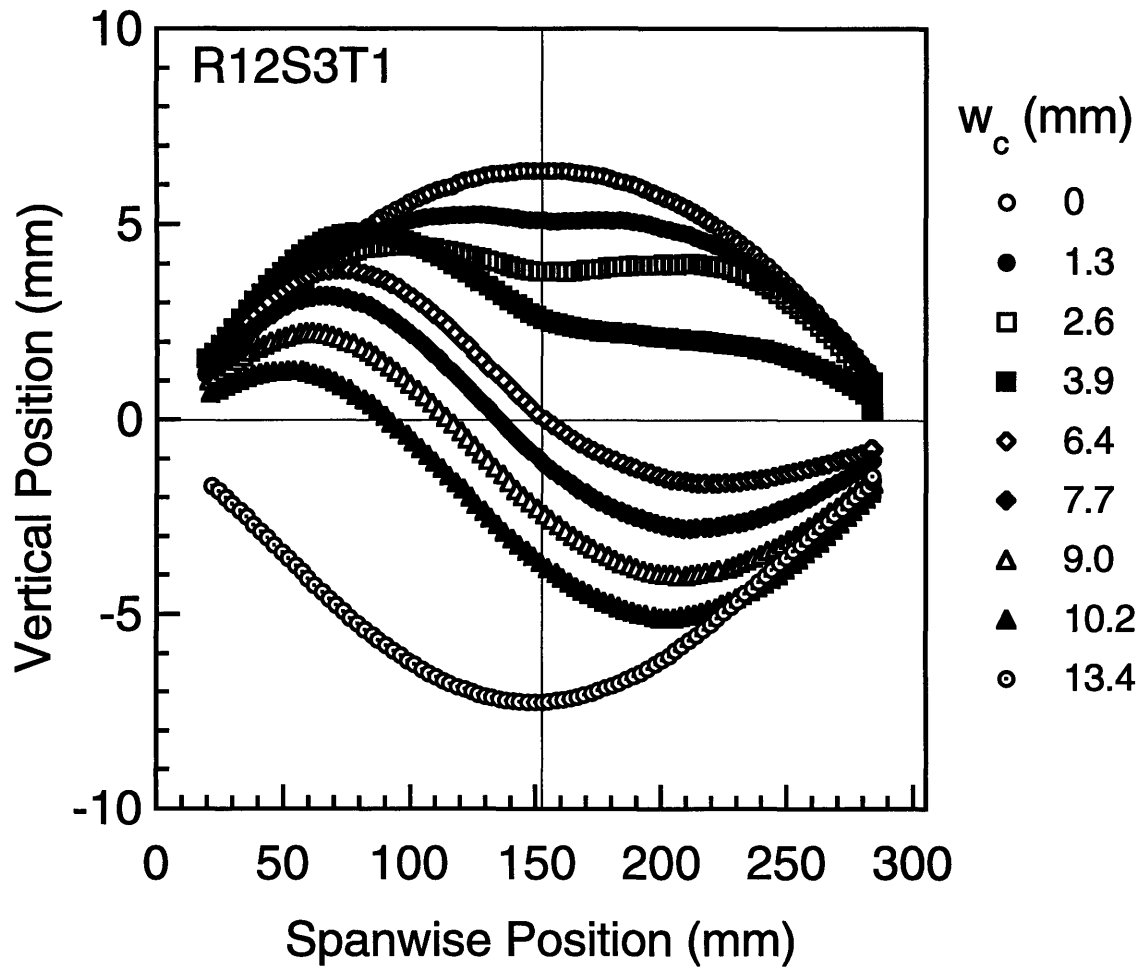


Figure 7.24 Experimental central spanwise deformation modes for specimen $R_{12}S_3T_1$ at different values of center deflection with axial edges free [21].

the "restrained" case, however, the bifurcation mode shapes do not display this sinusoidal bifurcation, *i.e.*, one circumferential half of the shell does not invert. Local deformations at the loading point are also evident in the "restrained" mode shapes (Figure 7.5) which are not evident in the "free" mode shapes (Figure 7.24). This same behavior is noted in the numerically evaluated central mode shapes for this specimen (compare Figures 7.6 and 4. 20) and in the experimental data and numerical mode shapes for specimens $R_{12}S_3T_2-2$ $R_{12}S_3T_3-2$ (Figures 7.11 to 7.14). This is due to the increased loading required to deform the "restrained" shell into a bifurcation mode which the axial edges resist, *i.e.*, the center of the shell bifurcates into an asymmetric mode but the shell edges, being restrained, resist this and any deformation. This distinct axial variation indicates that, as was found for the load-deflection responses, the "restrained" response is more complex than that of the "free" shells.

In this section, "restrained" shells have been noted to bifurcate into a dominant asymmetric mode much like shells with the "free" axial boundary condition. However, the loading responses of the "restrained" shells are more complex – there are three equilibrium paths rather than two in the "free" case, and the response contains both a bifurcation and limit point rather than one or the other. Differences in the mode shapes (due to axial variation) are also evident and again, the "restrained" mode shapes are found to be more complex than the "free" modes. Thus, although bifurcation into a dominant asymmetric mode occurs in the more realistic "restrained" cases, the behavior is different in many respects from the "free" response. Differences in the "restrained" shell response relative to the "free" cases clearly indicate that the axial restraint is important.

7.3 Damage Resistance

A primary objective of this work with regard to composite shell damage resistance is to investigate the effect of bifurcation, and the associated asymmetric deformation modes, on the resulting damage. As discussed in chapter 2, asymmetric and atypical (with regard to extent and distribution) damage states at the loading site have been observed for composite shells similar to those tested in this work [19, 38]. However, results in chapter 6 have shown that the damage found for specimens in this work is typical of that observed for composite plates having the same layup. Specimen type $R_{12}S_3T_1$, which was observed to bifurcate into asymmetric modes, was undamaged. The specimens which did damage were not observed to bifurcate, and therefore did not experience asymmetric modes. Atypical damage states are not expected in such cases. Damage results for the "free" composite shell geometries discussed in section 7.3 and chapter 4, are also consistent with typical plate damage. Thus, in regard to damage resistance, nothing atypical of that observed previously for composite plates of the same material and geometry are observed in this work. However, this result is certainly not conclusive based on the three specimen geometries considered in this work, *i.e.*, the hypothesis of damage away from the loading site due to asymmetric bifurcation modes has not been disproved. In fact, the mechanism for atypical damage formation (bifurcation into asymmetric modes) was observed, it just happens that this specimen type was undamaged during testing. Recommendations for further work in regard to damage resistance, particularly to investigate plate and shell differences, are made in chapter 8.

The finding in section 7.3 regarding loading-response agreement between "free" and "restrained" shells may have implications for damage-resistance

testing of composite shells. Atypical damage found in previous work with composite shells was noted to occur on the first equilibrium path, likely due to compressive membrane loading of the shell on this path [19]. Investigation of this atypical damage is of considerable interest as it is the key difference between plate and shell damage resistance, *i.e.*, it represents one area of composite damage resistance which is *not* well understood. Numerical and experimental results from this work indicate that the response for the "free" and "restrained" shell configurations respond similarly in this region. Therefore, "free" shells, which are straightforward to test relative to the "restrained" configuration, are likely to provide damage resistance data that is applicable to the more realistic (fuselage or similar structure) "restrained" case. This hypothesis does need further experimental evidence, however, particularly in regard to damage, because it is based solely on observed similarities in the loading response at this time. Suggestions for further work in this area are made in chapter 8.

7.4 Asymmetric Meshing Technique (AMT)

The asymmetric meshing technique developed and utilized in this work has shown great utility in evaluating the nonlinear response of shells. The technique is useful for evaluating bifurcation, particularly from nonlinear prebuckling paths, using nonlinear finite element formulations. The effect of the asymmetry is to introduce perturbations into the model such that lower-energy bifurcation states can be assessed. This is done without altering the problem geometry, and thus solutions to the problem of interest can be generated without resorting to geometric imperfections or assumed solutions. The asymmetric meshing has no effect on the linear response of the structure because neither the problem geometry, boundary conditions, nor loading has

been modified. While the AMT has only been utilized within the STAGS finite element package in this work, the technique should be effective in any nonlinear finite element formulation.

The AMT is seen as an alternative to the already existing "tools" for analyzing bifurcation in shell structures. In this work it has been used to great advantage where both limit-point and bifurcation buckling are aspects of the shell response. Relative to the alternative techniques considered in this work (equivalence transform and geometric imperfections), the AMT is straightforward, efficient, and robust. It is relatively straightforward because it avoids arbitrary choices associated with the other techniques such as the amplitude and number of eigenmodes used as either imperfections or assumed solutions in a branch switch. The AMT has been shown to identify and traverse both bifurcation and limit points (sometimes both) in a single analysis run. In fact, the AMT was utilized to "discover" the correct bifurcation solution to the benchmark problem - only later was this response verified by traditional techniques. The AMT's direct identification and traversal of bifurcation points is in contrast to the other techniques which require repeated analysis to converge to the bifurcation point and secondary path. In this sense, the AMT is efficient, *e.g.*, the bifurcation response for the eighteen shells in Appendix B were each evaluated through a single numerical analysis. Traditional techniques would incur significant additional computation and repeated analysis to assess the same bifurcation response.

The AMT is perceived as more robust than traditional techniques with regard to the effect of arbitrary choices on the resulting predicted response. As with traditional techniques, the AMT requires the analyst to make an arbitrary choice. Traditional techniques require choices regarding amplitude and mode of the imperfection or assumed solution. The AMT requires the

analyst to choose the form of the asymmetric mesh. For example, a number of different asymmetric meshes were explored in chapters 4 and 6 for various shell analyses. The effect of subjective choices on the resulting computed response for both the traditional techniques and the AMT can be compared. This does not refer to typical meshing refinements which are an aspect of all finite element analyses. Rather, with traditional bifurcation techniques, different choices of mode number and amplitude results in a range of responses. In the AMT, different choices of asymmetric discretization results in a maximum of two different responses – either the limit point or bifurcation response (if it exists) is found. In this sense, the AMT is robust relative to the traditional techniques. The effect of subjective discretization choices in the AMT is limited to only two responses.

The AMT thus represents a method for evaluating the effect of perturbations in nonlinear structural problems. The type of spatial discretization used in the AMT to introduce perturbations in finite element formulations is recommended for further exploration in chapter 8.

CHAPTER 8

CONCLUSIONS AND RECOMMENDATIONS

The present work was conducted to better understand the response of composite shells to transverse loadings which may damage these structures. To do this, a combined experimental and numerical approach was undertaken to study the response of composite shells to transverse loading. Buckling instabilities are found to be a dominant feature of the observed shell response. Nonlinear finite element models, including a novel technique for evaluating bifurcation, were successfully developed to predict the shell response. In this chapter, conclusions are drawn from the results of this investigation and recommendations for future work are made.

8.1 Conclusions

The work conducted and the data and discussion presented herein lead to the following conclusions:

1. Finite element models developed in this work utilizing the novel asymmetric meshing technique (AMT) have successfully modeled the response of various shell configurations including bifurcation, postbuckling, and mode-shape evolutions. The technique and associated models have been validated by comparison to traditional benchmark analyses and verified by comparison to composite shell data.
2. Advantages of the AMT over traditional techniques for inducing

bifurcation in the shells in this work have been identified and include simplicity, efficiency, and robustness.

3. A large-rotation, large-deflection shell buckling problem, used as a benchmark problem in the finite-element literature, is found to bifurcate prior to the limit point predicted in previous work.
4. Bifurcation and limit-point buckling occur within the nonlinear region of shell response for the structures considered in this work.
5. Bifurcation in the response of shells considered herein can be difficult to identify experimentally using the transition from symmetric to asymmetric deformation modes as an indicator.
6. Antisymmetry in measured and predicted left and right mode shapes is due to laminate bending-twisting coupling with the effect being more pronounced at larger deflections and for thicker specimens, as expected.
7. Generally, there is excellent agreement in the initial loading portion of the predicted and experimental response with larger differences as the response progresses.
8. Compliance of the test fixture is found to strongly influence a number of measured shell responses as it causes a more compliant measured load-deflection response, inhibits bifurcation, and promotes a symmetric limit-point response.
9. As specimen thickness increases, bifurcation loads increase whereas the associated deflections are approximately constant.
10. Increased thickness causes a more stable, stiffer response as the deflection and load ranges associated with the instability region (postbuckling after bifurcation) are reduced. The thickest specimen bifurcates to a stable secondary path with no instability region.
11. Restraining the in-plane displacement along the hinged boundary

condition has little effect on the predicted shell response.

12. Restraining axial edges has little or no effect on the response prior to bifurcation but results in a more complex response thereafter including higher critical bifurcation loads, an instability region that is unstable in deflection- and load-control, a second critical (limit) point on a stable secondary equilibrium path, and a third (final) equilibrium path.
13. No damage atypical of that previously observed for composite plates was observed in this work and is attributed to the lack of observed asymmetric bifurcation modes in cases where the specimens were damaged.

8.2 Recommendations

The present work raises a number of issues which need to be addressed by further investigation. Therefore, the following recommendations are made:

1. Asymmetric spatial discretization is a novel way to introduce perturbations into nonlinear finite element problems. This technique deserves further investigation as it may also be useful in other applications, such as crack-turning problems.
2. Modeling refinements such as the inclusion of transverse shear and contact elements at the loading point should be undertaken to understand the relative importance of each on the resulting response. These analysis refinements are necessary to obtain improved predictive capabilities for shell response and damage resistance.
3. Evaluating bifurcation from nonlinear prebuckling states using the asymmetric meshing technique should be explored for other problem geometries, such as axially compressed cylinders and shell sections,

particularly in regard to its perceived efficiency relative to current techniques. Such investigations will lead to a more general understanding of the applicability of the technique including its advantages and limitations.

4. The hypothesis that atypical and asymmetric damage formation can occur due to bifurcation (asymmetric deformation modes) should be further explored. Damaged specimens in this work did not bifurcate, but an undamaged specimen was observed to bifurcate, so a direct link between damage and bifurcation has not yet been made. Analyses will provide insight into laminate and structural parameters which would likely lead to bifurcation and thus to atypical damage formation.
5. The effect of other boundary conditions, such as fully clamped, should be considered to explore the range of possible shell responses, particularly with regard to bifurcation as this is seen to influence damage resistance. Analysis will indicate which shells bifurcate and thus which shells are likely to incur atypical damage. These structural configurations then become likely candidates for experimental damage resistance studies.
6. Effects of test fixture compliance, in the direction which affects separation of the hinged supports, should be further explored both experimentally and through analysis. For example, separation of the two hinged restraints can be measured during testing using a displacement transducer to provide information about test fixture compliance which can then be utilized in numerical models to determine the magnitude of this effect relative to other modeling assumptions.
7. The effect of damage formation on the resulting measured response should be addressed, particularly with regard to bifurcation. To first order, damage can be modeled as an area of reduced stiffness. Results of

such analyses can be utilized to guide further experimental studies. Experimentally, the effect of damage can be considered by comparing the loading response of a virgin shell with that of a shell which has previously been damaged.

8. If damage is to be understood in relation to asymmetric bifurcation modes, identification and monitoring of bifurcation modes is necessary. Comparative strain gages should be used to monitor bifurcation experimentally. Gages placed symmetrically (circumferential direction) with regard to the loading point on one shell surface will indicate bifurcation when the gages diverge.
9. Comparisons between shells with free and restrained axial edges indicate good agreement prior to bifurcation of the unrestrained shells. This agreement should be further explored with regard to damage formation because this agreement would facilitate future damage resistance studies by allowing tests of specimens with free axial edges to determine the effects of those with the more realistic boundary conditions (restrained).

References

1. Nolet, S. C. and Sandusky, P. M., "Impact Resistant Hybrid Composite for Aircraft Leading Edges", *SAMPE Quarterly*, Vol. 17, No. 4, 1986, pp. 46-53.
2. Olivia, P. V., "SF-340 Airfoil Structure - A Unique Approach", *17th National SAMPE Technical Conference*, Kiamasha Lake, NY USA, 1985,
3. Amatore, D., "Composite Hydrogen Tank Test Completed for DC-XA", NASA News Press Release: 96-13, Marshall Space Flight Center, January 25, 1996.
4. Malone, J., "Shuttle's New Lighter, Stronger External Tank Completes Major Pressure Tests", NASA News Press Release: 97-58, Marshall Space Flight Center, March 28, 1997.
5. Smith, P. J., Thomson, L. W., and Wilson, R. D., "Development of Pressure Containment and Damage Tolerance Technology for Composite Fuselage Structures in Large Transport Aircraft", NASA-CR-3996, Boeing Aerospace Co., August, 1986.
6. Chen, G.-S., Bidinger, G. M., and Lou, M. C., "Impact Damage in Small Diameter Graphite/Epoxy Composite Struts", *Proceedings of the 33rd AIAA/ASME/ASCE/AHS Structures, Structural Dynamics, and Materials Conference*, Dallas, TX, 1992, pp. 2945-2954.
7. Abrate, S., "Impact on Laminated Composites: Recent Advances", *Applied Mechanics Review*, Vol. 47, No. 11, November, 1994, pp. 517-544.

8. Breivik, N. L., Gurdal, Z., and Griffin, O. H., "Compression of Laminated Composite Beams with Initial Damage", *Proceedings of the American Society for Composites 7th Technical Conference*, University Park, PA, 1992, pp. 972-981.
9. "Military Handbook; Polymer Matrix Composites, Volume III - Utilization of Data", MIL-HDBK-17-3D, 4-99 to 4-100, Department of Defense, February, 1994.
10. "Composite Aircraft Structures", Federal Aviation Administration, Advisory Circular 20-107A, U. S. Department of Transportation, April 25, 1984.
11. "Air Force Guide Specification", AFGS-87221A, United States Air Force, June, 1990.
12. Cairns, D. S. and Lagace, P. A., "A Consistent Engineering Methodology for the Treatment of Impact in Composite Materials", *Journal of Reinforced Plastics and Composites*, Vol. 11, No. 4, April, 1992, pp. 395-412.
13. Sjöblom, P. O., Hartness, J. T., and Cordell, T. M., "On Low-Velocity Impact Testing of Composite Materials", *Journal of Composite Materials*, Vol. 22, January, 1988, pp. 30-52.
14. Abrate, S., "Impact on Laminated Composite Materials", *Applied Mechanics Review*, Vol. 44, No. 4, April, 1991, pp. 155-190.
15. Wardle, B. L. and Lagace, P. A., "On the Use of Dent Depth as an Impact Damage Resistance Metric for Thin Composite Structures", *Journal of Reinforced Plastics and Composites*, Vol. 16, No. 12, 1997, pp. 1093-1110.
16. Cantwell, W. J. and Morton, J., "The Impact Resistance of Composite Materials", *Composites*, Vol. 22, No. 5, September, 1991, pp. 55-97.

17. Lin, H. J. and Lee, Y. J., "Impact-Induced Fracture in Laminated Plates and Shells", *Journal of Composite Materials*, Vol. 24, November, 1990, pp. 1179-1199.
18. Wardle, B. L., "Impact and Quasi-static Response of Cylindrical Composite Shells", TELAC Report 95-4, S. M. Thesis, Massachusetts Institute of Technology, May, 1995.
19. Wardle, B. L. and Lagace, P. A., "Importance of Instability in Impact Response and Damage Resistance of Composite Shells", *AIAA Journal*, Vol. 35, No. 2, February, 1997, pp. 389-396.
20. Wardle, B. L. and Lagace, P. A., "On the Behavior of Composite Shells Under Transverse Impact and Quasi-static Loading", *Proceedings of the 38th AIAA/ASME/ASCE/AHS/ASC Structures, Structural Dynamics, and Materials Conference*, Kissimmee, FL, 1997, pp. 1832-1842.
21. Tudela, M. A., "Structural Response and Damage Development of Cylindrical Composite Panels", TELAC Report 96-11, S. M. Thesis, Massachusetts Institute of Technology, 1996.
22. Kwon, Y. S. and Sankar, B. V., "Indentation-Flexure and Low-Velocity Impact Damage in Graphite Epoxy Laminates", *Journal of Composites Technology and Research*, Vol. 15, No. 2, Summer, 1993, pp. 101-111.
23. Lagace, P. A., Williamson, J. E., Tsang, P. H. W., Wolf, E., and Thomas, S., "A Preliminary Proposition for a Test Method to Measure (Impact) Damage Resistance", *Journal of Reinforced Plastics and Composites*, Vol. 12, No. 5, May, 1993, pp. 584-601.
24. Lee, S. and Zahuta, P., "Instrumented Impact and Static Indentation of Composites", *Journal of Composite Materials*, Vol. 25, February, 1991, pp. 204-222.

25. Tan, T. M. and Sun, C. T., "Use of Statical Indentation Laws in the Impact Analysis of Laminated Composite Plates", *Journal of Applied Mechanics*, Vol. 52, March, 1985, pp. 6-12.
26. Jackson, W. C. and Poe, C. C., Jr., "The Use of Impact Force as a Scale Parameter for the Impact Response of Composite Laminates", *Journal of Composites Technology & Research*, Vol. 15, No. 4, Winter, 1992, pp. 282-289.
27. Wu, E. and Shyu, K., "Response of Composite Laminates to Contact Loads and Relationship to Low-Velocity Impact", *Journal of Composite Materials*, Vol. 27, No. 15, 1993, pp. 1443-1464.
28. Gresczuk, L. B., "Damage in Composite Materials Due to Low Velocity Impact", in *Impact Dynamics*, ed. Zukas, J. A., Nicholas, T., Swift, H. F., and Curran, D. R., Wiley-Interscience, New York, 1982, pp. 55-94.
29. Yang, S. H. and Sun, C. T., "Indentation Law for Composite Laminates", *Composite Materials: Testing and Design (Sixth Conference)*, ASTM STP 787, ASTM, 1982, pp. 425-449.
30. Olsson, R., "Impact Response of Orthotropic Composite Plates Predicted from a One-Parameter Differential Equation", *AIAA Journal*, Vol. 30, No. 6, June, 1992, pp. 1587-1596.
31. Ambur, D. R. and Starnes Jr., J. H., "Nonlinear Response and Damage-Initiation Characteristics of Curved Composite Plates Subjected to Low-Speed Impact", *Proceedings of the 38th AIAA/ASME/ASCE/AHS/ASC Structures, Structural Dynamics, and Materials Conference*, Kissimmee, FL, 1997, pp. 1821-1831.
32. Palazotto, A., Perry, R., and Sandhu, R., "Impact Response of Graphite/Epoxy Cylindrical Panels", *AIAA Journal*, Vol. 30, No. 7, July, 1992, pp. 1827-1832.

33. Kistler, L. S., "Experimental Investigation of the Impact Response of Cylindrically Curved Laminated Composite Panels", *Proceedings of the 35th AIAA/ASME/ASCE/AHS/ASC Structures, Structural Dynamics, and Materials Conference*, Hilton Head, SC, 1994, pp. 2292-2297.
34. Palazotto, A. N., Chien, L. S., and Taylor, W. W., "Stability Characteristics of Laminated Cylindrical Panels Under Transverse Loading", *AIAA Journal*, Vol. 30, No. 6, June, 1992, pp. 1649-1653.
35. Marshall, I. H. and Rhodes, J., "Snap-buckling of Thin Shells of Rectangular Planform", in *Stability Problems in Engineering Structures and Components*, ed. Richards, T. H. and Stanley, P., Applied Science Publisher, London, 1979, pp. 249-264.
36. Marshall, I. H., Rhodes, J., and Banks, W. M., "Experimental Snap-buckling Behaviour of Thin GRP Curved Panels Under Lateral Loading", *Composites*, Vol. 8, No. 2, April, 1977, pp. 81-86.
37. Marshall, I. H., Rhodes, J., and Banks, W. M., "The Nonlinear Behaviour of Thin, Orthotropic, Curved Panels Under Lateral Loading", *Journal of Mechanical Engineering Science*, Vol. 19, No. 1, 1977, pp. 30-37.
38. Wardle, B. L. and Lagace, P. A., "On the Use of Quasi-static Testing to Assess Impact Damage Resistance of Composite Shells", *Mechanics of Composite Materials and Structures*, Vol. 5, No. 1, January-March, 1998, pp. 103-121.
39. Riks, E., "The Application of Newton's Method to the Problem of Elastic Stability", *Journal of Applied Mechanics*, Vol. 39, 1982, pp. 1060-1066.
40. Bushnell, D., *Computerized Buckling Analysis of Shells*, Mechanics of Elastic Stability, ed. Leipholz, H. H. E. and Oravas, G. Æ. Vol. 9, Martinus Nijhoff Publishers, Dordrecht, 1985, pp. 1-28.

41. Bazant, Z. P. and Cedolin, L., *Stability of Structures: Elastic, Inelastic, Fracture, and Damage Theories*, The Oxford Engineering Science Series, Oxford University Press, New York, 1991, pp. 984.
42. Timoshenko, S., *Theory of Elastic Stability*, Engineering Societies Monographs, McGraw-Hill, New York, 1936.
43. Bushnell, D., "Buckling of Shells – Pitfalls for Designers", *AIAA Journal*, Vol. 19, No. 9, September, 1981, pp. 1183-1226.
44. Fitch, J. R., "The Buckling and Post-buckling Behavior of Spherical Caps Under Concentrated Load", *International Journal of Solids and Structures*, Vol. 4, 1968, pp. 421-446.
45. Kollár, L. and Dulácska, E., *Buckling of Shells for Engineers*, John Wiley & Sons, Budapest, Hungary, 1984,
46. Riks, E., Brogan, F. A., and Rankin, C. C., "Numerical Aspects of Shell Stability Analysis", in *Computational Mechanics of Nonlinear Response of Shells*, Springer-Verlag, New York, 1990, pp. 125-151.
47. Knight, N. F. and Starnes Jr., J. H., "Developments in Cylindrical Shell Stability Analysis", *Proceedings of the 38th AIAA/ASME/ASCE/AHS/ASC Structures, Structural Dynamics, and Materials Conference*, Kissimmee, FL, 1997, pp. 1933-1948.
48. Ericksen, J. L., *Introduction to the Thermodynamics of Solids*, Applied Mathematics and Mathematical Computation, ed. Knops, R. J. and Morton, K. W. Chapman & Hall, New York, 1991, pp. 39-61.
49. Arbocz, J., "Future Directions and Challenges in Shell Stability Analysis", *Proceedings of the 38th AIAA/ASME/ASCE/AHS/ASC Structures, Structural Dynamics, and Materials Conference*, Kissimmee, FL, 1997, pp. 1949-1962.

50. Singer, J., "Experimental Studies in Shell Buckling", *Proceedings of the 38th AIAA/ASME/ASCE/AHS/ASC Structures, Structural Dynamics, and Materials Conference*, Kissimmee, FL, 1997, pp. 1922-1932.
51. Arbocz, J. and Hoi, J. M. A. M., "The Role of Experiments in Improving the Computational Models for Composite Shells", in *Analytical and Computational Models of Shells*, ed. Noor, A. K., Belytschko, T., and Simo, J. C., Winter Annual Meeting of the ASME. ASME, New York, 1989, pp. 613-640.
52. Fung, Y. C. and Kaplan, A., "Buckling of Low Arches or Curved Beams of Small Curvature", NASA TN 2840, California Institute of Technology, November, 1952.
53. Kaplan, A. and Fung, Y. C., "A Nonlinear Theory of Bending and Buckling of Thin Elastic Shallow Spherical Shells", NACA-TN-3212, California Institute of Technology, April, 1954.
54. Rhodes, J. and Marshall, I. H., "Unsymmetrical Buckling of Laterally Loaded Reinforced Plastics Shells", *Proceedings of the Second International Conference on Composite Materials (ICCM/2)*, Toronto, Canada, 1978, pp. 303-315.
55. Johnson, E. R., Hyer, M. W., and Carper, D. M., "Response of Composite Material Shallow Arch to Concentrated Load", *Journal of Aircraft*, Vol. 123, No. 6, June, 1986, pp. 529-536.
56. Tudela, M. A., Lagace, P. A., and Wardle, B. L., "Buckling Response of Transversely Loaded Composite Shells - Part I: Experiments", *Proceedings of the 39th AIAA/ASME/ASCE/AHS/ASC Structures, Structural Dynamics, and Materials Conference*, Long Beach, CA, 1998.
57. Gong, S. W., Shim, V. P. W., and Toh, S. L., "Impact Response of Laminated Shells With Orthogonal Curvatures", *Composites Engineering*, Vol. 5, No. 3, 1995, pp. 257-275.

58. Stolarski, H., Belytschko, T., and Lee, S.-H., "A review of shell finite elements and corotational theories", *Computational Mechanics Advances* 2, 1995, pp. 125-212.
59. Riks, E., "Some Computational Aspects of the Stability Analysis of Nonlinear Structures", *Computer Methods in Applied Mechanics and Engineering*, Vol. 47, 1984, pp. 219-259.
60. Riks, E., "Bifurcation and Stability, A Numerical Approach", *Innovative Methods for Nonlinear Problems*, 1984, pp. 313-344.
61. Sabir, A. B. and Lock, A. C., "The Application of Finite Elements to the Large Deflection Geometrically Non-linear Behaviour of Cylindrical Shells", in *Variational Methods in Engineering*, ed. Brebbia, C. A. and Tottenham, H., Vol. 2, Southampton University Press, Surrey, 1973, pp. 7/66-7/75.
62. Chang, T. Y. and Sawamiphakdi, K., "Large Deformation Analysis of Laminated Shells by Finite Element Method", *Computers and Structures*, Vol. 13, No. 1, 1981, pp. 331-340.
63. Kim, D. and Chaudhuri, R. A., "Full and Von Kármán Geometrically Nonlinear Analyses of Laminated Cylindrical Panels", *AIAA Journal*, Vol. 33, No. 11, November, 1995, pp. 2173-2181.
64. Tsai, C. T., Palazotto, A. N., and Dennis, S. T., "Large-rotation Snap-through Buckling in Laminated Cylindrical Panels", *Finite Elements in Analysis and Design*, Vol. 9, No. 1, April, 1991, pp. 65-75.
65. Saigal, S., Kapania, R. K., and Yang, T. Y., "Geometrically Nonlinear Finite Element Analysis of Imperfect Laminated Shells", *Journal of Composite Materials*, Vol. 20, March, 1986, pp. 197-214.

66. Kim, S. J., Goo, N. S., and Kim, T. W., "The Effect of Curvature on the Dynamic Response and Impact-induced Damage in Composite Laminates", *Composites Science and Technology*, Vol. 57, 1997, pp. 763-773.
67. Talbot, M. and Dhatt, G., "Three Discrete Kirchoff Elements for Shell Analysis with Large Geometrical Non-linearities and Bifurcations", *Engineering Computations*, Vol. 4, March, 1987, pp. 15-22.
68. Laschet, G. and Jeusette, J.-P., "Postbuckling Finite Element Analysis of Composite Panels", *Composite Structures*, Vol. 14, 1990, pp. 35-48.
69. Simo, J. C., Fox, D. D., and Rifai, M. S., "Geometrically Exact Stress Resultant Shell Models: Formulation and Computational Aspects of the Nonlinear Theory", in *Analytical and Computational Models of Shells*, ed. Noor, A. K., Belytschko, T., and Simo, J. C., Winter Annual Meeting of the ASME. ASME, New York, 1989, pp. 161-190.
70. Voyiadjis, G. Z. and Shi, G., "Nonlinear Postbuckling Analysis of Plates and Shells by Four-Noded Strain Element", *AIAA Journal*, Vol. 30, No. 4, April, 1992, pp. 1110-1116.
71. Crisfield, M. A., *Non-linear Finite Element Analysis of Solids and Structures*, Vol. 1, John Wiley and Sons, New York, 1991, pp. 268-269.
72. Rankin, C. C. and Brogan, F. A., "An Element-Independent Corotational Procedure for the Treatment of Large Rotations", *Collapse Analysis of Structures: The 1984 Pressure Vessel and Piping Conference and Exhibition*, San Antonio, TX, 1984, pp. 85-100.
73. Brogan, F. A., Rankin, C. C., Cabiness, H. D., and Loden, W. A., "STAGS User Manual - Version 2.3", LMMS PO32594, Lockheed Martin Missiles and Space Co., Inc., July, 1996.

74. Mirmiran, A. and Amde, A. M., "Effects of Fabrication Process on Prestressed Composite Arches", *Journal of Structural Engineering*, Vol. 121, No. 1, January, 1995, pp. 124-131.
75. Greer Jr., J. M. and Palazotto, A. N., "Non-linear Finite Element Analysis of Isotropic and Composite Shells by a Total Lagrangian Decomposition Scheme", *Mechanics of Composite Materials and Structures*, Vol. 3, No. 3, September, 1996, pp. 241-271.
76. Bathe, K.-J., *Finite Element Procedures*, Prentice Hall, Englewood Cliffs, NJ, 1996, pp. 630-636.
77. Ranniger, C. U., Lagace, P. A., and Graves, M. J., "Damage Tolerance and Arrest Characteristics of Pressurized Graphite/Epoxy Tape Cylinders", *Composite Materials: Fatigue and Fracture—Fifth Volume, ASTM STP 1230*, ASTM, 1995, pp. 407-426.
78. Niu, M. C. Y., *Airframe Structural Design - Practical Design Information and Data on Aircraft Structures*, 8th ed. Conmilit Press Ltd., Los Angeles, 1995, pp. 384-389.
79. Rankin, C. and Brogan, F., "The Computational Structural Mechanics Testbed Structural Element Processor ES5: STAGS Shell Element", NASA-CR-4358, Lockheed Missiles and Space Company, Inc., 1991.
80. Tsai, S., "A Survey of Macroscopic Failure Criteria for Composite Materials", *Journal of Reinforced Plastics and Composites*, Vol. 3, January, 1984, pp. 40-62.
81. Nahas, M. N., "Survey of Failure and Post-Failure Theories of Laminated Fiber-Reinforced Composites", *Journal of Composite Technology and Research*, Vol. 8, No. 4, Winter, 1986, pp. 138-153.
82. Chang, F.-K. and Kutlu, Z., "Strength and Response of Cylindrical Composite Shells Subjected to Out-of-Plane Loadings", *Journal of Composite Materials*, Vol. 23, January, 1989, pp. 11-31.

83. Wardle, B. L., Lagace, P. A., and Tudela, M. A., "Buckling Response of Transversely Loaded Composite Shells - Part 2: Numerical Analysis", 1998, *in preparation*.
84. Lin, H. J. and Lee, Y. J., "Use of Statical Indentation Laws in the Impact Analysis of Composite Laminated Plates and Shells", *Journal of Applied Mechanics*, Vol. 57, No. 3, 1990, pp. 787-789.
85. Lagace, P. A., Brewer, J. C., and Varnerin, C., "TELAC Manufacturing Course Notes", TELAC Report 88-4B, Massachusetts Institute of Technology, May, 1988.
86. Lagace, P. A. and Wolf, E., "Impact Damage Resistance of Several Laminated Material Systems", *AIAA Journal*, Vol. 33, No. 6, June, 1995, pp. 1106-1113.

APPENDIX A

MANUFACTURING DATA

Manufacturing data for all specimens is presented in Table A.1. Three radii are calculated from measurements, as described in chapter 5, and their average reported as well as the percent difference between the average and nominal values. The nominal value for radius is 1829 mm (72"). Thickness is averaged from nine points measured following the procedure given in chapter 5. The percent difference between the average and nominal values are presented as well as the coefficient of variation for the thickness data. Nominal values for the three thicknesses, T_1 , T_2 , and T_3 are 0.804 mm, 1.608 mm, and 2.412 mm, respectively.

Table A.1 Radius and Thickness Data

Specimen	Radius		Thickness		C. V. ^a
	Average	Difference	Average	Difference	
<i>R₁₂S₃T₁-1</i>	1978 mm	+8.2 %	0.822 mm	+2.3 %	1.0 %
<i>R₁₂S₃T₁-2</i>	1959 mm	+7.1 %	0.836 mm	+3.9 %	0.9 %
<i>R₁₂S₃T₂-1</i>	1942 mm	+6.2 %	1.634 mm	+1.6 %	0.9 %
<i>R₁₂S₃T₂-2</i>	1968 mm	+7.6 %	1.526 mm	-5.1 %	0.9 %
<i>R₁₂S₃T₃-1</i>	1959 mm	+7.1 %	2.493 mm	+3.4 %	0.3 %
<i>R₁₂S₃T₃-2</i>	1915 mm	+4.7 %	2.334 mm	-3.2 %	0.7 %

^a Indicates coefficient of variation.

APPENDIX B

NUMERICAL COMPARISON TO PREVIOUS EXPERIMENTAL LOAD-DEFLECTION DATA

Results from numerical analysis performed in this work are compared in this appendix with experimental data for specimens tested in Reference [21]. The loading response comparison is based on load-deflection histories at the center of the shell as described in chapter 4. All analyses utilize experimentally determined values for shell radius given in Table B.1 as explained in chapter 4. Three analyses utilizing the STAGS code are provided for comparison to the experimental data: limit point, bifurcation, and simple support. The limit-point solutions are generated with a symmetric 10x10 mesh and result in symmetric deformation modes. The bifurcation response is evaluated with the AMT (see chapter 4) using an asymmetric 10x6 / 10x5 mesh. Bifurcation involves branching from a symmetric prebuckling deformation mode to an asymmetric bifurcation mode. The simple support analysis utilizes the AMT and asymmetric mesh but the shell has a traditional simple support along the circumferential edges rather than a hinge.

Table B.1 Measured^a Values of Radius Used in Numerical Analysis

Specimen	Radius (m)
$R_6S_1T_1$	0.857
$R_6S_1T_2$	0.880
$R_6S_1T_3$	0.867
$R_6S_2T_1$	0.926
$R_6S_2T_2$	0.852
$R_6S_2T_3$	0.913
$R_6S_3T_1$	0.912
$R_6S_3T_2$	0.890
$R_6S_3T_3$	0.899
$R_{12}S_1T_1$	1.554
$R_{12}S_1T_2$	1.808
$R_{12}S_1T_3$	1.746
$R_{12}S_2T_1$	1.628
$R_{12}S_2T_2$	1.540
$R_{12}S_2T_3$	1.729
$R_{12}S_3T_1$	1.743
$R_{12}S_3T_2$	1.677
$R_{12}S_3T_3$	1.713

^a Measured in [21] but previously unreported.

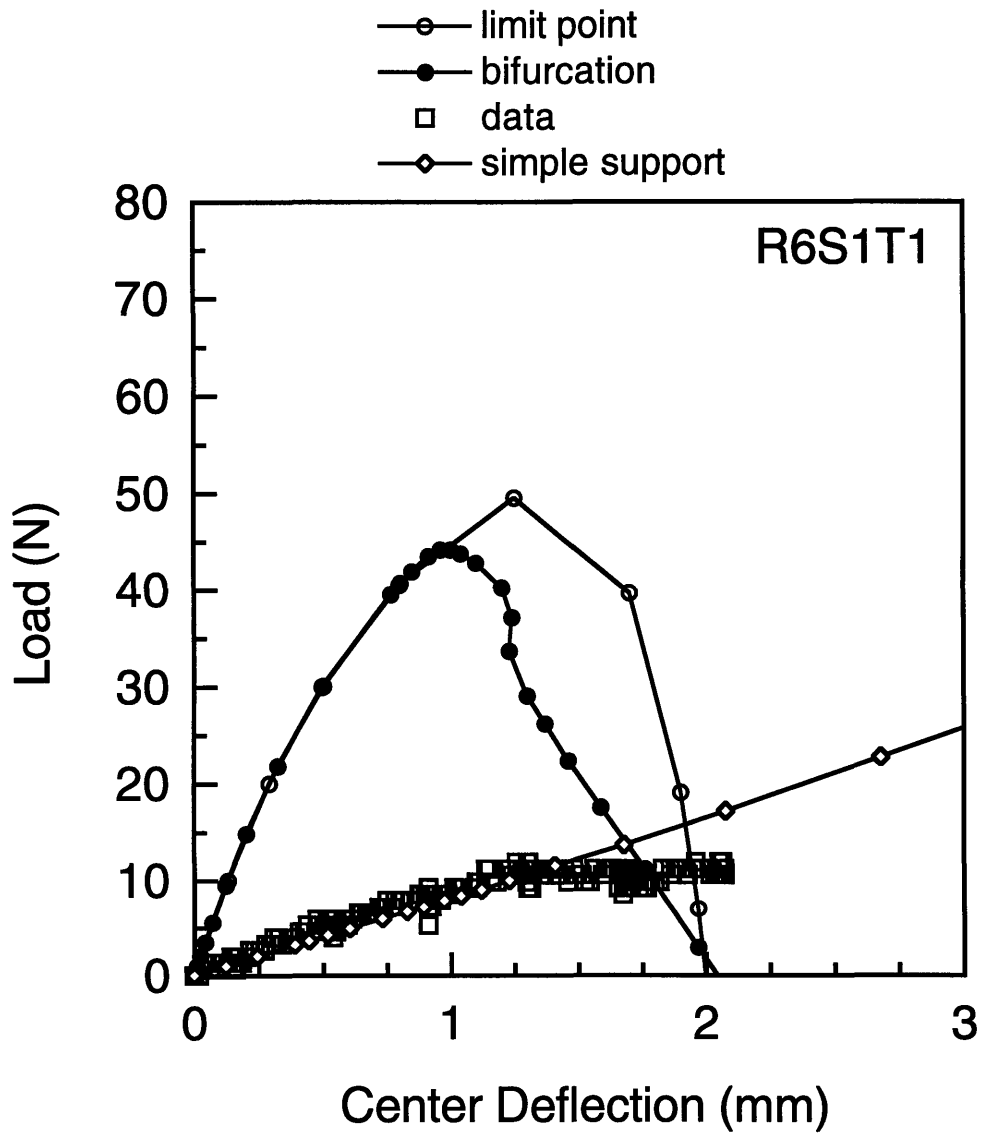


Figure B.1 Comparison of results from numerical analysis and experimental data [21] for the loading response of specimen $R_6S_1T_1$.

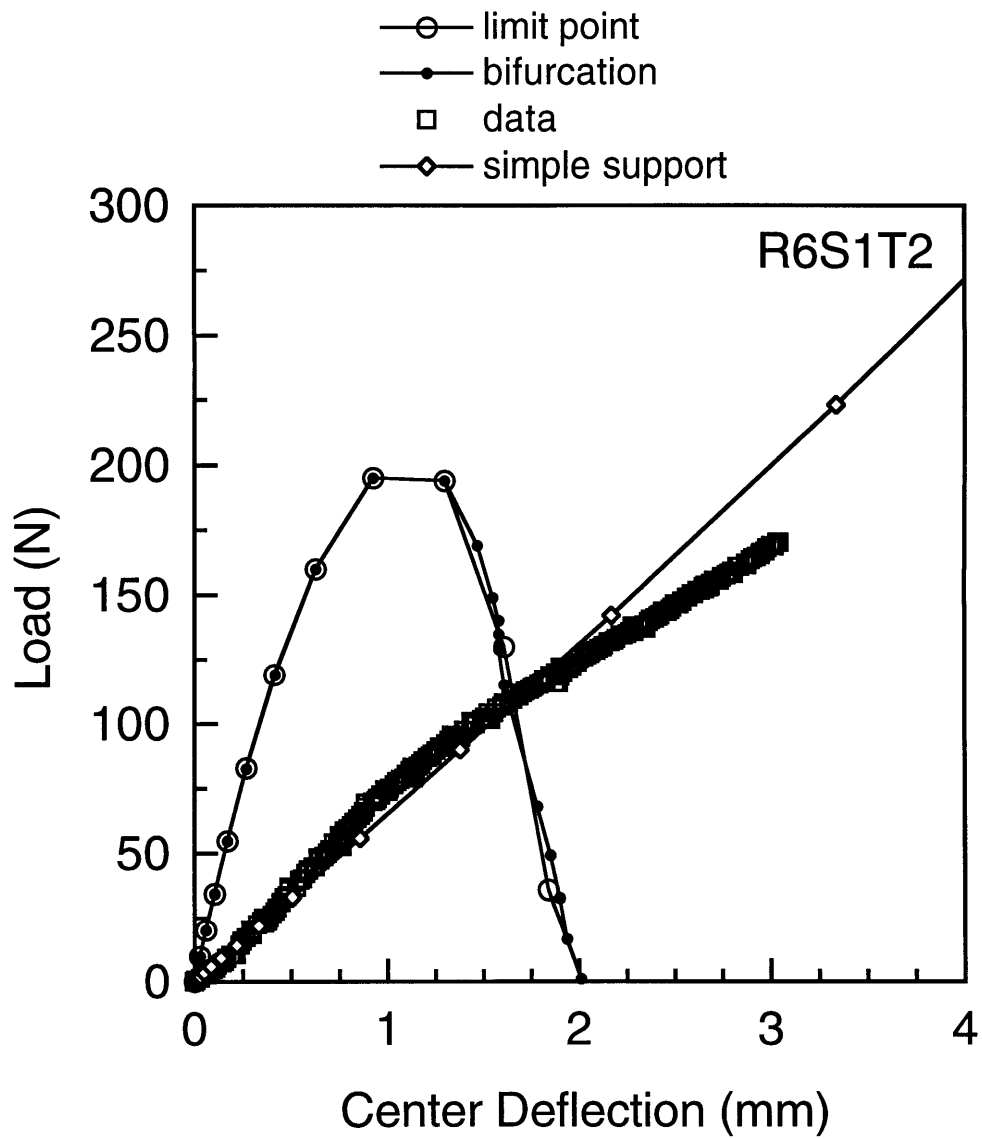


Figure B.2 Comparison of results from numerical analysis and experimental data [21] for the loading response of specimen $R_6S_1T_2$.

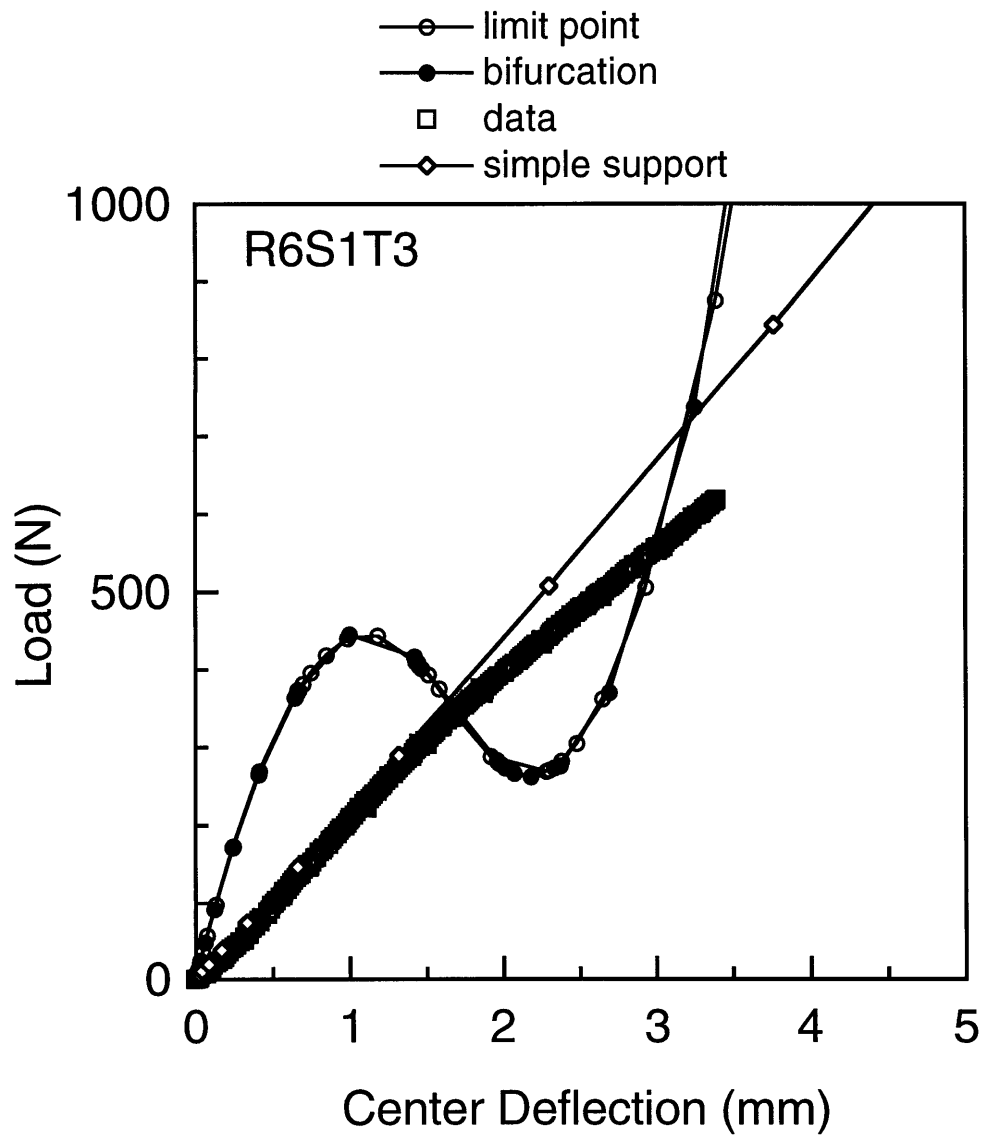


Figure B.3 Comparison of results from numerical analysis and experimental data [21] for the loading response of specimen $R_6S_1T_3$.

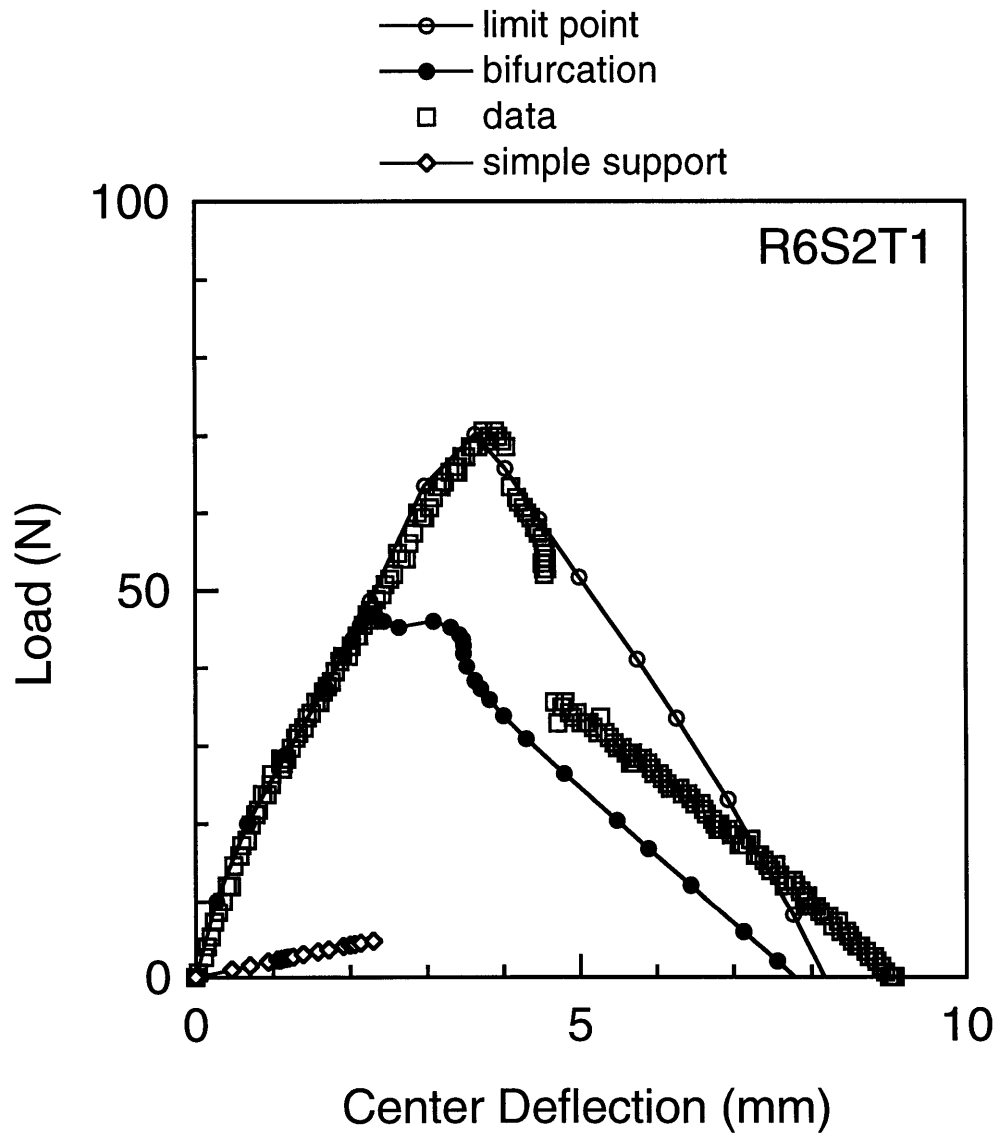


Figure B.4 Comparison of results from numerical analysis and experimental data [21] for the loading response of specimen $R_6S_2T_1$.

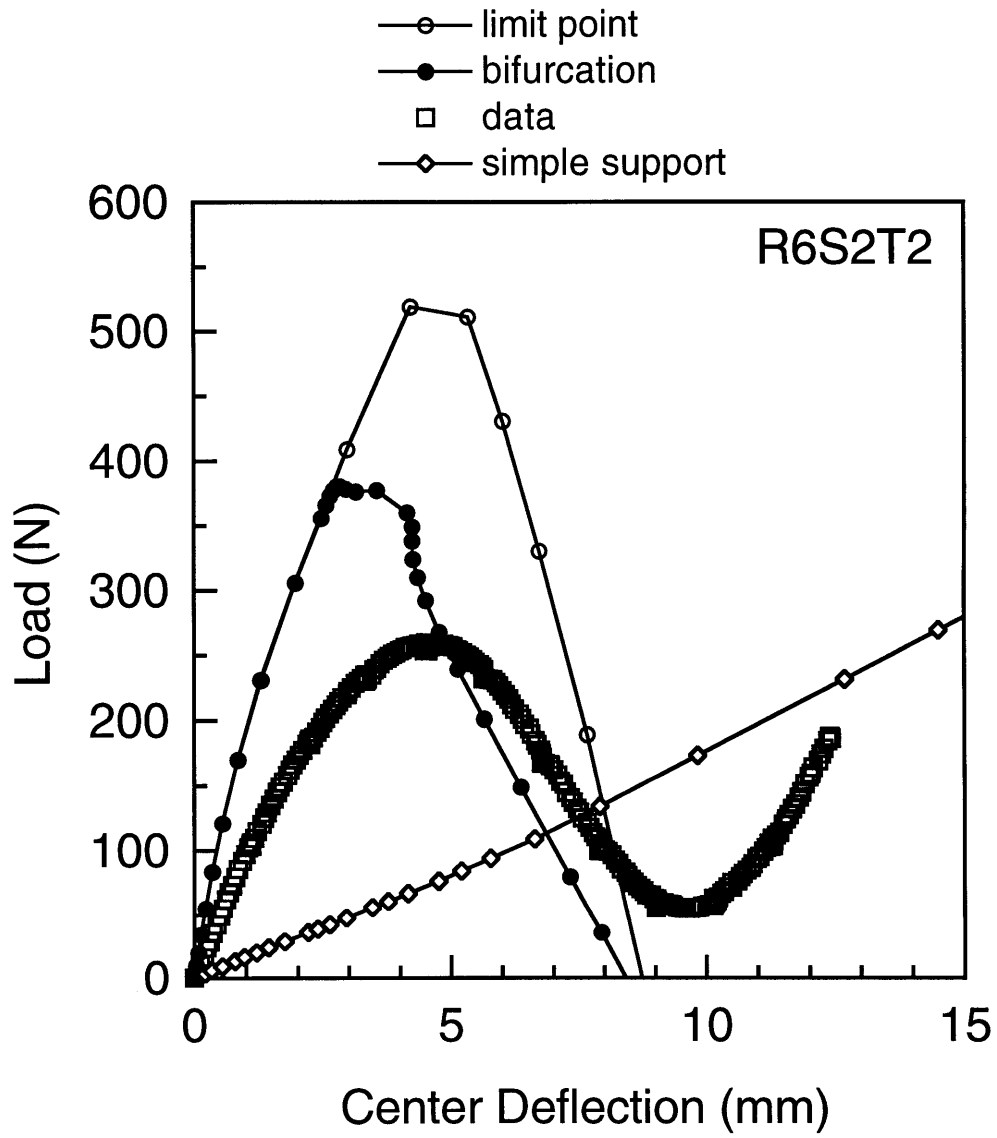


Figure B.5 Comparison of results from numerical analysis and experimental data [21] for the loading response of specimen $R_6S_2T_2$.

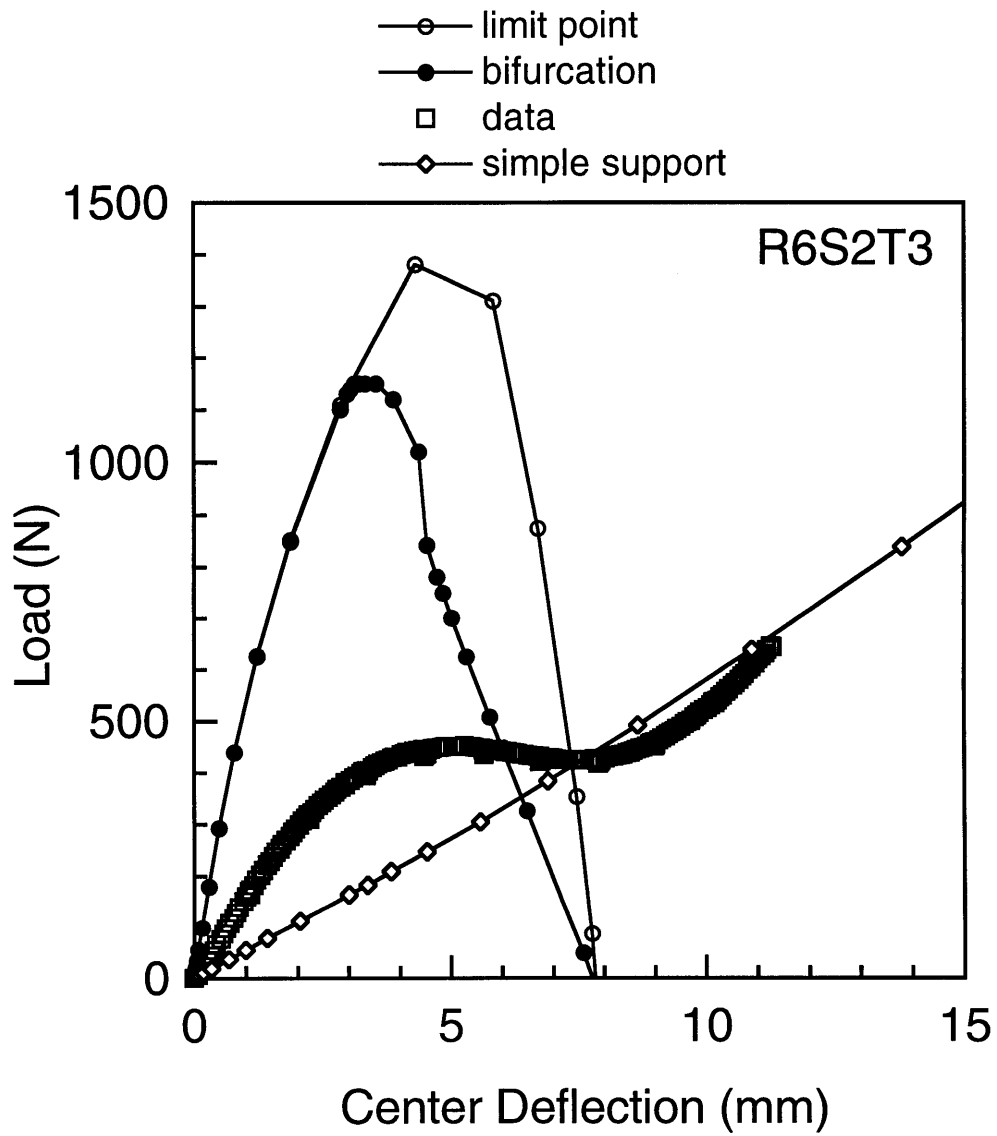


Figure B.6 Comparison of results from numerical analysis and experimental data [21] for the loading response of specimen $R_6S_2T_3$.

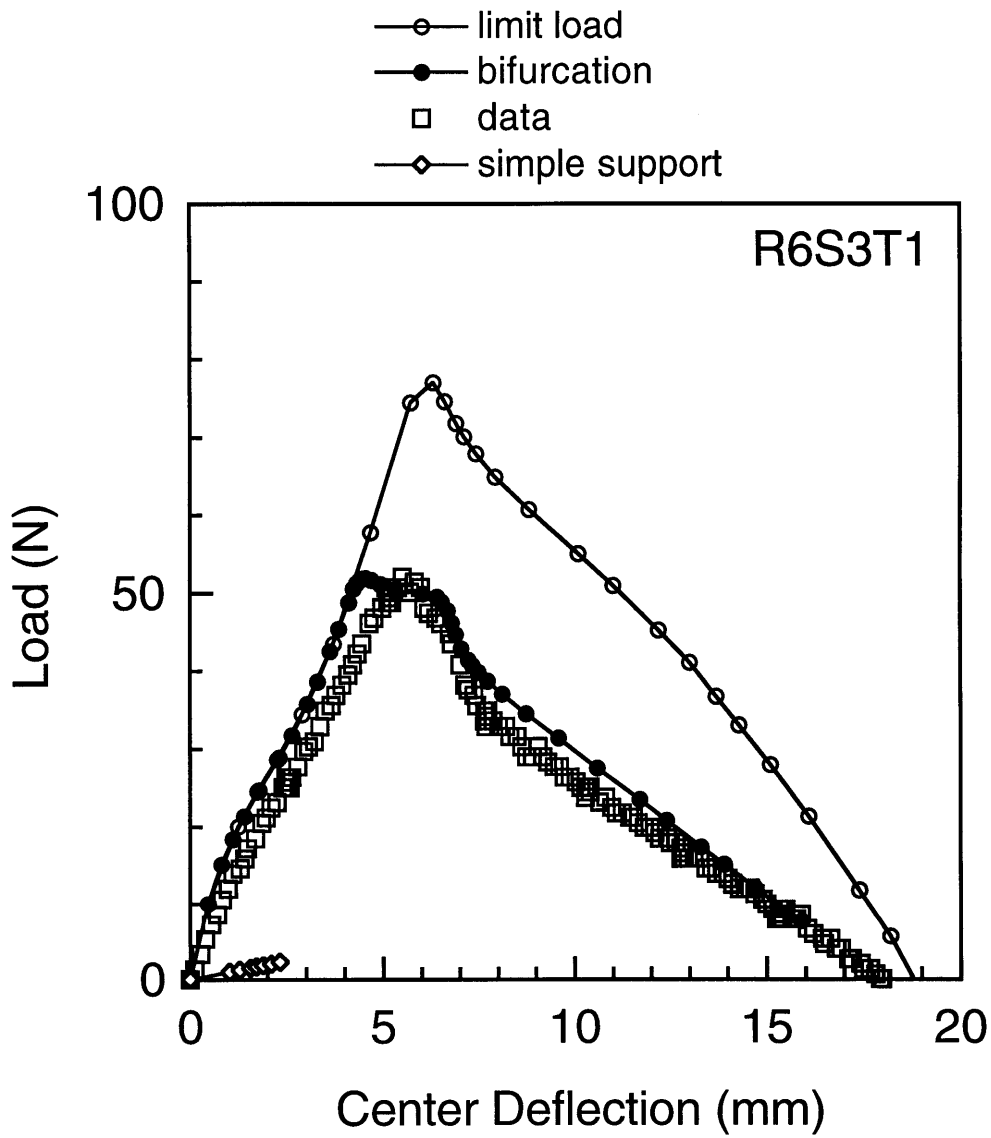


Figure B.7 Comparison of results from numerical analysis and experimental data [21] for the loading response of specimen $R_6S_3T_1$.

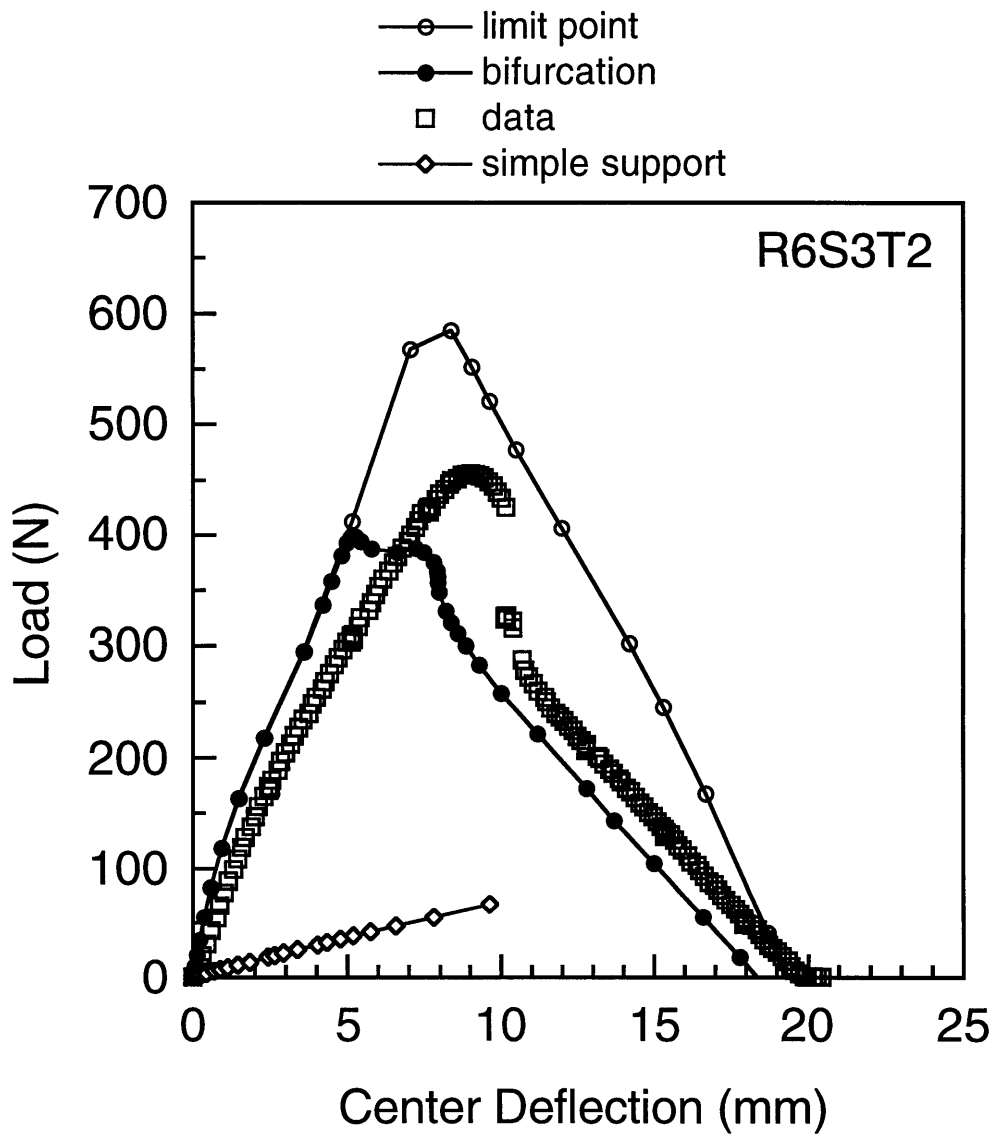


Figure B.8 Comparison of results from numerical analysis and experimental data [21] for the loading response of specimen $R_6S_3T_2$.

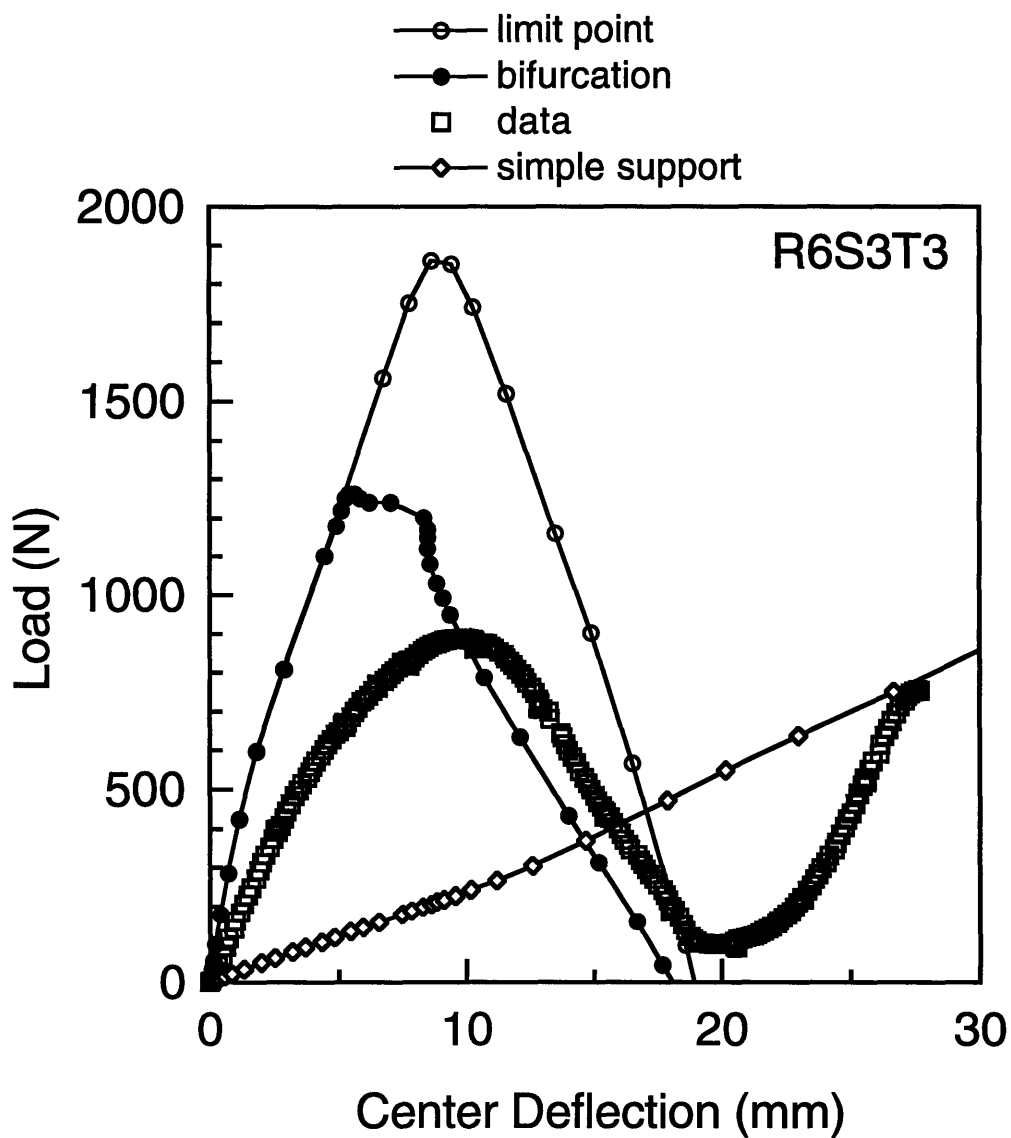


Figure B.9 Comparison of results from numerical analysis and experimental data [21] for the loading response of specimen $R_6S_3T_3$.

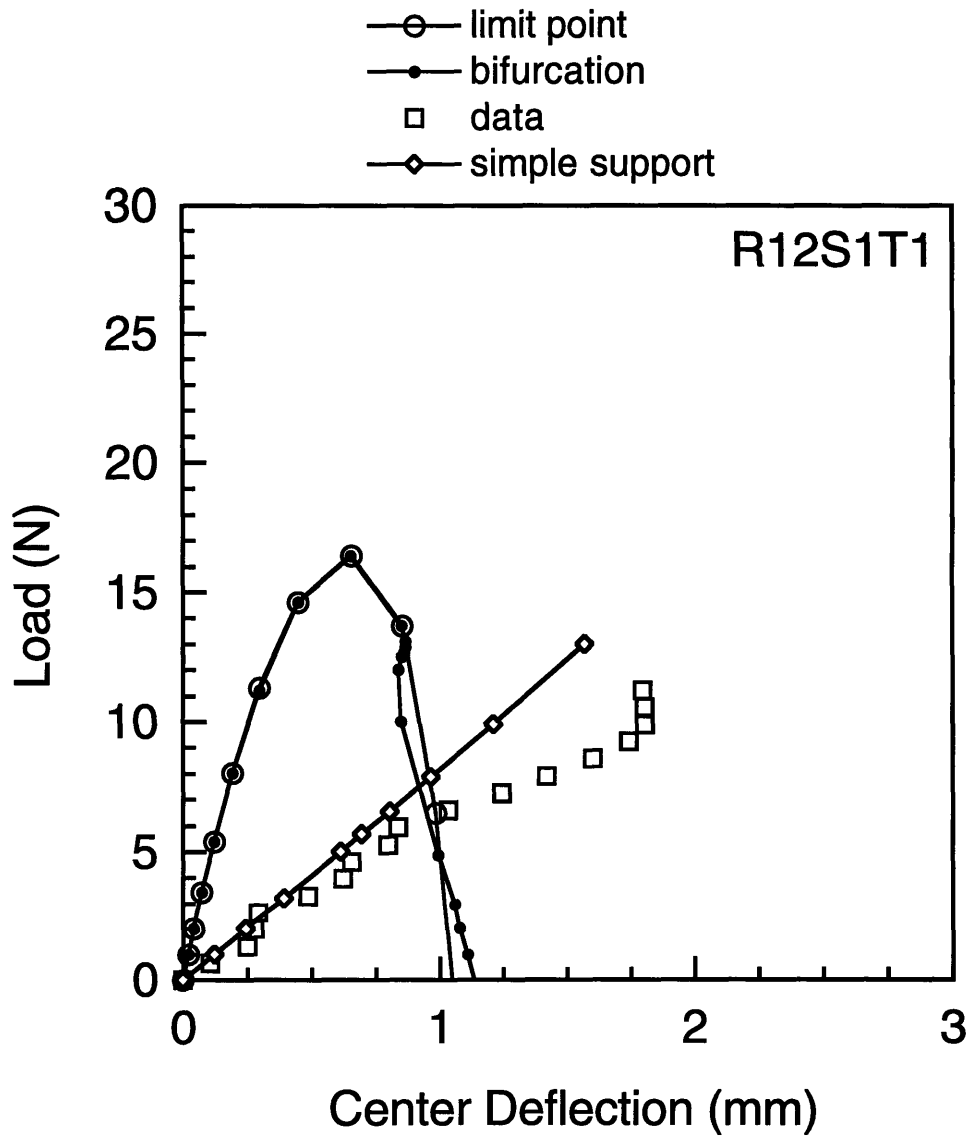


Figure B.10 Comparison of results from numerical analysis and experimental data [21] for the loading response of specimen $R_{12}S_1T_1$.

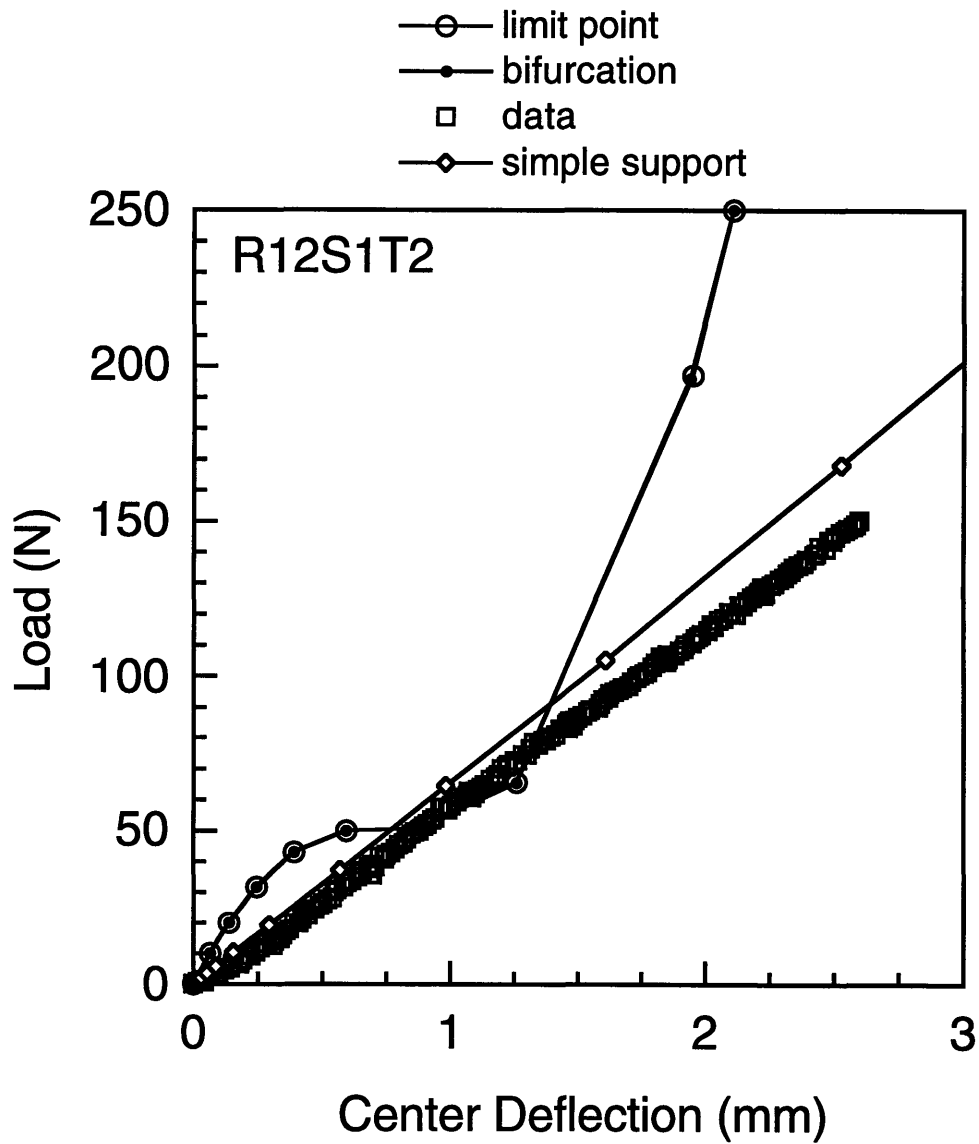


Figure B.11 Comparison of results from numerical analysis and experimental data [21] for the loading response of specimen $R_{12}S_1T_2$.

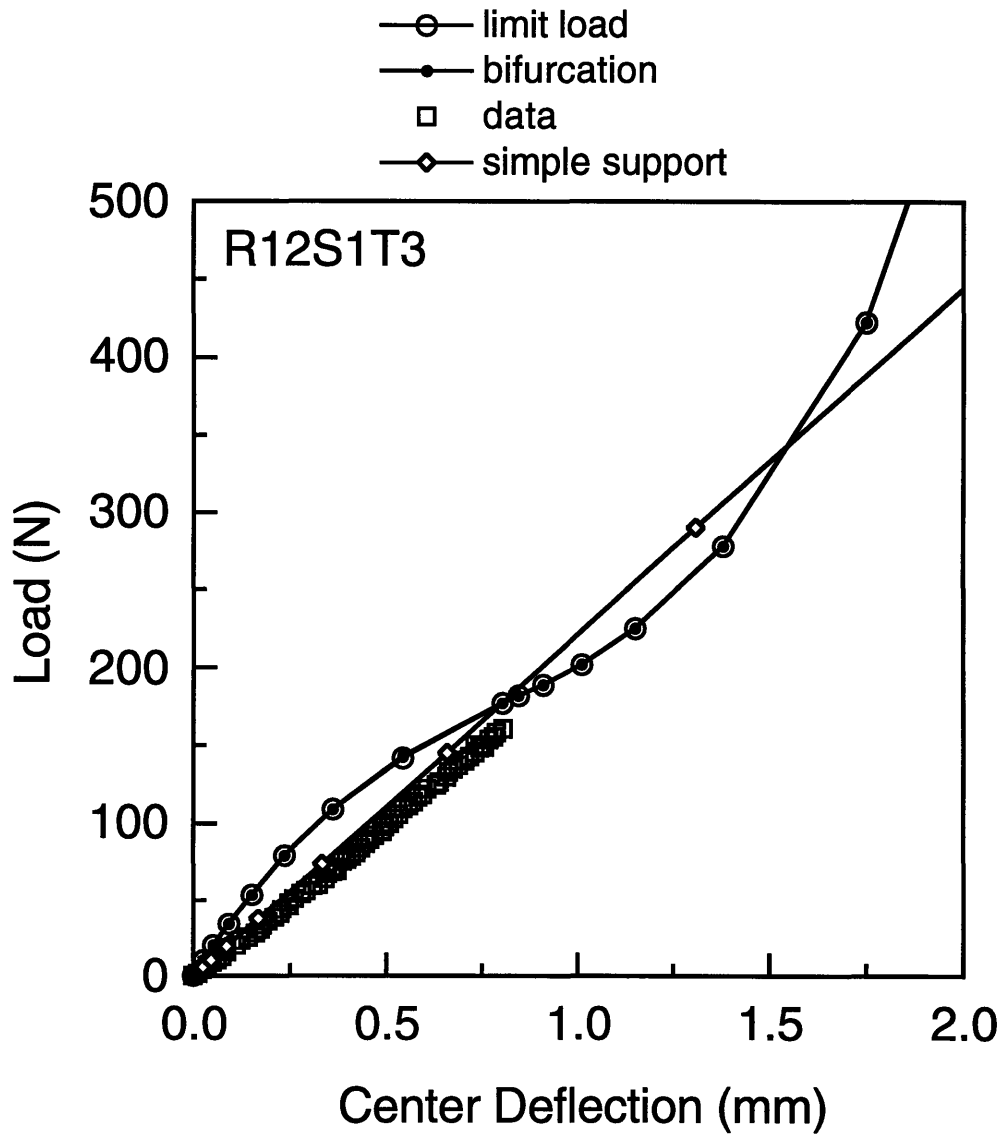


Figure B.12 Comparison of results from numerical analysis and experimental data [21] for the loading response of specimen $R_{12}S_1T_3$.

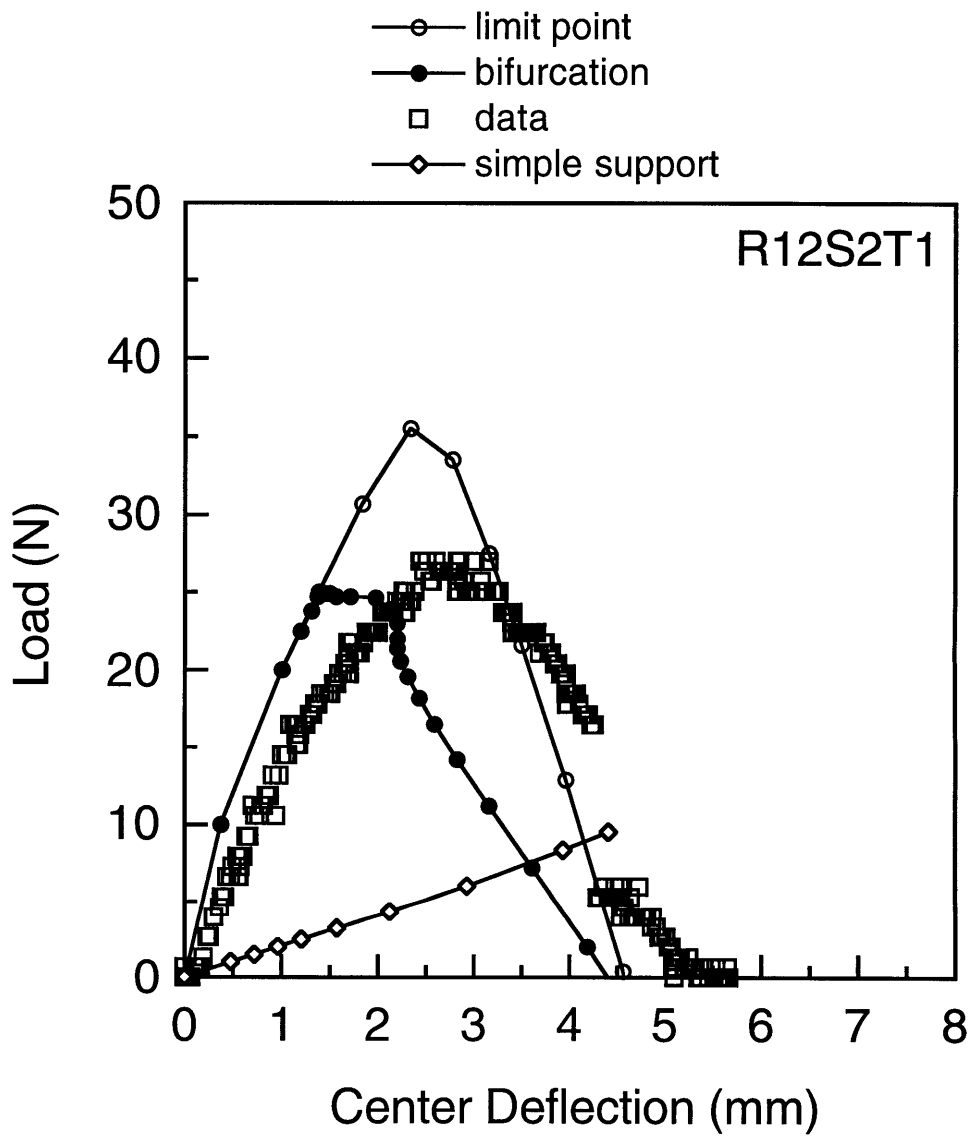


Figure B.13 Comparison of results from numerical analysis and experimental data [21] for the loading response of specimen $R_{12}S_2T_1$.

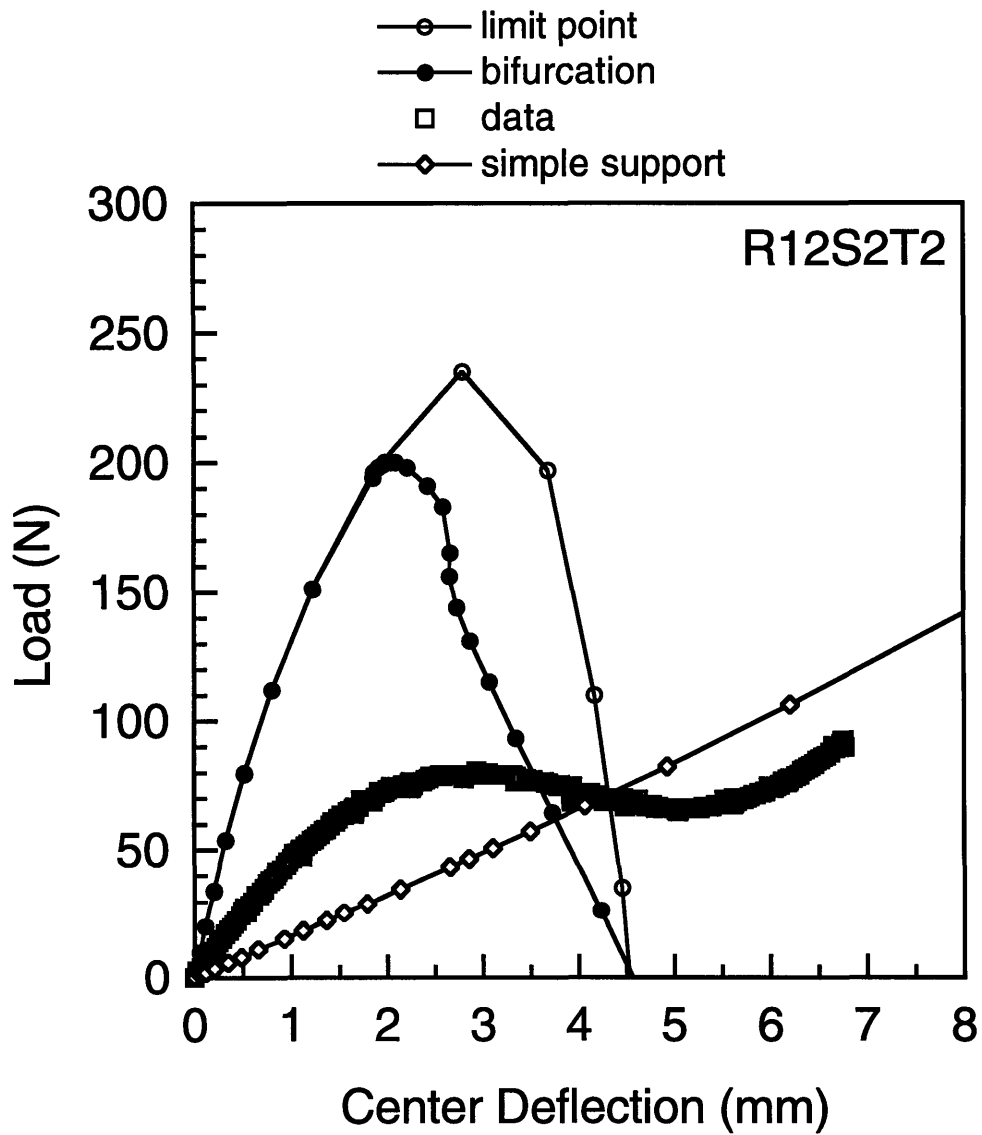


Figure B.14 Comparison of results from numerical analysis and experimental data [21] for the loading response of specimen $R_{12}S_2T_2$.

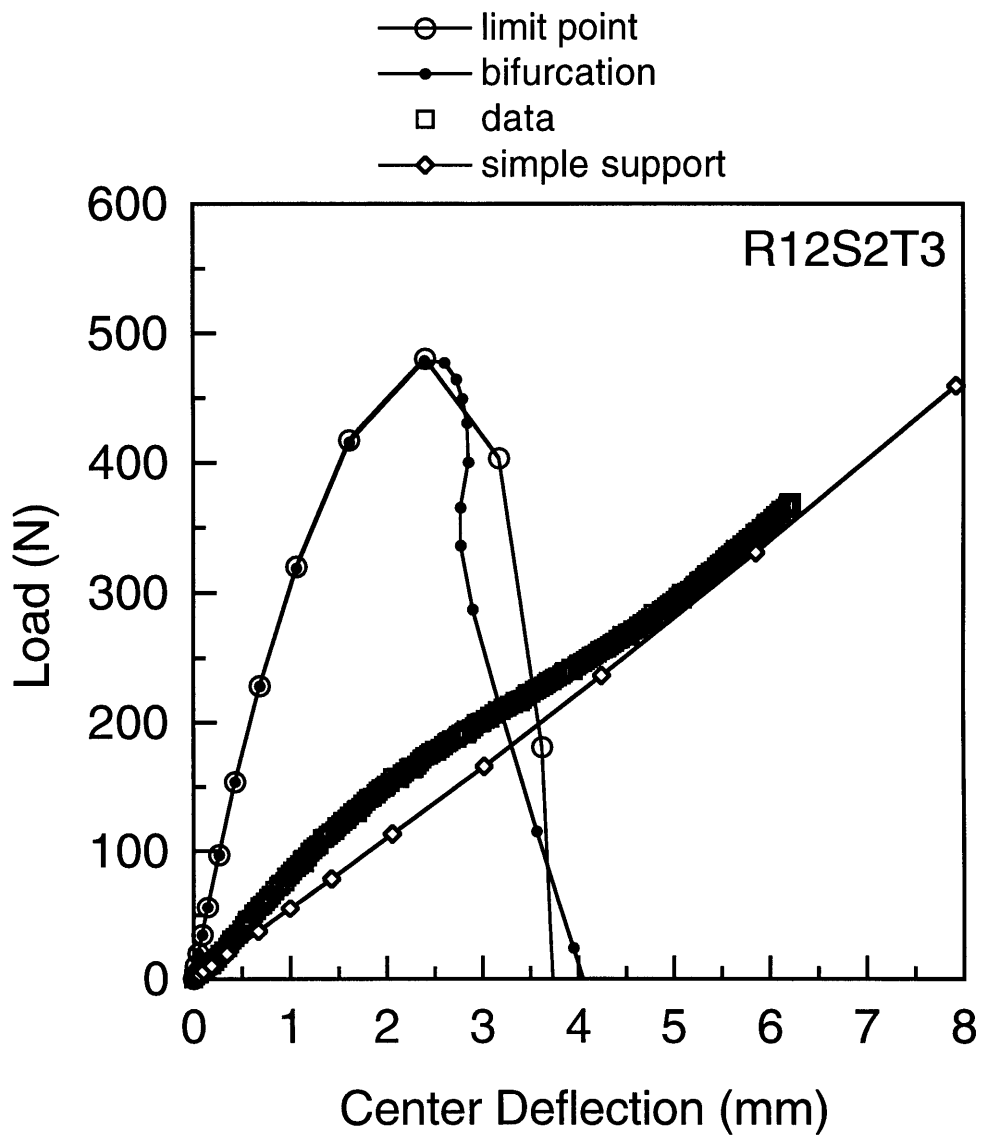


Figure B.15 Comparison of results from numerical analysis and experimental data [21] for the loading response of specimen $R_{12}S_2T_3$.

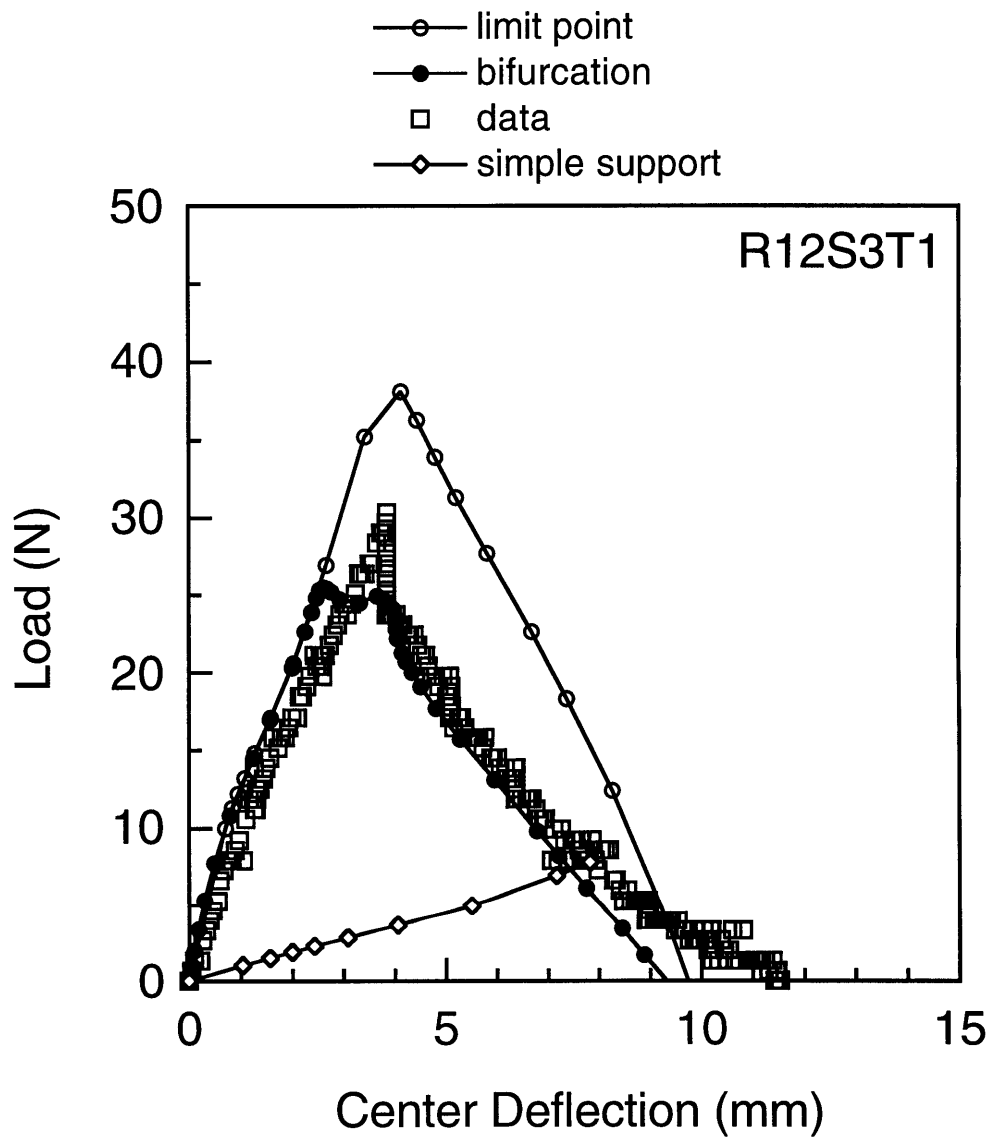


Figure B.16 Comparison of results from numerical analysis and experimental data [21] for the loading response of specimen $R_{12}S_3T_1$.

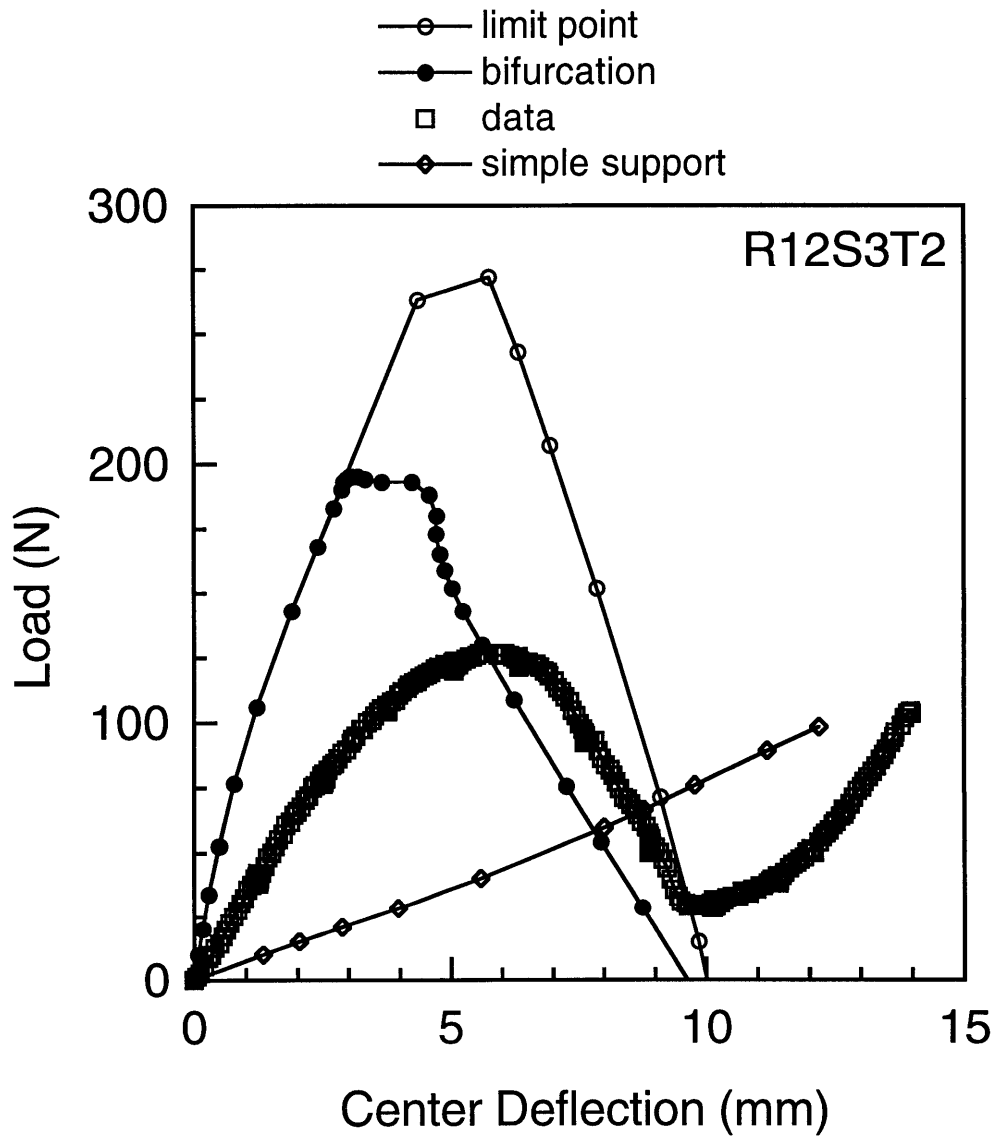


Figure B.17 Comparison of results from numerical analysis and experimental data [21] for the loading response of specimen $R_{12}S_3T_2$.

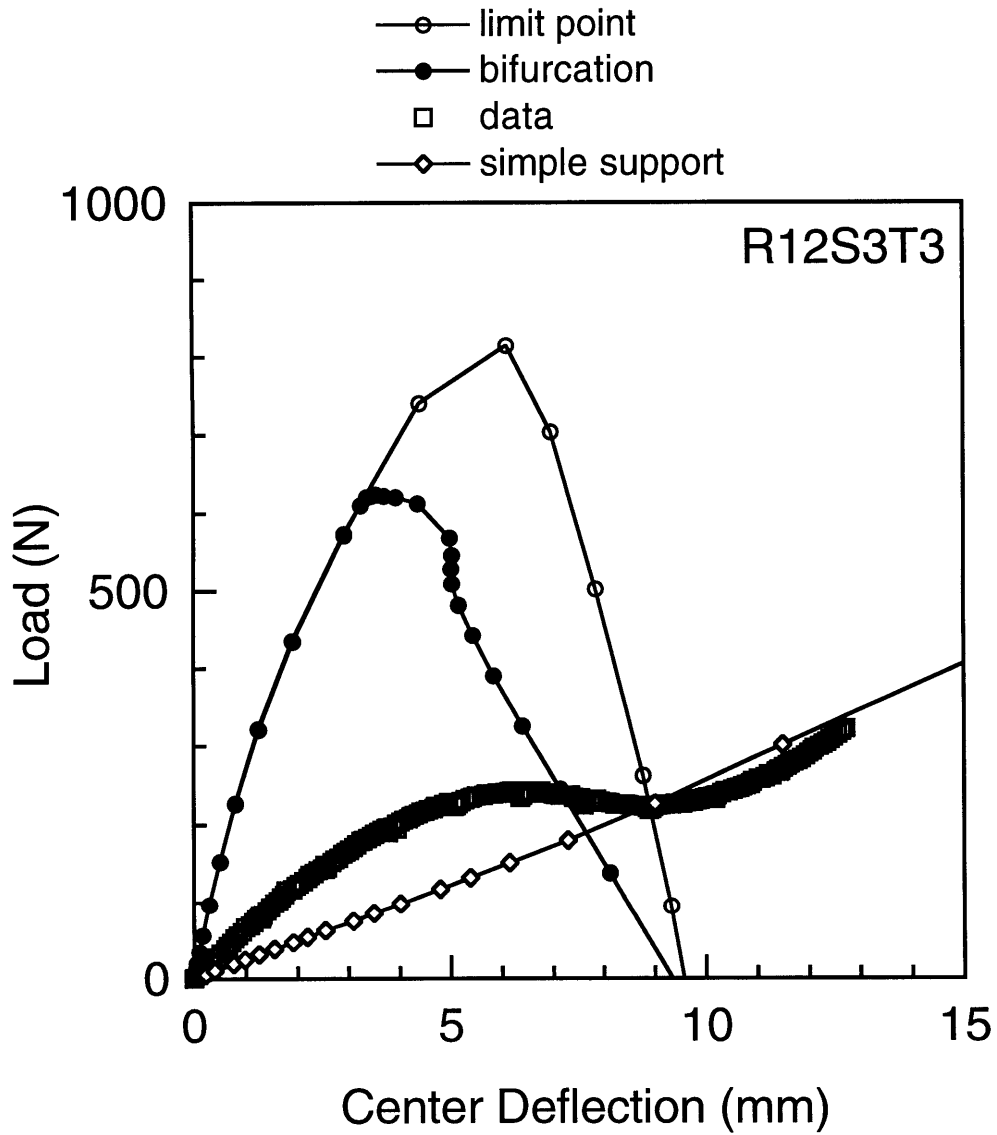


Figure B.18 Comparison of results from numerical analysis and experimental data [21] for the loading response of specimen $R_{12}S_3T_3$.